TOTEM-TDR-003

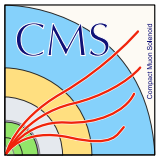

CMS-TDR-13

CERN-LHCC-2014-021

September 8, 2014

CMS-TOTEM Precision Proton Spectrometer Technical Design Report

The CMS and TOTEM Collaborations

Abstract

This report describes the technical design and outlines the expected performance of the CMS-TOTEM Precision Proton Spectrometer (CT-PPS). CT-PPS adds precision proton tracking and timing detectors in the very forward region on both sides of CMS at about 200m from the IP to study central exclusive production (CEP) in proton-proton collisions. CEP provides a unique method to access a variety of physics topics at high luminosity LHC, such as new physics via anomalous production of W and Z boson pairs, high-p_T jet production, and possibly the production of new resonances. The CT-PPS detector consists of a silicon tracking system to measure the position and direction of the protons, and a set of timing counters to measure their arrival time with a precision of the order of 10 ps. This in turn allows the reconstruction of the mass and momentum as well as of the z coordinate of the primary vertex of the centrally produced system. The framework for the development and exploitation of CT-PPS is defined in a Memorandum of Understanding signed by CERN as the host laboratory and the CMS and TOTEM Collaborations. The expected performance of CT-PPS is discussed, including detailed studies of exclusive WW and dijet production. The planning for the implementation of the new detectors is presented, including construction, testing, and installation.

Editors

Contents

1 Introduction

1.1 Overview of the CMS-TOTEM Precision Proton Spectrometer

We plan to add precision proton tracking and timing detectors in the very forward region on both sides of CMS, to study central exclusive production in proton-proton collisions, namely the process $pp \to pXp$, in which the protons do not dissociate and interact via photon or colour-singlet exchange to produce the system X in the central region. The CMS-TOTEM Precision Proton Spectrometer (CT-PPS) is a magnetic spectrometer that uses the LHC magnets between the Interaction Point (IP) and detector stations at $\sim$ 210m from the IP on both sides, to bend protons that have lost a small fraction of their momentum out of the beam envelope so their trajectories can be measured. The layout of the beam line in the 210 m region after the first Long Shutdown (LS1) is shown in Figure 1.

The CT-PPS detectors consists of a silicon tracking system to measure the position and direction of the protons, and a set of timing counters to measure their arrival time. This in turn allows the reconstruction of the mass and momentum as well as the z coordinate of the primary vertex of the centrally produced system, irrespective of its decay mode. The detector covers an area of about 4 cm^2 on each arm. In total it uses 144 pixel readout chips and has $\sim$200 timing readout channels. The total cost of the detectors and infrastructure is below 1 MCHF.

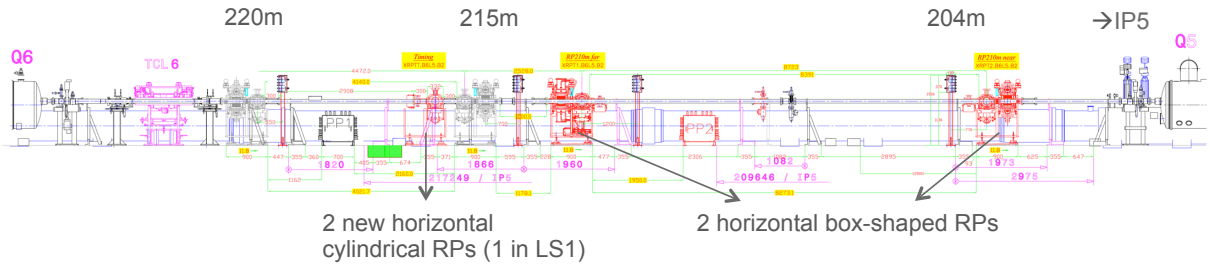

Figure 1: The layout of the CT-PPS detectors in the 210 m region after LS1. The cylindrical Roman Pots are equipped with timing detectors for PU rejection. The upgraded box-shaped Roman Pots (RPs) are equipped with pixel detectors to measure the displacement of the scattered protons w.r.t. the beam.

Central exclusive production (CEP) provides a unique method to access a variety of physics topics, such as new physics via anomalous production of W and Z boson pairs, high transverse momentum (p_T) jet production, and possibly the production of new resonances. These studies can be carried out in particularly clean experimental conditions thanks to the absence of proton remnants. The detection of the two final state protons, scattered at almost zero-degrees, in very forward near-beam detectors, provides a striking signature. The measurement of the leading protons allows to fully determine the kinematics of the central system. Well defined final states in the CMS central detector matching the protons kinematics can then be selected and precisely reconstructed.

The exclusive two-photon production of pairs of photons, W and Z bosons provides a novel and unique testing ground for the electroweak gauge boson sector. The virtualities of the exchanged photons are on average very small, which makes the LHC a quasi-real photon collider with centre-of-mass energy approaching 1 TeV – a region so far unexplored. The detection of $\gamma\gamma \to W^+W^-$ events allows to measure the quartic gauge coupling $WW\gamma\gamma$ with high precision. We expect to achieve of the order of 10^{3-4} times better sensitivity to anomalous quartic gauge couplings than LEP [1]-[8] and Tevatron [9].

A number of physics studies will be aimed at the understanding of the QCD mechanisms involved in CEP. Exclusive di-jet production with $M(jj)$ up to $\sim 700 - 800$ GeV allows the study of pure gluon jet samples with small contamination of quark jets. The detailed characterization of gluon jets in this data sample relative to quark jets may improve the efficiency of gluon vs. quark jets separation, which is of

particular interest for Vector Boson Fusion (VBF) forward jet tagging.

One of the reasons that make CEP particularly attractive is that if the outgoing protons remain intact and scatter through small angles then, to a very good approximation, the di-gluon system obeys a $J_z = 0$, C-even, P-even, selection rule [10]. This selection rule readily permits a clean determination of the quantum numbers of any new resonance.

A major concern for the CT-PPS physics programme is the background expected in the high pile-up environment of normal LHC running. The leading background results from inelastic events overlapping with two protons from single diffraction events occurring in the same bunch crossing. This pile-up background can be reduced by using proton timing for primary vertex determination. The physics performance studies presented in Chapter 2 are carried out for two values of the time resolution (baseline 10 ps and conservative 30 ps). Further background rejection is achieved by requiring the kinematics of the system measured in the central detector to be compatible with the kinematics of the two protons. In some channels, in particular W^+W^-, requiring a small number of tracks associated to the main vertex provides a quite effective rejection of pileup and other Standard Model (SM) backgrounds.

The present TDR addresses only the detector configuration proposed for the Phase 1 Upgrade. In this phase, the CT-PPS detectors will be located in the region at $200-240$m from the interaction point. In this configuration, the spectrometer is not sensitive to the central exclusive production of the recently discovered Higgs resonance at 125 GeV since its mass acceptance is above a threshold between 200 and 300 GeV depending on the distance of detectors to the beam. If the detection of only one proton is required, the acceptance is sizable, but the background may be too large. The possibility of detecting central exclusive Higgs production was investigated in 2005-2009 in the frame of the FP420 R&D project, which studied the feasibility of installing and operating spectrometers based on silicon trackers and fast timing detectors in the LHC tunnel at about 420 m from the ATLAS and CMS IPs [11]. However, the low cross section for central exclusive production of the Higgs (less than 10 fb), along with the need to install the detectors in the cryogenic region of the LHC make this measurement difficult. The evaluation of the interest and feasibility of pursuing a Phase2 Upgrade of CT-PPS with sensitivity to invariant masses down to ~ 100 GeV is outside the scope of this TDR.

1.1.1 CMS-TOTEM Memorandum of Understanding

The framework for the development and exploitation of CT-PPS is defined in a Memorandum of Understanding (MoU) signed in December 2013 by CERN as the host laboratory and the CMS and TOTEM Collaborations.

CMS wants to integrate in the detector apparatus a new Proton Spectrometer at ~ 210m from the IP allowing the measurement of scattered protons, with the aim of studying, during standard low β^* running at high luminosity, low cross section Electroweak (EW) and QCD physics in CEP. The CMS Collaboration Board (CB) has approved the physics motivations and detector concept, recognizing it as a potentially important part of the CMS programme.

TOTEM, with its own apparatus and relative upgrades, will pursue the high cross section forward physics programme at 14 TeV in high β^* special runs, which will be supported by CMS as joint runs in terms of trigger and detector readout. Moreover, TOTEM is interested in studying low cross section EW and QCD physics in CEP processes with CMS.

The MoU states that CMS and TOTEM are willing to combine efforts to jointly undertake the initial phase of the CEP low cross section physics programme through a Joint Project to be carried until LS2. The possible continuation of the programme after LS2 will be decided after the review of the initial phase results.

The programme until LS2 has two phases:

- Exploratory phase (2015-16), with the following goals:
  - Prove the ability to operate detectors close to the beam-line at high luminosity, showing that the beam impedance caused by the Roman Pots (RPs) (and later the Movable Beam Pipes(MBPs)) and the losses caused by particles interacting in the CT-PPS components do not prevent the stable operation of the LHC beams and do not affect significantly the luminosity performance of the machine. In 2015, evaluate RPs in the $204 - 215$ m region. Evaluate the option of MBPs in the 240 m region, possibly in 2016. The joint programme may be redefined or cancelled if it proves to be an impediment to the rest of the CMS or TOTEM Physics programmes;
  - Start tests with existing TOTEM silicon strip detectors in two horizontal RPs at sustainable radiation intensity and upgrade to pixel detectors as soon as possible;
  - Demonstrate the timing performance and the pile-up rejection capabilities with the detector technologies that will be available;
  - Integrate the CT-PPS detectors into the CMS trigger/DAQ system.
- Initial production phase (2016-17):
  - Finalize the CT-PPS detector commissioning;
  - Aim at accumulating ~ 100 fb^{-1} of data.

The decision to pursue the programme based on the results obtained in the exploratory phase requires the approval of both the CMS and TOTEM Collaborations. The two Collaborations will make their best efforts to assure the success of the Joint Project.

1.1.2 Detectors and experimental conditions

The detectors will operate at a few mm from the beam during data taking but will be moved away from the beam during injection, acceleration, and luminosity tuning. In each arm, two tracking stations instrumented with radiation-hard pixel sensors will be installed ten meters apart in z, and will be followed by the timing stations. The stations will be installed along the beam-line, between 204 and 215 m from the IP, the region already used by TOTEM. Downstream of the detectors a new collimator (TCL6) is foreseen by the machine in order to protect quadrupole Q6 from shower particles originating in the CT-PPS detectors.

The CT-PPS tracking is designed for position resolution of approximately $10(30)\mu$m in $x(y)$ and $1(3)\mu$rad angular resolution in the $x-z$ $(y-z)$ plane. In each arm the tracking detector is formed by two RPs with six pixel layers each. Each layer includes a 16×24 mm^2 pixel sensor matched by six PSI46 front-end ASICs and one Token Bit Manager (TBM) readout ASIC. 3D-silicon pixel sensors have been chosen as the CT-PPS baseline for their superior radiation hardness, as also established by CMS in the frame of the R&D for the Phase 2 Pixel Upgrade. 3D-sensors have been also widely tested by the ATLAS collaboration and have been qualified for installation in the forward part of the ATLAS Insertable B-Layer (IBL). Studies based on the observed TOTEM detector rates and on simulations indicate particle fluxes up to 5×10^{15}cm^{-2} per 100 fb^{-1} in the pixel detectors. Planar sensors are kept as backup. The CT-PPS pixel detectors will use the CMS Phase 1 Upgrade pixel readout chain. A detailed description of the tracking detectors is presented in Chapter 4.

The timing detectors in both arms measure the difference of arrival time of the two protons. A time resolution of $\sigma(t) = 10$ ps corresponds to a vertex resolution $\sigma(z_{pp}) = 2.1$ mm, allowing pileup rejection by a factor of approximately 25 when no spurious pileup protons are also detected. The baseline timing detector is based on the Cherenkov L-bar Quartic (Quartz Timing Cherenkov) design, which allows $x-y$ segmentation; in this approach, the photodetectors (Silicon Photomultipliers as baseline) can be several

centimeters away from the beam. Prototype Quartic detectors were tested with 120 GeV proton beams, and a resolution of $\sigma(t) = 31$ ps for a 30 mm quartz bar was found. Two in-line detectors as proposed in the exploratory phase allow for a time resolution of 22 ps; further optimization is being pursued. Other timing technologies are also being pursued in view of improved performance in a latter phase. The reference clock system provides time synchronization with less than 1 ps jitter between the detectors in opposite arms. A detailed description of the timing detectors is presented in Chapter 5.

Studies based on radiation monitors placed on the 220 m TOTEM RP stations yield a total dose of about 100 Gray and a fluence of the order of 10^{12} neq/cm^2 per 100 fb^{-1} of integrated luminosity [12]. Measurements reported in the literature indicate that the Silicon Photo Multiplier (SiPM) leakage current increases by only a small amount up to a few hundred Gray. On the other hand, the Hadron Calorimeter (HCAL) Upgrade project requires SiPM tolerance up to 2×10^{12} neq/cm^2 and to 100 Gray. The SiPMs would probably require replacement after 100 fb^{-1}, which is feasible given the small number of devices involved.

TOTEM data collected in 2012 in several RP test insertions in normal high-luminosity fills were used to estimate the particle multiplicity in the CT-PPS detectors. Extrapolating from these data and assuming pile-up $\mu = 50$, the combined effect of beam backgrounds and physics translates into a rate of the order of 15 MHz of events with 1 or 2 tracks per side. The Quartic detectors have $x - y$ dimensions of 3×3 mm^2 (baseline design). For this granularity and at high luminosity the hit rate in the bars closest to the beam is of the order of 10 MHz, and in a sizable fraction of the detector, rates per channel of 1 MHz or above are expected. Therefore the inefficiency due to double hits in the same bar can be as high as 50%. While the impact of this inefficiency, taken into account in the physics performance results presented in Chapter 2, is manageable, we foresee an upgrade of the timing detectors in a second phase of the programme. We therefore propose an R&D programme on alternative technologies allowing good timing and fine granularity. This programme is also described in Chapter 5.

The expected radiation in the RP stations should not create problems to the readout electronics. However a significant rate of single event upsets in FPGAs, leading to an unacceptable rate of necessary resets, may disrupt the operation of digital and data transmission electronics located in this region. We are evaluating with machine experts the possibility of making a hole in the floor concrete where this electronics could be located and therefore protected from radiation.

The CT-PPS detectors will be integrated in the CMS trigger and data acquisition system, and the pixel and timing data acquisition electronics will be largely based on existing components. The standard CMS Level-1 (L1) Trigger provides full efficiency for the exclusive production of EW final states. Regarding the L1 di-jet trigger, the addition of a timing trigger that selects events in the tails of the vertex distribution along the z axis will reduce the trigger rate to manageable levels. A trigger signal generated at 210 m can be included within the CMS L1 latency. In a future upgrade, a L1 CT-PPS trigger based on high granularity detectors capable of computing the missing mass and comparing it with the mass of the centrally produced jet system could be foreseen. Dedicated High Level Trigger (HLT) selecting protons reconstructed in CT-PPS will be necessary.

The main challenge of the CT-PPS experimental programme is the ability to operate the detectors close to the beam ($10 - 20\sigma$) at high luminosity. To maximize acceptance for low momentum-loss protons, the detectors must operate at distances of few mm from the beam centre and be active as close to their physical edge as possible. Two different beam pockets have been considered, RPs and MBPs. RPs have been used in the LHC, both in special low intensity runs and at high intensity in test runs. These tests highlighted some important issues that have since been addressed, leading to several improvements that may allow to use RPs in standard high-luminosity runs. In particular, the present box RP design has been improved and a new cylindrical RP version was developed. These developments have been carried out by TOTEM in collaboration with the Accelerator and Beam Physics (BE-ABP) group. While there is experience with MBPs on an electron beam at DESY, there is still no experience in using these devices in the high intensity LHC environment.

The additional Radio Frequency (RF) impedance (transversal and longitudinal) introduced by these devices is a major concern. As a guideline, the machine (BE-ABP) established that the additional impedance should not be larger than about 1% of the total LHC impedance. Nevertheless this threshold is a safety indication and not a sharp limit. At 1 mm from the beam, the cylindrical RP increases the LHC transverse impedance by 0.5% and the longitudinal by 1.2%. These figures need to be multiplied by four, as four RPs per arm are foreseen. While these values are above the indicative limit mentioned above, we point out that in the low β^* beam tests done in 2012 there were no direct evidence of beam instabilities induced by the RP (see Section 1.3). The MBP design aims at a beam pocket with smaller RF impedance. The present design includes 11-degree tapering structures as in the standard LHC collimators. At 1 mm from the beam the transverse impedance increases by 0.05% and the longitudinal by 0.5%. The total impedance increase for a single arm (two MBPs per arm) is then about 0.10% transversely and 1.0% longitudinally. To these values we should add the impedance of the bellows. On the other hand, the increased material traversed by particles due to the MBP small tapering angle may require using beryllium for the thin windows, which raises some mechanical challenges. Additionally, the MBP would need bellows capable to accommodate a 25 mm transverse stroke.

The test runs performed in 2012 complemented by Fluka simulations indicate that the approach of the RPs to the beam at the distance demanded by physics requires to absorb the showers produced by the RPs in order to protect the downstream quadrupole. The solution envisaged was the addition of the new collimators (TCL6), which are already installed. A detailed description of the beam pocket structures, including the proposed MBP development programme, is presented in Chapter 3.

We consider that the RP is a more mature solution, in an advanced stage of implementation and suitable for post-LS1 testing, and therefore we have adopted it for the exploratory phase in 2015. However, considering the uncertainties associated with the operation of these devices at high luminosity, and given the potential good performance of MBPs and the benefits for physics of operating the detectors as close as possible from the beam, we propose that the development of the MBP solution be pursued in parallel with the goal of installation of a test structure in 2016.

Based on the above considerations, we propose that for the exploratory phase in 2015-16 we use RPs and available silicon strip detectors in conjunction with the central detector. This configuration would allow to understand the performance of the new RPs with high intensity beams. One cylindrical RP per arm would also be installed in LS1, allowing the installation Quartic timing detectors in the fall of 2015 (during a technical stop) to evaluate the pileup rejection capability of this detector. At the year-end technical stop 2015-16 the new pixel detectors would replace the silicon strips. A MBP structure may also be installed for tests. The results of the evaluation of MBPs compared to RPs would determine how to proceed in the following years in view of optimizing the CT-PPS physics potential. Using the experience acquired in the exploratory phase we expect that significant luminosity could be integrated in 2016-17. The aim is to integrate a total luminosity of 100 fb^{-1} before LS2.

1.2 Physics with the CMS-TOTEM Precision Proton Spectrometers

1.2.1 Introduction to physics with CT-PPS

The addition of the CT-PPS with capability to operate in normal LHC high luminosity conditions will open a new window into some high-Q^2 physics in both the electroweak sector (W, Z and γ) and QCD with high transverse energy (E_T) jets [13], with unique sensitivity to physics beyond the Standard Model (SM) as well as the possibility to perform important measurements of subtle QCD effects. The new proton spectrometers, at $z = \pm 204 - 215$ m with tracking resolution $\sigma(x)$ $\sim$10 μm and timing resolution $\sigma(t)$ $\sim$20 ps, will allow measurements of some specific, relatively simple, reactions, especially CEP [14] $p + p \to p \oplus X \oplus p$, where $\oplus$ indicates "rapidity gaps" adjacent to the state X. Rapidity gaps are regions without primary particle production. In these events the state X, which may be a particle or a

more complex, but well-defined state, is measured by the main central detector and its four-momentum is determined from the two scattered protons. In this way, CEP events resemble more electron-positron annihilation events than normal LHC events, in which the initial state of the interacting partons or particles is not well known since hadrons are composite objects.

In CEP reactions, the mass of state X, $M(X)$, can be reconstructed from the fractional momentum loss, ξ_1 and ξ_2, of the scattered protons by $M(X) = M(pp) \sim \sqrt{\xi_1 \xi_2 s}$. The $M(X)$ reach at the LHC will be significantly larger than that of previous colliders (ISR, Sp$\bar{\text{p}}$S and Tevatron) because of the larger $\sqrt{s}$. For the first time we will be able to study CEP at the electroweak scale.

In standard LHC high-luminosity optics, the scattered protons can be observed mainly thanks to their momentum loss, via their horizontal deviation from the beam centre at the position of the CT-PPS. This translates into a lower limit in ξ (and hence in $M(X)$), below which there is no acceptance for the simultaneous detection of the two protons in a CEP reaction. The value of this threshold depends on the distance from the IP and on how close to the beam the proton detectors can be moved. At $\sqrt{s}$ = 13 TeV and in normal high-luminosity conditions, with the CT-PPS detectors at 15σ from the beam, values of $M(X) \gtrsim 300$ GeV will be accessible. CEP reactions at such high masses have cross sections that are typically about 1 fb and thus can only be studied in the normal high-luminosity running, with $\mu \gtrsim 30$ inelastic interactions per bunch crossing. This is complementary to the special high β^* runs [15], where any CEP $M(X)$ can be studied as long as the cross section is of order 1 pb or higher.

CEP is a t-channel exchange process, and the absolute value of the four-momentum-transfer squared, $|t|$, follows an approximately exponentially decreasing distribution. The carrier of this t-channel exchange must be neutral in flavour, colour, and electric charge. In the SM, the allowed t-channel exchanges are only photons γ, gluons g (if their colour is neutralised), and Z-bosons. We first discuss two-photon collisions, then gluon-gluon fusion with an additional gluon exchange to neutralise the colour, and finally photoproduction.

1.2.2 Two-photon collisions

The LHC is also a photon-photon collider, with lower $\gamma\gamma$ luminosity than an e^+e^- collider but a unique energy range, $\sqrt{s_{\gamma\gamma}}$ up to $\sim$ 1 TeV, higher than that of the International Linear Collider (ILC) [16]. The photon energies are measured by the CT-PPS proton detectors, so $\sqrt{s_{\gamma\gamma}}$ is known on an event-by-event basis with resolution $\sigma(\sqrt{s_{\gamma\gamma}}) \sim 10$ GeV. In the high mass region accessible to CT-PPS with both protons detected, the main states are $X = e^+e^-, \mu^+\mu^-, \tau^+\tau^-$ and W^+W^-. Hadronic final states from $\gamma\gamma \to q\bar{q}$ are not visible because of the very large backgrounds from $gg \to$ hadrons with an additional gluon exchange. In the case of the dilepton final states, these backgrounds are not present. Even with an average of 50 pileup events, the backgrounds can be suppressed by matching the reconstructed values of M_X (in the central detector) and M_{pp} (in the CT-PPS), by requiring small charged multiplicity associated to the dilepton vertex, and by exploiting the proton timing constraint on the z-vertex position. The exclusive interaction itself has no additional charged particles, but experience shows that a few poorly-measured charged particles from different interactions should be allowed to be associated to the reconstructed vertex to maintain good efficiency at high pileup. The cross sections for $X = e^+e^-, \mu^+\mu^-$ and $\tau^+\tau^-$ are equal by lepton universality with small theoretical uncertainties, as this is a QED process with a small "shadowing" correction from strong interaction effects. For $M(\ell\ell) \gtrsim 350$ GeV the cross sections are only $\sim$ 1.5 fb [17, 18] (per flavour), but still accessible in 100 fb^{-1}.

At large $\sqrt{s_{\gamma\gamma}}$, the two-photon process $\gamma\gamma \to W^+W^-$ has a higher cross section by at least a factor of $\simeq$ 20 larger than $\gamma\gamma \to \ell^+\ell^-$ because the spin in the t-channel exchange is J = 1 instead of J = $\frac{1}{2}$. This provides a window on BSM physics, since it is sensitive to triple and quartic gauge boson couplings [19]. Indeed CMS has observed [20] two candidate events in a final state with $e^\pm\mu^\mp$ and large missing E_T ($\not{E}_{\text{T}}$) and no other tracks, but without detecting the protons. Two candidate events were observed in 5.05 fb^{-1} of $\sqrt{s}$ = 7 TeV data, consistent with the SM prediction of 2.2 $\pm$ 0.4 events and 0.84 $\pm$ 0.15

background. This resulted in limits on the Anomalous Quartic Gauge Couplings (AQGC) parameters of the order of 1.5(5) $\times 10^{-4}$ GeV^{-2} for $a^W_{0(c)}/\Lambda^2$, assuming a dipole form factor with the energy cutoff scale at $\Lambda_{\rm cutoff}$ = 500 GeV, which are about 20 times more stringent than the best Tevatron limits, and two orders of magnitude better than the best LEP limits.

With an integrated luminosity of 100 fb^{-1}, the CT-PPS is expected to improve the limits by at least two orders of magnitude, or perhaps observe a deviation from the SM prediction. The SM cross section is higher at $\sqrt{s}$ = 13 TeV by a factor ~ 2.5 [21] and the matching of the reconstructed proton vertex coordinate, z_{pp}, with that from the leptons, $z_{\ell\ell}$, should allow also the study of the $e^+e^-\not{E}_{\rm T}$ and $\mu^+\mu^-\not{E}_{\rm T}$ final states, thus increasing the signal yields. The $\not{E}_{\rm T}$ requirement effectively excludes backgrounds from $\gamma\gamma \to \ell^+\ell^-$, which tend to have $p_T(\ell\ell) \lesssim$ a few GeV and, for a given $M(X)$, the $\gamma\gamma \to \ell^+\ell^-$ cross sections are smaller than the $\gamma\gamma \to W^+W^-$ ones by more than an order of magnitude. Measuring the protons provides kinematic constraints and reduces significantly the backgrounds. The semileptonic case, $X = W^+W^- \to \ell^\pm\nu jj$, is also accessible by requiring "track gaps", i.e. no tracks associated to the vertex with large momentum transverse to any jet axis. The proton measurements give $M(W^+W^-)$, and one can even check that $M(\ell^\pm\nu) = M(W)$. These modes give a factor of six more statistics. Kinematic distributions may also be used to increase the sensitivity to AQGC [19]. Results on the CT-PPS sensitivity to W^+W^- CEP obtained from detailed simulations are presented in Chapter 2.

Exclusive $\gamma\gamma \to ZZ$ and $\gamma\gamma \to \gamma\gamma$ provide unique measurements of quartic gauge couplings with only neutral particles [22]. They measure dimension-eight operators; one example, from R.S. Gupta [23], is the exchange of a Kaluza-Klein graviton if there are large extra dimensions. The $\gamma\gamma \to ZZ$ or $\gamma\gamma$ processes are only allowed through loops in the SM resulting in ab-range cross sections within the CT-PPS mass acceptance, so even a few events in 100 fb^{-1} may offer an opportunity for a new physics discovery. Both $X = \gamma\gamma$ and ZZ processes can be accessible with cross sections of the order of $1-10$ fb within the CT-PPS mass range in some allowed scenarios. In the ZZ case, one may study the case where one of the Z decay hadronically, using kinematic constraints and track-gap requirements to reduce the backgrounds. In the $\gamma\gamma$ case, the primary vertex is reconstructed from the protons: allowing one of the photons to be a converted one, a match between the vertexes (from photons and protons) is possible and a better background rejection can be achieved. In addition, the two photons have similar transverse momentum ($p_{\rm T}$) values, and are approximately back-to-back in azimuthal angle. These selection criteria should allow sensitivity for the $\gamma\gamma$ channel even in high pile-up conditions [24].

1.2.3 Tests of Quantum Chromodynamics

Normally, in gluon-guon interactions the colour exchange results in multi-hadron production. However in multi-jet (two-, three-, or four-jet) exclusive production a third gluon of opposite colour is exchanged and a colour string does not form. This may result in one or more rapidity gaps unless another parton-parton interaction occurs. The probability that this does not happen and the gap is preserved is called the "rapidity gap survival probability" $\hat{S}^2$. The overall suppression relative to inclusive jj production is about 10^{-5} for $M(X) \sim 350$ GeV. In low-Q^2 interactions, including elastic scattering and diffractive excitation, this colour-singlet gluon pair is the leading order description of the *Pomeron* IP.

CEP of high-E_T jets will shed light on a number of crucial aspects of the proton structure and the strong interaction. On the one hand, the two-gluon proton vertex measures the (skewed) unintegrated gluon parton distribution function of the proton, in a region never explored before. On the other hand, the experimental study of the rapidity gap survival probability opens up a new window on the study of soft multiple parton interactions. Finally, to a very good approximation, the final state obeys a $J_z = 0$, C-even, P-even, selection rule [25]. Here J_z is the projection of the total angular momentum along the proton beam axis. This selection rule readily permits a clean determination of the quantum numbers of any new resonance. In other words, if a new state were to be produced in CEP, not only could its mass be determined precisely from the scattered protons momenta, independent of the decay mode, but also

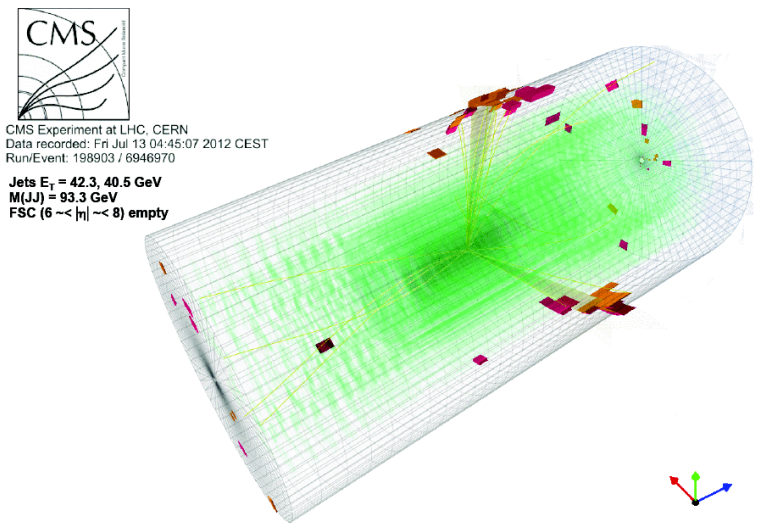

Figure 2: A two-jet event recorded by TOTEM and CMS in a low pile-up (β^* = 90m) run at $\sqrt{s}$ = 8 TeV. Two leading protons and two jets with $E_T > 20$ GeV were required.

its J^{PC} numbers would immediately be known.

Hard exclusive QCD processes, such as $X = jj$ or $X = jjj$, are described in QCD as originating from $gg \to gg$, ggg or $q\bar{q}g$. Exclusive $q\bar{q}$ dijets are strongly suppressed by the $J_z = 0$ rule [25]. Most events with two scattered protons and central jets will not be exclusive $X = jj$ or $X = jjj$, but will have additional particle production. These will be difficult to study with high pileup. The most interesting exclusive subsets are selected by four-momentum balance between initial and final states. That is: (1) $M(X) = M(pp)$ the missing mass measured by the two leading protons in the CT-PPS, with resolution $\sigma(M(pp)) \sim 10$ GeV, (2) longitudinal momentum balance $p_z(X) = -(p_z(p_1) + p_z(p_2))$, and (3) transverse momentum balance $\vec{p_T}(X) = -(\vec{p_T}(p_1) + \vec{p_T}(p_2))$. Two jets have about the same p_T, balanced by the two protons, and are back-to-back in azimuth. With high pileup the calorimeters cannot be used to detect rapidity gaps, but it is possible to use "track-gaps" as an approximation.

Theoretically, exclusive dijets should be purely gluon jets $\sim 99\%$ of the time [25], a unique situation that can be exploited for studying jet fragmentation. The LHC is then used as a "gluon jet factory". Light-quark dijets should be suppressed approximately as $(m(q)/m(jj))^2$ according to the $J_z = 0$ rule [25]. Note that in exclusive dijet events one b-tag implies that the opposite jet is a $\bar{b}$ jet, unless it is due to gluon-splitting; this could be used as a tool for testing b-jet tagging algorithms. Exclusive three-jet events can be both ggg and $q\bar{q}g$. In the $q\bar{q}g$ case we expect a democratic population of quark flavours (except top): $\sigma(u\bar{u} = d\bar{d} = s\bar{s} = c\bar{c} = b\bar{b})$. The kinematic distributions of the three jets are expected to be different for ggg and $q\bar{q}g$ [26].

Some two- and three-jet events, though not exclusive since $M(jj, jjj) \ll M(pp)$, were already seen by CMS and TOTEM during the short high β^* run in July 2012. Common data were recorded with a CMS trigger on two jets with $p_{\mathrm{T}} > 20$ GeV. Selecting events with a proton in each direction in the TOTEM RPs, extremely clean events with two and three jets were found, as shown in Figures 2 and 3.

These exclusive two- and three-jet events allow studies of many other aspects of QCD, especially involving both perturbative and non-perturbative effects in the same process. Thus apart from the matrix elements for perturbative $gg \to gg$ and $gg \to ggg$ $(q\bar{q}g)$, the cross sections depend on the unintegrated, generalized gluon parton distribution functions, on Sudakov suppression of gluon radiation (which would cause additional hadron production), and on the rapidity gap survival probability. Also, other processes such as single and double diffractive dissociation, photoproduction of Z-bosons, exclusive $X = \gamma\gamma$, etc. involve some, or all, of these issues. With the data from CT-PPS, together with other studies, we hope

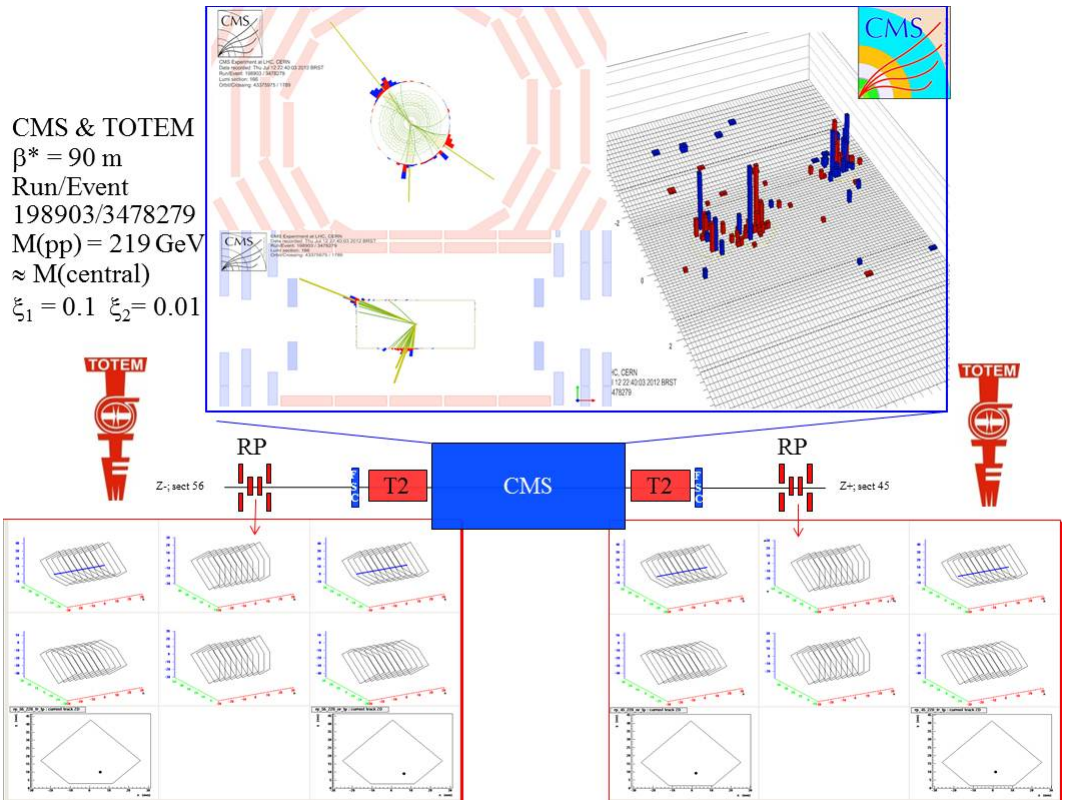

Figure 3: A central diffractive three-jet event recorded by TOTEM and CMS in a β^* = 90m run at $\sqrt{s}$ = 8 TeV. The upper part of the figure displays the central part of the event, as seen in CMS; the lower part displays the proton information in the TOTEM Roman Pots.

for a unified description of this area of strong interaction physics, which has been elusive up to now, but at low Q^2 represents a large part of the inelastic pp cross section.

With 100 fb^{-1} of data in normal LHC high luminosity running, we can expect to reach $M(jj, jjj) \sim$ 700-800 GeV. The data sample collected will enable studies of the azimuthal difference $\Delta\phi$ between the scattered protons, of the shape of the proton $|t|$ distribution, and the overall cross section behaviour with $M(pp)$, providing a good test of different models [27, 28]. Results on the CT-PPS sensitivity to central exclusive dijet production obtained from a detailed simulation are presented in Chapter 2.

1.2.4 Photoproduction

Single exclusive Z-production can happen only through photoproduction: $\gamma^*\text{IP} \to Z$. Photoproduction of vector mesons ($\rho, \phi, J/\psi, \psi(2S), \Upsilon$) has been studied extensively in ep at HERA, and more recently in $p\bar{p}(p)$ at the Tevatron (CDF) [29] and the LHC [30]. The basic process is that a virtual photon radiated from one proton fluctuates to a $q\bar{q}$ pair, which scatters via IP exchange off the other proton and forms the vector meson. The process for Z-photoproduction is similar: $\gamma^* \to q\bar{q} \to Z$. The intermediate quark-loop scatters via IP exchange off the other proton. The photon-emitting (Coulomb scattered) proton will have small $|t|, < 0.1$ GeV^2, and the other will have larger $|t|$ values typical of strong diffractive processes, $\lesssim 0.5$ GeV^2. In this case, the Z-boson will have $p_T(Z) \lesssim 0.7$ GeV, the leptons from $Z \to \ell^+\ell^-$ will be almost back-to-back in azimuth, and the additional charged multiplicity on the dilepton vertex will be small. Since $M(X) \gtrsim 300$ GeV for CT-PPS we do not have acceptance for exclusive Z production with both protons detected. If the Z is boosted ($2 \lesssim |y(Z)| \lesssim 3$) the proton in that direction has larger ξ and comes into the CT-PPS acceptance. Without both protons measured we cannot use missing mass, but $p_z(Z)$ determines both protons' momenta if it is an exclusive event. For $Z \to$

$\mu^+\mu^-$ events, as well as with the two-photon events $\gamma\gamma \to \mu^+\mu^-$, this provides a valuable calibration (or check) of the momentum scale of the proton spectrometers. One can also use the low additional charged multiplicity requirement on the vertex and the kinematics to observe Z photoproduction without detecting the protons, but in that case either one or both protons could dissociate into massive clusters and the cross section is affected in a way that is not very well known.

It should be noted that high mass central exclusive dijet production, $pp \to p \oplus jj \oplus p$, can also occur via photoproduction in a $C = -1$ state [31]. The cross section of this process is expected to be significantly lower than the corresponding one from gg fusion.

To conclude, the addition of small but very precise tracking and timing detectors far along the beams, CT-PPS, opens up a whole new field in both electroweak physics, including BSM sensitivity, and QCD, for a very modest cost.

1.3 Strategy and running scenarios

1.3.1 Exploratory phase

LHC Start-Up Scenario

The LHC strategy for the start-up after LS1 is outlined in [32]. After a short commissioning period at a bunch spacing of 50 ns, operation at 25 ns will be attempted. Reaching the desired peak luminosity of $(1 \div 2) \times 10^{34}\,\mathrm{cm}^{-2}\mathrm{s}^{-1}$ with 50 ns bunch spacing would imply bunches of 1.6×10^{11} protons leading to a pileup level of $\mu \sim 80 \div 120$, more than the experiments can tolerate. Operation with 50 ns bunch spacing and luminosity levelling would be a fall-back scenario for the first year in case of major difficulties with 25 ns bunch spacing. This option would bring considerable complications for the CT-PPS programme. Firstly, the enormous pileup would be difficult to resolve even with 10 ps time resolution. Secondly, the luminosity levelling is implemented by changing β^* in steps during a fill, modifying each time the beam optics and the beam width at the RP positions. Whether the RP positions need to be adapted in every β^* step remains to be studied. However, as laid out in the following sections, RP operation for physics production at high luminosity is not expected for the first year. When the timing detectors are installed in the RPs, operation at 25 ns bunch spacing will very likely be standard.

Roman Pot insertion commissioning

The first important goal after LS1 is to gain experience with RP insertions and their interplay with the collimation system. After the impedance heating and the resulting vacuum deteriorations observed in high-luminosity insertion tests in late 2012, the RP system underwent a series of improvements [15, 33], and the new cylindrical RPs were designed accordingly [34]. Verifying the effectiveness of these measures is the first milestone to be met.

The RP insertion tests will exploit the following diagnostic instrumentation:

- Beam Loss Monitors (BLMs): The BLMs measure the dose rate due to showers produced by the interaction of beam halo or IP5 collision debris with RPs or collimators. Their beam dump thresholds are defined in view of protecting downstream magnets from quenching.
- Vacuum gauges: A pressure rise near the RPs can be an indication of impedance heating.
- Early detector instrumentation in the new cylindrical RPs: In the very first stage after LS1, while timing detectors are not yet available for installation, the new RPs will be equipped with temporary diagnostic detectors. In addition to temperature measurements with PT100 sensors, to assess impedance heating, particle rate information will be available either from scintillators (segmented or monolithic) or from a pair of TOTEM's edgeless silicon strip detectors. Together with the BLMs, these detectors will enable the mapping of the halo and debris profile.

The insertion tests will proceed in a sequence of increasingly challenging beam conditions.

The first step will be the beam-based RP alignment subsequent to the alignment of the collimators. At low β^* all the RP units (horizontal and vertical pots) and the new cylindrical RPs have to be aligned. This part of the LHC commissioning procedure will be performed with a beam intensity allowing the "restricted setup beam flag" to be set, i.e. not more than 1.4×10^{11} protons per beam at 6.5 TeV. According to pre-LS1 RP alignment experience, no insertion difficulties are expected, but first knowledge about the rate profile can be obtained. This alignment, followed by loss-map validations of the collimator hierarchy for the nominal RP position settings is a prerequisite for all later RP insertions. The nominal horizontal RP positions depend on the details of the collimation scheme, which has not yet been finalised. They are expected to lie between 12 and 15 sigma from the beam centre, i.e. about 1 sigma in the shadow of the tertiary collimators, TCTs.

The next RP insertions will be carried out in end-of-fill studies, i.e. with a certain time delay after declaration of stable beams, to be agreed in the LPC, in order to minimise the impact of possible beam dumps on the LHC data production. The goal of these insertion tests is to find an optimal set of positions not only of the RPs but also of the collimators TCL4, TCL5 and TCL6, offering sufficient protection for the magnets downstream of RPs without cutting too much into the proton acceptance of the RPs. Conservatively, for the first such insertion the beams will be separated by $5 \div 6\,\sigma$ in IP5 to reduce the luminosity (cf. Table 1) and thus the debris background, facilitating the RP approach. This separation can then be successively reduced, leading to increasingly harsh background conditions. Once a viable set of RP and TCL positions has been found for zero beam separation, the system will be ready for the first physics runs.

Timing Detector Commissioning

After establishing the optimal set of TCL and RP positions, and after installation of timing detectors in the new RPs, first physics runs for timing studies will be performed. To avoid entering immediately into the most difficult pileup domain with $\mu \sim 40$, the commissioning of the timing detector system will be done in end-of-fill studies with separated beams like in the RP insertion commissioning phase. Table 1 shows the luminosity reach and the pileup level as a function of the beam separation for a typical standard running scenario with 25 ns bunch spacing. For separations above about $3.8\,\sigma$, the pileup level drops below 1. At $\mu = 1$, an end-of-fill run of 1 hour would not only allow tests of the timing system at a comfortable occupancy but also the collection of about 1 pb^{-1} of data. Finally, the beam separation could be gradually reduced to arrive at the full luminosity and the full pileup of regular LHC fills.

1.3.2 Data production phase

After the commissioning steps described in the previous sections, the RP system will be fully validated for continuous operation in all regular LHC fills. At that stage, the RP insertion movements will be implemented in operational sequences to be executed by the LHC operator immediately after declaration of stable beams.

While details of the beam conditions and bunching schemes are not yet fully defined and will depend on the experience gathered in the post-LS1 recommissioning phase, the common aim of the LHC experiments and the machine experts is to operate with 25 ns rather than 50 ns bunch spacing in order to keep the pileup manageable. Possible options are shown in Table 2. In all cases a peak luminosity of the order $10^{34}\,\text{cm}^{-2}\,\text{s}^{-1}$ and a pileup between 20 and 50 are envisaged. In such conditions, 100 fb^{-1} can be collected in about 100 full days.

d [σ]	[μm]	μ	$\mathcal{L}$ [$\mathrm{cm}^{-2}\,\mathrm{s}^{-1}$]	L/day
0	0	39.1	1.30×10^{34}	1.1 fb^{-1}
1	11.7	30.4	1.01×10^{34}	0.85 fb^{-1}
2	23.4	14.4	4.79×10^{33}	0.41 fb^{-1}
3	35.1	4.12	1.37×10^{33}	0.12 fb^{-1}
3.8	44.8	1.00	3.34×10^{32}	28 pb^{-1}
4	46.8	0.715	2.38×10^{32}	20 pb^{-1}
5	58.6	0.075	2.51×10^{31}	2.1 pb^{-1}
6	70.3	0.005	1.61×10^{30}	0.14 pb^{-1}

Table 1: Inelastic pileup μ and luminosity $\mathcal{L}$ as a function of the beam separation d in the IP. Common parameters: $\beta^* = 0.5\,\mathrm{m}$, $E = 6.5\,\mathrm{TeV}$, 2520 colliding bunches (i.e. with a spacing of 25 ns) of 1.15×10^{11} protons, full crossing angle = 310 μrad, $\varepsilon_n = 1.9\,\mu\mathrm{m\,rad}$, bunch length $\sigma_z = 10.12\,\mathrm{cm}$, inelastic cross-section = 85 mb.

β* [m] (separation/crossing planes)	0.4/0.55	0.4/0.45
ε*[mm] at start of fill	3.75	1.9
Max. Bunch Population [10^{11} p]	1.15	1.15
Max. Number of bunches/colliding pairs IP1/5	2760	2520
Bunch length (4 σ)[ns]/ (r.m.s.) [cm]	1.35/10.1	1.35/10.1
Max. Beam Current [A]/population[10^{14} p]	0.57 / 3.2	0.52 / 2.9
Max. Stored energy [MJ]	330	300
Peak luminosity [10^{34} $\mathrm{cm}^{-2}\mathrm{s}^{-1}$] in IP1/5	0.85	1.5
Half External Crossing angle IP1/5 [μrad]	195	155
Beam-beam tune shift (start fill)/IP [0.001]	2.5	4.3
Min. beam-beam separation (σ) d_{sep}	12	12
Maximum Average pile-up ($\sigma_{inel.}$=85 mb)	23	44

Table 2: Expected beam parameters and peak performance for 25 ns bunch spacing at 6.5 TeV (from [32]).

References

[1] G. Belanger et al., "Bosonic quartic couplings at LEP-2", Eur. Phys. J. C 13 (2000) 283.

[2] ALEPH Collaboration, "Constraints on anomalous QGCs in e^+e^- interactions from 183 GeV to 209 GeV", Phys. Lett. B 602 (2004) 31.

[3] OPAL Collaboration, "Constraints on anomalous quartic gauge boson couplings from $\nu\bar{\nu}\gamma\gamma$ and $q\bar{q}\gamma\gamma$ events at LEP-2", Phys. Rev. D 70 (2004) 032005.

[4] OPAL Collaboration, "A study of $W^+W^-\gamma$ events at LEP", Phys. Lett. B 580 (2004) 17.

[5] OPAL Collaboration, Measurement of the $W^+W^-\gamma$ cross-section and first direct limits on anomalous electroweak quartic gauge couplings, Phys. Lett. B 471 (1999) 293.

[6] L3 Collaboration, "The $e^+e^- \to Z\gamma\gamma \to q\bar{q}$ reaction at LEP and constraints on anomalous quartic gauge boson couplings", Phys. Lett. B 540 (2002) 43.

[7] L3 Collaboration, "Study of the $W^+W^-\gamma$ process and limits on anomalous quartic gauge boson couplings at LEP", Phys. Lett. B 527 (2002) 29.

[8] DELPHI Collaboration, "Measurement of the $e^+e^- \to W^+W^-\gamma$ cross-section and limits on anomalous quartic gauge couplings with DELPHI", Eur. Phys. J. C 31 (2003) 139.

[9] D0 Collaboration, "Search for anomalous quartic $WW\gamma\gamma$ couplings in dielectron and missing energy final states in ppbar collisions at $\sqrt{s}$ = 1.96 TeV", arXiv:1305.1258 (2013).

[10] See e.g. V.A.Khoze,A.D.Martin and M.G.Ryskin, "Double diffractive processes in high resolution missing mass experiments at the Tevatron", Eur.Phys.J.C19:477-483,2001; Erratum-ibid.C20:599,2001 [hep-ph/0011393].

[11] M.G. Albrow et al., The FP420 R&D Project, "Higgs and New Physics with forward protons at LHC", JINST 4 (2009) T10001.

[12] F. Ravotti, "Update on TOTEM Roman Pots, T1 and T2 Radiation Levels (Summary of first three year LHC running period)", CERN EDMS 1353932. https://edms.cern.ch/document/1353932

[13] The CMS and TOTEM diffractive and forward physics working group, "Prospects for Diffractive and Forward Physics at the LHC", CERN/LHCC 2006-039/G-124 (2006).

[14] See e.g. M.G. Albrow, T.D. Coughlin, and J.R. Forshaw, Prog. Part. Nucl. Phys. **65** (2010) 149.

[15] TOTEM Collaboration, "TOTEM Upgrade Proposal", CERN-LHCC-2013-009; LHCC-P-007 and "Timing Measurements in the Vertical Roman Pots of the TOTEM Experiment", CERN-LHCC-2014-020 (TOTEM-TDR-002).

[16] K. Piotrzkowski, "Tagging Two-Photon Production at the LHC", Phys. Rev. D 63, 071502(R).

[17] J.A.M. Vermaseren, Nucl. Phys. B229 (1983) 347.

[18] S.P. Baranov, O. Duenger, H. Shooshtari, J.A.M. Vermaseren, "LPAIR: a generator for lepton pair production", in the proceedings of Physics at HERA, October 29-30, Hamburg, Germany (1991).

[19] See e.g. T. Pierzchala and K. Piotrzkowski, Nucl. Phys. Proc. Suppl. 179-180 (2008) 257.

[20] S.Chatrchyan et al. (CMS Collaboration), JHEP 1307 (2013) 116.

[21] M. Luszczak and A. Szczurek, "Subleading processes in production of W^+W^- pairs in proton-proton collisions", arXiv:1405.0018, (2013).

[22] D.d'Enterria and G.G.Silveira, "Observing light-by-light scattering at the Large Hadron Collider", Phys.Rev.Lett. 111 (2013) 080405

[23] R.S. Gupta, Phys. Rev. D 85 (2012) 014006.

[24] S. Fichet et al., "Probing new physics in diphoton production with proton tagging at the Large Hadron Collider", arXiv:1312.5153.

[25] V.A. Khoze, A.D. Martin, and M.G. Ryskin, Eur. Phys. J. **C 48** (2001) 477 and erratum ibid. C 20 (2001) 599.

[26] V.A. Khoze, M.G. Ryskin and W.J. Stirling, Eur. Phys. J. **C 19** (2006) 477.

[27] L.A. Harland-Lang, V.A. Khoze, M.G. Ryskin and W.J. Stirling, "Central exclusive production within the Durham model: a review", IPPP-14-42, DCPT-14-84 (2014), arXiv:1405.0018.

[28] V.A. Petrov and R.A. Ryutin, J.Phys. G 35 (2008) 065004; R.A. Ryutin, Eur. Phys. J. C 73 (2013) 2443.

[29] T.Aaltonen et al., PRL 102, 242001 (2009).

[30] R. Aaij et al, J. Phys. G: Nucl. Part. Phys. 41 (2014) 055002.

[31] V.A. Khoze, private communication.

[32] G. Arduini, " Post LS1 Operation", Proceedings of the MPP Workshop, March 2013. https://indico.cern.ch/event/227895

[33] J. Baechler et al., "TOTEM Consolidation Project", LHC-XRP-EC-0010, EDMS 1314925.

[34] M. Deile et al., "TOTEM Upgrade Project", LHC-XRP-EC-0011, EDMS 1361537.

2 Detector and Physics Performance

A discussion of the performance of the CT-PPS tracking and timing detectors is presented. Specifically, the feasibility is discussed of measuring central exclusive production of dijets through gluon-gluon interaction, and central exclusive production of W boson pairs in two-photon interactions, in the experimental conditions foreseen for Run 2.

A brief description of the beam optics is provided in Section 2.1, details of the simulated samples are given in Section 2.2, detector acceptance and resolution are presented in Sections 2.3 and 2.4. The estimate of the machine-induced background is described in Section 2.6, and the RP alignment in Section 2.7. Finally, the sensitivity of CT-PPS to the two reference physics processes mentioned above is discussed in Section 2.8.

2.1 Beam optics

The proposed forward tracking and timing detector stations are to be installed in the regions located at approximately z=204 m and z=215 m from the IP, in both beam directions downstream of the central detector. Protons that have lost energy in the primary interaction emerge laterally after passing through the bending magnets. At z=204-215 m one can detect protons that have lost a few percent ($\simeq 3-20\%$) of the initial beam energy.

The trajectory of protons produced with transverse position (x^*, y^*) and angle (Θ_x^*, Θ_y^*) at the IP location (the '*' superscript indicates the IP location at IP5) is described by the equation

$$\vec{d} = T \cdot \vec{d^*}\,, \tag{2.1}$$

where the vector $\vec{d} = (x, \Theta_x, y, \Theta_y, \Delta p/p)$ and T is the transport matrix; p and Δp denote the nominal beam momentum and the proton longitudinal momentum loss, respectively. The transport matrix is defined by the optical functions as:

$$T = \begin{pmatrix} v_x & L_x & m_{13} & m_{14} & D_x \\ \frac{dv_x}{ds} & \frac{dL_x}{ds} & m_{23} & m_{24} & \frac{dD_x}{ds} \\ m_{31} & m_{32} & v_y & L_y & D_y \\ m_{41} & m_{42} & \frac{dv_y}{ds} & \frac{dL_y}{ds} & \frac{dD_y}{ds} \\ 0 & 0 & 0 & 0 & 1 \end{pmatrix} \tag{2.2}$$

where the magnification $v_{x,y} = \sqrt{\beta_{x,y}/\beta^*}\cos\Delta\phi_{x,y}$, and the effective length $L_{x,y} = \sqrt{\beta_{x,y}\beta^*}\sin\Delta\phi_{x,y}$ are functions of the betatron amplitude $\beta_{x,y}$ and the relative phase advance up to the RP location $\Delta\phi_{x,y} = \int_{\text{IP}}^{\text{RP}} \frac{\mathrm{d}s}{\beta(s)_{x,y}}$. Together with the dispersion $D_{x,y}$ (where nominally $D_y = 0$), they are of particular importance for the reconstruction of the proton kinematics. In these studies, a proton beam energy of 6.5 TeV with the LHC standard optics files (v6.5) is used.

Figure 4 shows the values of the effective lengths in x and y (L_x and L_y) and the corresponding dispersions (D_x and D_y) as a function of $\xi = \Delta p/p$ (momentum loss of the surviving proton) at the detector location at z=204 m. These values, together with the beam widths and divergences, determine acceptance and resolution for the proton kinematic variables t (four-momentum transfer squared) and ξ. In the present study, no uncertainty in the optical function is assumed. Once data-taking starts, the optical functions (and their resolutions) will be determined from the beam optics actually used for any given fill, according to the method discussed in Ref. [1].

The configuration of the LHC beam-line around the CMS IP is shown in Figure 5 for $z > 0$.

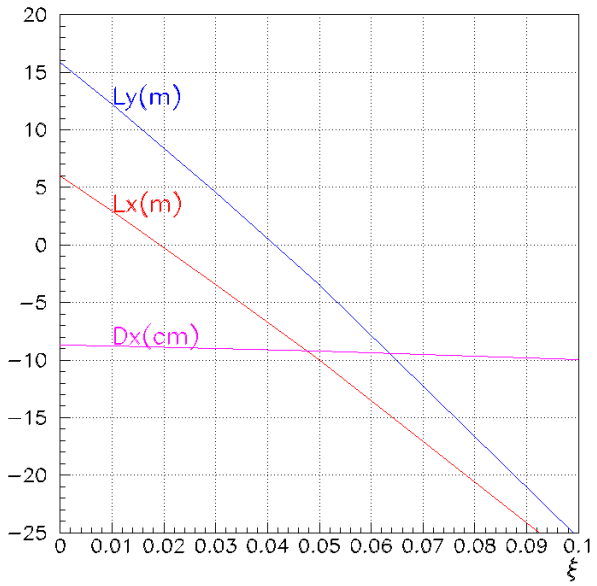

Figure 4: Effective lengths in x and y (L_x and L_y), and the corresponding dispersion (D_x) as a function of the proton momentum loss ξ at z=204 m from the interaction point.

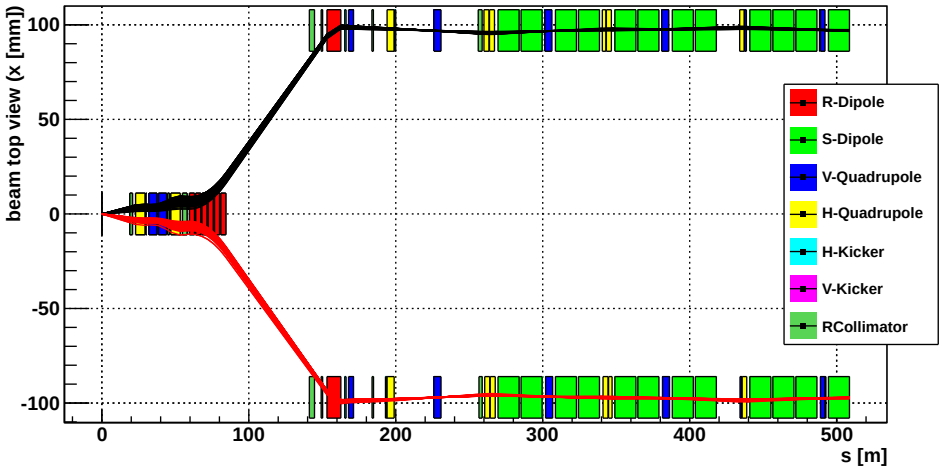

Figure 5: Top view of the beam-line for $z > 0$, with the proton trajectories as simulated by HECTOR (see text). The IP is located at $s = 0$. The red (black) lines correspond to the particles going into (out of) the IP. Here, the horizontal curvature of the beam-line has been straightened out for clarity.

Particle transport from the IP to the CT-PPS detector location is performed with HECTOR [2], which is incorporated in the CMSSW detector simulation and reconstruction package. Results are found to be in good agreement with MAD-X [3], the standard LHC beam transport program used at CERN. The HECTOR package tracks protons (or other particles) that emerge in the forward direction from the interaction region along the LHC beam-line. The LHC beam-line is simulated, along with the collimators and the apertures of the beam-line elements. The beam transport can be modified for different optics configurations.

The beam size can be expressed in terms of the emittance ϵ, and the amplitude function β. The horizontal beam size in the range of the CT-PPS detector location is shown in Figure 6. The emittance is inversely proportional to the beam momentum; increasing the momentum of the beam reduces the emittance and hence the physical size of the beam. Therefore, the normalized emittance $\epsilon_n = \epsilon \cdot \beta \cdot \gamma$ (where β, γ are the

relativistic functions) is often used instead. The amplitude function at the IP is taken to be $\beta^* = 0.6$ m, the normalized emittance $\epsilon_n \simeq 3.75 \cdot 10^{-6}$ m (emittance $\epsilon \simeq 5.4 \cdot 10^{-10}$ m), and the crossing angle 142.5μrad in the horizontal plane. A vertex resolution of $\sigma^*_{x,y} = 15\mu$m and an angular beam divergence of $\sigma^*_\theta = 30\mu$rad at the IP are assumed [4].

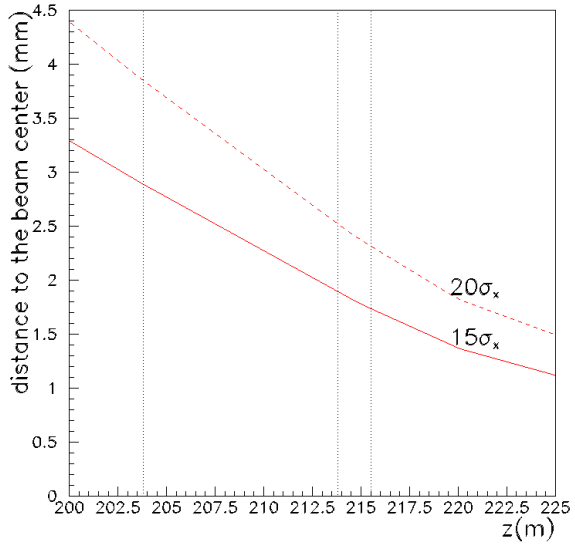

Figure 6: Horizontal distance to the beam center in the region $200 < z < 225$ m corresponding to the location of tracking and timing detector stations with the $15\sigma_x$ and $20\sigma_x$ Roman Pot approaches. The parameters used for the optics are described in the text.

2.2 Simulated samples

The performance of the CT-PPS is quantified in terms of the ability to measure two reference processes: central exclusive production of dijets, $pp \to p\mathrm{JJ}p$, and central exclusive production of W pairs, $pp \to pWWp$. The exclusive dijet sample is simulated with the ExHuME (v1.3.2) [5] generator interfaced with PYTHIA (v6.426) [6]; the $\gamma\gamma \to$ WW signal is generated using FPMC (v1.0) [7], with HERWIG 6.5 [8] used to simulate the decay of the $\mathrm{W^+W^-}$ pair. Events are generated for $\sqrt{s} = 13$ TeV in the region $0 < |t| < 4$ GeV^2 and $0.01 < \xi < 0.2$. For the backgrounds, Single Diffractive (SD) and Double Pomeron Exchange (DPE) exclusive events are generated using POMWIG (v2.0) interfaced with HERWIG (v6.521) [8], multijet QCD events are simulated using PYTHIA (v8.175) [9], inclusive WW events with PYTHIA (v6.426), while the exclusive $\gamma\gamma \to \tau\tau$ events are generated with FPMC.

The presence of multiple interactions per bunch crossing (pileup) is incorporated by simulating additional interactions with an average pileup multiplicity of $\mu = 50$ matching that expected during Run 2. PYTHIA (v6.4 for the exclusive WW analysis, and v8.175 for that of the exclusive dijets) is used to generate minimum bias samples, including diffractive events. These events are mixed with the signal events to simulate the data-taking conditions expected during Run 2.

The generated events are processed through the GEANT4 (v9.4p03) [10] simulation of the CMS central detector and the standard reconstruction chain. Protons are tracked through the beam-line all the way to the position of the tracking and timing detectors. The simulation includes the beam energy dispersion, the beam crossing angle, smearing due to the beam divergence, vertex smearing, and detector resolution effects. In the CT-PPS, tracking and timing detectors are not fully simulated. The baseline timing detector (QUARTIC) has dimensions of 20×18 mm^2 (in x, y), with a segmentation of 3×3 mm^2; time resolution values of 10 ps (baseline) and 30 ps (conservative) are considered. For the tracking detectors, the resolution is simulated by a gaussian smearing of 10 μm on the proton position propagated

at z=204 m and z=215 m.

The $|t|$ and ξ distributions for the exclusive dijet and WW samples at "generator level" of the simulation and with the leading protons required to be within the CT-PPS geometrical acceptance are shown in Figures 7 and 8, respectively, separately for signal and background events. No selection is required in the central detector. The few events at $\xi > 0.2$ (Figure 7) are outside of the CT-PPS kinematical acceptance and correspond to the events at large $|t|$ values above $|t| \simeq 1.5$ GeV^2. These events will be rejected offline.

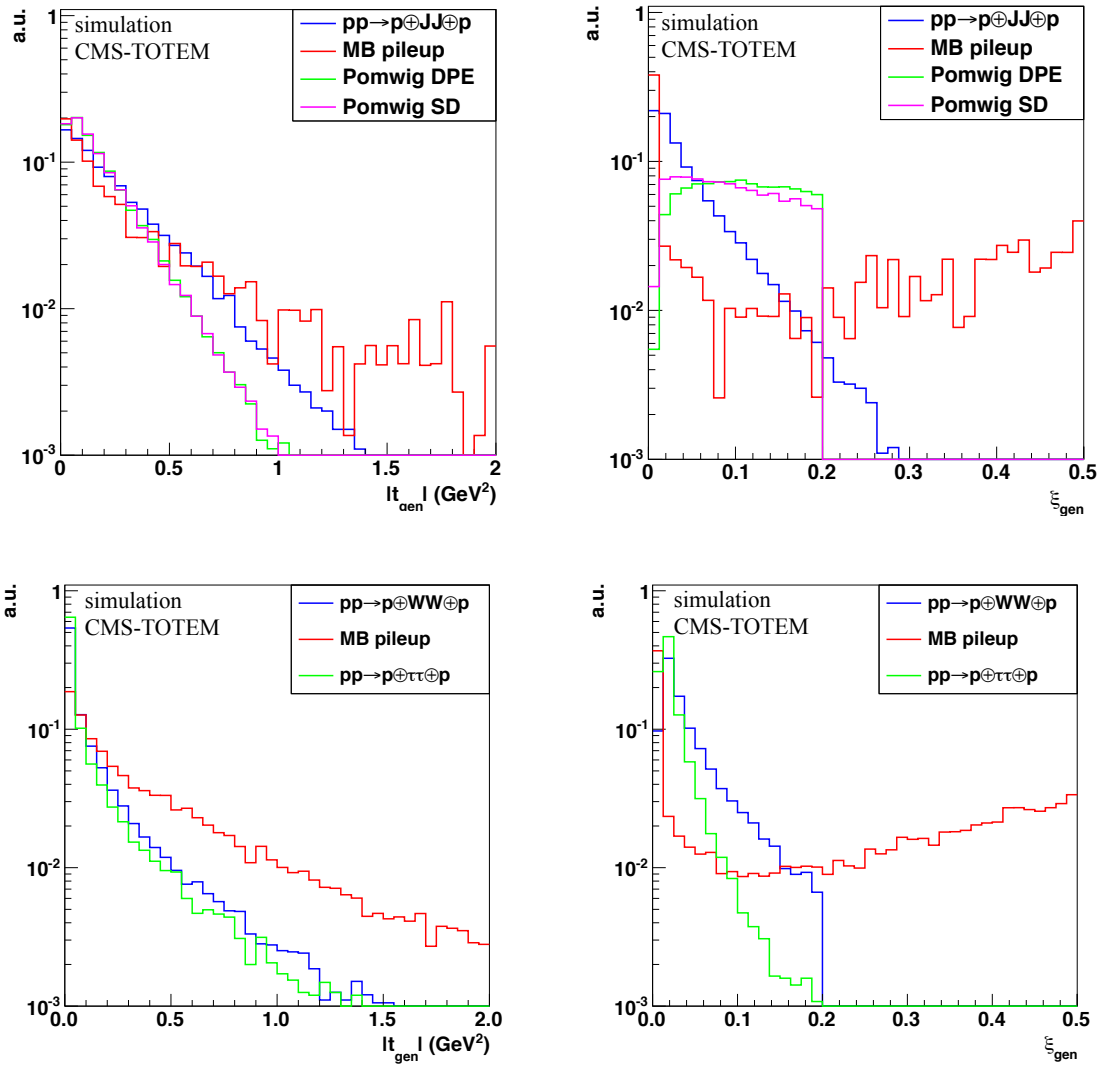

Figure 7: Generator-level distributions of $|t|$ (left) and ξ (right) for signal and background events in the exclusive dijet (top) and exclusive WW (bottom) samples. Distributions are normalized to unit area.

2.3 Detector acceptance and resolution: ξ, t

The dimensions of the CT-PPS detectors (both timing and tracking) are constrained by the allocated space in the RP, and eventually determine the coverage in $|t|, \xi$. The x, y distributions of protons with fixed values of $(|t|, \xi)$ at the two tracking stations is shown in Figure 9. The distributions are ellipses centered at $y = 0$ and reflect the effect of the quadrupole magnets along the beam-line. The acceptance for given $(|t|, \xi)$ values can be estimated as the fraction of the corresponding ellipse covered by the detectors.

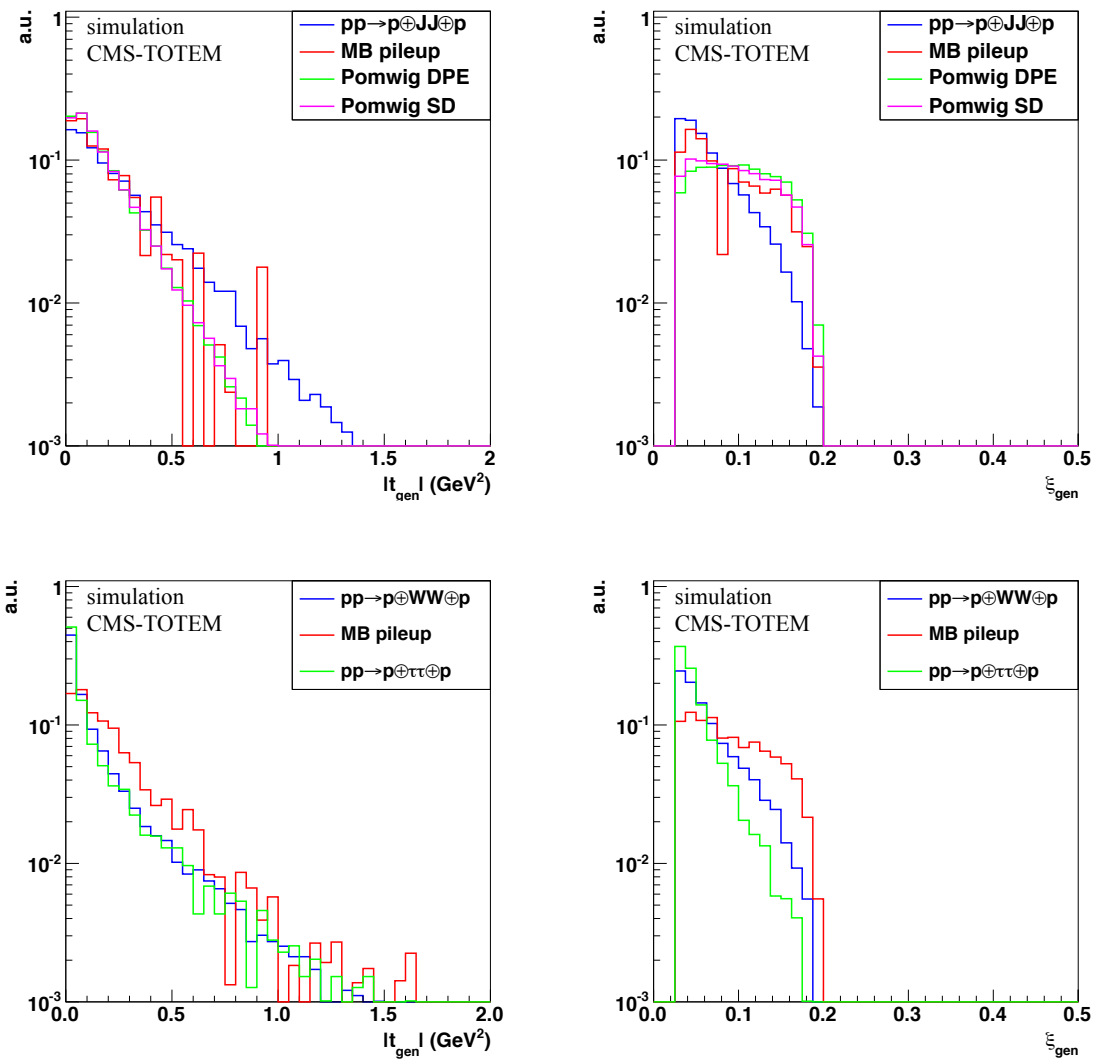

Figure 8: Distributions of generated $|t|$ (left) and ξ (right) for signal and background events in the exclusive dijet (top) and exclusive WW (bottom) samples. Distributions are normalized to unit area. Coincidence of hits in the tracking stations at z=204 m and z=215 m (on one side of the IP) is required. Tracking detectors are located at a distance of 15 σ from the beam center. Smearing effects due to vertex position, beam energy dispersion and crossing angle are accounted for.

Figure 9 is obtained with a "particle gun", generating protons at fixed $(|t|, \xi)$ values, in conjunction with HECTOR.

Concerning the detector distance from the beam center, the following approach is used: the RP window is placed at 15 (20) σ from the beam center and the distance of the sensors from the RP window is assumed to be 0.3 mm. The additional dead region due to the inefficiency of the sensor edge is not accounted for; it is estimated to be between 0.1 mm and 0.2 mm, which corresponds to $1-2\sigma$ of the beam dimensions. In Figure 9, the rectangle drawn by a dashed (solid) black line illustrates the boundaries of a detector with an area (in x, y) of 20×18 mm^2 located at 15σ (20σ)+0.3 mm from the beam center, whereas the beam envelopes are schematically drawn by ellipses centered at zero.

As mentioned above, no detailed simulation of the silicon detectors has been included, as their final design and characteristics are still being finalized. A detector resolution of 10 μm is accounted for by smearing the proton simulated position at the detector location. The other key parameters in the present

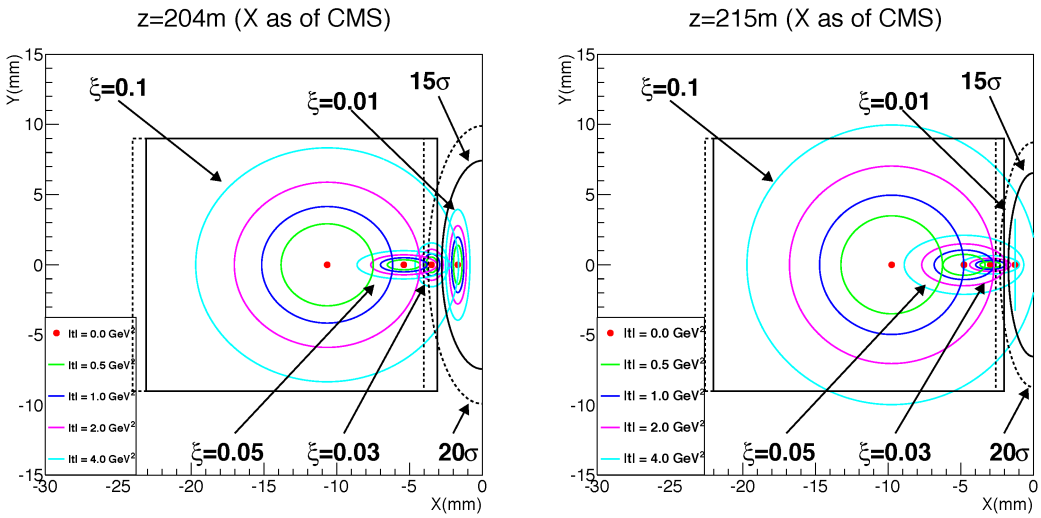

Figure 9: Particles with fixed $|t|$ and ξ values propagated to the CT-PPS detector position, at z=204 m (left) and z=215 m (right). The solid (dashed) black rectangle illustrates the detector boundaries at 15σ (20σ) from the beam center. The beam dimensions are also shown by circles. A "particle-gun" simulation based on HECTOR is used to generate protons at different $(|t|, \xi)$ values.

study are: the distance of the detector sensitive area from the beam center and the spatial resolution. Other important beam related effects have been included (as explained earlier in the text).

The particle hit distribution is studied for dimensions of the active area of the tracking stations at z=204 m and z=215 m, where detector planes are assumed to be orthogonal to the beam direction. Detector segmentation is not implemented in the simulation, as tracking detectors are expected to have a finely segmented active area (pixel size in x, y is $\approx 100 \times 150$ μm^2). Figure 10 shows the hit distributions in the tracking detectors at z=204 m for exclusive dijet (left) and WW (right) events. The black squared lines schematically illustrate the detector boundaries in x and y (20×18 mm^2) at 15σ from the beam center.

Figure 11 shows the single-arm distribution in the two-dimensional $(\xi, |t|)$ plane of the protons seen by both tracking stations at z=204 m and z=215 m, as simulated by ExHuME, for tracking detectors at 15σ (left) and 20σ (right) from the beam center. A track reconstruction efficiency of 100% is assumed. The loss of efficiency due to proton interactions with the RP window is estimated to be 1-2% [11]. For exclusive dijet events, a single-arm acceptance of approximately 49% is estimated (at 15σ) when the protons are within the CT-PPS detector geometrical acceptance. The acceptance is estimated as the number of protons that arrive at the CT-PPS divided by the number of generated ones in the same bin. Acceptance values are estimated with respect to the cross section of the generated events ($0 < |t| < 4$ GeV^2, $0.01 < \xi < 0.2$). Similar distributions in the $(\xi, |t|)$ plane are shown in Figure 12 for a double-arm coincidence, i.e. when hits in the tracking stations on both sides of the IP are required.

Single-arm and double-arm distributions in the $(\xi, |t|)$ plane for exclusive WW events produced with the FPMC signal generator are shown in Figures 13 and 14, respectively. Distributions are shown for a distance of the tracking detectors at 15σ (left) and 20σ (right) from the beam center. A single-arm acceptance of approximately 55% is estimated.

The full set of kinematic variables is reconstructed with the use of Eq. (2.1). The scattering angle resolution depends mainly on the angular beam divergence and on the detector resolution. As the values of the optical function parameters vary with the proton momentum loss, the resolution of the main variables $\Theta^*_{x,y}$ and ξ will depend on ξ. Moreover, as a dispersion term is present in the horizontal projection (cf. Eq. (2.1)), both Θ^*_x and ξ contribute in determining the horizontal trajectory, thus resulting in a correlation of these two variables.

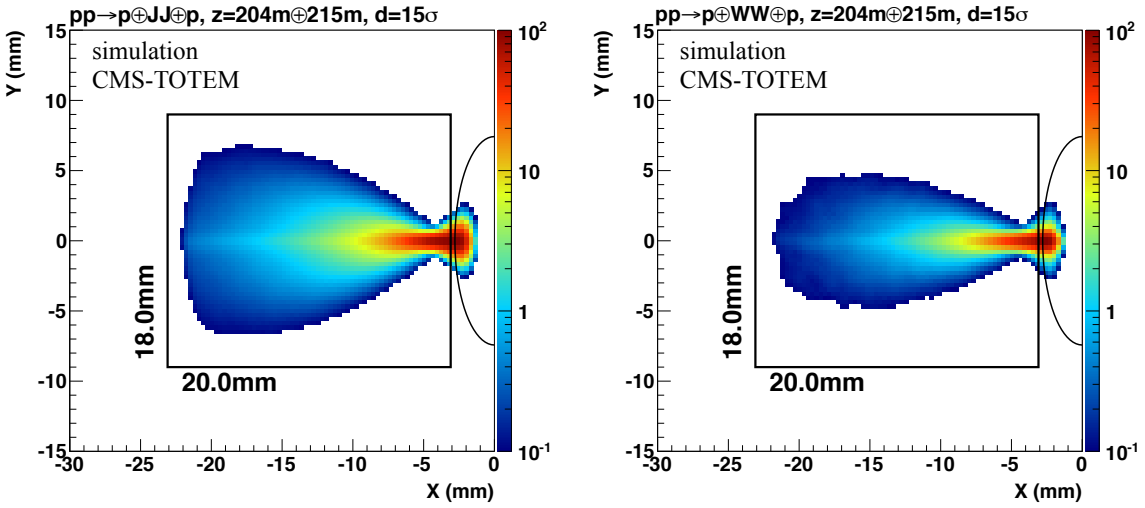

Figure 10: Hit distributions for centrally produced exclusive dijet (left) and WW (right) events are shown for the tracking detectors located at z=204 m. The black squared line schematically illustrates the boundaries of the tracking detectors in x and y, when located at 15σ (circle line) from the beam center. Beam energy and vertex smearing, as well as detector resolution are accounted for. Distributions are normalized to unity.

Generated and reconstructed values of $|t|$ and ξ are compared in Figures 15 and 16, respectively. The distributions are shown for the sample of exclusive dijet events. A linear correlation is found between the generated and reconstructed values over the entire $|t|$ and ξ ranges. The corresponding resolutions as a function of the generated variables, $|t_{gen}|$ and ξ_{gen}, are also shown. Similar $|t|$ and ξ distributions for exclusive WW events yields similar results.

2.4 Detector acceptance and resolution: mass

The mass acceptance closely reflects the ξ acceptance, since ξ is proportional to the mass, and it ultimately depends on the LHC beam optics and on the position of the CT-PPS detectors relative to the beam.

The acceptance as a function of the mass of the produced central system is shown in Figure 17 for central exclusive dijet (left) and WW (right) events. With detectors at 15σ from the beam, the CT-PPS selects exclusive systems with masses in the 350-1700 GeV range, with an acceptance of at least 5%. The lower mass reach is strongly dependent on the distance of closest approach of the detectors. In general, both stations have larger acceptance for central systems in photon-photon than in gluon-gluon interactions (because of the smaller $|t|$). The distributions also show that the acceptance varies substantially with the distance of the tracking detectors from the beam. Operation of the detectors at 15σ (blue bands in the plot) increases the acceptance by a factor of two in the lower mass value region. Beam energy dispersion, beam angular divergence, crossing angle at the IP, and detector resolution effects are included in the estimate of the acceptance.

The mass is reconstructed with a resolution of approximately 1.5% at 500 GeV. The expected reconstructed mass resolution for the entire mass system range studied ($0.3 < M_X < 2$ TeV) is shown in Figure 18. Figure 19 shows the mass resolution estimated as a function of the mass of the centrally produced events in exclusive dijet (left) and WW (right) events.

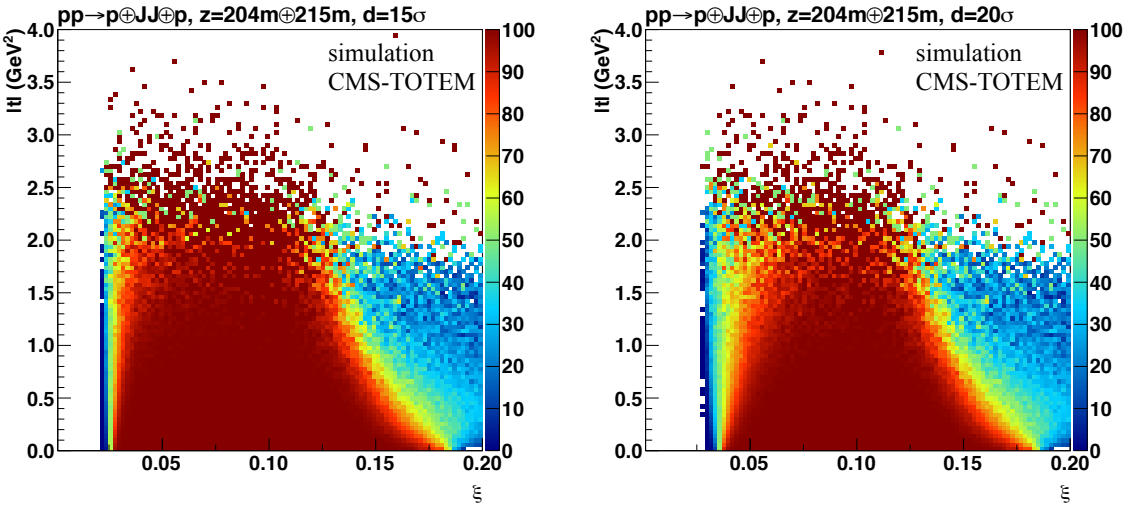

Figure 11: Exclusive dijet events: distributions in the $(\xi, |t|)$ plane, when requiring the coincidence of hits in the tracking stations at z=204 m and z=215 m only on one side of the IP. Distributions are shown for a distance of the tracking detectors at 15σ (left) and 20σ (right) from the beam center. Pileup events are not included. Distributions are normalized to unity.

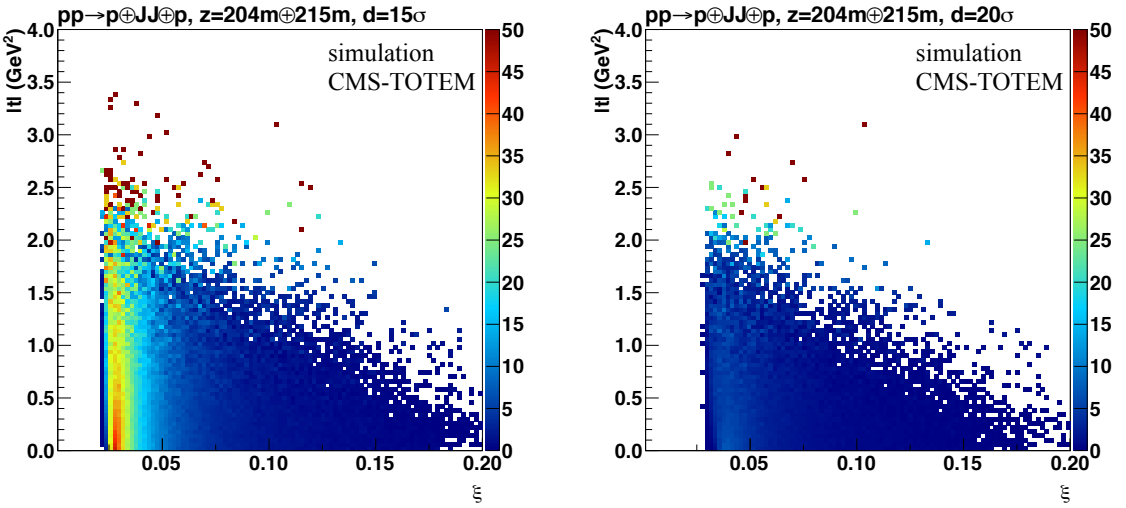

Figure 12: Exclusive dijet events: distributions in the $(\xi, |t|)$ plane, when requiring the coincidence of hits in the tracking stations at z=204 m and z=215 m on both sides of the IP. Distributions are shown for a distance of the tracking detectors at 15σ (left) and 20σ (right) from the beam center. Pileup events are not included. Distributions are normalized to unity.

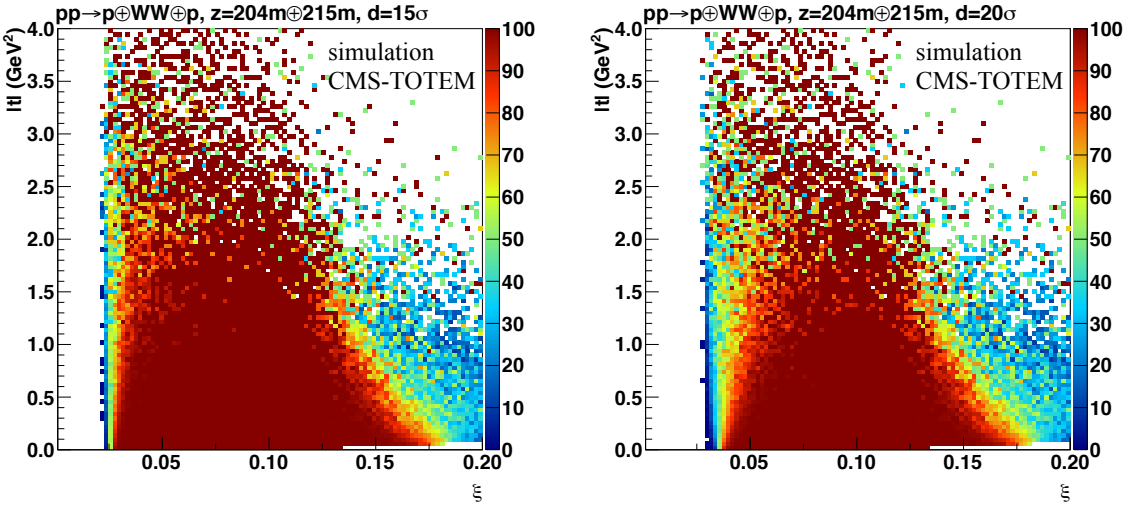

Figure 13: Exclusive WW events: distributions in the $(\xi, |t|)$ plane, when requiring the coincidence of hits in the tracking stations at z=204 m and z=215 m only on one side of the IP. Distributions are shown for a distance of the tracking detectors at 15σ (left) and 20σ (right) from the beam center. Pileup events are not included. Distributions are normalized to unity.

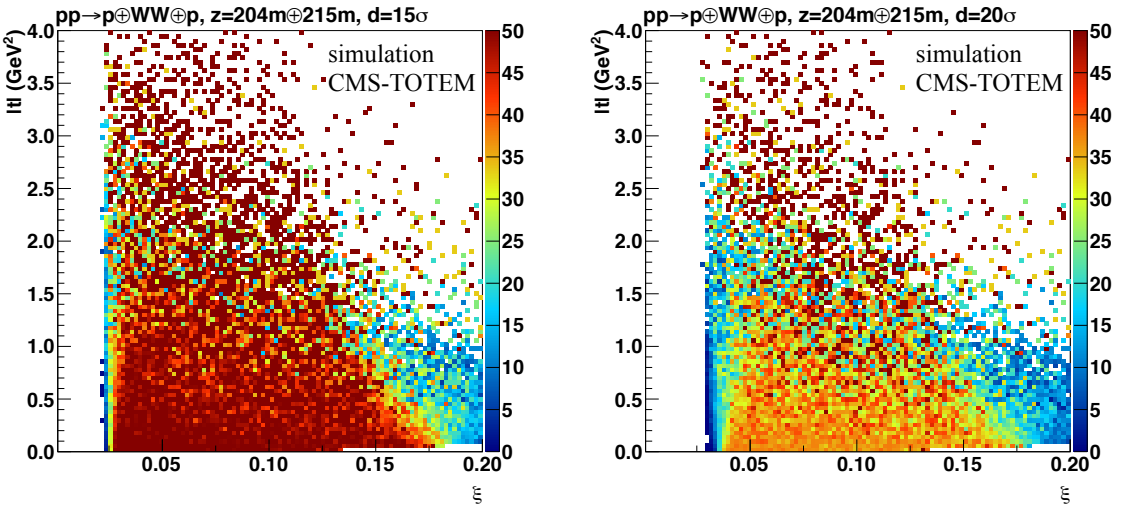

Figure 14: Exclusive WW events: distributions in the $(\xi, |t|)$ plane, at z=204 m and z=215 m on both sides of the IP. Distributions are shown for a distance of the tracking detectors at 15σ (left) and 20σ (right) from the beam center. Pileup events are not included. Distributions are normalized to unity.

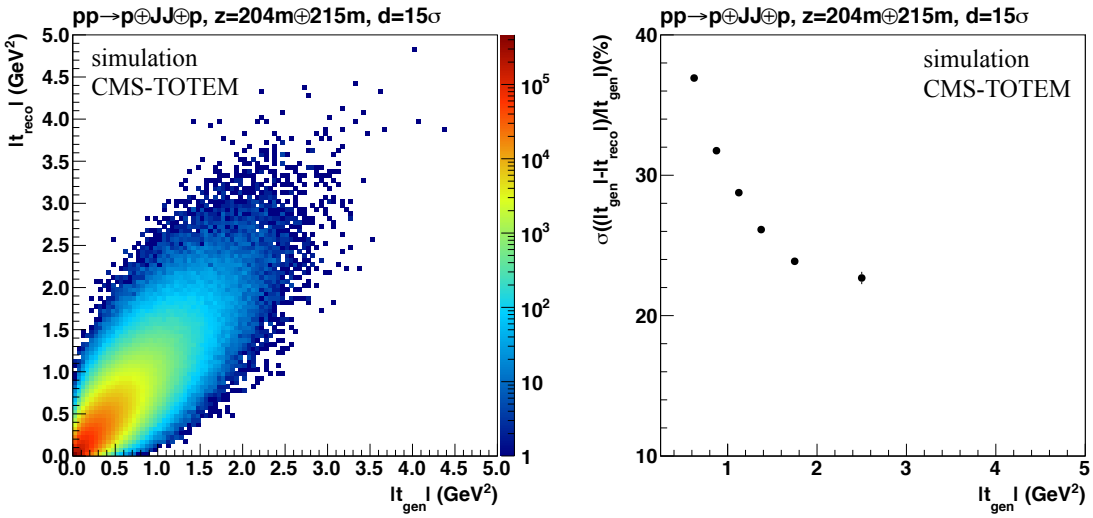

Figure 15: *Left:* Generated vs. reconstructed values of $|t|$ for the protons within the CT-PPS detector acceptance. In the reconstruction, smearing effects due to vertex position, beam energy dispersion and beam angular divergence are accounted for. *Right:* Resolution of the reconstructed $|t|$ measurement, $(t_{reco} - t_{gen})/t_{gen}$ as a function of the generated value, $|t_{gen}|$. Distributions for exclusive dijet events are shown for a distance of the tracking detectors at 15σ from the beam center.

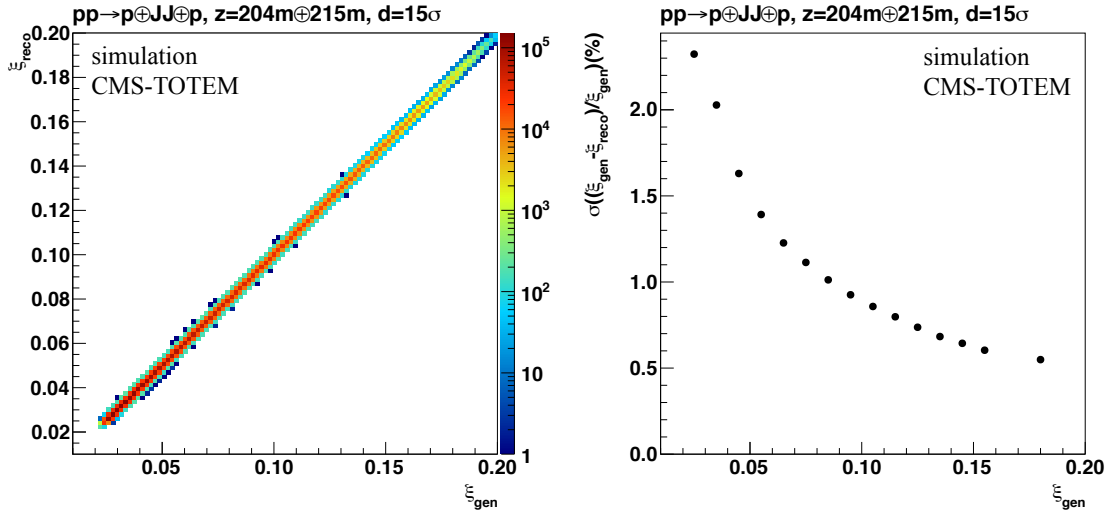

Figure 16: *Left:* Generated vs. reconstructed values of ξ for the protons within the CT-PPS detector acceptance. In the reconstruction, smearing effects due to vertex position, beam energy dispersion and beam angular divergence are accounted for. *Right:* Resolution of the reconstructed ξ measurement, $(\xi_{reco} - \xi_{gen})/\xi_{gen}$ as a function of the generated value, ξ_{gen}. Distributions for exclusive dijet events are shown for a distance of the tracking detectors at 15σ from the beam center.

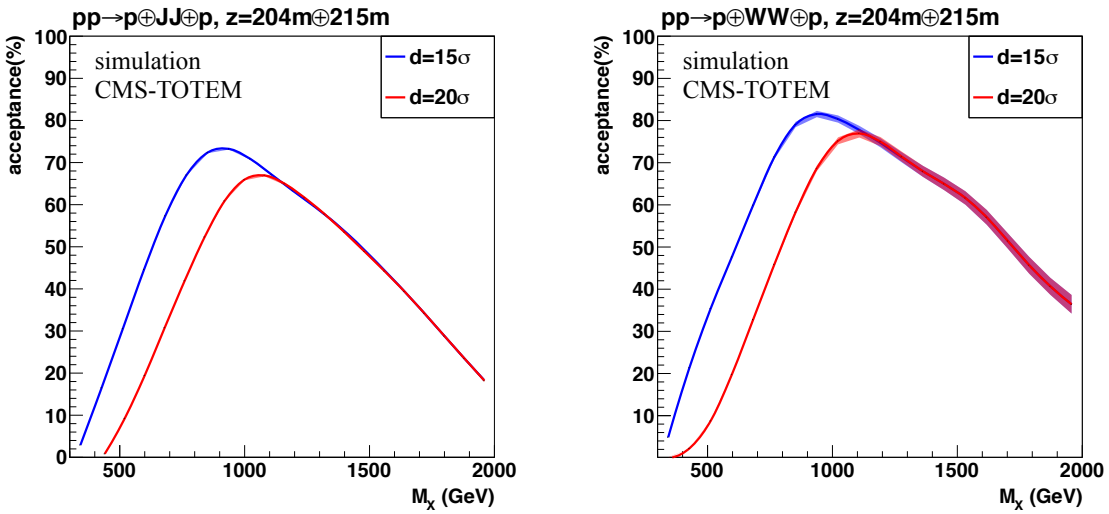

Figure 17: Mass acceptance as a function of centrally produced mass for exclusive dijet events produced in gluon fusion (left, computed with ExHuME), and exclusive WW events produced in photon-photon processes (right, computed with FPMC). In the simulation, a coincidence of the tracking detectors placed at z=204 m and z=215 m is required. The estimated acceptance is shown as a solid blue (red) line when the tracking detectors are located at a distance of 15 (20) σ from the beam center. Shaded bands indicate the statistical uncertainties.

2.5 Timing detectors

The occupancy and performance of the time-of-flight detectors are studied for different detector geometries. Here again, an average of 50 pileup interactions mixed with the primary interaction is assumed. Smearing effects due to vertex position, beam energy dispersion, beam angular divergence, and crossing angle are simulated.

Segmentation of the timing detector active area is considered for both the baseline option of the QUARTIC detectors, and for the study-option of solid state finely-segmented "diamond-like" detectors (discussed in Sections 5.5 and 5.6). The QUARTIC timing detector geometry is physically limited by the transversal dimensions of the detector bars and by the size of the available photodetectors, but also by the outgoing proton direction/angle, as each particle must be contained within the same detector bar in order to maximize the signal yield and minimize the cross-talk between neighboring bars. We estimate that the latter is not a limiting factor as, at the CT-PPS location, the deflection in x per mm travelled in z is small, and less than $\Delta x(\text{per mm}) \simeq 0.10$ μm. On the other hand, the "diamond-like" detector segmentation offers a flexible geometry by allowing the optimization of the detector occupancy depending on the distance from the beam center, thus reducing the occupancy rates closer to the beam. In the simulation, each L-shaped QUARTIC bar has the same (x, y) transversal section of 3×3 mm^2; the "diamond-like" cells have a y-dimension of 5 mm, with a variable width (in x) varying from 0.3 mm (close to the beam) up to 4.6 mm (away from the beam). Multiple hits in the same cell "blind" the detector functionality, and therefore –when this happens– the time-of-flight information cannot be used for rejecting pileup events. Such instances are thus contributing as a source of inefficiency to the data analysis. Figure 20 shows the resulting occupancies for the two geometries, when pileup and beam-related backgrounds (as discussed in detail in Section 2.6) are considered. It is clear that the diamond-like configuration is superior. However, even with average pileup of 50, the baseline configuration is still able to function.

Occupancy distributions (at the z-location of the timing detectors) are compared in Figure 21 for different average pileup multiplicities of $\mu = 25$ and $\mu = 50$. For this additional study, samples analogous to those discussed in Section 2.2 and with an average number of pileup interactions $\mu = 25$ are produced. In view

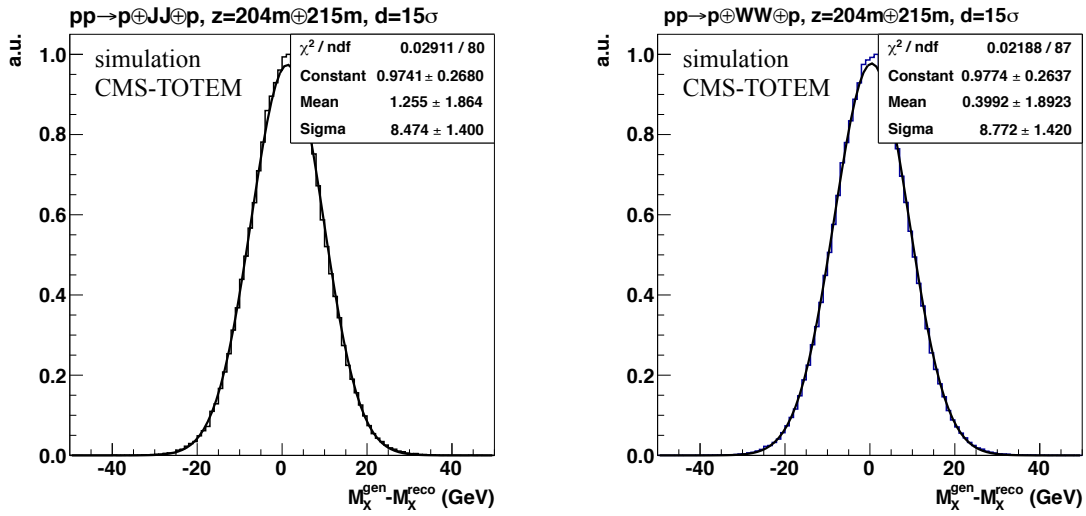

Figure 18: Reconstructed mass resolution for centrally produced events in the entire range of the mass system studied ($0.3 < M_X < 2$ TeV), in exclusive dijet (left) and in WW (right) events. The estimated resolution is shown for tracking detectors located at a distance of 15 σ from the beam center.

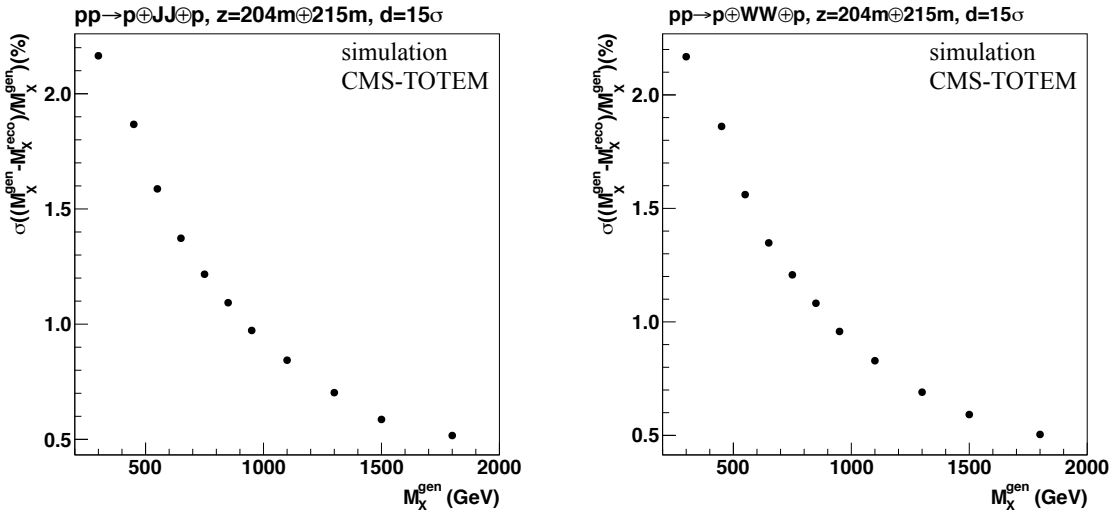

Figure 19: Mass resolution as a function of the mass M_X of the centrally produced events in exclusive dijet (left) and WW (right) events. The estimated resolution is shown for tracking detectors located at a distance of 15 σ from the beam center.

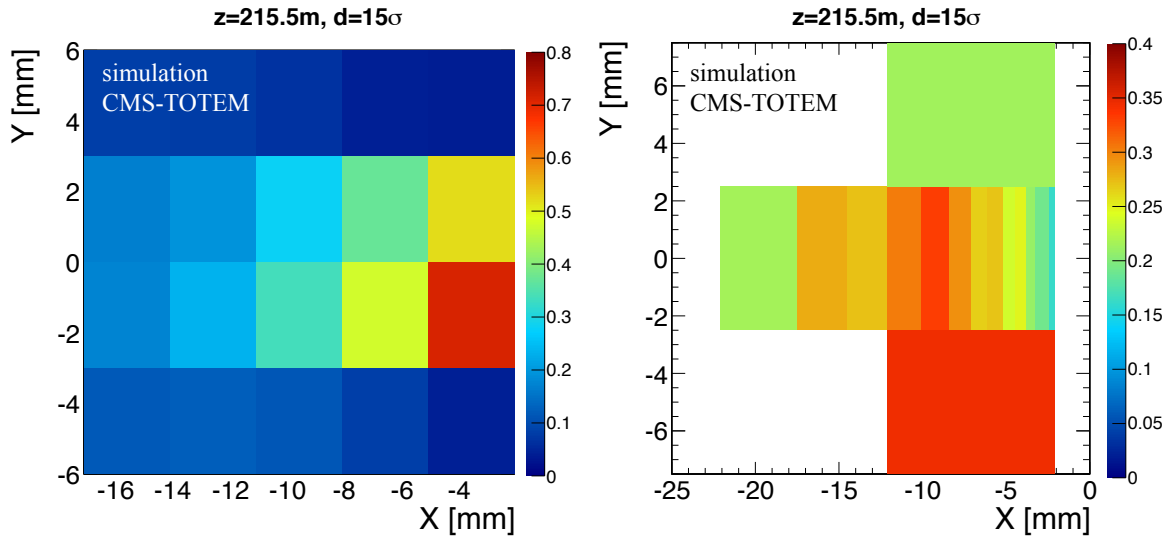

Figure 20: Detector occupancy of the time-of-flight detectors at 15σ from the beam center, with a segmentation corresponding to QUARTIC (left) or "diamond-like" (right) geometries, in the presence of background. Beam-related background (as discussed in Section 2.6) and 50 pileup interactions are considered.

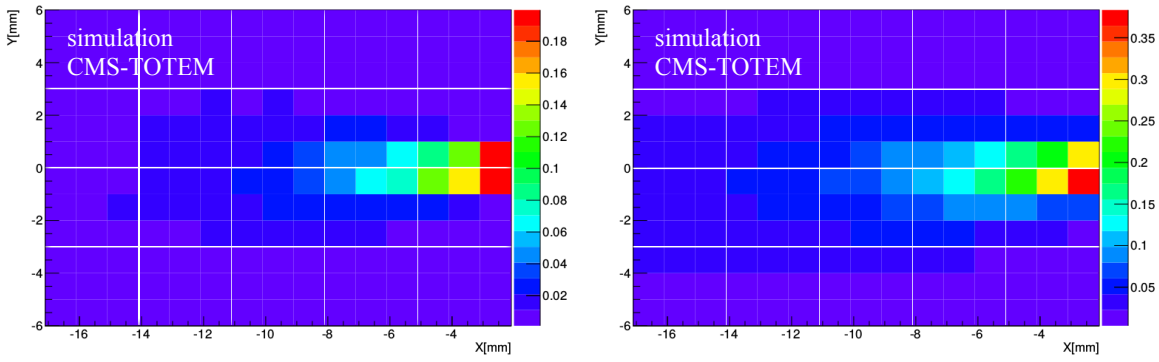

Figure 21: Detector occupancy of the time-of-flight detectors at 15σ from the beam center, with a segmentation of 1×1 mm^2, in the presence of background alone. Beam-related background (as discussed in Section 2.6) and 25 (left plot) and 50 (right plot) pileup interactions are considered. White thin lines, corresponding to the baseline of 3×3 mm^2 segmentation, are overlaid.

of a possible optimization, a detector segmentation of 1×1 mm^2 is used. White thin lines, corresponding to the baseline of 3×3 mm^2 segmentation, are overlaid.

2.6 Background: pp induced background

In addition to the genuine physics processes from the hard interaction or from pileup events, "machine-induced" backgrounds mainly due to beam halo or secondary particles must be estimated. The machine-induced background contribution at z=204-215 m is estimated by extrapolating the TOTEM 2012 measurements at $\sqrt{s} = 8$ TeV, carried out at the same location, to the Run 2 data-taking conditions. Any possible dependence of the spatial distribution of the machine-induced background on the collision en-

ergy and the number of bunches in LHC is not taken into account. Different approaches have been used to understand how to extract the background component from the data and how to extrapolate it to higher pile-up conditions. The detailed procedure is described in [12]. It can be summarized as in the following: the background probability per bunch-crossing is estimated from a zero-bias data sample. The zero-bias sample includes all events, from both background and physics processes. In order to subtract the contribution from physics processes, the multiplicity of the leading protons reconstructed in the horizontal pots is estimated with a dedicated sample of simulated events (without pileup). By comparing the multiplicity of the primary tracks with the average cluster multiplicity per detector plane from the data (zero-bias data sample) it is then possible to subtract this contribution, and to extract the probability distribution of the background per bunch-crossing. These results are then used to extract the scale factors to be applied to a simulation with $\mu = 50$, and extrapolate the tracking multiplicity due to machine-induced backgrounds expected for Run 2 conditions. The resulting forward ($z > 0$) and backward ($z < 0$) RP cluster multiplicities extrapolated to $\mu = 50$ are shown in Figure 22. The cluster multiplicity reproduces well the number of tracks in the RPs for small multiplicity values, whereas large values are mostly due to particles showering in the RPs.

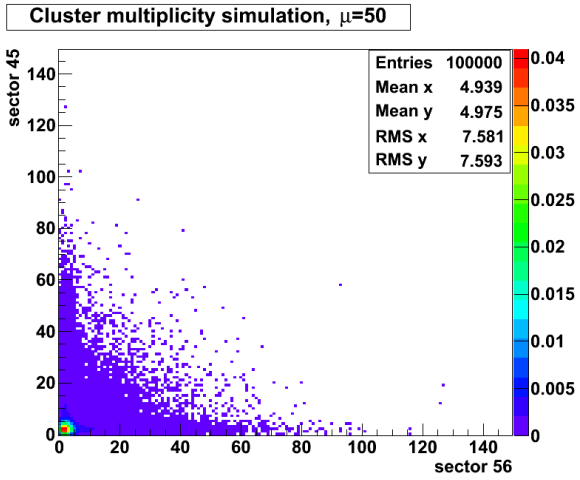

Figure 22: Average cluster multiplicity per detector plane in the forward (vertical axis, labeled "sector45") and backward (horizontal axis, labeled "sector56") RP detectors per bunch crossing, and estimated for a pileup of $\mu = 50$.

2.7 Roman Pot detector alignment

The values of both ξ and $|t|$ can be accurately determined from the reconstructed proton track parameters and the position of the event vertex at the IP by using the beam-transport matrix between the interaction point and the CT-PPS. Crucial for this determination is the detector (x, y) alignment with respect to the circulating beam. Precise knowledge of the position of the detector (with an accuracy of a few μm) is needed for optimizing the physics performance. The alignment procedure must be repeated for each data-taking period. This is also required by the LHC to determine the positions at which the RP can be inserted and safely operated.

The procedure described below is the one developed and used by TOTEM for the alignment of their proton spectrometer in Run 1. The alignment process consists of three subsequent steps: 1) alignment of the detector RP housing position with respect to the beam, 2) relative alignment of the individual RP detector positions with respect to each other, and 3) global alignment of detectors in different RPs (performed using elastic events). The steps are described in the following.

1. Alignment between the RP and the circulating beam: A special LHC beam filling scheme is re-

quired to determine the position of RPs and the active detectors with respect to the circulating beam, through a procedure similar to the one employed for the LHC collimators. The precision of this procedure is determined by the size of the RP motor steps, which vary between 10 μm and 50 μm. In this first step, the alignment has an accuracy of 200-300 μm, because of the uncertainty on the distance between the RP window and the active edge of the detectors. This special beam filling scheme requires only a few low-intensity proton bunches. This procedure must be repeated whenever the optics or the energy are changed.

2. Relative internal detector alignment: Individual detector planes in a detector package and in a single RP unit (horizontal and vertical) are aligned with respect to each other by using reconstructed tracks. This procedure uses the inter-calibration of horizontal and vertical RPs to determine their relative alignment. The precision of the alignment procedure depends on the number of events collected and on the number of reconstructed tracks. Typical uncertainties obtained are a few μm for the (x, y) shifts, and less than 0.1 mrad for the rotation.

3. Global alignment using elastic events: The global alignment modes (e.g. common shifts or rotations of the entire unit with respect to the beam) can be constrained by exploiting known symmetries of certain physics processes. This is performed by using elastic scattering events and exploiting the fact that, once the optics has been properly understood, the two elastically scattered protons act as an ideal ruler. This method is illustrated in Figure 23. The left plot shows a distribution of track intercepts for vertical detectors in a detector plane in a RP station at 220 m. The tilt of the vertical band is mainly caused by optics imperfections. The center plot shows the number of hits (x-axis) at different distances from the beam (y-axis); after excluding the detector edges (grey strips labeled "removed band"), the detector vertical offset is adjusted until a symmetric distribution of the event yields is found. Finally, the horizontal alignment and the unit rotation are established by fitting a straight line to the top and bottom hit distributions, as shown in the right plot.

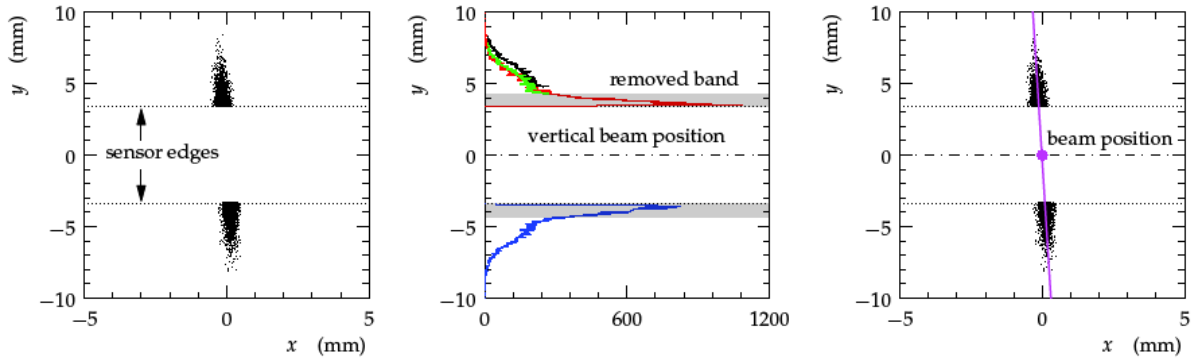

Figure 23: RP alignment with elastic events. A selection of elastic events (*left:*); vertical alignment where the x-axis contains the number of events per bin (*center*); horizontal alignment and the unit rotation are established by fitting the track distribution (*right*). The alignment procedure is discussed in the text.

A detailed discussion of this method is presented in Refs. [1, 13].

The alignment procedure just illustrated worked reliably for the TOTEM runs at low luminosity. The feasibility of applying this method at high luminosity will be investigated at the beginning of Run 2. If the TOTEM vertical RP are inserted at 13σ from the beam, the smallest observable $|t|$ would be 4.5 GeV^2. The corresponding visible cross section ranges, depending on the model used, between $3 \cdot 10^{-8}$ mb and $1 \cdot 10^{-6}$ mb. With an instantaneous luminosity of $\sim 10^{34}\mathrm{cm}^{-2}\mathrm{s}^{-1}$, the observable elastic rate is between 0.3 and 10 Hz, allowing the collection of 1k-33k events/h, sufficient to perform the alignment with a resolution of the order of 10μm.

An alternative method developed to dynamically determine the alignment of the CDF RP Spectrometer at the Tevatron is also briefly described below. This is a self-consistent data-driven method, and it uses an *in-situ* calibration to perform the alignment. It uses the fact that in the proximity of $|t| = 0$, the $|t|$-distribution can be represented as $d\sigma/dt = Ne^{-b|t|}$, where N is an arbitrary normalization factor and b the slope of the distribution. Alignment is achieved by seeking the maximum of the $d\sigma/dt$ distribution at $|t| = 0$. The implementation of the alignment method consists of introducing software offsets in the X and Y coordinates of the tracking detectors with respect to the physical beam-line position, and iteratively adjusting them until a maximum for $d\sigma/dt$ at $|t| = 0$ (or of the dominant slope b) is found. The (x, y) position for which this happens corresponds to that of the aligned tracking detector. This method is limited by the size of the data sample, the detector resolution, and the variations of the beam position during data taking. A resolution of $\simeq 60$ μm has been obtained at the Tevatron; for the LHC beam optics and energy, and with the new CT-PPS detector resolution, the accuracy has not yet been estimated. The method is discussed in detail in Ref. [14].

Relative alignment between the tracking and the timing stations is not discussed here. More details can be found in Section 5.2.5.

2.8 Physics processes

Study of physics processes with forward protons may extend the physics reach of the LHC experiments. Here, we consider two physics cases that address different issues: exclusive dijet and exclusive WW production. These processes will allow us to investigate central exclusive production with both protons measured in the mass region above 300 GeV, as well as to learn about rates, backgrounds, and operational aspects of the forward detectors. Knowledge already gained in operating the TOTEM experiment during Run 1, and the experience of the combined CMS-TOTEM data-taking will be used. The exclusive dijets produced in gluon-gluon fusion will allow improving our understanding of the proton structure as well as of the transition between non-perturbative and perturbative QCD. These jets are predicted to be nearly 100% gluon jets with a small admixture of $b\bar{b}$. The more rare high-energy two-photon exclusive production of $\gamma\gamma \rightarrow$WW will extend the possibility to study quartic gauge-couplings as well as to study deviations from the expected WW mass spectrum due to possible new BSM physics. Schematic leading-order diagrams of these two processes are shown in Figure 24.

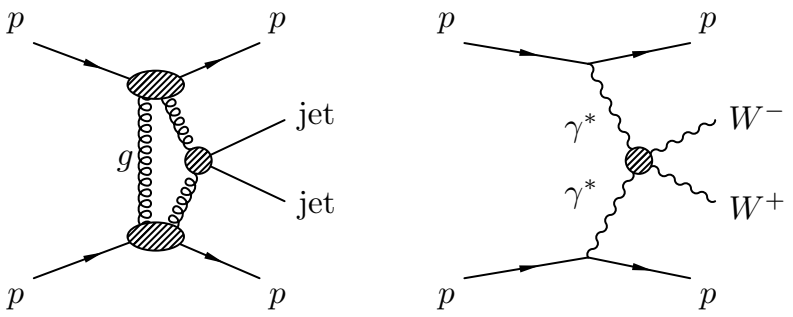

Figure 24: Leading order diagrams for exclusive dijet (left) and exclusive WW (right) production in pp collisions.

2.8.1 Central exclusive dijet production

In exclusive dijet production both protons escape intact the hard interaction, and a two-jet system is centrally produced, $pp \rightarrow p'\mathrm{JJ}p'$. Exclusive production may occur through a t-channel two-gluon exchange at leading order in perturbative QCD as shown schematically in Figure 24 (left). This process is

a particular case of dijet production in Double Pomeron Exchange (DPE), a diffractive process in which the protons suffer a small fractional momentum loss, and a system X containing two jets is produced, $pp \to (p'\mathbb{P})(p'\mathbb{P}) \to p'Xp'$. The Pomeron $\mathbb{P}$ is an exchange consisting of a colorless combination of gluons carrying the quantum numbers of the vacuum. Dijet production in DPE may occur as an exclusive process with only the jets in the final state, and no Pomeron remnants. In a special case, exclusive dijets may be produced through an intermediate state of a Higgs boson decaying into $b\bar{b}$.

Exclusive dijet production was first observed at the Tevatron [15] in hadronic collisions. The first study of dijet production at $\sqrt{s} = 7$ TeV is presented in Ref. [16], which however is limited to single-diffractive (SD) dijet production and has no measurement of the scattered proton. Here, the sensitivity to high-p_{T} exclusive dijet events is investigated. In addition to providing information on QCD aspects of vacuum quantum number exchange, any centrally produced system of mass X may appear as an excess over background expectations. With the addition of the PPS as "proton tagger", a significant enhancement of the sensitivity to these physics processes may be reached. The current study is based on the experimental techniques developed in Refs. [15, 16].

Events are selected by requiring a time coincidence in both arms of the CT-PPS. Leading protons are required to be in the CT-PPS fiducial region, and the arrival time difference at the CT-PPS location depends on the z-vertex position, $\mathrm{z_{PPS}}$, and must be consistent with the vertex position of the central dijet system, $\mathrm{z_{vertex}}$. The expected time resolution of 10 ps (30 ps) is assumed. Two jets with reconstructed transverse momenta $p_{\mathrm{T}} > 100(150)$ GeV in the central ($|\eta| < 2.0$) detector are required. Jets are reconstructed using the anti-k_{T} jet clustering algorithm with a distance parameter of 0.5 [17]. Finally, the instrumental background in the PPS from additional sources is accounted for, following the method discussed in Section 2.6. The main physics backgrounds are from minimum bias events –including SD and DPE events– in coincidence with either two jets in the central detector or another leading proton within the PPS detector acceptance.

The time-of-flight difference Δt (in ns) between the two leading protons arriving at the PPS detector location on opposite sides of the IP as a function of the z-vertex position of the leading jet is shown in Figure 25. A selection cut varying according to the z-vertex position (corresponding to the solid straight lines) keeps approximately 60% (50%) of signal events while reducing the inclusive dijet background by a factor 33 (18), for a 10 (30) ps timing resolution.

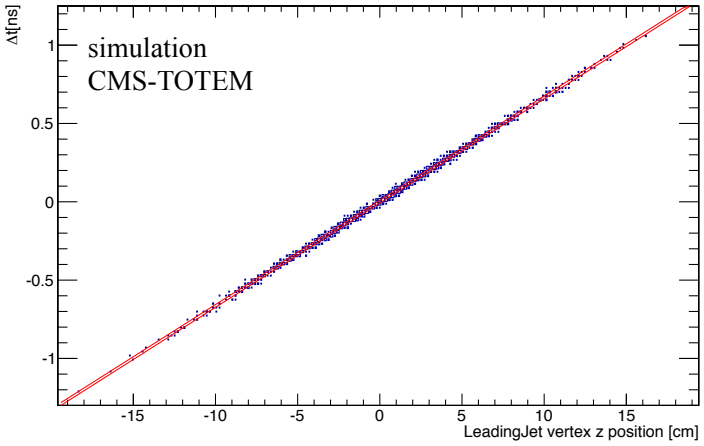

Figure 25: Time-of-flight difference between the two leading protons arriving at the PPS detector location on opposite sides of the IP as a function of the z-vertex position of the leading jet. A time resolution of 10 ps is assumed. The distribution is shown for exclusive dijet signal events and is normalized to an arbitrary value. The two solid straight lines contain approximately 60% of the events.

Kinematic distributions after the PPS tagging selection are shown in Figure 26. The leading jet p_{T} and the azimuthal angle difference between the two leading jets are shown for signal and background events. The dijet invariant mass M_{jj} and the missing mass $M_{\mathrm{X}} = \sqrt{s \cdot \xi_1 \cdot \xi_2}$ are also shown. M_{X} is estimated from the reconstructed fractional momentum loss values of the two leading protons, ξ_1 and ξ_2. Figure 27 (left) shows the dijet mass fraction, $R_{\mathrm{jj}} = M_{\mathrm{jj}}/M_{\mathrm{X}}$, and the rapidity difference (right) of the jet system (y_{jj}) and the proton system, $y_{\mathrm{X}} = 0.5 \cdot \ln(\xi_1/\xi_2)$. Consistency is required between the values of the jet mass system measured in the central detector (M_{jj}) and in the PPS (M_{X}), and the requirement $0.70 < R_{\mathrm{jj}} < 1.15$ is applied. A selection cut of $|(y_{\mathrm{jj}} - y_{\mathrm{X}})| < 0.1$ is also required.

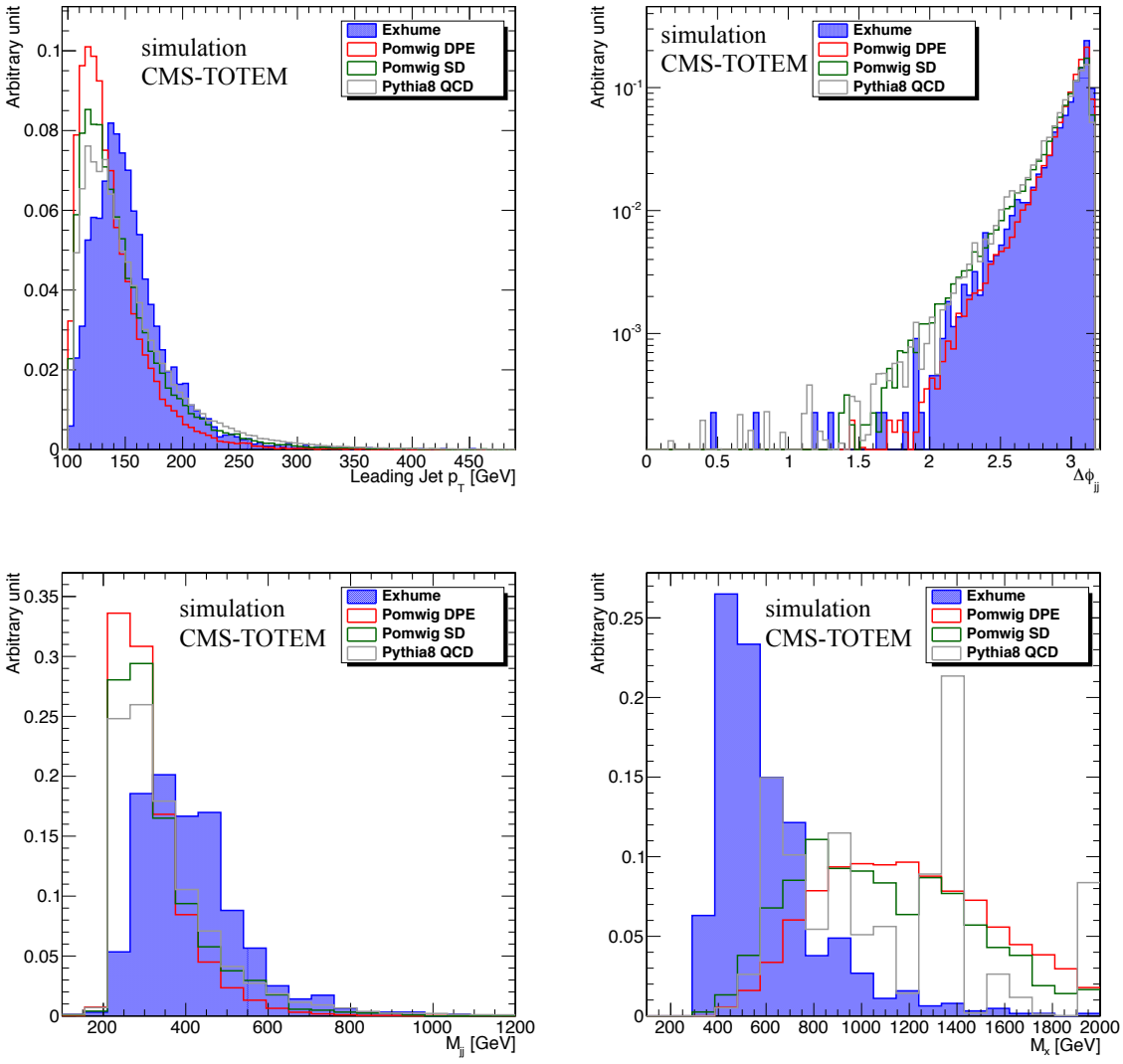

Figure 26: Leading jet p_{T} (top, left), azimuthal angle difference between the two leading jets (top, right), dijet invariant mass M_{jj} (bottom, left), and the missing mass $M_X = \sqrt{s \cdot \xi_1 \cdot \xi_2}$ (bottom, right) estimated from the reconstructed values of the two leading protons, ξ_1 and ξ_2. Distributions are shown for exclusive dijet signal (ExHuME) and for background (SD, DPE, inclusive dijets) events, and are normalized to unit area.

The track multiplicity associated to the dijet vertex is used to discriminate exclusive signal events against backgrounds. In particular, we exploit techniques developed in Ref. [18]. We build two variables that account for the "exclusitivity" of the event by counting the number of extra tracks between the jets, both in ϕ and η. We call these variables $N^{\phi}_{\mathrm{tracks}}$ and $N^{\eta}_{\mathrm{tracks}}$. Figure 28 shows a sketch of the central detector coverage with the two jets (dark shaded circles), and the areas between them that are used to count the

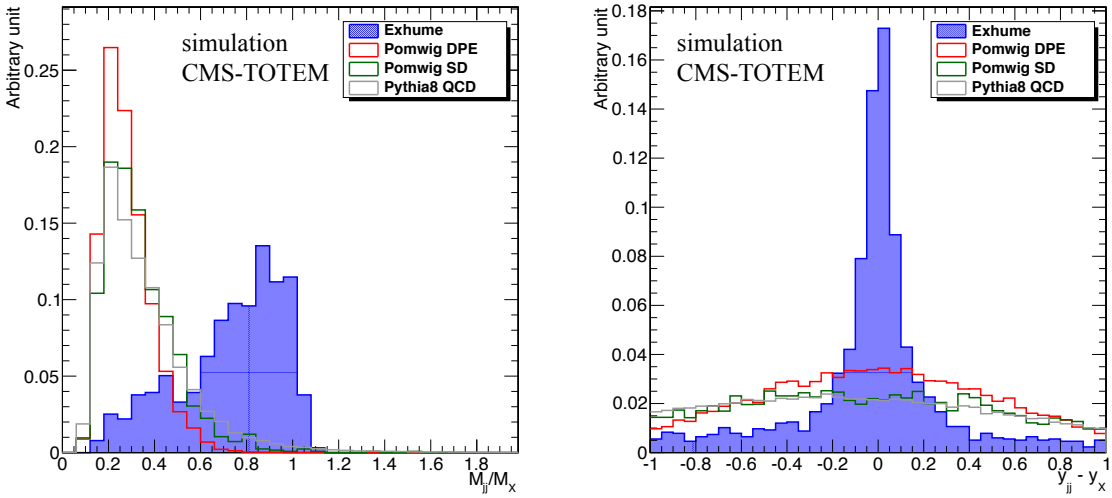

Figure 27: *Left:* Dijet mass fraction $R_{\rm jj} = M_{\rm jj}/M_{\rm X}$ (left). *Right:* Rapidity difference of jet ($y_{\rm jj}$) and proton ($y_{\rm X}$) systems. Distributions are shown for exclusive dijet signal (ExHuME) and for background (SD, DPE, inclusive dijets) events and are normalized to unit area.

number of extra tracks in ϕ and in η. We consider all tracks from the primary vertex and define the area of -1.0 ($+1.0$) away from the minimum (maximum) jet η coordinates, $\eta_{\rm min}$ and $\eta_{\rm max}$ (vertical white areas in Figure 28). Then, we count the number of extra tracks that are below (above) the $\eta_{\rm min}$ ($\eta_{\rm max}$) position. Similarly, the $N^{\phi}_{\rm tracks}$ variable is built. In this case, we count the number of tracks that are perpendicular to the plane formed by the two-jet system, in the region $0.54 < \phi < 2.60$ (horizontal white area in Figure 28).

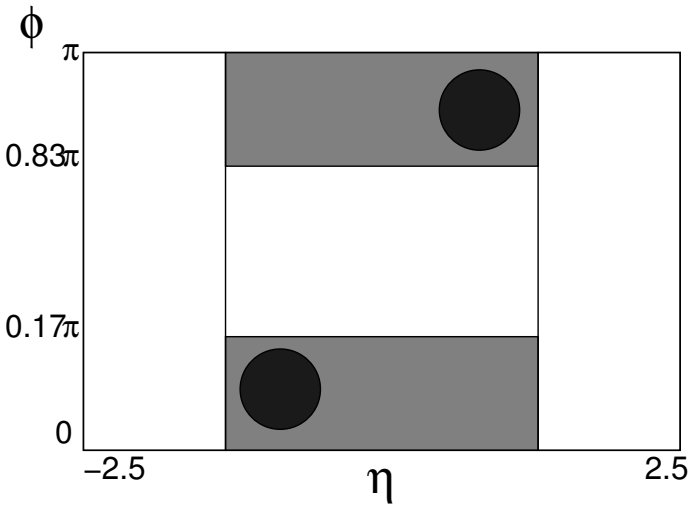

Figure 28: A drawing showing the two jets (dark circles) and the areas between them that are used to count the number of extra tracks in ϕ and in η.

The track multiplicity variables after the timing selection cuts are shown in Figure 29, for exclusive dijet signal events and for the background processes. Two-dimensional distributions of track multiplicity in ϕ vs. η are shown in Figure 30 for signal and background events. Exclusive signal events tend to have significantly lower track multiplicity than inclusive dijet events in either ϕ and η. The tracking multiplicity separation in η helps in further rejecting SD and DPE events. Events are kept if the conditions

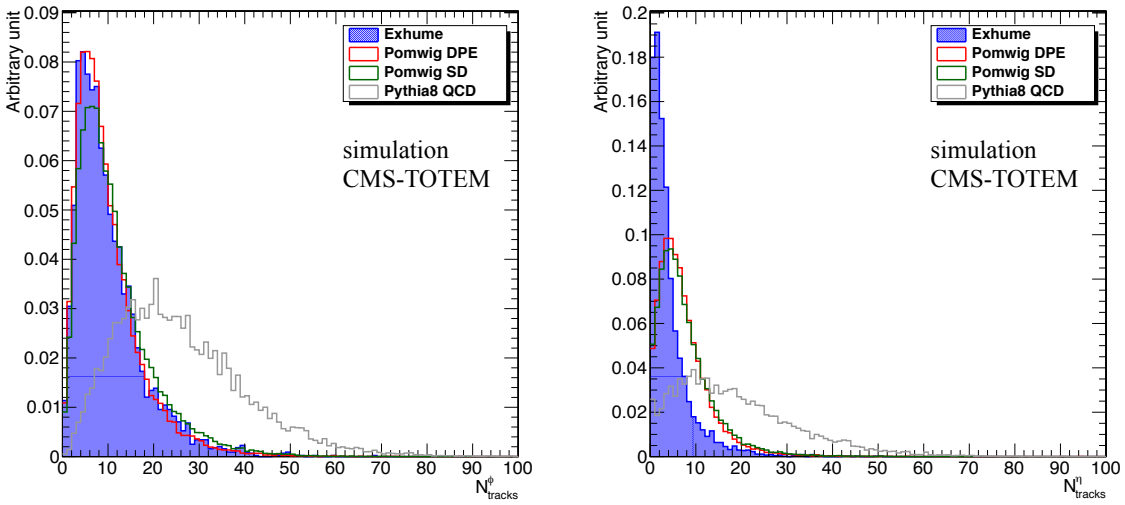

Figure 29: Number of extra tracks outside the jet system in ϕ (left) and in η (right), associated to the dijet vertex for exclusive dijet and background processes. Distributions are shown after the leading proton time-of-flight correlation requirements (with a 10 ps resolution). Event yields are normalized to unit area.

$N^{\phi}_{\rm tracks} \leq 9$ and $N^{\eta}_{\rm tracks} \leq 2$ are satisfied. Event candidate yields and relative cumulative efficiencies, for signal and for background (from SD, DPE, and inclusive dijets) events are summarized in Table 3 for an integrated luminosity of 1 fb^{-1}. Figure 31 illustrates the evolution of the event yields as a function of the cuts applied for a time resolution of 10 ps. The cross-section for signal events (given by ExHuME) is multiplied by a factor of 5/3 to simulate a gap survival probability of 5% (i.e. the same used for DPE dijet event processes in POMWIG), instead of the gap survival probability given by ExHuME of 3%.

The present study demonstrates the feasibility of measuring exclusive dijet production in Run 2 with the PPS with an average pileup of $\mu = 50$. A signal-to-background ratio of S:B$\simeq$1:8 can be achieved (after the "$N_{\rm tracks}$" cut), with the signal events appearing as an enhancement of the M_{jj}/M_X distribution around $M_{jj}/M_X = 1$. A time resolution of 10 ps is assumed. This would give access to the study of important aspects of QCD, and would pave the way to searching for new, beyond the SM, centrally produced resonances.

We also studied the case of a lower average number of pileup interactions, $\mu = 25$. For this additional study we produced analogous samples to those discussed in Section 2.2. By applying the same sequence of cuts, we obtain the yields for signal and background processes presented in Table 4. A signal-to-background ratio of S:B$\simeq$1:3 can be achieved in the less harsh condition with pileup of $\mu = 25$ (after the "$N_{\rm tracks}$" cut). Figure 32 illustrates the evolution of the event yields as a function of the cuts applied for a time resolution of 10 ps.

Table 5 summarizes the yields of signal and background events (after the $N_{\rm tracks}$ cut) estimated in bins of separate missing mass regions, $M_{\rm X} < 500$ GeV (where most of the signal is expected), $500 < M_{\rm X} < 800$ GeV, and $M_{\rm X} > 800$ GeV. Yields normalized to an integrated luminosity of 1 fb^{-1} are shown for average pileup multiplicities of $\mu = 25$ and $\mu = 50$. A timing resolution of 10 ps is assumed.

In order to optimize its sensitivity, the study of this physics process will be first pursued at pileup with $\mu = 25$, accumulating $\sim$ 100 fb^{-1} of data in the first years after LS1 and before the instantaneous luminosity reaches close to $\mathcal{L} = 2 \cdot 10^{34}$ cm^{-2}s^{-1}. After this period, we will be using the second half of the fills and/or the timing trigger (see Chapter 6) to select a data sample with 25 average pileup events corresponding to 30-40% of the full sample.

Selection	Exclusive dijets		DPE		SD		Inclusive dijets	
	events	ϵ (%)	events	ϵ (%)	events	ϵ (%)	events	ϵ (%)
total number of events	652±7	100	290×10^3	100	2.6×10^6	100	2.4×10^{10}	100
≥ 2 jets ($p_{\mathrm{T}} >$100 GeV, $\lvert\eta\rvert < 2.0$)	287±5	44	36×10^3	12.2	270×10^3	10	4.4×10^8	1.8
PPS tagging (fiducial)	77±3	12	23×10^3	7.8	39×10^3	1.5	0.5×10^8	0.2
no overlap hits in ToF detectors	54±2	8	18×10^3	6.3	25×10^3	1.2	0.3×10^8	0.12
ToF difference, Δt	32 (27)±2	5	$14\ (11) \times 10^3$	4.8	6×10^3	0.3	$95\ (180) \times 10^4$	4×10^{-3}
$0.70 < [R_{\mathrm{jj}} = (M_{\mathrm{jj}}/M_{\mathrm{X}})] < 1.15$	20 (16)±1	3.1	43 (39)±8	0.01	200 (250)±40	0.01	$45\ (85) \times 10^3$	2×10^{-4}
$\Delta(y_{\mathrm{jj}} - y_{\mathrm{X}}) < 0.1$	15 (12)±1	2.3	10 (11)±4	-	12±10	-	$5\ (9) \times 10^3$	-
N_{tracks}	5 (4)±1	0.8	1.3 (1.5)±0.5	-	1±1	-	$40\ (77) \pm 1$	-
≥ 2 jets ($p_{\mathrm{T}} > 150$ GeV, $\lvert\eta\rvert < 2.0$)	2.5 (1.9)±0.2	0.4	0.4±0.2	-	0±1	-	$20\ (36) \pm 1$	-

Table 3: Number of expected signal events and relative cumulative efficiency ϵ (in %) after each selection cut, for exclusive dijet signal events, and for SD and DPE background events. A timing resolution of 10 ps; in case of different values, numbers in parentheses are for a timing resolution of 30 ps. Yields are normalized to an integrated luminosity of 1 fb^{-1}. Events with an average pileup multiplicity of $\mu = 50$ are included. Statistical uncertainties are shown.

Selection	Exclusive dijets		DPE		SD		Inclusive dijets	
	events	ϵ (%)	events	ϵ (%)	events	ϵ (%)	events	ϵ (%)
total number of events	652±5	100	290×10^3	100	2.6×10^6	100	2.4×10^{10}	100
≥ 2 jets (p_{T} >100 GeV, $\lvert\eta\rvert < 2.0$)	250±4	38	25×10^3	8.7	190×10^3	7.6	3.4×10^8	1.4
PPS tagging (fiducial)	50±2	8	15×10^3	5.1	12×10^3	0.5	0.1×10^8	0.05
no overlap hits in ToF detectors	43±2	7	14×10^3	4.8	$10\ (18) \times 10^3$	0.4	0.1×10^8	0.04
ToF difference, Δt	30 (23)±2	4.6	$11\ (9) \times 10^3$	3.8	3×10^3	0.1	$0.3\ (0.6) \times 10^6$	1×10^{-3}
$0.70 < [R_{\mathrm{jj}} = (M_{\mathrm{jj}}/M_{\mathrm{X}})] < 1.15$	20 (15)±1	3.1	15 (14)±3	0.01	85 (110)±15	-	$16\ (30) \times 10^3$	1×10^{-4}
$\Delta(y_{\mathrm{jj}} - y_{\mathrm{X}}) < 0.1$	15 (12)±1	2.4	6 (4)±2	-	3 (11)±3	-	$1.8\ (3.4) \times 10^3$	-
N_{tracks}	7.4 (5.8)±0.4	1.1	0.8 (0.6)±0.3	-	1±1	-	$19\ (35) \pm 1$	-
≥ 2 jets ($p_{\mathrm{T}} > 150$ GeV, $\lvert\eta\rvert < 2.0$)	3.5 (2.6)±0.2	0.5	0.2 (0.1)±0.1	-	1±1	-	$9\ (17) \pm 1$	-

Table 4: Number of expected signal events and relative cumulative efficiency ϵ (in %) after each selection cut, for exclusive dijet signal events, and for SD and DPE background events. A timing resolution of 10 ps; in case of different values, numbers in parentheses are for a timing resolution of 30 ps. Yields are normalized to an integrated luminosity of 1 fb^{-1}. Events with an average pileup multiplicity of $\mu = 25$ are included. Statistical uncertainties are shown.

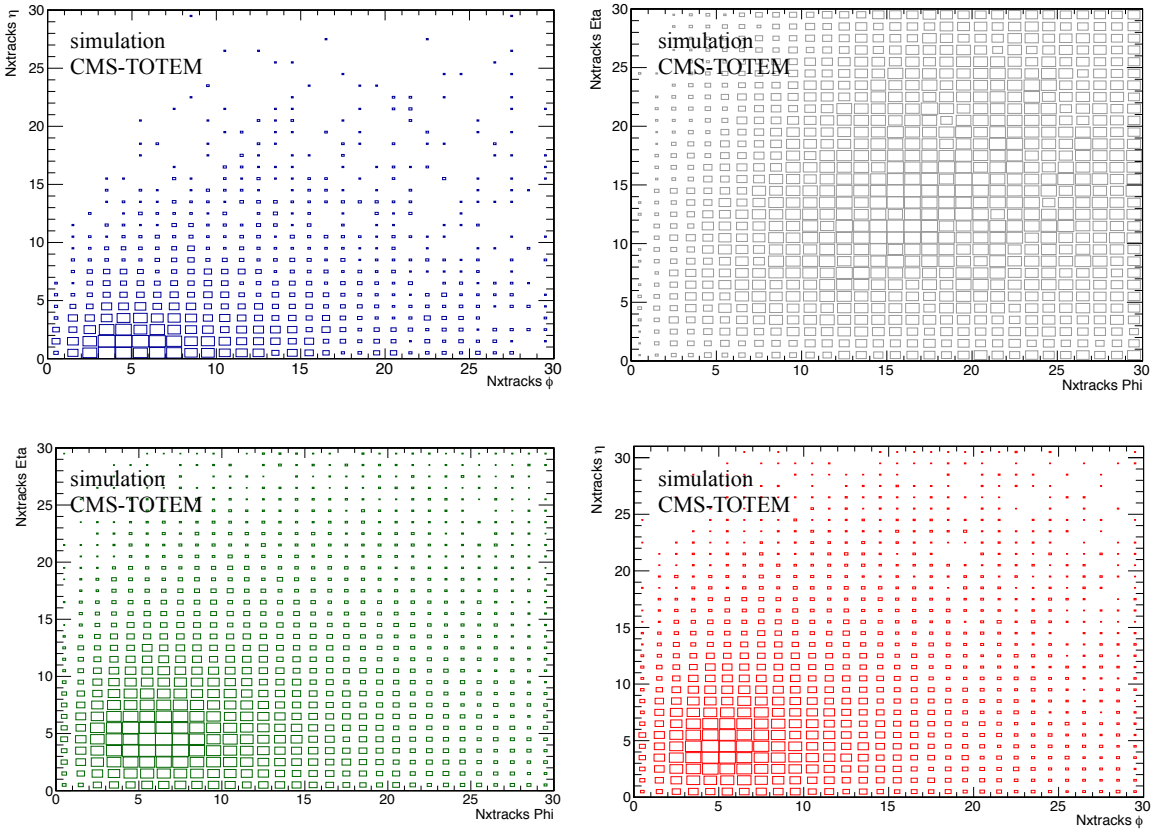

Figure 30: Number of extra tracks in ϕ vs η for exclusive signal events (top, left), inclusive dijet (top, right), SD (bottom, left), and DPE (bottom, right) events. Distributions are shown after the leading proton time-of-flight correlation requirements (with a 10 ps resolution), and are normalized to unit area.

	Exclusive dijets	DPE	SD	Inclusive dijets	S:B
pileup $\mu = 25$					
$M_X \leq 500$ GeV	4.0±0.2	0.2±0.1	0±1	1 ± 1	3:1
$500 < M_X \leq 800$ GeV	3.1±0.2	0.3±0.1	0±1	15 ± 1	1:5
$M_X > 800$ GeV	0.3±0.1	0.3±0.1	1±1	4 ± 1	1:18
pileup $\mu = 50$					
$M_X \leq 500$ GeV	2.8±0.2	0.6±0.2	0±1	5 ± 1	1:2
$500 < M_X \leq 800$ GeV	2.3±0.2	0.7±0.3	1.3±1.0	26 ± 1	1:12
$M_X > 800$ GeV	0.3±0.1	0±1	0±1	9 ± 1	1:30

Table 5: Number of expected signal and background (SD, DPE, and inclusive dijets) events (after the N_{tracks} cut), for separate bins of missing mass M_X. Yields normalized to an integrated luminosity of 1 fb^{-1} are shown for average pileup multiplicities of $\mu = 25$ and $\mu = 50$. Statistical uncertainties are shown. A timing resolution of 10 ps is assumed.

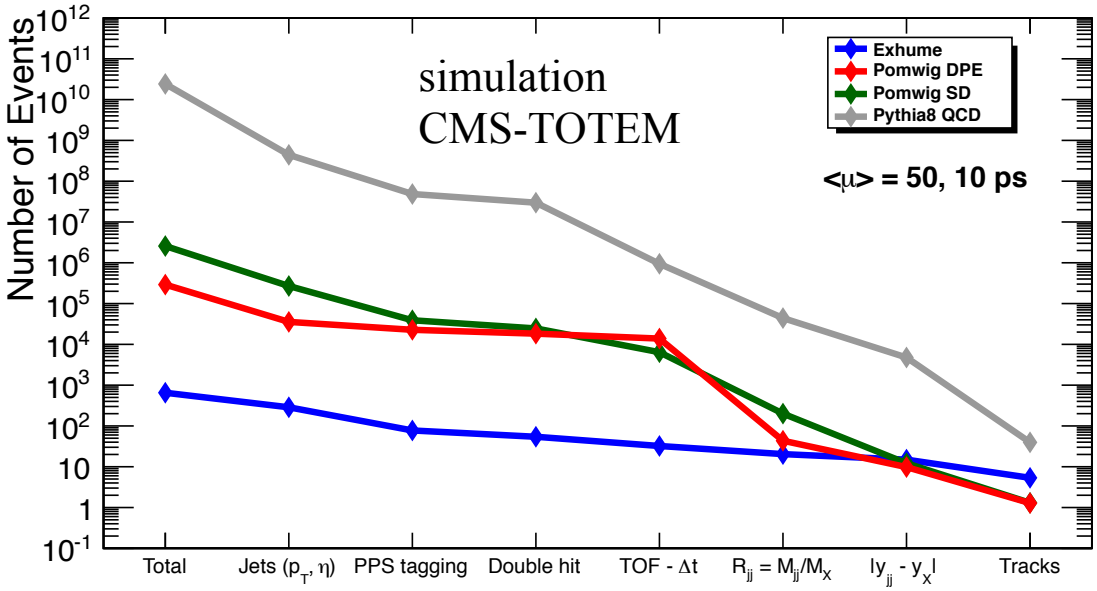

Figure 31: Graphical illustration of the event yields for signal and background processes as a function of the cuts applied. A time resolution of 10 ps and an average pileup multiplicity of $\mu = 50$ are assumed. Yields are normalized to an integrated luminosity of 1 fb^{-1}.

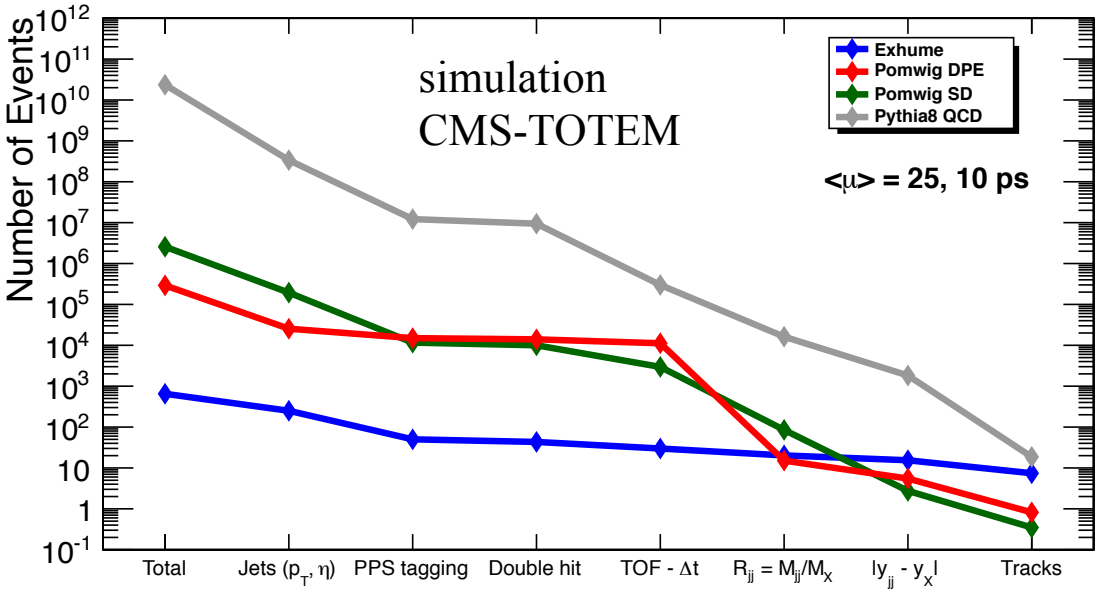

Figure 32: Graphical illustration of the event yields for signal and background processes as a function of the cuts applied. A time resolution of 10 ps and an average pileup multiplicity of $\mu = 25$ are assumed. Yields are normalized to an integrated luminosity of 1 fb^{-1}.

2.8.2 Central exclusive WW production

The study of high-energy photon interactions at the LHC opens up the possibility of interesting and novel research [19, 20]. In particular, measurements of the two-photon production of a pair of W-bosons provide sensitivity to anomalous quartic gauge couplings of the gauge bosons. Measurements of the exclusive two-photon production of W boson pairs, in the process $pp \to p\mathrm{W}^+\mathrm{W}^-p$, were performed in the $\mu^\pm\mathrm{e}^\mp$ final state, using 5.05 fb^{-1} of data collected in proton-proton collisions at $\sqrt{s} = 7$ TeV with the CMS detector at the LHC in 2011, but without the proton tagging [21]. Model-independent upper limits were extracted and compared to predictions involving anomalous quartic gauge couplings (AQGCs).

The current study is based on the experimental techniques developed in Ref. [21]. With the integrated luminosity expected to be collected during Run 2 and with the CT-PPS detectors, the experimental reach can be extended by several orders of magnitude with respect to the best limits obtained so far. In the process $pp \to p\mathrm{WW}p$, both forward-scattered protons are detected in the CT-PPS, depending on the acceptance on the mass of the WW central system produced (Figure 17). The CT-PPS detector is assumed to be at 15 σ from the beam (including the dead region of 0.3 mm due to the RP window).

This process is characterized by a primary vertex from the two leptons $\ell^\pm\ell'^\mp$ (where $\ell = e, \mu$) from the W boson pair decays, no other track, a large transverse momentum of the dilepton system, $p_\mathrm{T}(\ell^\pm\ell'^\mp)$, and a large invariant mass, $M(\ell^\pm\ell'^\mp)$. A simulated sample of SM exclusive $pp \to p\mathrm{WW}p$ signal events is used, in conjunction with samples in which anomalous quartic gauge couplings (AQGC) are assumed. The dominant SM backgrounds come from inclusive $\mathrm{W}^+\mathrm{W}^-$ and exclusive $\tau^+\tau^-$ pair production. Drell-Yan (DY) production of $\tau^+\tau^-$, where one τ decays via the electron channel and the other one via the muon channel, in combination with pileup protons, may lead to a similar event configuration as the exclusive WW signal. A selection cut on the transverse momentum of the dilepton pair $p_T(\ell^\pm\ell'^\mp) > 30$ GeV was used in Ref. [21] to reject the DY background almost completely. A further rejection of the other SM backgrounds, and a reduction of signal events by approximately 20% is expected. In this study, only the eμ final state is selected. The inclusion of same-flavor channels (ee and $\mu\mu$) will also be addressed as it brings an enhancement in sensitivity. However, in this case the gain can be mitigated as, in order to reduce the background from DY processes, additional selection cuts may be necessary.

The simulated samples for the signal process are compared to the SM background expectations. Tails of the M_X distribution ($M_X = \sqrt{s \cdot \xi_1 \cdot \xi_2} > 1$ TeV), where the SM $\gamma\gamma \to \mathrm{W}^+\mathrm{W}^-$ contribution is expected to be small, are investigated to look for AQGCs. Events are selected by requiring two central ($|\eta| < 2.4$) leptons with a minimum transverse momentum $p_\mathrm{T} > 20$ GeV. In order to reduce the contamination from the W+jet (or other non-prompt lepton) background, "tight" lepton identification criteria are imposed (as in Ref. [21]). Leptons are also required to have charges of opposite sign and to come from the same primary vertex. For signal events (either SM or AQGC), the scattered protons are in the region covered by CT-PPS, and the presence of hits in both tracking and timing detectors is therefore required: a large background suppression is expected. A source of inefficiency comes from detector segmentation, as hits are required not to overlap in the timing detector cells.

Signal events from SM exclusive WW events are correlated in time with the leading protons detected in the CT-PPS detectors, whereas inclusive WW events -superimposed with additional pileup events- are not. Therefore, the information of the proton time-of-flight arrival at the CT-PPS detector location can be used as an additional background rejection. After requiring the coincidence of hits in both tracking and timing detector stations, the time-of-flight difference between the two leading protons arriving at the CT-PPS detector location on opposite sides of the IP is shown in Figure 33 as a function of the z-vertex position of the leading central lepton, for signal (left) and background (right) events. For each event, if there is more than one pp combination in the CT-PPS detector, only the one with the closest match between the time-of-flight Δt and the lepton vertex position in z is kept ("vertex matching" in Table 6). The background is shown for inclusive WW events in coincidence with pileup events. Distributions cor-

responding to timing resolutions of 10 ps (top) and 30 ps (bottom) are shown for signal and background events.

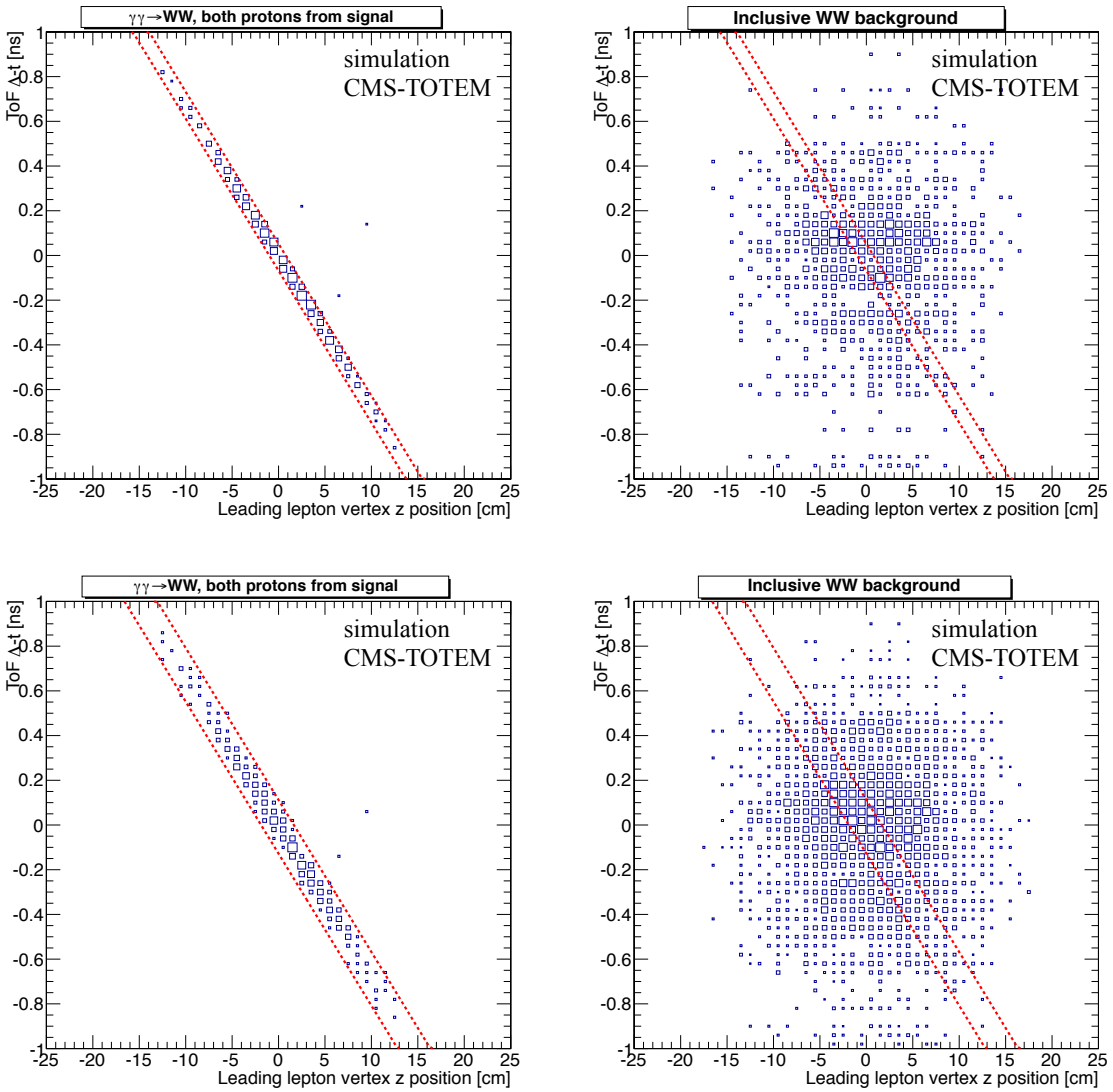

Figure 33: Time-of-flight difference between the two leading protons arriving at the CT-PPS detector location on opposite sides of the IP as a function of the z-vertex position of the leading central lepton for exclusive signal (left) and background inclusive WW (right) events. Timing resolutions of 10 ps (top) and 30 ps (bottom) are assumed. Distributions are shown for events where both leading protons are within the CT-PPS detector acceptance (after selecting the closest match of the vertices of the dilepton system and of the leading protons), and before the time-of-flight difference requirement. The dotted lines show an ideal window retaining close to 100% of signal events. An arbitrary normalization is used in the distributions.

The distance (in z) of the vertex positions measured from the CT-PPS timing detectors and from the leading lepton in the central detector, $\Delta z = z_{\mathrm{PPS}} - z_{\mathrm{lead\ lep}}$, is shown in Figure 34 for SM exclusive WW/$\tau\tau$ and inclusive WW events, and for AQGC exclusive WW events. Time-of-flight requirements may help reducing the inclusive WW background by a factor of 10 (5), for a timing resolution of 10 ps (30 ps).

The track multiplicity associated to the dilepton vertex after the timing selection cuts is shown in Figure 35 for SM signal and backgrounds. The number of extra tracks associated to the dilepton vertex is

significantly larger for inclusive WW events, and a selection of $N_{\text{tracks}} < 10$ is expected to suppress the inclusive background by 90%, while retaining approximately 90% of the exclusive events. A signal-to-background ratio of 1:1 can be achieved after applying a cut on the maximum number of reconstructed tracks in the central detector (except the two selected leptons).

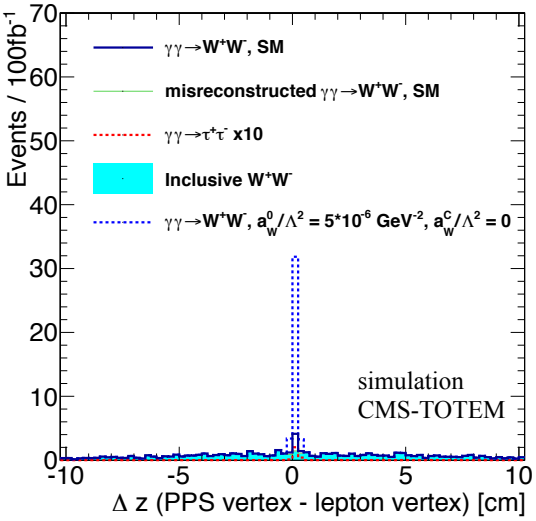

Figure 34: Distance along the z-axis (in cm) of the vertex positions as measured from the CT-PPS timing detectors and from the leading lepton in the central detector, $\Delta z = z_{\text{PPS}} - z_{\text{lead lepton}}$. A timing resolutions of 10 ps is assumed. Distribution is shown for SM exclusive WW/$\tau\tau$, inclusive WW events, and AQGC exclusive WW events after all cuts, except for the time-of-flight information requirement. Event yields are normalized to an integrated luminosity of 100^{-1}fb. Histograms are stacked, except for that of the exclusive $\tau\tau$ background, which is not stacked and is multiplied by a factor of 10.

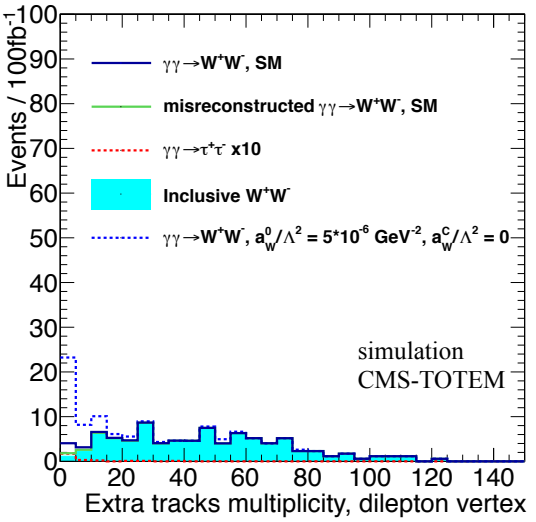

Figure 35: Number of extra tracks associated to the dilepton vertex for exclusive (WW and $\tau\tau$) and inclusive (WW) events. Distribution is shown after all cuts (with a 10 ps resolution), except for the track multiplicity cut. Event yields are normalized to an integrated luminosity of 100^{-1}fb. Histograms are stacked, except for that of the exclusive $\tau\tau$ background, which is not stacked and is multiplied by a factor of 10.

Kinematic distributions after the full event selections are shown in Figure 36. The transverse momentum of the dilepton system, the azimuthal angle difference between the two leading muons, and the missing

mass distributions are shown for signal and for the background exclusive $\tau\tau$ event yields. The missing mass $M_X = \sqrt{s \cdot \xi_1 \cdot \xi_2}$ (also indicated as $W_{\gamma\gamma}$ in Figure 36) is estimated from the reconstructed values of the two leading protons, ξ_1 and ξ_2. The yields of exclusive $\tau\tau$ background events are multiplied by a factor of 10, in order to allow comparison of the shapes.

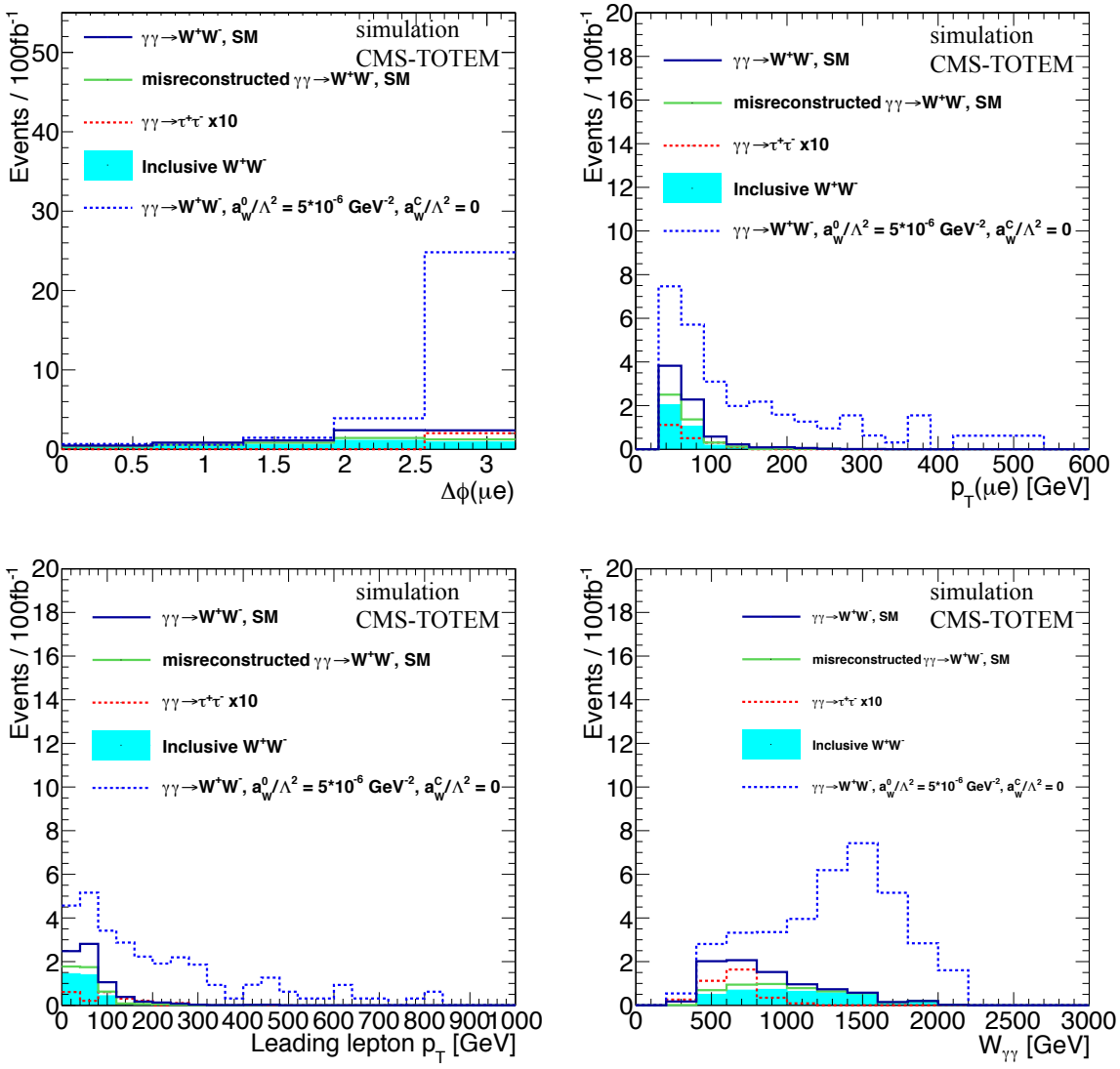

Figure 36: Azimuthal angle difference between the two leading leptons (top, left), transverse momentum of the dilepton pair (top, right), leading lepton transverse momentum (bottom, left), and missing mass (bottom, right) for signal and background events, and in the presence of exclusive WW events due to AQGC processes. Distributions are shown after the full event selection, for an integrated luminosity of 100 fb^{-1}. Histograms are stacked, except for that of the exclusive $\tau\tau$ background, which is not stacked and is multiplied by a factor of 10.

Table 6 summarizes the cross sections (in fb) after each selection cut. Cross sections include the branching fractions and are given for the dominant SM processes within the geometrical and detector acceptance. A small contribution from incorrectly reconstructed exclusive WW signal events, where at least one of the leading protons comes from a pileup or SD/DPE event, is also estimated separately.

Table 7 summarizes the cross sections (in fb) for the expected exclusive WW events due to AQGC for two different values of the coupling parameters, a_0^W and a_C^W. Cross section values include the branching fractions and are given for the dominant SM processes within the geometrical and detector acceptance.

Selection	Cross section (fb)			
	exclusive WW	exclusive WW (incorrectly reconstructed)	inclusive WW	exclusive $\tau\tau$
generated $\sigma \times \mathcal{B}(WW \to e\mu\,\nu\bar{\nu})$	0.86±0.01	N/A	2537	1.78±0.01
≥ 2 leptons ($p_{\mathrm{T}} > 20$ GeV, $\eta < 2.4$)	0.47±0.01	N/A	1140±3	0.087±0.003
opposite sign leptons, "tight" ID	0.33±0.01	N/A	776±2	0.060±0.002
dilepton pair $p_{\mathrm{T}} > 30$ GeV	0.25±0.01	N/A	534±2	0.018±0.001
protons in both PPS arms (ToF and TRK)	0.055 (0.054)±0.002	0.044 (0.085)±0.003	11 (22)±0.3	0.004±0.001
no overlapping hits in ToF + vertex matching	0.033 (0.030)±0.002	0.022 (0.043)±0.002	8 (16)±0.2	0.003 (0.002)±0.001
ToF difference, $\Delta t = (t_1 - t_2)$	0.033 (0.029)±0.002	0.011 (0.024)±0.001	0.9 (3.3)±0.1	0.003 (0.002)±0.001
$N_{\mathrm{tracks}} < 10$	0.028 (0.025)±0.002	0.009 (0.020)±0.001	0.03 (0.14)±0.01	0.002±0.001

Table 6: Cross section (in fb) for the expected SM processes, exclusive and inclusive WW, and exclusive $\tau\tau$ events, after each selection cut (for a timing resolution of 10 ps). In case of different values, numbers in parentheses are for a timing resolution of 30 ps. Only the eμ final state is considered. Statistical uncertainties are shown.

Unlike the backgrounds, the signal yields are not affected by the timing resolution.

Selection	Cross section (fb)	
	$a_0^W/\Lambda^2 = 5 \cdot 10^{-6}\text{GeV}^{-2}$ ($a_C^W = 0$)	$a_C^W/\Lambda^2 = 5 \times 10^{-6}\text{GeV}^{-2}$ ($a_0^W = 0$)
generated $\sigma \times \mathcal{B}(WW \to e\mu\,\nu\bar{\nu})$	3.10±0.14	1.53±0.07
≥ 2 leptons ($p_\text{T} > 20$ GeV, $\eta < 2.4$)	2.33±0.08	1.00±0.04
opposite sign leptons, "tight" ID	1.82±0.08	0.78±0.03
dilepton pair $p_\text{T} > 30$ GeV	1.69±0.07	0.68±0.03
protons in both PPS arms (ToF and TRK)	0.52 (0.50)±0.04	0.18 (0.17)±0.02
no overlapping hits in ToF detectors	0.35 (0.32)±0.03	0.12 (0.11)±0.01
ToF difference, $\Delta t = (t_1 - t_2)$	0.35 (0.32)±0.03	0.12 (0.11)±0.01
$N_\text{tracks} < 10$	0.27 (0.24)±0.03	0.11 (0.10)±0.01

Table 7: Cross section (in fb) for the expected exclusive WW events due to anomalous quartic gauge couplings, for different values of anomalous coupling parameters (a_0^W and a_C^W) after each selection cut (for a timing resolution of 10 ps). In case of different values, numbers in parentheses are for a timing resolution of 30 ps. Only the eμ final state is considered. Statistical uncertainties are shown.

The cross section times the acceptance for SM exclusive WW events is already sizeable at small reconstructed values of the missing mass ($M_X \simeq 300 \div 400$ GeV), and a close approach to the beam can provide a rapid increase of SM signal event yield. We evaluated the variation of the acceptance as a function of the detector distance from the beam. Figure 37 (left) shows that the visible cross section for signal exclusive WW events increases by a factor of two when the detector distance from the beam decreases from 15 σ to 10 σ. For a similar variation, the misreconstructed signal event yields remain more or less constant. The missing reconstructed mass is shown in Figure 37 (right) for three values of the distance from the beam (10, 15, and 20 σ).

The selected events are used to set limits on the AQGC parameters, a_0^W/Λ^2 and a_C^W/Λ^2. The resulting limit values are of the order of $a_0^W/\Lambda^2 = 2 \times 10^{-6}$ (3×10^{-6}), and $a_C^W/\Lambda^2 = 7 \times 10^{-6}$ (10×10^{-6}), in case of a 10 ps (30 ps) time resolution. Approximate 95% CL limits expected with 10 ps and 30 ps timing resolutions (Figure 38, left) are compared to the 2011 CMS results [21] from exclusive WW events (Figure 38, right). Expected limits for Run 2 are estimated for an integrated luminosity of 100 fb^{-1}. The areas outside the contours are excluded at 95% CL.

The present study demonstrates the feasibility of measuring exclusive WW production in Run 2 with the CT-PPS detector. With an integrated luminosity of 100 fb^{-1}, approximately 3 SM exclusive WW signal events are expected and a similar number of background events, even when looking at the eμ channel alone. Anomalous quartic gauge couplings would produce a striking, very visible signal. Approximately 30 (10) events would be visible in the presence of AQGC, with coupling parameters $a_0^W(a_C^W)/\Lambda^2 = 5 \cdot 10^{-6}\text{GeV}^{-2}$. As discussed in Section 1.2, several more channels are available, which would further enhance the significance of the measurement.

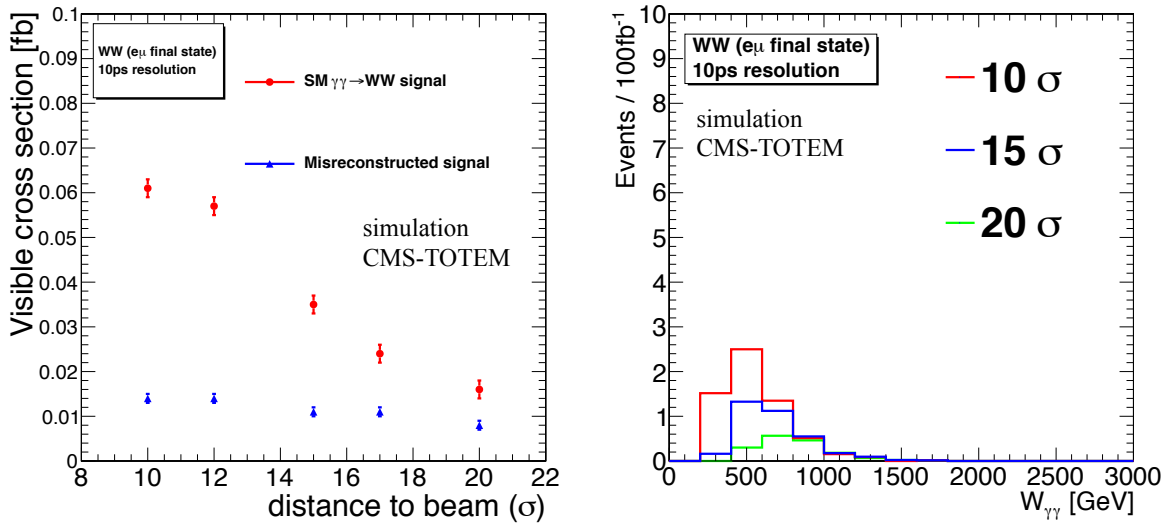

Figure 37: *Left:* The visible cross section for signal exclusive WW events as a function of the distance from the beam (in σ), for SM exclusive WW signal events and for misreconstructed background events. Only the eμ final state is considered; a time resolution of 10 ps is assumed. *Right:* The missing mass is shown for three values of the distance from the beam (10, 15, and 20 σ).

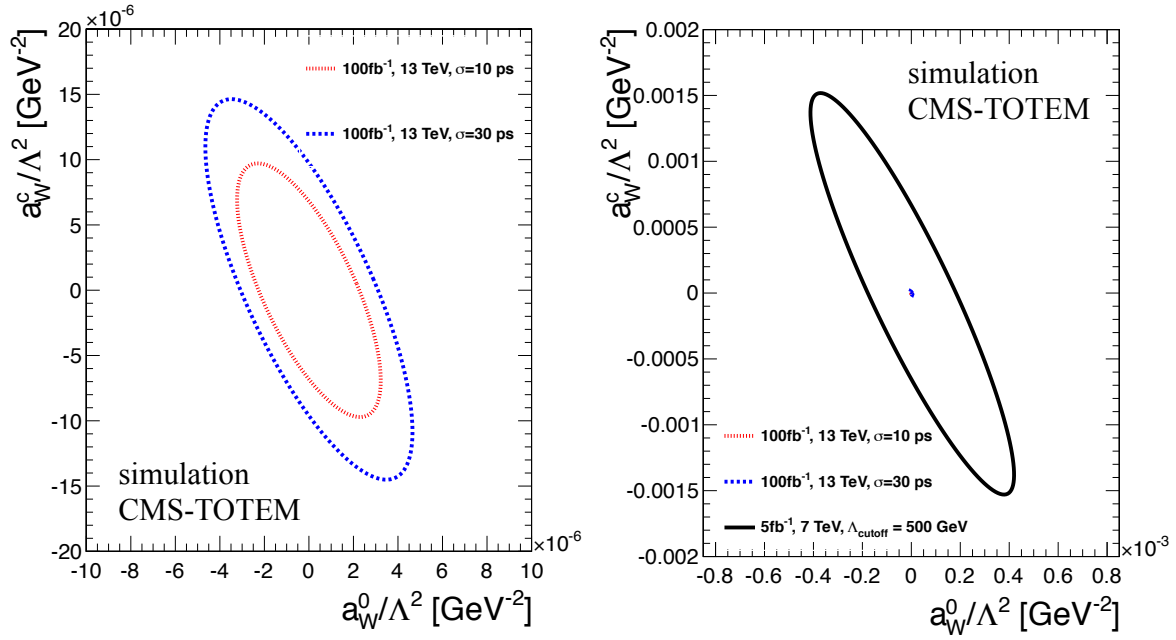

Figure 38: Excluded values of the anomalous coupling parameters a_0^W/Λ^2 and a_C^W/Λ^2. The areas outside the contours are excluded at 95%CL. Approximate limits expected with 10 ps and 30 ps timing resolutions (left) compared to the current 2011 CMS limits from exclusive WW events (right).

References

[1] G. Antchev *et al.* [TOTEM Collaboration], "LHC optics measurement with proton tracks detected by the roman pots of the TOTEM experiment", arXiv:1406.0546 [physics.acc-ph].

[2] J. Favereau de Jeneret, X. Rouby, K. Piotrzkowski, JINST 2 (2007) P09005; arXiv:0707.1198.

[3] A. Latina and L. Deniau, "Evolution of MAD-X in the Framework of LHC Upgrade Studies", Conf. Proc. C 1205201, 304 (2012).

[4] M. Benedikt, P. Collier, V. Mertens, J. Poole and K. Schindl, "LHC Design Report. 3. The LHC injector chain", CERN-2004-003-V-3.

[5] J. Monk and A. Pilkington, "ExHuME: A Monte Carlo event generator for exclusive diffraction", Comput. Phys. Commun. 175, 232 (2006) [hep-ph/0502077].

[6] T. Sjöstrand, S. Mrenna and P. Z. Skands, "PYTHIA 6.4 Physics and Manual", JHEP 05 (2006) 026 [hep-ph/0603175].

[7] M. Boonekamp, A. Dechambre, V. Juranek, O. Kepka, M. Rangel, C. Royon and R. Staszewski, "FPMC: A Generator for forward physics", arXiv:1102.2531 [hep-ph].

[8] G. Corcella, I. G. Knowles, G. Marchesini, S. Moretti, K. Odagiri, P. Richardson, M. H. Seymour and B. R. Webber, "HERWIG 6.5 release note", hep-ph/0210213.

[9] T. Sjöstrand, S. Mrenna and P. Z. Skands, "A Brief Introduction to PYTHIA 8.1", Comput. Phys. Commun. 178 (2008) 852 [arXiv:0710.3820 [hep-ph]].

[10] J. Allison, K. Amako, J. Apostolakis, H. Araujo, P. A. Dubois, M. Asai, G. Barrand and R. Capra *et al.*, "Geant4 developments and applications", IEEE Trans. Nucl. Sci. 53 (2006) 270.

[11] H. Niewiadomski, "Reconstruction of protons in the TOTEM roman pot detectors at the LHC", PhD thesis, CERN-THESIS-2008-080.

[12] M. Berretti, "Performance studies of the Roman Pot timing detectors in the forward region of the IP5 at LHC", TOTEM-NOTE 2014-001

[13] J. Kaspar, "Elastic scattering at the LHC", Ph.D. thesis, CERN-THESIS-2011-214.

[14] T. Aaltonen *et al.* [CDF Collaboration], "Diffractive dijet production in $\bar{p}p$ collisions at $\sqrt{s} = 1.96$ TeV", Phys. Rev. D 86, 032009 (2012) [arXiv:0712.0604 [hep-ex]].

[15] T. Aaltonen *et al.* [CDF Collaboration], "Observation of exclusive dijet production at the Fermilab Tevatron $p\bar{p}$ Collider", Phys. Rev. D 77, 052004 (2008), [arXiv:0712.0604 [hep-ex]].

[16] S. Chatrchyan *et al.* [CMS Collaboration], "Observation of a diffractive contribution to dijet production in proton-proton collisions at $\sqrt{s} = 7$ TeV", Phys. Rev. D 87, 012006 (2013), [arXiv:1209.1805 [hep-ex]].

[17] M. Cacciari, G. P. Salam and G. Soyez, "The anti-k_T jet clustering algorithm", JHEP 0804 (2008) 063 [arXiv:0802.1189 [hep-ph]].

[18] M. Trzebinski, "Study of QCD and Diffraction with the ATLAS detector at the LHC", CERN-THESIS-2013-166.

[19] T. Pierzchala and K. Piotrzkowski, "Sensitivity to anomalous quartic gauge couplings in photon-photon interactions at the LHC", Nucl. Phys. Proc. Suppl. 179-180, 257 (2008) [arXiv:0807.1121 [hep-ph]].

[20] E. Chapon, C. Royon and O. Kepka, "Anomalous quartic WW$\gamma\gamma$, ZZ$\gamma\gamma$, and trilinear WWγ couplings in two-photon processes at high luminosity at the LHC", Phys. Rev. D 81, 074003 (2010) [arXiv:0912.5161 [hep-ph]].

[21] S. Chatrchyan *et al.* [CMS Collaboration], "Study of exclusive two-photon production of W^+W^- in pp collisions at $\sqrt{s} = 7$ TeV and constraints on anomalous quartic gauge couplings", JHEP 1307, 116 (2013) [arXiv:1305.5596 [hep-ex]].

3 Beam Pockets

3.1 The Roman Pot system and collimators in the 200 m region of IP5

Within the combined TOTEM consolidation [1, 2] & CT-PPS project the beam line in the LHC region of ±200 m from IP5 combines the RP220 m stations (220-Near, 220-Far), the relocated 147 m stations (210-Near, 210-Far) and new RP timing stations downstream of the 220 near station (Figure 39). The 210 m far units are rotated by 8 degrees with respect to the beam line to improve the multitrack resolution (Figure 41). During LS1 the vertical 210 m RPs and all 220 m RPs have been equipped with new ferrites (TT2) and improved mechanical support frames to compensate for thermal expansion and allowing mechanical stress release. Within the TOTEM R&D project a cylindrical RP has been newly designed to house timing detectors and was optimized in view of material budget and RF interaction with the LHC beam. Furthermore, the horizontal RP210 have been optimized to reduce the RF interaction with LHC by keeping the original box design of the standard TOTEM RP. Furthermore TCL4 and TCL6 collimators have been installed [3] in front of the Q4 and Q6 quadrupoles, respectively. Figure 40 shows the beamline in Sector 4-5 with the RPs installed.

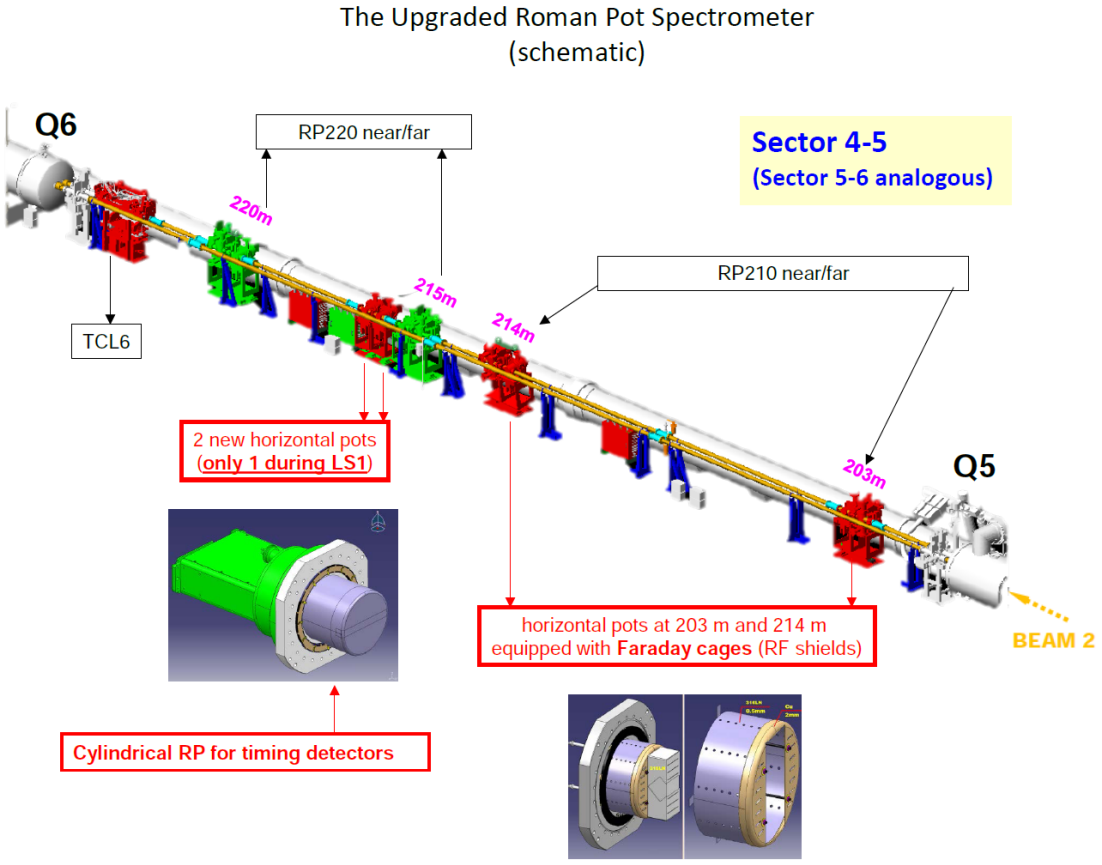

Figure 39: The layout of the beam line in the 200 m region after LS1

3.2 New Roman Pots for timing detectors

The new RPs installed between the existing units 220-N and 220-F are intended to host timing detectors. Hence their design was subject to the following main requirements:

1. Among several potential detector technologies for the timing measurements (see Section 5.1),

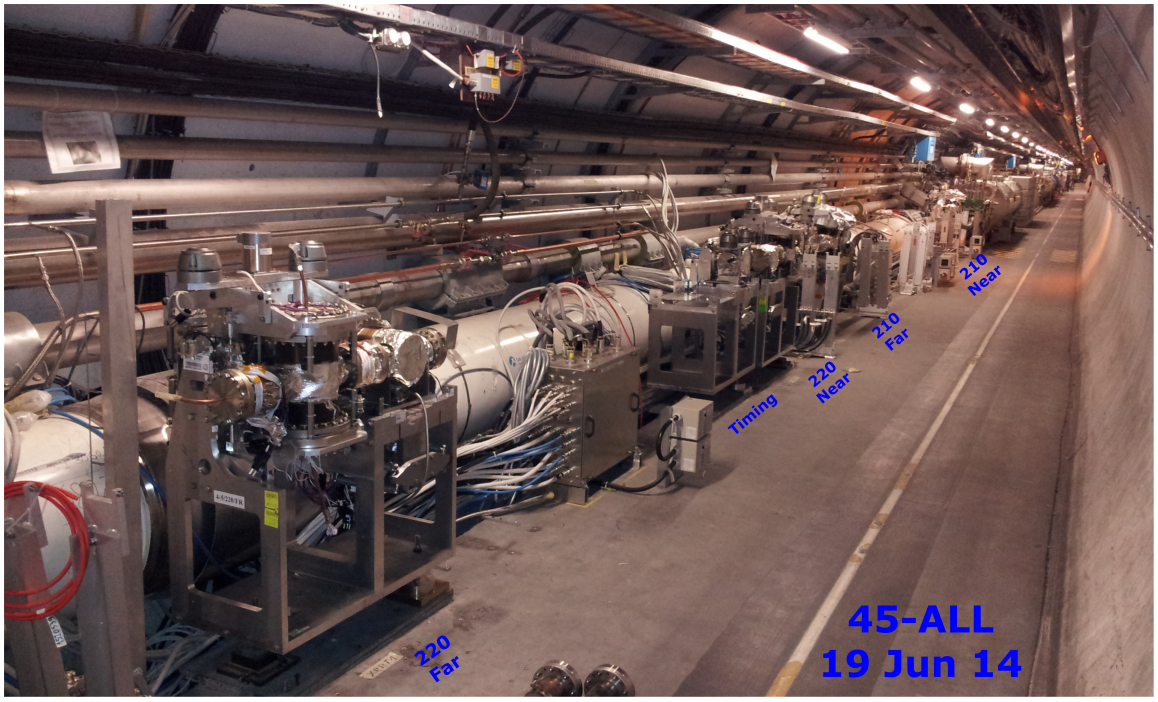

Figure 40: The beamline in Sector 4-5 with the RPs installed

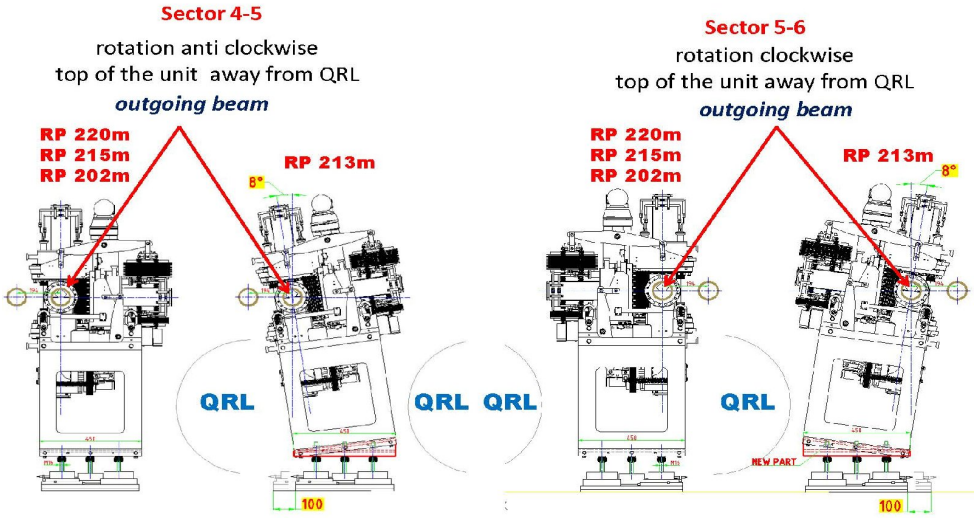

Figure 41: Drawings of the rotated RP units. The view is directed along the outgoing beam.

Čerenkov counters [4, 5] are already at well advanced development stage. For the full timing resolution of $\sim$ 15 ps a total length of 24 cm of quartz is needed. Distributing this length over the two new pots requires each pot to accomodate two slabs of 6 cm length, too big for the space provided by the traditional TOTEM pots. If at a later stage thinner timing detectors (e.g. diamond detectors) become available, tracking and timing functionality may be combined in the same pots, reducing the number of pots to be inserted.

2. The RPs housing the timing detectors will have to operate in high luminosity running scenarios. They will have to approach very intense beams to the same distance as the tracking RPs, i.e. down to about a mm from the centre. At that distance beam-coupling impedance effects, machine

vacuum compatibility in terms of outgassing, and particle shower development have to be taken into account in the geometrical design and in the choice of materials (Section 3.4).

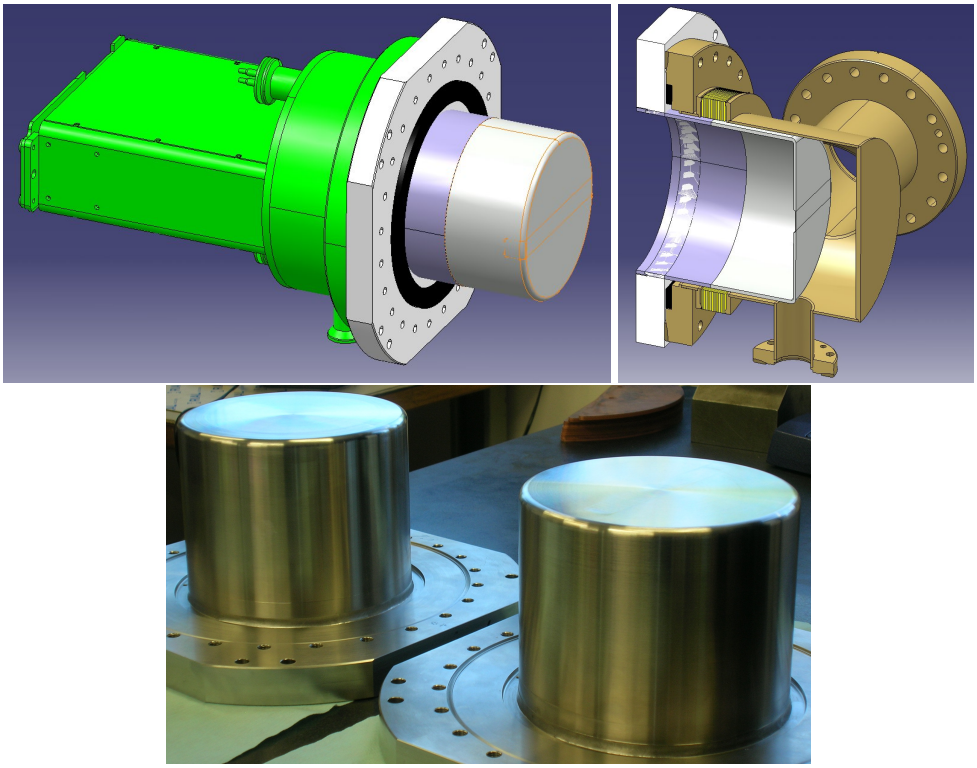

Figure 42: Top: drawings of the cylindrical detector housing for the new RPs designed to accomodate timing detectors. Bottom: the manufactured pots.

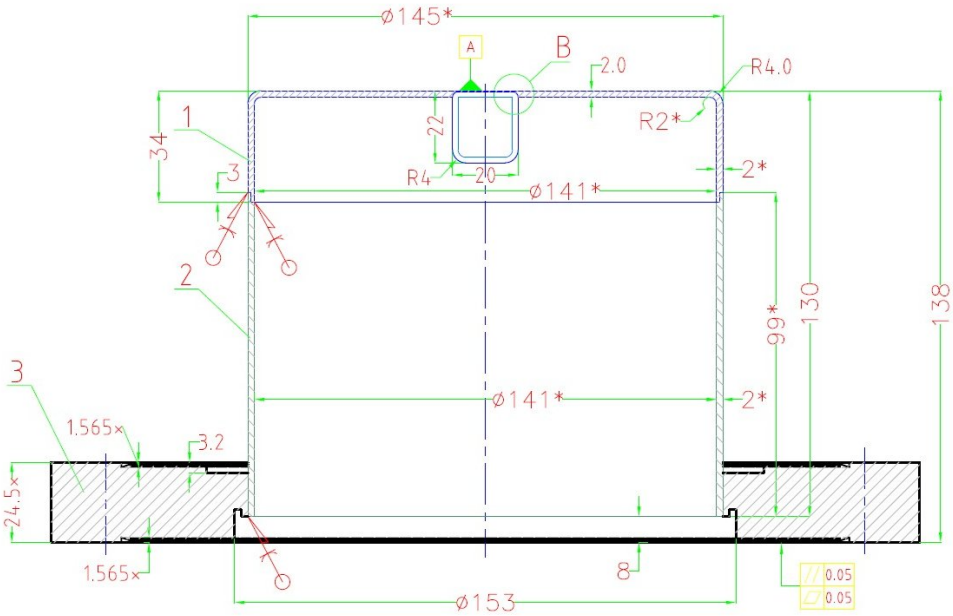

Figure 43: Dimensions of the cylindrical RP.

After considering various options and after an iterative optimisation, the following design has been adopted for the new RPs (Figures 42 and 43) [6]. The volume housing the detectors will have a cylindrical

rather than rectangular box shape. This choice provides the necessary space for all potential technologies of timing detectors and at the same time reduces the beam coupling impedance by minimising resonant cavities. The ferrite in this design will be integrated in the (stationary) flange rather than mounted on the moving detector housing. It will have a ring geometry (inner diameter = 150 mm, radial width = 15 mm, thickness = 5 mm). Furthermore, all vacuum-side surfaces of the RP stations are foreseen to receive a 2 μm thick Non-Evaporative Getter (NEG) coating.

3.2.1 The mechanical tests of new Roman Pot cylinders

The new cylindrical Roman Pots with the thin window of 300 μm thickness have been produced (see Figure 42) in a collaboration of CERN with industries. After the production of the first prototype in fall 2013 a series of test have been performed at CERN in collaboration with different support groups, to approve the compatibility of this new RP design with the LHC requirements. The deflection of the thin window was measured as function of the applied air overpressure simulating the possible pressure difference seen by the RP when the LHC beam tube is under vacuum and the inner side of the RP is under atmospheric pressure. Such pressure difference will arrive during the installation of the detector components or a failure of the vacuum system and a leak of the feedthrough integrated in the flange separating the atmosphere from the inner side of the RP [7]. Furthermore the He transmission was measured in a special setup and the compatibility of this design with the LHC leak rate requirements was shown [8].

3.3 The RF Shield for the box-shaped horizontal Roman Pots

Given that the existing horizontal pots housing tracking detectors will have to cope with the same high luminosity conditions as the new timing RPs, some adaptations will be made:

- To reach the same impedance reduction as for the new cylindrical pots (see Section 3.4.2), the rectangular detector boxes will be successively equipped with 1 mm thick cylindrical copper RF shields (Figure 44). Holes in the shield allow for the gas flow necessary to establish a vacuum equilibrium inside and outside the shield. The number and dimensions of these holes have been defined in cooperation with the LHC vacuum group: In the lateral, cylindrical wall there are 3 rows of 15 circular holes each with a diameter of 1 cm; the wall facing the beam has 8 slits of $3 \times 12\mathrm{mm}^2$ with rounded corners (2 mm radius). The shield is retracted by 30 mm from the box window facing the beam, in order not to intercept any signal protons with the shield material. In the first step, during LS1, the horizontal pots of the RP210 station will receive the RF shields, in order to gain experience without touching the RP220 station.
- The horizontal RP210 stations will be equipped with new vacuum bellows and modified flanges that allow to integrate the same ferrite geometry as used in the new RPs. The ferrites of the vertical RPs of the RP210 stations will be exchanged with the new TT2 material as in the RP220 stations.

3.4 Interaction with the beam environment

3.4.1 Experience from 2012

In October and November 2012 several test insertions of the RPs in normal high-luminosity fills at $\sqrt{s} = 8$ TeV with $\beta^* = 0.6$ m were performed. While the vertical pots had no problems to reach the target distance of 12 σ from the beam centre, the horizontal pots encountered a very intense collision debris halo, and repeatedly the beam was dumped by showers hitting the Beam Loss Monitors at a pot

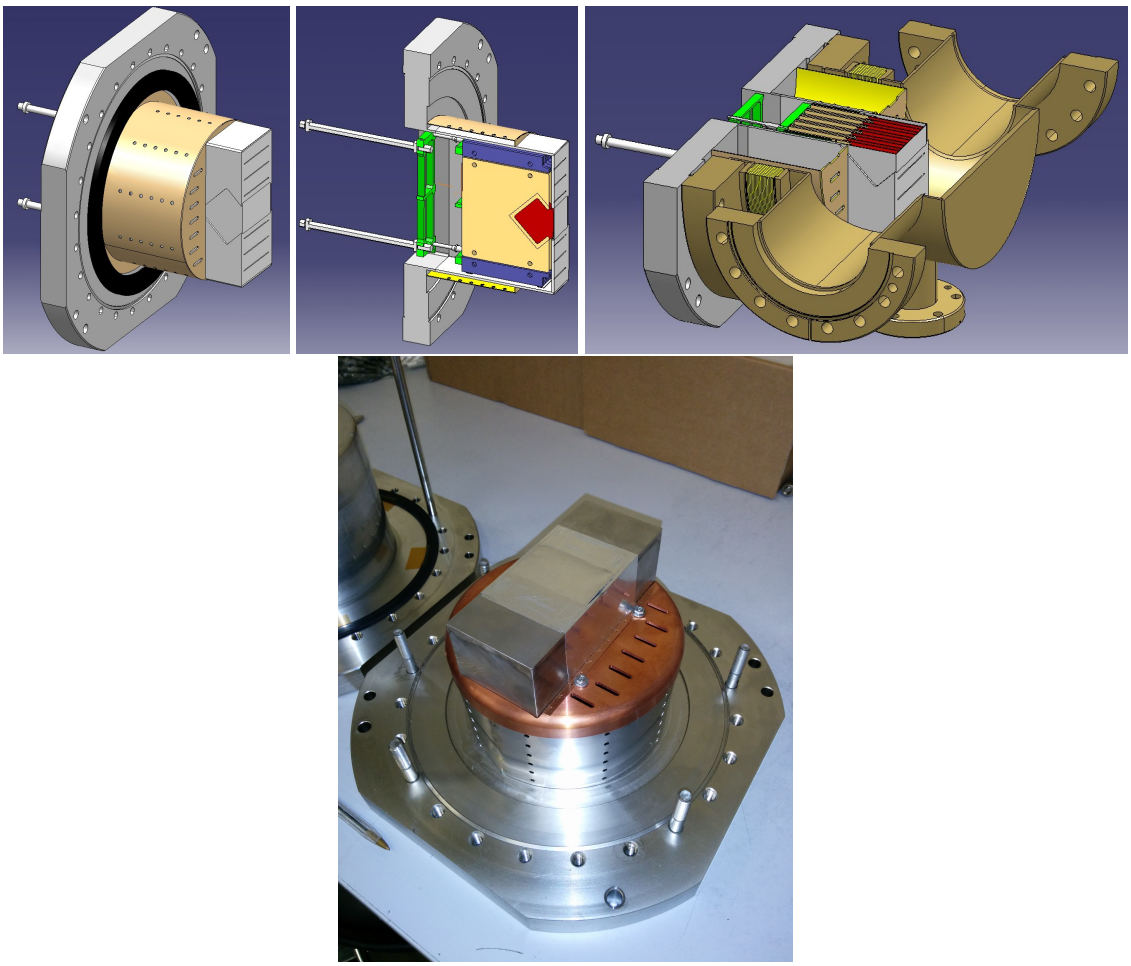

Figure 44: Top: Drawings of the cylindrical RF shield for the box-shaped horizontal RPs. Bottom: the manufactured shield.

position of about $30\,\sigma$. Separating the beams in IP5 finally reduced the luminosity – hence the debris halo – by a factor 22.7, enabling the approach to the horizontal target distance of $14\,\sigma = 1.6\,\text{mm}$ from the beam containing 1368 bunches of – at RP insertion time – 1.1×10^{11} protons or a total charge of 1.45×10^{14} protons. The beam profiles (Figure 45) measured during these insertions can be used to benchmark shower simulations (Section 3.4.5). The first lesson for the upgrade from this exercise is that a horizontal RP approach to physics-relevant positions of $10 \div 15\,\sigma$ will require to absorb the showers produced by the RPs in order to protect the quadrupole Q6. The solution is the addition of the new collimators TCL6 between the RR220 station and Q6 (see Section 3.5).

While the horizontal pots were stationary at $14\,\sigma$ from the beam centre, i.e. for about 30 minutes, the temperature sensors on the detector hybrid boards in those RPs registered a temperature increase by about 4°C, despite the active cooling of the detector packages. This effect is explained by impedance heating of the ferrite collar mounted around the box-shaped housing on the beam vacuum side. A direct temperature measurement near the ferrite was not available, but given the long thermal conduction path from the heat source to the detector package, and the absence of convection inside the pot due to the secondary vacuum, the temperature of the ferrites may have reached values well above 100°C, the Curie temperature of the ferrites (material 4S60 from Ferroxcube) above which they are ineffective. Another piece of evidence for substantial heating of the ferrites was given by the vacuum deterioration observed after the very close insertion of the horizontal RPs. First laboratory tests have shown that the ferrite material installed around the pots shows substantial outgassing at high temperatures.

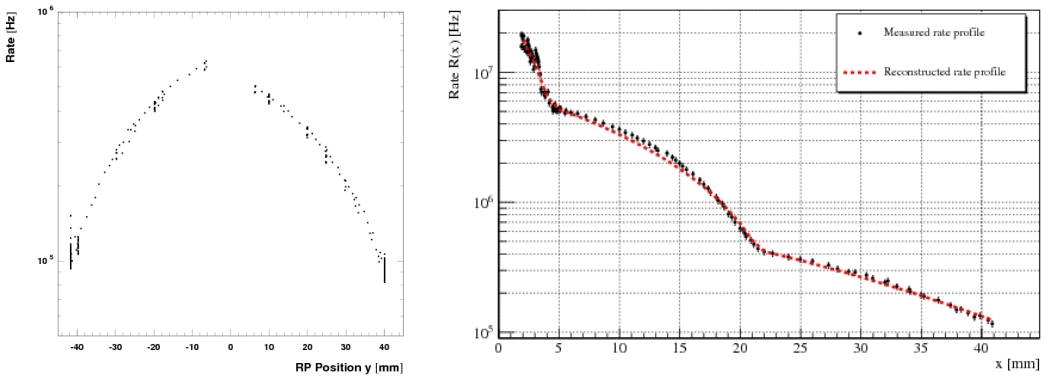

Figure 45: Left: vertical beam profile measured via the trigger rates in the detectors of the top and bottom pots of Sector 56,220-N. Right: horizontal beam profile measured in Sector 45,220-N; the luminosity reduction by beam separation has been corrected for. The reconstructed curve is the result of a convolution fit discussed in [9].

Triggered by the problems and observations described above, a programme of simulations, extended laboratory tests, and design optimisations was defined; it is discussed in the following section.

3.4.2 Impedance

As mentioned in the previous section, during a RP insertion to 1.6 mm from a high-intensity beam (1368 bunches of 1.1×10^{11} protons) a temperature increase was observed on the detector hybrid boards. This effect can probably be attributed to impedance heating. It is hypothesised that the 4S60 ferrite mounted around the RP box reached a temperature above 100°C, the Curie temperature, which resulted in the loss of ferrite effectiveness and hence even stronger heating by the now non-damped cavity resonance near 550 MHz [10]. Note, however, that no other impedance effects were observed, in particular, no beam instabilities.

The aim of the work presented here [11] is the optimisation of the RP design to minimise the beam-coupling impedance, in particular at very close distances to the beam, in view of more regular and extended RP insertions in the future.

The impedance seen by a beam of particles has contributions from the shape of the vacuum chamber (geometrical impedance) and from the finite conductivity of the material used for its construction. The remainder of this section focusses on the dominant geometrical contribution of three RP designs: the standard box-shaped RP, the new cylindrical RP, and the improved box-shaped RP with shield (introduced in Section 3.3).

The study was performed by simulating the passage of a charge distribution (source charge) through a cavity, in this case through a RP, and computing the wake field felt by a longitudinally or transversely displaced second charge (test charge). The potential felt by the test charge is then used to compute the longitudinal or transverse impedance using Fourier Transforms.

Three impedance effects have to be addressed:

- **Beam-induced heating**, i.e. the transfer of power from the beam to the lossy wall of a cavity, is determined by the frequency-dependent real part of the longitudinal impedance in conjunction

with the power spectrum of the beam:

$$P_{\text{loss}} = 2\,I^2 \sum_{p=0}^{\infty} PS(pM' f_{\text{rev}}) \Re[Z_{\text{long}}(p\,M'\,f_{\text{rev}})]\,, \tag{3.3}$$

where

- $PS(f)$ is the power spectrum;
- f_{rev} is the revolution frequency, 11.245 kHz for the LHC;
- M' is the number of buckets, 1782 for the LHC with a bunch spacing of 50 ns;
- $I = MeN_B f_{\text{rev}}$ is the beam current, with M number of bunches, e charge of the proton, N_B number of protons per bunch;
- Z_{long} is the longitudinal impedance.

The main contribution to the heating comes from resonances below 1.5 GHz; at higher frequencies the beam power spectrum is attenuated by more than ~ 30 dB relative to its value at $f = 0$ [12]. For all power calculations a current of 0.6 A (corresponding to M=2808 and N_B= $1.2 \cdot 10^{11}$ protons) was used.

- **Longitudinal instabilities** are related to the effective longitudinal impedance. The effective impedance is the impedance actually felt by the beam: it is given by the impedance convolved with a weighting function $\sigma(f)$ which is determined by the bunch profile:

$$Z^{\text{eff}} = \frac{\sum\limits_{f} Z(f)\sigma(f)}{\sum\limits_{f} \sigma(f)} \tag{3.4}$$

A conservative estimation of the effective longitudinal impedance is the slope of the imaginary part of the longitudinal impedance at low frequencies Z^0_{long}/n:

$$\Im Z^0_{\text{long}}/n = \lim_{f \to 0} f_{\text{rev}} \frac{\mathrm{d}\Im Z_{\text{long}}}{\mathrm{d}f} \tag{3.5}$$

where $n = f/f_{\text{rev}}$ is the harmonic number. It is possible to show [11] that $\Im Z^0_{\text{long}}/n < (\Im Z_{\text{long}}/n)^{\text{eff}}$.

The simulated value for $\Im Z^0_{\text{long}}/n$ will be compared with the measured value for $(\Im Z_{\text{long}}/n)^{\text{eff}}_{\text{LHC}} = 90\,\text{m}\Omega$ [13].

- **Transverse instabilities** have, analogously, their origin in the low-frequency behaviour of the transverse impedance. Following the same approach for the effective transverse impedance, it is possible to compute the *driving* (or *dipolar*) impedance and relate it to the transverse impedance [14]:

$$\Im Z_{\text{t}}^{\text{driving}} = \frac{\partial \Im Z_{\text{t}}}{\partial t_{\text{source}}} \tag{3.6}$$

where $t = x, y$ and t_{source} represents a small transverse displacement of the source charge, which creates the wake field, from the nominal position. The value is usually constant at low frequency ($<$ 500 MHz). A normalisation with the ratio of the beta function value at the equipment under study, β_t, and the average over the ring, $\langle\beta_t\rangle = 70$ m, facilitates the comparison with other equipments at different positions in the machine:

$$\overline{\Im Z_{\text{t}}^{\text{driving}}} = \Im Z_{\text{t}}^{\text{driving}} \frac{\beta_t}{\langle\beta_t\rangle} \tag{3.7}$$

The new RP will be horizontal ($t = x$); moreover, among all the RPs the highest value (worst case) of $\beta_x = 98$ m is reached at the unit 210-N. This value can be compared with 25 $\text{M}\Omega/\text{m}$, a conservative value of the value expected for the full machine [15].

For the new cylindrical pots, simulation results indicate that no low frequency resonances (< 1.4 GHz) are present if the gap between the detector housing and the flange is completely closed, which of course prevents any RP movement. Mechanical constraints require at least 2.5 mm gap between the housing and the flange. With this gap a resonance at 470 MHz appears, as shown in Figure 46; its impedance, however, is smaller than for the standard box-shaped RP. The position and the dimensions of the ferrite

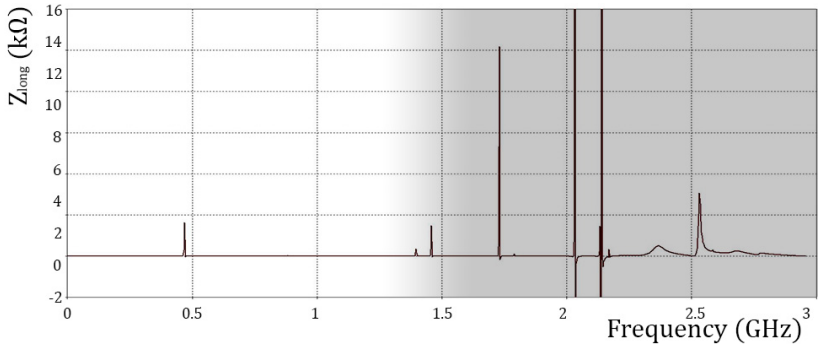

Figure 46: Simulated $\Re[Z_{\text{long}}]$ of the cylindrical RP without ferrite. The resonance at 470 MHz is due to the cavity between the flange and the detector housing. The darkened part of the graph has negligible impact on the heating due to the strongly attenuated LHC power spectrum at such high frequencies.

has been optimised through various iterations considering also vacuum and mechanical construction. The final design consists of a ferrite ring (inner diameter = 150 mm, radial width = 15 mm, thickness = 5 mm) integrated into the flange, as far as possible from the beam (Figure 47). This design is feasible and can be easily integrated in the existing design.

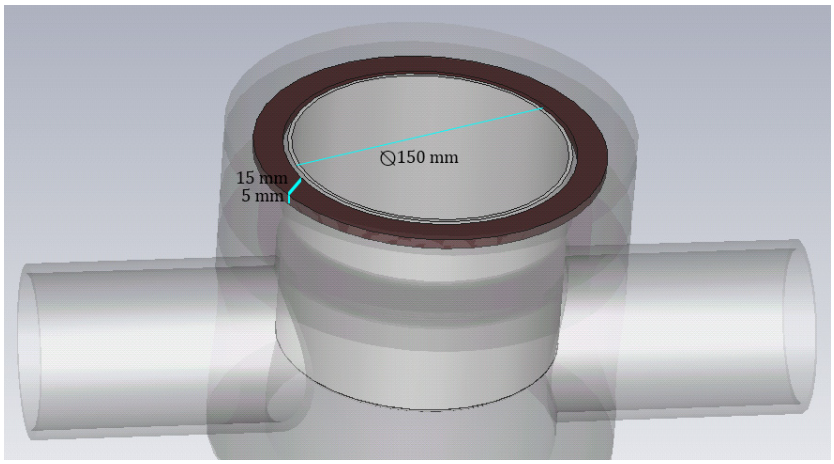

Figure 47: Detail of the geometrical model used in the impedance simulations. It shows the new ferrite ring to be integrated in the flanges of the cylindrical pots and of the improved pots with shields.

Figure 48 shows the real and imaginary parts of the longitudinal impedances of the three RP designs with ferrites. In all cases, the 470 MHz resonance is damped and smeared beyond recognition. At low frequencies, the cylindrical and shielded RPs have a smaller $\Re[Z_{\text{long}}]$ than the standard RP. This is also reflected by the reduced heating for the new designs (Figure 49). Figure 50 shows the effective longitudinal impedance as a function of the RP distance from the beam. Also here, the new designs have led to a significant reduction.

These results are numerically summarised in Table 8.

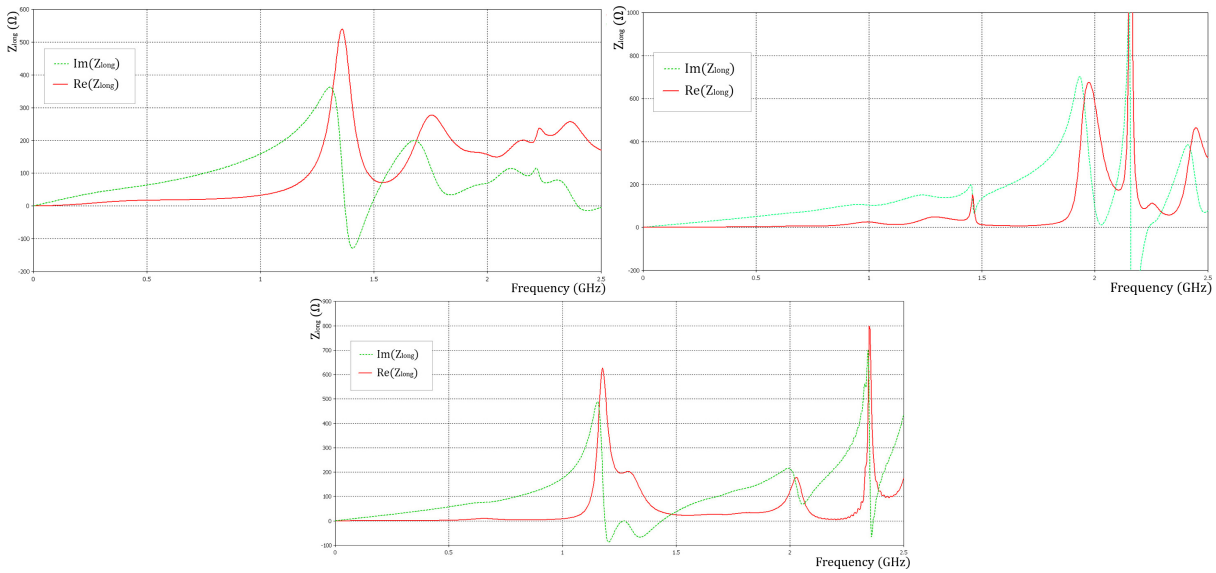

Figure 48: Simulated longitudinal impedance for the standard box-shaped RP (top left), the cylindrical RP (top right) and the shielded RP (bottom). Both real and imaginary part are shown.

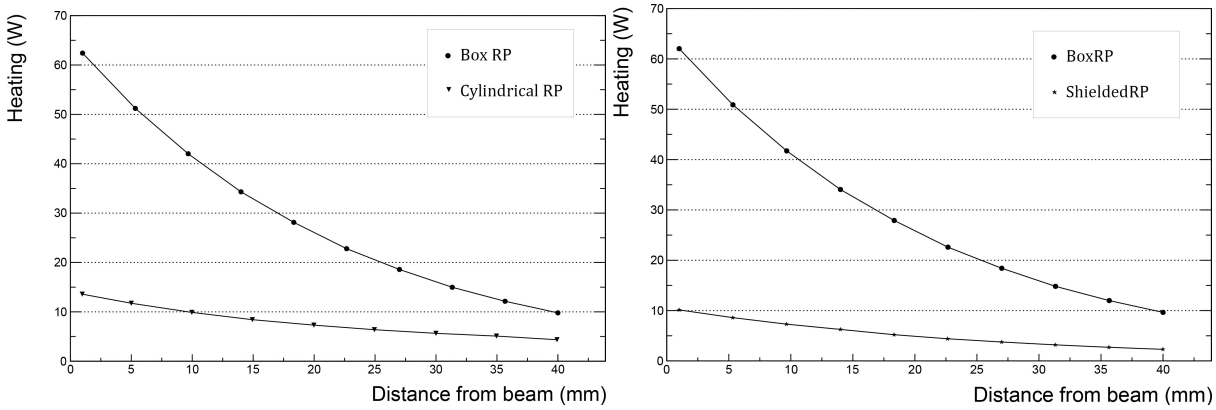

Figure 49: Power lost by the beam passing through the RP, for the three RP designs (I=0.6 A).

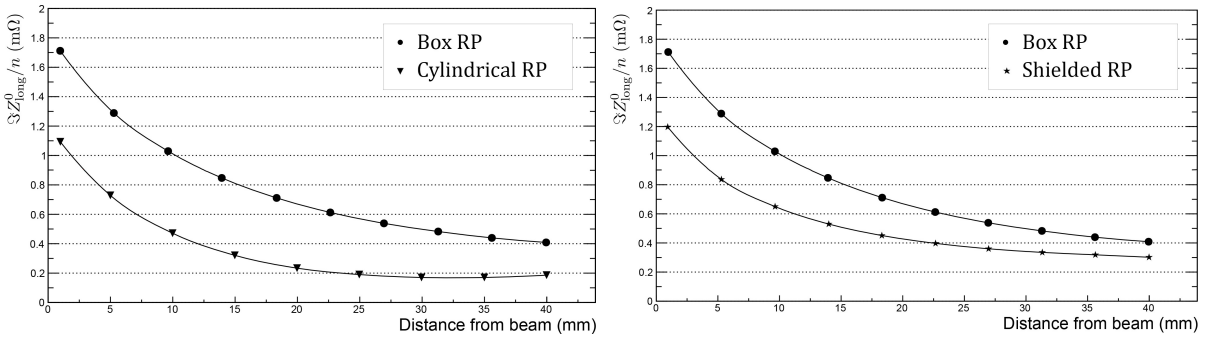

Figure 50: Effective longitudinal impedance as a function of the RP distance from the beam, for the three RP designs.

	Distance from the beam [mm]	$\frac{\Im Z^0_{\rm long}}{n}$ [mΩ]	fraction of $(\frac{\Im Z_{\rm long}}{n})^{\rm eff}_{\rm LHC}$ (90 mΩ)	$\overline{\Im Z^{\rm driving}_{\rm trans}}$ [MΩ/m]	fraction of $\Im(Z_{\rm x})^{\rm eff}_{\rm LHC}$ (25 MΩ/m)	Heating [W] I=0.6 A
Box RP	1	1.7	$< 1.9\,\%$	0.15	$< 0.6\,\%$	62
	5	1.3	$< 1.4\,\%$			52
	40 (garage)	0.41	$< 0.45\,\%$			10
Cylindrical RP	1	1.1	$< 1.2\,\%$	0.11	$< 0.5\,\%$	13
	5	0.73	$< 0.81\,\%$			11
	40 (garage)	0.18	$< 0.20\,\%$			4
Shielded RP	1	1.2	$< 1.3\,\%$	0.2	$< 0.8\,\%$	10
	40 (garage)	0.30	$< 0.33\,\%$			2

Table 8: Main results of the simulation of the present box RP (Box RP), the cylindrical RP (Cylindrical RP), and the Box RP with Shield. Longitudinal and transverse impedances are compared with the total values estimated for the present LHC effective impedances.

3.4.3 The RF test in the lab

The new cylindrical RP and the RF shield in combination with ferrites were developed to reduce the RF interaction with the LHC beam. Prior the serial production of components a new RP cross with flanges and bellow was manufactured. The prototype of the cylindrical RP and the RF shield in combination with the box-shaped RP have been integrated in this new RP cross for RF measurements. In February 2014 measurements were performed by TOTEM and the LHC impedance group in the TIF lab of CERN. In detailed measurements with and without the new ferrites and at different insertion positions of the RP, the RF characteristics of this new geometry could be determined and good agreement with the predictions, based on simulations could be found [16].

3.4.4 Vacuum

The vacuum degradations observed in 2012 after very close horizontal RP insertions to high-intensity beams triggered the following consolidation activities for improving the vacuum compatibility of the RP system:

- Ferrite material improvements:
  The 4S60 ferrites used in the RP system before LS1 are now (but not in 2006) known to show high outgassing rates unless they are baked out at 1000°C [17]. In the TOTEM RPs these ferrites were installed as received from the manufacturer and then baked out *in situ* at about 200°C like all other beam-pipe components, which turned out not to be sufficient. Since the 4S60 ferrites have in addition a low Curie temperature of only 100°C, alternative ferrite materials are being investigated instead of only baking out the 4S60 material at 1000°C. The material used for the TOTEM RPs is TT2-111R from TransTech with a Curie temperature of 375°C and an acceptable outgassing after bake-out at 1000°C [18]. An alternative material for possible future use is 4E2 (Ferroxcube) with a Curie temperature of about 400°C; its outgassing behaviour remains to be tested.

- The new geometrical ferrite configuration reduces the ferrite surfaces exposed to the vacuum by an order of magnitude from 220 $\rm cm^2$ per standard RP to 23 $\rm cm^2$ per cylindrical RP.

- All components exposed to the primary beam vacuum have been proposed by the vacuum group to be coated with NEG, as far as technically possible.

3.4.5 Generation of particle showers

To assess the generation of particle showers by RPs interacting with the intense debris halo (see 2012 experience discussed in Section 3.4.1), Geant4 simulations implementing detailed models of the rectangular and the new cylindrical RPs have been carried out [9].

The first goal of the study was to identify the contributions from the different structural elements of a RP to the shower creation. For this purpose, 7 TeV protons with a delta-function profile distribution, i.e. zero width and zero angular spread, were shot parallel to the beam onto three elements of a pot:

- through the beam-facing window, 50 μm from the outer surface;
- through the front window, the detector planes and the rear window, 2 cm from the outer surface of the beam-facing window;
- through the body wall of the pot, 6 cm from the outer surface of the beam-facing window.

This was performed for the standard rectangular pot geometry and for the new cylindrical one (see Table 9 for some key dimensions). For each case a sample of 2000 protons was processed. Figure 51 shows the resulting angular distributions of the secondary particles produced in the RP material.

RP Element	Standard Pot	Cylindrical Pot
Beam-facing window length along beam	54 mm	145 mm
Beam-facing window thickness	0.15 mm	0.3 mm
Front / back window	0.5 mm	0.3 mm
Body wall thickness	2 mm	3 mm

Table 9: Comparison of the standard and cylindrical RP elements most relevant for the material budget and hence for shower production.

As expected, the number of secondary particles is mostly determined by the amount of material traversed. The key observations are:

- In both RP designs, the bottom foil produces by far the highest number of secondary particles, followed by the thick body walls with 2 to 3.5 orders of magnitude lower rates. The orthogonally traversed thin front and back windows produce the lowest numbers of secondaries.
- The bottom foil of the cylindrical pots produces more than 10 times more secondaries than the much shorter foil of the standard pots. In the other elements the shower production is similar in the two designs.
- The showers from the bottom foil of the cylindrical pot are 3 times wider than the ones from the standard pots: 99% contained in 0.6 rad $= 34^\circ$ rather than in 0.2 rad $= 11^\circ$.
- The two projections, horizontal and vertical, are almost identical.

The second part of the study addressed the shower production by particles distributed according to the rate density profile $dN/dt\,dx\,dy$ deconvoluted [9] from the trigger rate profile measured in November 2012 (Figure 45). This gives a picture of the total shower distribution, in contrast to the first study that focused on the delta-response of the individual components. Figure 52 shows the simulated secondary particle distribution in a scoring plane 6 m downstream of a standard horizontal RP inserted to 2 mm from

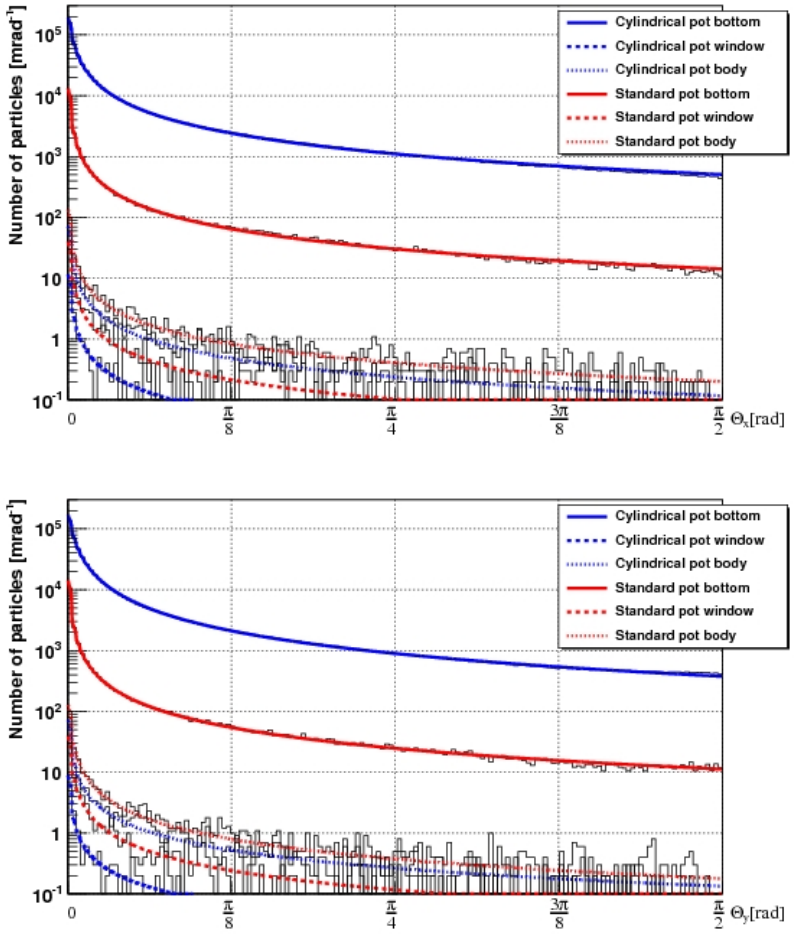

Figure 51: The horizontal (top) and vertical (bottom) scattering angle distribution of secondary particles produced by different elements of the standard and the cylindrical RP. Fits with the function $\frac{\mathrm{d}n}{\mathrm{d}\Theta} = C\left(\frac{\Theta - b}{1\,\mathrm{mrad}}\right)^{-a}$, where $a \approx 1$ are superimposed (see [9] for details). The bin width is 10 mrad. Note that a particle emitted with an angle of 10 mrad travels 4 cm (= 1 beam pipe radius) transversely within a longitudinal distance of 4 m.

the beam centre. The position of the scoring plane relative to the RP corresponds roughly to the TCL6 position relative to the unit 220-N-Horizontal. The important message is that at the entrance point of TCL6, 25 % of the secondary particles, carrying 90 % of the energy, are contained within the beam-pipe radius and thus intercepted by TCL6. How much of this flow leaks through the TCL6 aperture and thus hits Q6 will be the subject of the FLUKA study discussed in Section 3.5.2.

In the final step of the study, the secondary particles created by interaction with a first RP impinge on a second RP after 4.6 m longitudinal distance. There the shower is amplified by the additional material. The amplification factor obtained from this simulation can be directly compared with the beam measurement in November 2012 (Table 10).

The simulation shows how the shower size increases within the second RP by successively passing through 10 detector planes. In the data, the trigger was defined as an OR of the u and the v projection triggers, each of which was a 3-out-of-5-plane majority coincidence. The simulated amplification factor at the last detector plane agrees reasonably with the measurement.

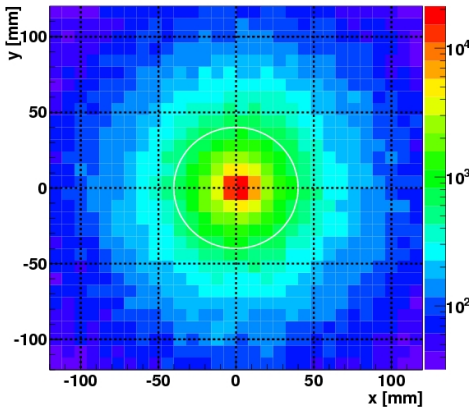

Figure 52: Distribution of the secondary particles created by a horizontal box-shaped RP and recorded in a scoring plane 6 m farther. The particle generator is based on the measured rate profile: to estimate the rate density a multiplication factor of 4.5 Hz/mm^2 has to be applied. The white circle around the origin with radius 40 mm indicates the beam pipe.

	first det. plane	middle det. plane	last det. plane
$(R_{\text{far}}/R_{\text{near}})_{\text{simulated}}$	1.5	1.8	2.5
$(R_{\text{far}}/R_{\text{near}})_{\text{measured}}$	3.5 (trigger condition: 3 out of 5 planes)		

Table 10: Rate amplification factor from the near to the far RP unit in simulation and measurement.

3.5 Interplay between Roman Pots and collimators

The modified RP system with relocated and additional units will be embedded in an upgraded collimation system. This section discusses the performance of the new combined layout in terms of physics acceptance and machine protection.

3.5.1 The new collimators TCL4 and TCL6

LHC operation at highest luminosities may require additional protection of the quadrupoles Q5 and Q6 against collision debris from IP5 [19].

To protect Q5, new collimators, TCL4, will be installed on the outgoing beams in the old location of the RP147 station, and the already existing collimators TCL5 may be partially closed. Since both TCL4 and TCL5 are located upstream of the RP stations and can intercept diffractive protons if too tightly closed, their aperture settings of these collimators will be the result of an optimisation study maximising the physics acceptance as far as compatible with the necessary magnet protection.

Downstream of the last RP unit, 220-F, another collimator, TCL6, has been installed [3] on the outgoing beam to protect the quadrupole Q6 against debris from IP5, thus taking over a part of the original role of TCL5 which cannot be too tightly closed without intercepting all the signal protons to be measured by the RP system. Another beneficial effect of this new collimator is its capability to absorb showers created by the insertions of the horizontal RPs close to the beam. RP operations at low β^* and high luminosities in 2012 have demonstrated that without any absorber behind the RP stations, insertions were limited to distances greater than 30 σ, because the showers caused by the pots' interaction with the debris halo brought the dose rates measured by the Beam Loss Monitors above the beam dump thresholds. The

improvement by the addition of TCL6 will be the subject of a FLUKA study.

3.5.2 Optimisation of Roman Pot and collimator settings

This section discusses the strategy for defining an optimal combined set of jaw positions for the RPs and the collimators TCL4, TCL5 and TCL6. Given that the TCLs are only required at highest luminosities, only the low-β^* running scenarios are relevant for these considerations. The TCL collimators are designed to protect the quadrupoles Q5 and Q6 against debris from collisions at IP5. Their jaws approach the beam horizontally and potentially intercept diffractively scattered protons, thus interfering with the physics measurements in the RPs. Therefore, the aim of the optimisation [20] is to find

1. jaw positions for TCL4 and TCL5 that leave the aperture as widely open as allowed by the protection needs of Q5, i.e. the dose rate received by Q5 has to stay well below the magnet quench threshold;
2. RP positions as close to the beam as allowed by the protection capacity of TCL6 to prevent Q6 from quenching.

The upper limit $\xi_{\max}$ for accepted momentum losses of diffractive protons is given by minimum value of the ratio d_x/D_x between horizontal aperture and dispersion along the path from the interaction point to the RP. Table 11 gives the values of $10\,\sigma_x$ beam width and the dispersion D_x in all TCL collimators and in some RP locations for the $\beta^* = 0.55$ m optics at $\sqrt{s} = 14$ TeV.

Beam Element	Position s [m] from IP5	$10\,\sigma_x(s)$ [mm]	$D_x(s)$ [mm]	$\lvert\xi(10\,\sigma)\rvert$
TCL4	149	5.2	-66	0.079
TCL5	185	2.8	-83	0.034
RP 210-N	202	2.2	-90	0.024
RP 220-F	220	0.90	-80	0.011
TCL6	221	0.89	-80	0.011

Table 11: Horizontal beam envelope ($10\,\sigma$) and dispersion at the TCL collimators and at the first and last RP unit. The last column gives the ξ-value at $10\,\sigma$ from the beam centre (for $t = 0$).

The most stringent impact on diffractive proton acceptance is made by TCL5 which at its nominal jaw position of $10\,\sigma$ from the beam centre would intercept all protons with $\xi > 0.034$ while for the physics programme a cut-off greater than 0.1 would be desirable. Therefore collimation group developed an alternative scheme for fills with RP operation where TCL5 would be fully open and both TCL4 and TCL6 closed to $10\,\sigma$. However, in that scheme TCL4 would be the bottleneck producing a cut at 0.079. A new study presently carried out by the FLUKA team investigates the possibility to open TCL4 to $15\,\sigma$ and complement its protection by closing TCL5 to $35\,\sigma$. In this way, both collimators would lead to the same upper ξ cut-off at 0.11.

Once the optimal settings for TCL4 and TCL5 will be fixed, another FLUKA study will focus on the impact of RP insertions on Q6 and its mitigation by closing TCL6 to $10\,\sigma$. It is expected that a horizontal RP approach to a minimum distance between 11 and $14\,\sigma$ should be possible, corresponding to minimum accepted ξ-values between 0.012 and 0.016.

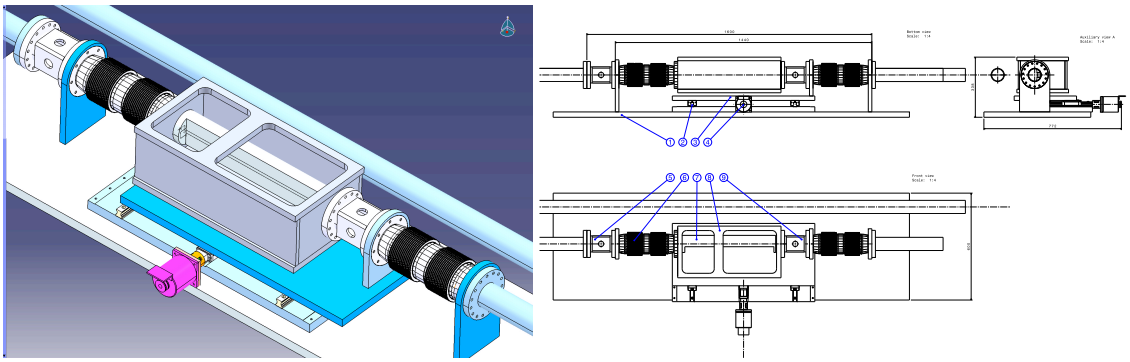

Figure 53: Left: Movable pipe with support table and detector box. The bellows, beam position monitors (square boxes), detector pocket, and drive motor are visible. Right: Detailed drawings of the movable pipe with support table and detector box. Shown are the (1) fixed support table; (2) guides; (3) moving support; (4) motor; (5) beam position monitor (fixed with respect to beam pipe); (6) bellows; (7) modified beam-pipe with the indentation for the detectors; (8) detector box inside which the detectors are housed; it can be made vacuum-tight if secondary vacuum is required; (9) beam position monitor (moving together with the movable beam-pipe).

3.6 Movable Beam-Pipe

As a possible alternative to Roman Pots, we are pursuing development of a technique used originally by the ZEUS collaboration at HERA [21], referred to as a movable beam-pipe or "Hamburg beam-pipe". This consists of a large-diameter section of beam-pipe with a thin flat side wall, with integrated tracking and timing detectors inserted in a detector box attached to the pipe. The movable-pipe technique allows easy access to the detectors, and maintains a fixed vacuum volume as the detectors are inserted into the vacuum. This results in low mechanical stress and consequently in a simple and robust design. In effect, the MBP is an instrumented collimator. Consequently, the LHC collimator control system and motor design can be adopted with little modifications.

In routine operation, two positions will be used: the parking position and the operational position close to the beam for data taking. The displacement between the two positions will be $\sim$25 mm. As discussed in Chapter 3, the distance of approach to the beam directly affects the low mass acceptance in exclusive production. The MBP should therefore be designed to approach the beam as close as possible, ideally to better than 15σ.

Deploying one such station during the 2015-2016 year end technical stop will allow evaluation of the MBP solution during the exploratory phase of CT-PPS. A similar approach has been studied within the ATLAS Forward Proton (AFP) project; the design described here incorporates several developments from AFP in view of allowing for a common design in the future.

Figure 53 (left) shows the layout of a full MBP station including one detector box and the support table. No secondary vacuum is assumed inside the detector box. However, secondary vacuum can be easily implemented in the current design if requested by the machine or desirable for detector operation. The MBP station is fixed to the floor with independent supports, while the movable section is connected to the standard beampipe by bellows. A single drive motor system is placed at the center. Two precision beam position monitors are required to measure the distance between the detectors and the beam center, one on the fixed pipe and one on the movable pipe. At each pocket there is a detector box, providing secondary vacuum if necessary, with a lid for access, and feed-throughs. Figure 53 (right) illustrates the proposed layout of the full system in more detail.

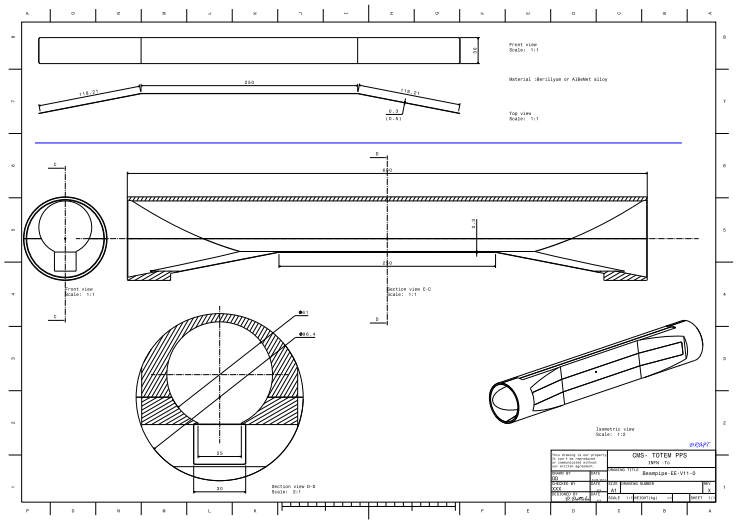

Figure 54: Detailed engineering drawings for the MBP design, with 11 degree tapering.

In the testing phase of CT-PPS, installation of one such MBP station is considered. In a full MBP system the detectors in each arm would be placed in two movable pipe stations per arm: a shorter one closer to CMS that houses tracking detectors, and a longer one, common for the tracking and timing detectors. The length of the detector pocked in the tracking station can be as short as 10 cm. The length of the longer station is mainly determined by the requirements of the timing detectors, subject to constraints of the impedance and material budget.

More detailed drawings of the MBP are shown in Figures 54 and 55. The inner dimensions of the movable pipe are such as not to cause aperture limitations: at injection, the minimum required aperture diameter is 47.7 mm (cf. LHC Project Document No. LHC-VSS-ES-0002 rev. 1.3), much smaller than the 58 mm diameter of the MBP. A simple and mechanically robust circular shape is used for the aperture. Stainless steel is suitable for the main body of the MBP, and will be copper coated for RF-shielding and Non-Evaporative Getter (NEG) coated. The beampipe body will be manufactured from a single stainless steel bar, with the interior surface tapered into a conical shape between the bellows and the section behind the pocket housing the detectors, creating a smooth transition to reduce the RF impedance effects. The thin-window thickness is 0.3 mm, also tapered to reduce the impedance effects. The material choice for the thin window will be discussed in detail in the following section. The length of the pocket housing the detectors is 25 cm. The length can be changed to suit the final timing detector technology chosen for CT-PPS.

3.6.1 Movable beam-pipe design considerations

In choosing the shape and material of the MBP, several variables were considered. The impedance should be within the constraints prescribed by the LHC, with minimal RF-induced heating, as previously described in Section 3.4.2 for Roman Pots. The impact of the thin window material on the resolution and production of showers should be minimized. The length of the MBP should be enough to accommodate the CT-PPS timing detectors, without adding unnecessary dead material near the beam.

3.6.2 Impedance

Detailed impedance simulations have been performed by the LHC impedance team for the movable pipe design developed by AFP [22, 23]. These indicate the impact of a full system of two MBP stations per

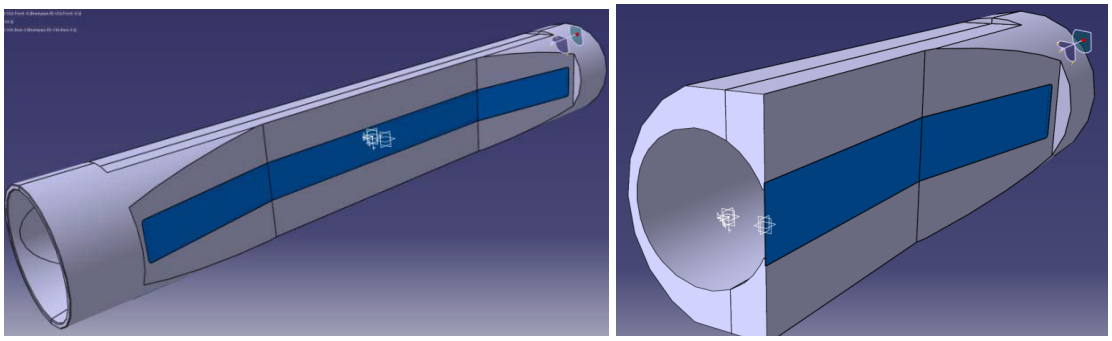

Figure 55: MBP design. Left: full MBP with 11 degree tapering. Right: cutaway, showing the aperture. The 300 μm thin window is indicated by the blue band.

arm can be reduced to less than $\sim 1\%$ of the overall impedance for both the transverse and longitudinal components of the impedance, for distances of approach to the beam as low as 1 mm ($\sim$10 σ). The estimated RF induced heating per station is approximately 10 W per station in this configuration. This was achieved by two minor modifications to the original AFP design (which was functionally equivalent to the original CMS design). First, adding a copper coating to the movable pipe reduces the resistive component of the impedance to an acceptable level. The second modification requires tapering the ends of the pocket, in order to limit the geometrical component of the impedance. A tapering at an angle of 11 degrees has been recommended by the LHC impedance experts, as this geometry has already been proven to work for the existing collimators. Both of these modifications have been incorporated into the CT-PPS design.

The AFP studies were performed for a longer pocket length ($\sim$50 cm) and closer approach to the beam ($\sim$1 mm) than forseen for CT-PPS. Since both of these differences, especially the distance of approach to the beam, increase the impedance, the AFP results can be taken as an upper limit on the impact of CT-PPS on the LHC impedance budget.

The movable beampipe is connected to the standard LHC beam-pipe with bellows, which must allow for the 25 mm transverse stroke required to move from the parking to the data-taking position. A set of two standard double bellows per station would also make a significant contribution to the impedance budget if unshielded [23]. The bellows will therefore require either a specialized design to limit the contribution of low frequency modes, or robust shielding capable of maintaining good contact during the transverse movement of the beam-pipe from the parking position to the data-taking position. Recent designs of improved shielding with fixed extremities for transverse movements have been produced for the LHC VMTSA modules [24, 25].

3.6.3 Thin window and material budget

As a consequence of the 11 degree tapering to reduce impedance, the effective amount of material traversed by a proton passing through the thin window is increased by approximately a factor of five, compared to a 90 degree thin window. Because of multiple scattering this degrades the angular resolution on the measured protons. A thin window design that minimizes the amount of multiple scattering is therefore desirable.

Three material options are considered: stainless steel, with a radiation length of X0=1.76 cm, beryllium, with X0=35.28 cm, and an AlBeMet AM162 (38% aluminum, 62% beryllium) alloy [26], with X0=18.68 cm. The effect of multiple scattering in the three cases is shown as a function of the thin window tapering angle in Figure 56, calculated [27] for a 6 TeV proton. In the case of a full MBP system with two stations, the proton would pass through three thin windows (the entrance and exit windows of the first station, and

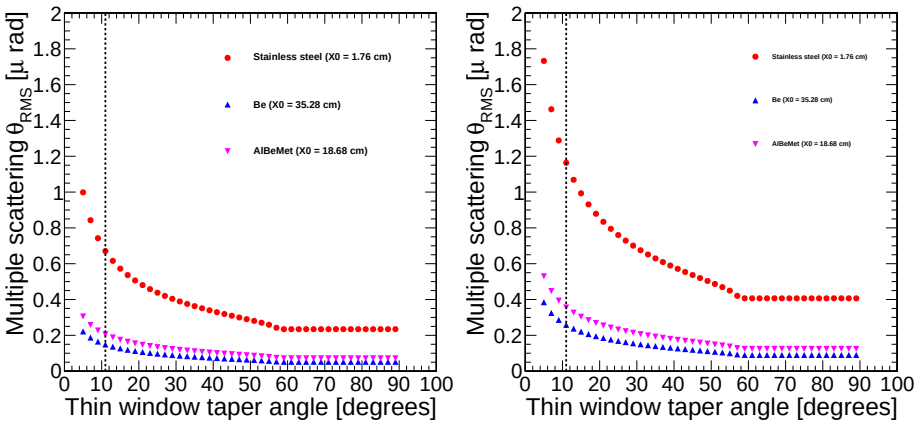

Figure 56: θ_{RMS} due to multiple scattering in microradians, as a function of thin window tapering angle. The results are shown for a 6 TeV proton passing through stainless steel, beryllium, or aluminum-beryllium alloy (AlBeMet). The vertical dashed line indicates the 11 degree angle chosen to reduce RF impedance. The left plot shows the results for a single thin window, the right plot shows results for a proton passing through three thin windows, corresponding to the effect seen at a second station.

the entrance window of the second station) to reach the detectors in the second station. As shown in the right panel of Figure 56, three stainless steel thin windows at 11 degrees would contribute 1.2μrad, compared to a total 1μrad target resolution for PPS as discussed in Chapter 1. In contrast, with beryllium or AlBeMet thin windows the resulting θ_{RMS} is of order 0.4μrad or less.

An additional benefit of the beryllium or AlBeMet thin window is to reduce the impact of showers arising from interactions of halo or beam debris with dead material near the beam. To investigate this a GEANT4 simulation of the MBP has been implemented, with the thin window composed of either stainless steel, beryllium, or AlBeMet. Samples of protons with a fixed energy of 6.5 TeV are then fired at the 25 cm long, 300 μm thick portion of the thin window parallel to the beam. Further studies to quantify the multiplicity dependence as a function of the thin window material and length of the MBP, and of the energy and angular distributions of the produced showers, as well as to estimate the effect of the showers on the quadrupoles, are ongoing.

Since machining and welding of the beryllium thin window can only be performed by a few specialized firms, another possible design under consideration is shown in Figure 57. In this design the stainless steel body is a simple tube with a cutout, laser welded to an AlBeMet top section with the thin window already machined in place. The effect on the impedance will be evaluated, however the essential features of the 11 degree tapering and large radiation length material for the thin window are retained, while simplifying the machining required to build a prototype.

3.6.4 Mechanical deformation

The MBP thin window must also have minimal deformation. Previous ANSYS simulations performed for a MBP design with a 300 μm stainless steel thin window indicated that the maximum deformation is less than 20 μm with a safety factor in excess of 10 (Figure 58), assuming a 1-atm pressure difference between outside and inside of the beam-pipe. The simulation results were found to be in good agreement with measurements performed on a stainless steel prototype with a 300 μm thin window, manufactured by electro-erosion (Figure 59). Similar studies will be repeated for the current design with tapered beryllium or AlBeMet thin windows.

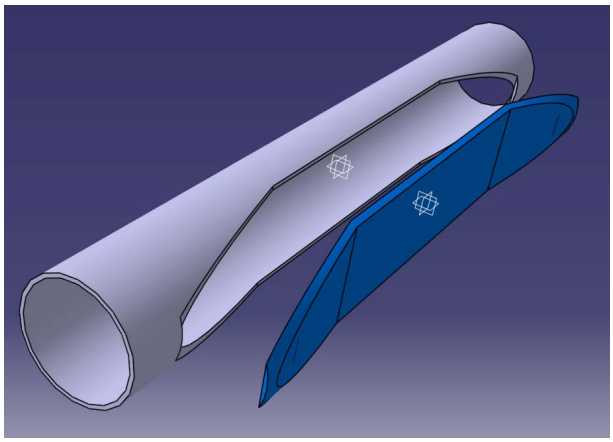

Figure 57: Alternative design with stainless steel tube laser welded to AlBeMet top piece (shown in blue), including the thin window.

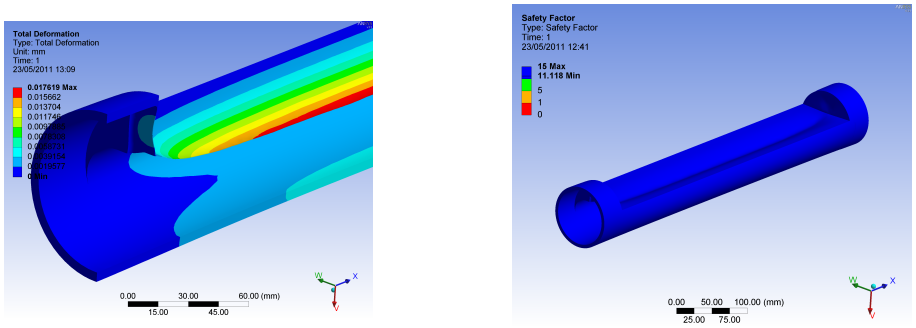

Figure 58: Right: Simulated deformation of a stainless steel beam-pipe assuming a pressure difference between outside and inside of 1-atm. Units are mm. Left: Simulated safety factor assuming a pressure difference between outside and inside of 1-atm.

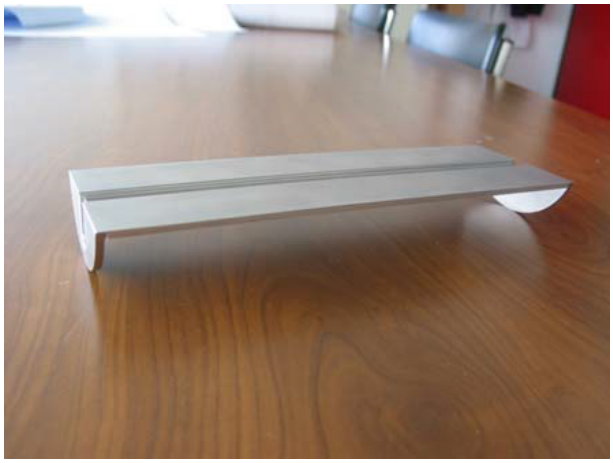

Figure 59: Prototype stainless steel MBP pocket with 300 μm thin window, produced by electro-erosion.

Item	Number (1 MBP station)	Unit cost (kCHF)	Total (kCHF, 1 MBP station)
Stainless steel beampipe body	1	1.2	1.2
Thin window material (Be or AlBeMet)	1	2.4	2.4
Electron-beam welding of thin window	1	12	12
BPM mechanics	2	3	6
Bellows	2	3	6

Table 12: Estimated cost for components of one MBP station in kCHF.

3.6.5 Cost and prototype development

Table 12 lists approximate costs estimated for the components and manufacturing of a single MBP station. The cost as shown does not include the step motor system and associated LVDT's (Linear variable differential transformer) for positioning of the MBP, or engineering support.

As a first step to developing a full MBP station we will proceed to manufacture a prototype of the stainless steel beampipe body, after the design is reviewed by the LHC impedance and vacuum groups. This will be performed at INFN Torino by electro-erosion of a single stainless steel cold-forged bar, followed by copper coating of the internal surface. The prototype will then be tested for vacuum tightness, deformation, geometry, and RF impedance. The estimated time to manufacture such a prototype is three months, including surface treatments and copper coating.

References

[1] TOTEM Collaboration, TOTEM Upgrade Proposal, CERN-LHCC-2013-009; LHCC-P-007 and "Timing Measurements in the Vertical Roman Pots of the TOTEM Experiment", CERN-LHCC-2014-020 (TOTEM-TDR-002).

[2] J. Baechler et al., "TOTEM Consolidation Projet", LHC-XRP-EC-0010, EDMS Doc. 1314925; "TOTEM Upgrade Project", LHC-XRP-EC-0011, EDMS 1361537.

[3] "Installation of Physics Debris Absorbers (TCL) on both sides of IP1 and IP5 in front of Q6 Quadrupole", LHC-LJ-EC-0040, EDMS 1357736.

[4] M.G. Albrow et al., "Quartz Cherenkov Counters for Fast Timing: QUARTIC", JINST 7 (2012) P10027.

[5] ATLAS Collaboration, "Letter of Intent for the Phase-I Upgrade of the ATLAS Experiment", CERN-LHCC-2011-012 ; LHCC-I-020.

[6] J. Baechler, D. Druzhkin, "Design and production of a cylindrical RP for LHC", EDMS note in preparation.

[7] J. Baechler et al., "Measurement of thin window deflection under variable air pressure exposure", EDMS note in preparation.

[8] J. Baechler et al., "Leak test of the new cylindrical Roman Pot with thin window", EDMS note in preparation.

[9] F. Nemes: "Geant4 simulations for the TOTEM upgrade program", CERN-TOTEM-NOTE-2013-002.

[10] M. Deile et al., "Beam Coupling Impedance Measurement and Mitigation for a TOTEM Roman Pot", Proceedings of EPAC08, arXiv:0806.4974 .

[11] N. Minafra, "RF Characterization of the New TOTEM Roman Pot", CERN-TOTEM-NOTE-2013-003.

[12] P. Baudrenghien et al., "The LHC RF System – Experience with beam operation", CERN-ATS-2011-048.

[13] E. Chapochnikova, "First measurements of longitudinal impedance and single-bunch effects in the LHC",
https://www.cern.ch/emetral/ICEsection/2010/Meeting_01-09-10/Longitudinal%20impedance.pptx

[14] E. Metral, "Procedures for frequency and time domain EM simulations in asymmetric structures",
http://sps-impedance.web.cern.ch/sps-impedance/documents/ProceduresForFrequencyAndTimeDomainEMSimulationsInAsymmetricStructures_EM.pdf

[15] E. Metral, "Pushing the limits: beam",Chamonix 2011 Workshop on LHC Performance.
http://indico.cern.ch/getFile.py/access?contribId=14&sessionId=6&resId=0&materialId=paper&confId=103957

[16] N. Minafra, "RF Measurement of the New TOTEM Roman Pot", TOTEM-LHC internal note in preparation.

[17] F. Carra, “Choice of material for TCTP ferrite and support”, LHC Collimation Working Group meeting 159, 22 April 2013.
https://indico.cern.ch/conferenceDisplay.py?confId=246742

[18] G. Cattenoz, “Vacuum degassing test report of TT2-111R ferrite after bake-out”, EDMS 1287626.

[19] S. Redaelli: Plans for collimation upgrade of IR1 and IR5 in LS1, 13th LTEX meeting, 11.10.2012,
https://indico.cern.ch/conferenceDisplay.py?confId=211226

[20] Collimation WG meeting, 22.04.2013,
https://indico.cern.ch/conferenceDisplay.py?confId=246742

[21] K. Piotrzkowski and U. Schneekloth, ZEUS collab. meeting, march 1994, DESY, Hamburg.

[22] B. Salvant, presentation at the 22nd LEB meeting, Sep. 10, 2012.
http://indico.cern.ch/conferenceDisplay.py?confId=204787

[23] B. Salvant, presentation at 17th LTEX meeting, March 21, 2013.
https://indico.cern.ch/event/233129/material/slides/1?contribId=0

[24] E. Metral et al., ”Lessons Learnt And Mitigation Measures For The CERN LHC Equipment With RF Fingers”, Proceedings of IPAC2013.
http://accelconf.web.cern.ch/accelconf/IPAC2013/papers/tupwa042.pdf

[25] C. Garion, A. Lacroix, H. Rambeau, ”Development of a New RF Finger Concept for Vacuum Beam Line Interconnections”, Proceedings of IPAC2012.
http://accelconf.web.cern.ch/accelconf/IPAC2012/papers/weppd017.pdf

[26] http://materion.com/~/media/Files/PDFs/Beryllium/AlBeMet%20Materials/MAAB-017AlBeMetPropertyDataSheet

[27] J. Beringer et al., PDG collaboration, ”Review of Particle Physics (RPP)” Phys.Rev. D86 (2012) 010001.

4 Tracking Detectors

The key requirements for the CT-PPS tracking system are:

- Efficient pixel based tracking as close as possible to the sensors physical edge, providing hit resolution better than 30 μm.
- Radiation hardness: a design figure of $5 \cdot 10^{15}$ protons/cm^2 for 100 fb^{-1} of integrated luminosity is required (Figure 60)
- Reliable operation at the highest LHC luminosity.

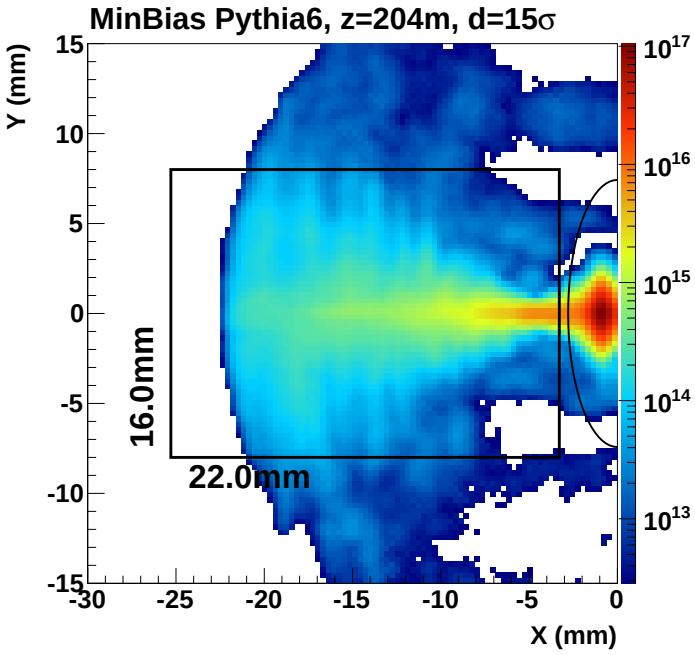

Figure 60: Simulated proton fluence in the tracking station at 204 m from the IP for the integrated luminosity of 100 fb^{-1}. The rectangle indicates the detector surface transverse to the beam assuming a detector tilt angle of 20°. The ellipse shows the 15 sigma beam contour. In the detector edge a value of the order of $5 \cdot 10^{15}$ p/cm^2 is obtained. This value is compatible with the extrapolation from TOTEM data.

Since the construction of the original pixel tracking systems for the LHC experiments, there has been considerable progress in silicon sensor technology. Both CMS and ATLAS have pursued improved pixel designs for the high-luminosity upgrades of the LHC. These ongoing R&D efforts have already achieved two proven sensor designs that meet the needs of CT-PPS and can be produced by industry: 3D and planar slim-edge silicon pixel sensors. Both types of sensors are being installed in the new Insertable Barrel Layer (IBL) of the ATLAS vertex detector [1].

3D sensors consist of an array of columnar electrodes (radius $\sim$5 μm) of both doping types that penetrate through the silicon bulk perpendicularly to the surface, as shown in Figure 61. The bulk is usually of type p. Junction n-type electrodes are read out on the front side of the sensor while ohmic p-type electrodes are connected on the back side for applying the bias voltage. This structure decouples the inter-electrode distance from the sensor substrate thickness, allowing to reduce the drift path of the charge carriers without decreasing the total generated charge.

The close electrode spacing provides several advantages compared to the planar sensor design:

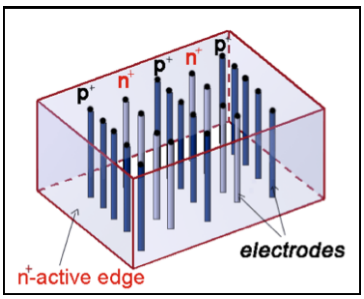

Figure 61: Sketch of a 3D sensor.

- low full depletion voltage ($\sim$10 V),
- fast charge collection time,
- reduced charge-trapping probability and therefore high radiation hardness.

As a result, 3D detectors are emerging as one of the most promising technologies for the innermost layers of tracking devices for the foreseen upgrades of the LHC. A very interesting feature of 3D technology is the possibility of realizing the so-called "active edge" [4], i.e. a deep trench all around the sensor that reduces the dead region to a few microns from the physical edge of the device, compared to the hundreds of μm for standard planar detectors.

As a backup solution, we have identified a second sensor concept, a slim-edge planar design produced by CIS (tested by ATLAS) and SINTEF (tested by CMS), based on a more mature fabrication process. We have designed the CT-PPS sensor readout and packaging to accept either sensors as a drop-in replacement.

The chosen configuration for the tracking system consists of two detector stations in each arm, for a total of four detector stations. These are the horizontal RPs located at $\sim$210 m. Each station will contain one stack of silicon tracking detectors. Each stack will consist of six planes, where each plane contains a 1.6×2.4 cm^2 pixel sensor read out by six PSI46dig readout chips ROCs [2]. Each ROC reads 52×80 pixels with dimensions 150×100 μm^2. Given the small area of the detector, covered by a small number of individual sensors, we have chosen a number of planes that provide confortable redundancy making the system resilient to possible failures. The design of the front-end electronics and of the DAQ is based on that developed for the Phase 1 upgrade of the CMS silicon pixel detectors [3].

The resolution of the x-coordinate is determined by the sharing of charge in the pixel clusters, which depends on the detector tilt angle in the x-z plane. While this parameter is not yet defined, test beam results with similar sensors indicate that for an angle of 20 degrees the two-pixel clusters have resolution of the order of 10 μm. Since there is no tilt in the y-z plane, the resolution of the y-coordinate is of the order of 30 μm.

4.1 Silicon sensors

4.1.1 Baseline solution: 3D silicon sensors

The baseline CT-PPS tracking system is based on 3D pixel sensors, produced either by FBK (Trento, Italy) or CNM (Barcelona, Spain), which we think provide the best performance in terms of active region and radiation hardness. These companies have already produced 200 μm slim-edge 3D sensors for the IBL project with satisfactory yield. However, for CT-PPS we would like to pursue the option with a 100 μm, or better, slim-edge design, where the active region of the sensor is as close as 100 μm to the

edge. Since such slim edges have not yet been produced, we mitigated our schedule risk by designing the CT-PPS tracking system to allow rapid installation, or replacement, of the unit during a LHC technical stop.

The three-dimensional (3D) architecture for radiation-hard silicon sensors was first proposed by Parker, Kenney and Segal in 1997 [5]. The first 3D devices with fully passing-through electrodes were produced by the Stanford Nano-fabrication Facility (Stanford, USA) [6] and the fabrication process was further developed at SINTEF (Oslo, Norway) [7] for larger-scale production. This fabrication process is single-sided, with the electrodes all initially formed (drilled) on the same side. It allows the fabrication of active edges but it requires a support wafer, which is difficult to remove. To avoid this problem, two other 3D producers, FBK (Trento, Italy) and CNM (Barcelona, Spain), independently developed a different technique without a support wafer [8, 9]. A double-sided fabrication technology is used, with junction electrodes etched from the front side and ohmic electrodes etched from the back side. These two vendors (FBK and CNM) have produced 3D sensors for the ATLAS IBL project, either with fully passing-through or with partially passing-through electrodes, respectively [10], and with a dead region of 200 μm from the sensor's edge (slim edge).

The particular structure of 3D sensors has a few drawbacks also: the fabrication process is more complicated and requires more steps with respect to the production of planar silicon detectors; the short electrode distance and the extension inside the bulk increase the pixel capacitance and, consequently, the noise induced on the readout electronics. Moreover, the response is not completely uniform because of the electrodes, which are less efficient or completely inefficient regions, depending on the fabrication process. Nevertheless, the fact that 3D sensors passed the requirements imposed by the stringent IBL environment [11] is an indication that these drawbacks can be overcome. The ATLAS 3D Collaboration measured the efficiency of these detectors in several test beams and found it to be well above 99% [10]. Because of the electrode geometry, 3D devices exhibit some loss of tracking efficiency for normal incident tracks but recover full efficiency with tilted tracks, or equivalently by tilting the detectors. Moreover, only minor degradation was observed after irradiation [12].

CMS-compatible sensors have been fabricated by SINTEF, FBK and CNM. Three different electrode configurations were manufactured up to now:

- single n-type electrode (1E),
- two n-type electrodes (2E), and
- four n-type electrodes (4E) per pixel cell.

The distance between n-type and p-type electrodes is of great importance since it affects parameters such as capacitance and noise, depletion voltage, charge collection, and radiation hardness. The inter-electrode distances in the 1E, 2E, and 4E configurations are 90, 62.5, and 45 μm, respectively. Sensor thicknesses varied between 200 and 230 μm.

Testing of these devices has been carried out together with the CMS pixel upgrade group, which is also exploring this novel technology. Several CNM and FBK sensors with standard guard rings or slim edges, and with different electrode configurations were characterized in the laboratory [13] and tested at Fermilab with a proton beam of 120 GeV. Data were taken for various values of depletion voltages, read-out electronics thresholds, temperatures and angles with respect to the beam. Some of these devices were irradiated at Los Alamos National Laboratory (USA) with 800 MeV protons at fluences up to 10^{15} n_{eq}/cm^2 and re-tested [14]. Results showed the best performance for the 2E configuration. For all the above measurements 3D sensors were read out with the PSI46 analog chip [15] presently used in the CMS pixel tracking detectors.

Recently (May 2014), in a test beam at Fermilab, seven un-irradiated FBK 1E 3D sensors, processed in the framework of the ATLAS IBL production [16], with 200 μm slim edges [17], have been tested coupled to the new PSI46dig ROC, developed for the Phase 1 upgrade of the CMS pixel tracking detectors.

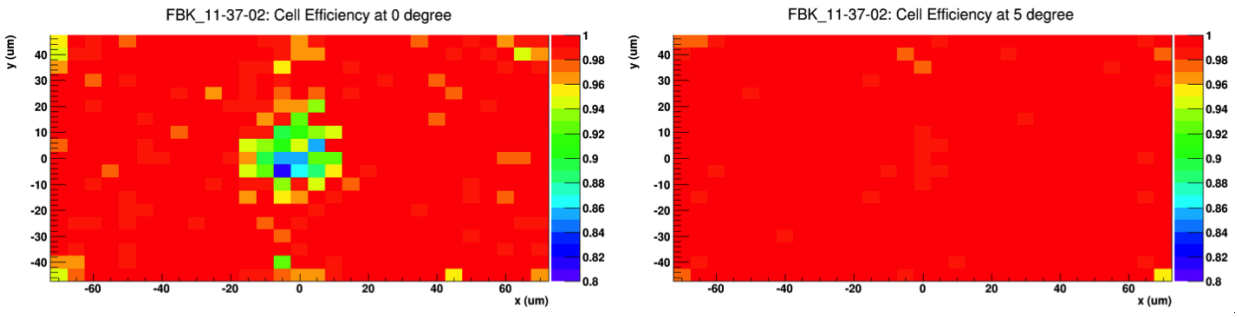

Figure 62: Cell efficiency map for the sensor FBK 11-37-02 obtained using normal incident tracks (left panel) and 5° inclined tracks (right panel). These measurements were performed at room temperature and with a bias voltage of $|V_{bias}|$ = 30 V.

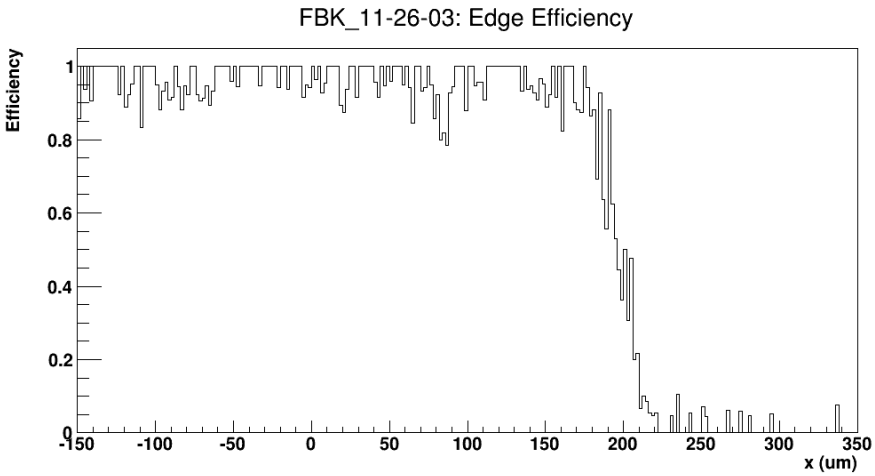

Figure 63: Edge efficiency measurement performed in a test beam at Fermilab with 120 GeV protons. The origin of the x axis is placed in the center of one edge pixel, whose area is 100x300 μm^2. The region between 150 μm and 350 μm corresponds to the slim edge. The bias voltage applied to the sensors is $|V_{bias}|$ = 30 V.

Data analysis is still ongoing but preliminary results are very promising. The possibility to lower the channel thresholds down to ∼2500 e$^-$ and to trim their values more accurately made it feasible to obtain efficiencies above 99.5%, with full charge collection at bias voltages above ∼15 V. Figure 62 shows the two-dimensional map of the cell efficiency for one of these sensors at normal beam incidence (left panel) and with the detector tilted by 5 degrees with respect to the beam axis (right panel). To increase the statistics, all cells have been added together, assuming they have a similar behaviour. Low efficiency structures, corresponding to the position of the electrodes, are clearly visible in the left plot. These structures, due to the fact that in FBK sensors the electrodes are empty and do not produce charge, disappear in the right plot, proving that a tilt of 5 degrees is sufficient to fully restore sensor efficiency.

The slim edge is realized by FBK as a multiple fence of ohmic columns that effectively stop the lateral depletion region from reaching the edge of the detector, thus significantly increasing the shielding of the active area from edge effects. Figure 63 shows that this design of the edge termination allows to maintain a stable and high efficiency up to ∼50 μm beyond the edge pixels, thus reducing the effective thickness of the inactive region to 150 μm. A similar effect has been observed in FBK sensors designed for ATLAS [18].

These devices were recently irradiated with 25 MeV protons at Karlsruhe Institute of Technology (KIT)

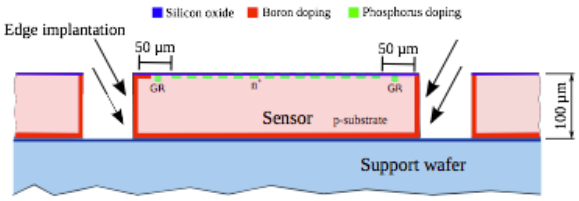

Figure 64: Schematic of the active edge as implemented by VTT for planar sensors.

to 4 different fluences ($1{\cdot}10^{15}$ n_{eq}/cm^2, $3{\cdot}10^{15}$ n_{eq}/cm^2, $6{\cdot}10^{15}$ n_{eq}/cm^2 and $1{\cdot}10^{16}$ n_{eq}/cm^2) and are currently being characterized in laboratory. The level of the leakage current measured at $-10°C$ is acceptable ($\sim$80 μA for sensors irradiated to $1{\cdot}10^{15}$ n_{eq}/cm^2). A significant increase of the breakdown voltage ($|V_{BD}|$ $\sim$35 V before irradiation) has been observed: the devices irradiated at the lower fluence reach a maximum operating voltage of $|V_{bias}| \sim 80$ V, while the ones at the larger fluence exceed 120 V. These values of breakdown voltage should be sufficiently high to allow to operate the sensors at the optimal bias also after irradiation.
A test beam at Fermilab is foreseen for the second half of August 2014 to perform further studies on the behaviour of irradiated detectors.

4.1.2 Alternative solutions: slim-edge planar sensors

In the past years a large effort went into studying strip and pixel planar sensors with slim edges, as they allow for a simplified tracker geometry with respect of traditional wide-edge sensors [19, 20] and they can instrument larger areas than what is possible to achieve with 3D slim-edge sensors.

The key factor determining the inactive edge extension are the defects introduced by detector dicing with diamond saws, which originate increased leakage currents and decreased breakdown voltages if the depletion region approaches the physical edge of the sensor. Therefore, the first approach to slim-edge sensors has been to improve the quality of the lateral cut, using laser dicing in combination with chemical etching. This technique, however, did not manage to obtain the results that were hoped for.

A second strategy relies on thin sensors: as the lateral field extends for a fraction of the sensors thickness, thin sensors are well suited to obtain slim edges. If a detector is 100 μm thick, the inactive edge is roughly of the same extension.

A completely different approach has been obtained by the introduction of active edges, proposed by the Stanford Nanofabrication Facility (SNF) for 3D detector technology [4] and later applied also to planar sensors [21]. In this design, the problems connected with the surface defects at the edge of the sensor are avoided by making the edge an active component in the definition of the electric field, as shown in Figure 64: the boron implant does not stop at the backplane, but continues along the detector edges, reaching the frontplane. Using this technique, the *ATLAS Planar Pixel Sensor Collaboration* has manufactured several prototypes with 50 and 100 μm slim edge or active edge.

An interesting alternative to the active-edge approach is based on a special treatment of the sensor edge via the sequence of three steps: scribing, cleaving and passivation [22]. Wafer scribing and cleaving are used to minimize the number of defects with respect to a standard dicing saw, whereas edge surface passivation aims at allowing for a bias voltage gradient along the sidewall surface, pratically turning the edge into a large resistor. This technique has the advantage that it can be used in post-production to obtain slim-edge sensors from finished wide-edge sensors.

With these techniques, slim- and active-edge planar sensors are reaching the same performance as 3D sensors, and represent viable fall back solutions.

4.2 The readout system

The readout of the pixel detector is largely based on components developed in the framework of the Pixel Upgrade Phase 1 readout project. This readout chain has been proven to work efficiently. Most components are currently at an advanced test stage and/or in final production. In this section, an overview of the readout system of the pixel detector is given shortly with special emphasis on CT-PPS specific points. Extensive documentation of each component can be obtained elsewhere [3].

The complete readout chain of one detector package is shown in Figure 65. By convention a detector package is a set of six modules, one for each sensor present in a RP. There are in total four detector packages. The specific CT-PPS elements in the readout system are the six RPix Modules (Roman Pot PIXel Modules) and the RPix Portcard. The low voltage system and high voltage system are part of the low voltage and high voltage system of TOTEM, already in place. The backend DAQ electronics, to be installed in the service cavern, is being actively developed by CMS as part of the Pixel Upgrade Phase 1 project.

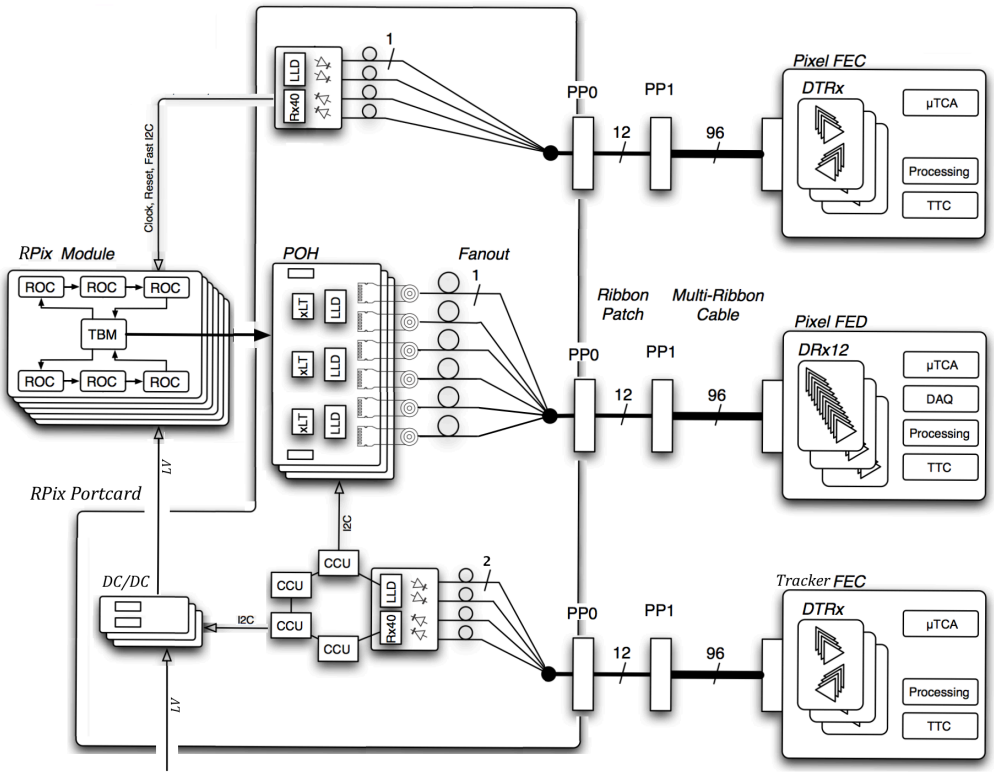

Figure 65: Detector readout and control strings. All components up to PP1 are in the LHC tunnel, while FEDs and FECs are in the service cavern.

Each RPix Module consists of a flexible hybrid circuit hosting: a silicon sensor, six ROCs "bump-bonded" to the silicon sensor, and one Token Bit Manager (TBM) chip. The ROC is responsible for charge collection, charge discrimination and data sparsification. Two slightly different versions of the chip, named V2.1 and V2.1b, are suitable: which version to use is currently under evaluation.

The TBM is responsible for reading out the six ROCs in the module (it can manage up to 16) using a token ring protocol and serialising the data over a single output line. The TBM versions suitable for

this application, named TBM08a and TBM08b, manage two token bit ring protocols at the same time, multiplexing the two data streams on the same output line before encoding the data stream using a 4B/5B NRZI schema. The net result is an uplink data stream running at 400 Mb/s. Dispatching these high speed signals on the flexible hybrid without degrading them is one of the major design requirements of the RPix Module, together with the need to deliver the high voltage to the sensor safely.

The RPix Portcard accomplishes a variety of tasks. The board receives the output data from six RPix modules and retransmits them on six optical fibres towards DAQ modules, using a POH7 opto-electrical converter mezzanine card [23]. This board also receives fast configuration commands from the Pixel FEC via optical fibres, translates these signals using detector optical receivers (DOH) and dispatches them to the modules. These functionality are similar to those of the Forward Pixel project portcard developed by Fermilab. Moreover the RPix Portcard integrates other components such as the radiation sensors, part of the TOTEM DCS radiation monitoring system, and the CMS Tracker Optical Control Link components which are capable of receiving and decoding the commands sent from the Tracker FEC. Finally, the newly developed DC/DC converters [24], developed by CMS, are installed on the board, in order to generate the different voltages needed by the portcard itself and by the attached modules.

For the backend DAQ system, the plan is to use the new uTCA crates and boards developed for the Pixel Upgrade Phase 1 project. A fallback solution, using VME electronics, is available in case the baseline solution could suffer long delays.

It should be noted that the tracking front-end based on the CMS pixel readout chip PSI46dig chip does not have trigger outputs and therefore can not be integrated in the L1 Trigger.

4.3 The detector assembly

The mechanical structure of the detector is designed so as to ensure a positioning accuracy comparable to the resolution of the detector and at the same time provide a proper thermal conductance for detector cooling. The material budget of the mechanical structure is not an issue, except for the area below the sensors, since most of the support is outside of the tracks path. Stiffness and thermal properties are more relevant. Moreover a desirable feature is the integration with the present cooling system.

The sensor planes are not mounted perpendicular to the beam direction: they are rotated by 18.5 degrees around the vertical axis. This angle is enough to remove the geometrical inefficiency, due to presence of the columnar electrodes in the 3D sensors, and guarantees optimal resolution in the horizontal direction thanks to charge sharing between nearby pixels.

An exploded view of one module is shown in Figure 66. Each module consists of several different parts. The support plate, consisting of two layers of different materials, can be seen at the bottom. The first, 1.25 mm thick, layer is made of CE7, a controlled expansion material composed of 70% Si and 30% Al. The second, 0.7 mm thick, layer is made of Thermal Pyrolithic Graphite (TPG), a low density material consisting of stacked graphite sheets and featuring an extremely high thermal conductivity on the sheets plane.

A long kapton flexible hybrid circuit is glued on top of the TPG layer, as well as the silicon detector, “bump-bonded” to six readout chips. Wire bonds provide electrical contacts between detector pads and hybrid electric lines. The flexible circuit hosts the TBM and provides connection, at the other end, to the readout board.

An exploded view of one detector package is shown in Figure 67. Pairs of modules are screwed face to face to two aluminium support bars, each one machined in a single piece to ensure the best thermal contact. These bars are in tight contact with the cooling pipes. The detector assembly is modular. Mechanics is arranged in such a way that when the modular pieces are brought together they enclose the cooling pipes and the detector package is complete. In order to maximise heat exchange, each TPG is in

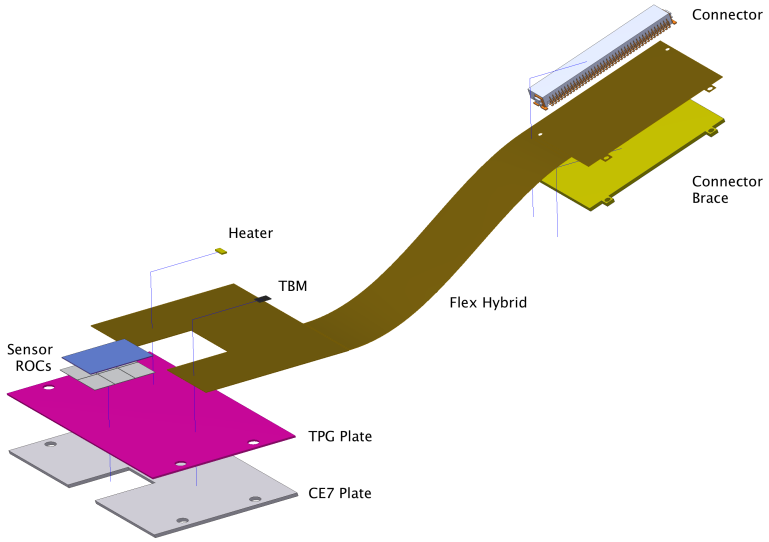

Figure 66: Exploded view of one pixel module. The support plate consists of two layers: the first layer is made of CE7 while the second is made of Thermal Pyrolithic Graphite (TPG). A long kapton flexible hybrid circuit is glued on top of the TPG layer, as well as the silicon detector. A flexible kapton circuit hosts the TBM and provides connection, at the other end, to the readout board (see text for full explanation).

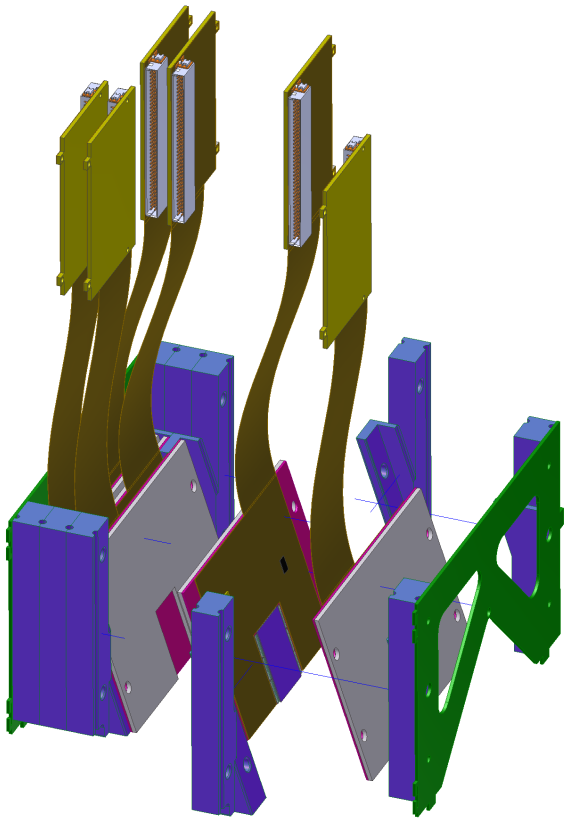

Figure 67: Exploded view of one detector package. Pairs of modules are screwed face to face to two aluminium support bars which are in tight contact with the cooling pipes (see text for full explanation).

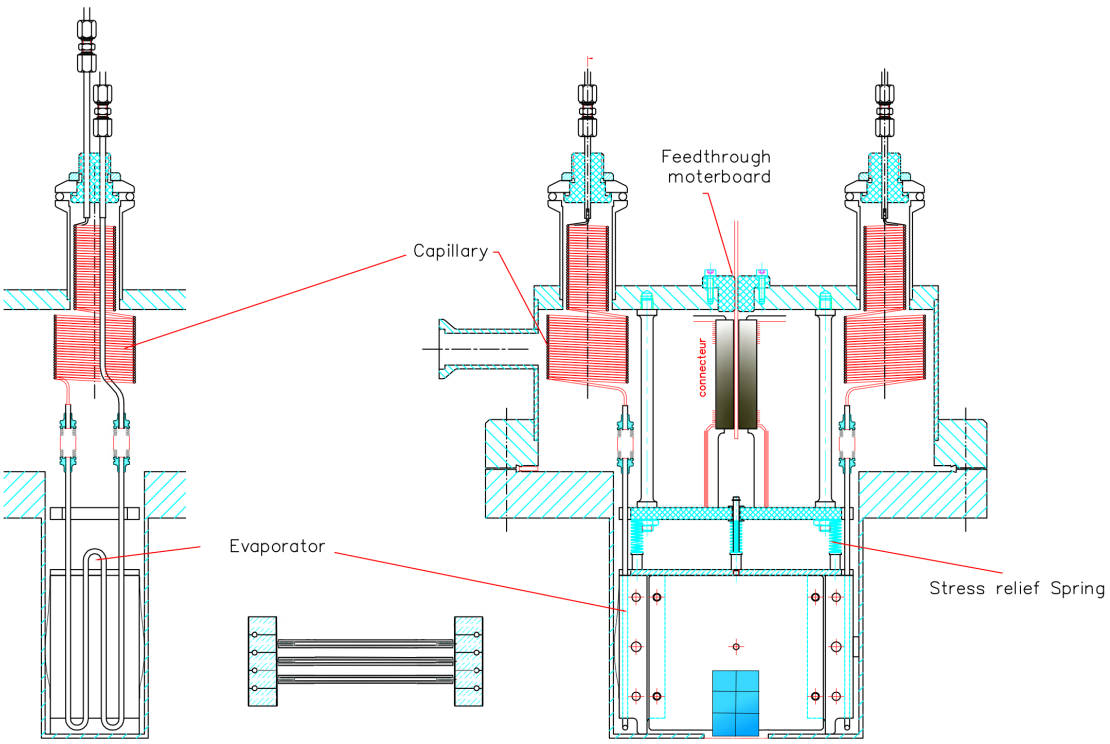

Figure 68: Overview of the RP inner volume. Detectors, coloured in blue, are hosted in the rectangular box at the bottom of the picture. The cooling lines are coloured in red. The RP readout board is visible in the right most picture. It is glued on the feed-through of the flange; only the connectors are visible, most of it extension is above the flange.

direct contact with the ROCs and the aluminium supports.

The readout board (see Figure 68) will be attached on the feedthrough of the flange between normal environment and secondary vacuum. Only the connectors will protrude into the secondary vacuum in order to connect to the detector package. Enough space exists on top of the flange to host the rest of the board.

A thermal prototype of one detector package will be assembled in order to test the conceptual design, the choice of the materials and the fluid-dynamical parameters of the cooling system. The ROCs will be replaced with heaters with equivalent power density. The prototype will be fixed to a vacuum chamber flange and inserted in an experimental vacuum chamber. All the connections of the pressure and temperature sensors will be read out through a vacuum feed-through.

4.4 The cooling system

The existing cooling system [25] is suitable to host the pixel detectors inside the pot. The requirements imposed by the pixel detector (< 10W per package, $\sim -20\,^0$C) are very similar to those imposed by the silicon microstrip detector (< 20W per package, $\sim -10\,^0$C). The main difference is the region where most of the heat is produced.

The system is designed to remove a thermal load from sensors, electronics and RF coupling up to ~ 50 W per pot. In the case of the Roman Pot equipped with the RF cylindrical collar shield, the power released

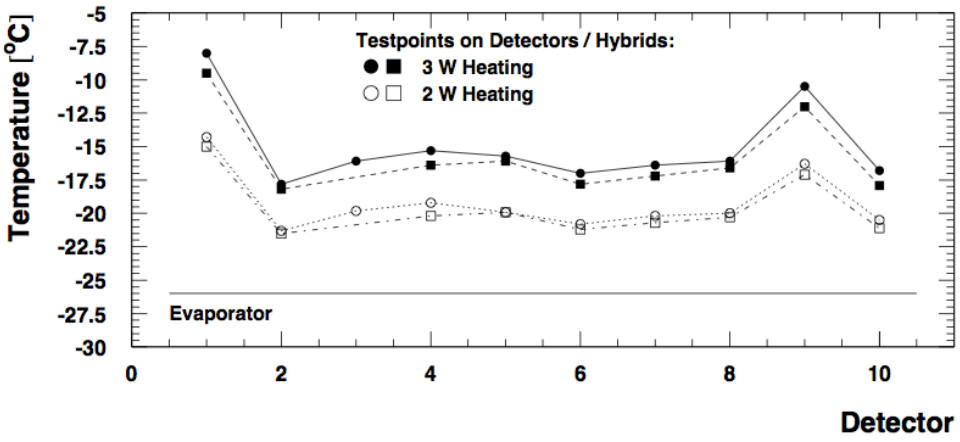

Figure 69: Temperature distribution measured on test points on the silicon micro-strip detectors hybrids for a heating power of 2 W and 3 W (open and solid markers respectively), compared with the evaporator temperature.

in the pot, due to residual RF coupling with the beam, is expected to be 10 W when the pot approaches the beam to 1 mm.

Because of the high radiation environment of the LHC tunnel, the main part of the refrigeration system is installed in the underground service area USC55 at IP5, a protected and always accessible place. An "fluorocarbon evaporative" cooling [26] strategy has been adopted since it can transport fluid at ambient temperature over long distances (from USC55 near IP5 to the RP stations at 210 m and 220 m) without heat losses. The fluid is supplied in liquid phase and at high pressure at the RP circuit inlet. The throttling of the fluid is done in the pot and is based on metal capillary tubes. An isenthalpic expansion process through capillaries decreases its pressure and tunes the temperature to the design evaporation value of $-30\,^0$C. The C_3F_8 fluorocarbon dielectric fluid has been selected because it is non-flammable, non-conductive and radiation resistant.

Inside the RP the cooling fluid flows through thin-walled copper-nickel pipes of 2.5 mm outer diameter. Two independent pipe evaporators supply fluid to the right and left side of the detector package. The evaporators, mechanically coupled to the detector package, are decoupled from the rest of the cooling system at the inputs and outputs by bellows. They are shaped in a double-S configuration and are squeezed in between the frame structure which foresees precisely machined grooves for this purpose. The evaporators are fed by capillary tubes that provide the throttling of the fluid. The coolant in gas phase is exhausted via larger diameter pipes. Both the capillaries and the exhausting pipes enter and leave the pot through two vacuum feed-throughs.

For the current frame structure, supporting 10 planes of micro-strip detectors, the measurements show that for an heating power of 2 W per plane the temperature spread on a single hybrid card is within 3 ^{0}C, and the maximum temperature difference between detectors is less than 10 ^{0}C (Figure 69). We expect to get similar or better results for the new six plane frame structure designed for the pixel detectors.

References

[1] ATLAS Insertable B-Layer Technical Design Report, ATLAS IBL Collaboration, CERN-LHCC-2010-013, ATLAS-TDR-19, 15 September 2010 (2010).

[2] H.Chr. Kästli, "Frontend electronics development for the CMS pixel detector upgrade", Nucl. Instr. and Meth. A 731 (2013) 88.

[3] CMS Technical Design Report for the Pixel Detector Upgrade, CMS Collaboration, CERN-LHCC-2012-016; CMS-TDR-11, 7 September 2012 (2012).

[4] C.J. Kenney *et al.*, "Results From 3-D Silicon Sensors With Wall Electrodes: Near-Cell-Edge Sensitivity Measurements as a Preview of Active-Edge Sensors", IEEE Trans. Nucl. Sci. 48 (2001) 2405.

[5] S.I. Parker *et al.*, "3D - A proposed new architecture for solid-state radiation detectors", Nucl. Instr. and Meth. A 395 (1997) 328.

[6] C.J. Kenney *et al.*, "Silicon Detectors with 3-D Electrode Arrays: Fabrication and Initial Test Results", IEEE Trans. Nucl. Sci. 46 (1999) 1224.

[7] T.E. Hansen *et al.*, "First fabrication of full 3D-detectors at SINTEF", JINST 4 (2009) P03010.

[8] A. Zoboli *et al.*, "Double-Sided, Double-Type-Column 3-D Detectors: Design, Fabrication, and Technology Evaluation", IEEE Trans. Nucl. Sci. 55 (2008) 2775.

[9] G. Pellegrini *et al.*, "First double-sided 3-D detectors fabricated at CNM-IMB", Nucl. Instr. and Meth. A 592 (2008) 38.

[10] The ATLAS IBL Collaboration, "Prototype ATLAS IBL modules using the FE-I4A front-end readout chip", JINST 7 (2012) P11010.

[11] C. Da Viá *et al.*, "3D active edge silicon sensors: Device processing, yield and QA for the ATLAS-IBL production", Nucl. Instr. and Meth. A 699 (2013) 18.

[12] A. Micelli *et al.*, "3D-FBK pixel sensors: Recent beam tests results with irradiated devices", Nucl. Instr. and Meth. A 650 (2011) 150.

[13] E. Alagoz *et al.*, "Simulation and laboratory test results of 3D CMS pixel detectors for HL-LHC", JINST 7 (2012) P08023.

[14] M. Obertino *et al.*, "Performance of CMS 3D silicon pixel detectors before and after irradiation", Nucl. Instr. and Meth. A 730 (2013) 33;
M. Bubna *et al.*, "Testbeam and laboratory test results of irradiated 3D CMS pixel detectors", Nucl. Instr. and Meth. A 732 (2013) 52;
A. Krzywda *et al.*, "Pre- and post-irradiation performance of FBK 3D silicon pixel detectors for CMS", Nucl. Instr. and Meth. A 763 (2014) 404.

[15] H.Chr. Kästli *et al.*, "Design and performance of the CMS pixel detector readout chip", Nucl. Instr. and Meth. A 565 (2006) 188.

[16] C. Da Viá *et al.*, "3D silicon sensors: Design, large area production and quality assurance for the ATLAS IBL pixel detector upgrade", Nucl. Instr. and Meth. A 694 (2012) 321.

[17] M. Povoli *et al.*, "Slim edges in double-sided silicon 3D detectors", JINST 7 (2012) C01015.

[18] J. Lange, "3D silicon pixel detectors for the ATLAS Forward Physics experiment", 9th Trento Workshop on Advanced Silicon Radiation Detectors (2014).

[19] http://pos.sissa.it/archive/conferences/198/042/Vertex2013_042.pdf.

[20] https://indico.cern.ch/event/265941/

[21] C.J. Kenney *et al.*, "Active-edge planar radiation sensors", Nucl. Instr. and Meth. A 565 (2006) 272.

[22] V. Fadeyev *et al.*, "Scribe-cleave-passivate (SCP) slim edge technology for silicon sensors", Nucl. Instr. and Meth. A 731 (2013) 260.

[23] J. Troska *et al.*, "Prototype pixel optohybrid for the CMS phase 1 upgraded pixel detector", JINST 7 (2012) C01113.

[24] L. Feld *et al.*, "Development of a DC-DC conversion powering scheme for the CMS Phase-1 pixel upgrade", JINST 9 (2014) C01048.

[25] The TOTEM Collaboration, G. Anelli *et al.*, "The TOTEM Experiment at the CERN Large Hadron Collider", JINST 3 (2008) S08007.

[26] V. Vacek *et al.*, "Perfluorocarbons and their use in cooling systems for semiconductor particle detectors", Fluid Phase Equil. 174 (2000) 191.

5 Timing Detectors

5.1 Requirements on the timing detectors and strategy

The need for precise timing detectors measuring the time difference of the protons in the two arms of the spectrometer is justified in Chapter 1 as an effective way to reduce the pileup background. A baseline time resolution of σ(t)=10 ps, corresponding to a vertex resolution $\sigma(z_{pp})$=2.1mm, is set as an ambitious target of the CT-PPS project. A backup scenario where the time resolution is limited to a conservative value of 30 ps is also evaluated and justified in the physics performance studies presented in Chapter 2.

The required detector area is small ($\leq$4 cm^2). In addition to a good time resolution, the use of a detector with a small dead region is a key requirement. On the side adjacent to the beam, the dead region should be at the level of $\sim$ 200 μm or below, matching that of the tracking detectors. The distance between the active area and the vacuum includes in addition the bottom of the RP ($0.3^{+0.02}_{-0.10}$ mm). The scattered protons are deflected out of the beam by the LHC magnets, but at the z position of the detectors they are displaced by only a few mm, so any inactive area (on the inner edge) causes a loss in acceptance at low masses.

The detectors should be radiation hard. Close to the beam where the detectors are located, we expect a proton flux of about 5×10^{15} cm^{-2} per 100 fb^{-1}. The expected thermal neutron flux extrapolated from TOTEM measurements is about 10^{12} cm^{-2} per 100 fb^{-1}. In the case of Cherenkov detectors the photodetectors will be farther from the beam, where radiation field is reduced to the neutron component. Replacing the photodetectors or solid-state timing detectors approximately once a year is feasible, as they are accessible and relatively inexpensive.

As there is often more than one proton in the acceptance from the same bunch crossing, a fine segmentation is also required. The detectors should have the capability of measuring the times of two or more particles from the same bunch crossing, and of being read out every 25 ns, with no significant remnant signals from earlier crossings. This implies segmentation.

A detector based on Cherenkov technology is developed for precise timing as the baseline proposal. Similar technology was studied earlier in the context of the FP420 project R&D project [1]. These included detectors based on quartz (or sapphire) radiators as well as gas Cherenkov detectors. Several prototypes have been built and evaluated in test beams. Recently there has been growing interest in timing measurements, which has led to several on-going R&D efforts on the use of solid state detectors for timing, notably in the frame of the LHC Phase 2 Upgrade programme. Several CT-PPS groups are participating to these efforts and are willing to explore the option of using such detectors in PPS.

Presently, the state-of-the-art of time resolution with minimum ionizing particles in a single detector layer is the following: 1) gas Cherenkov $\sim$ 15 ps [2]; quartz Cherenkov $\sim$ 30 ps [3]; diamond sensors $\sim$ 100 ps [4], [5]; silicon sensors $\sim$ 100 ps [6]. Complete systems with several detector layers allow for improved performance.

While Cherenkov based detectors have intrinsically better time resolution and are more mature timing technologies, they have some important drawbacks. In the existing prototype implementations, the quartz detector is segmented in elements of 3×3 mm^2, which implies a large rate of double hits in the same bar per bunch crossing, approaching 50% in the sensors close to the beam. We assume that two hits in the same channel cannot be resolved. This source of inefficiency is taken into account in the physics performance simulations in Chapter 2. Finer granularity near the beam, where it is most needed, may be possible but needs further development.

The amount of material introduced by the quartz detector itself is not negligible. In the foreseen configuration, the probability that a proton has a nuclear interaction in one detector is between 7.2% and 14.6% (depending on the proton position in the detector). As the timing detector is located downstream of the pixel detectors these interactions do not affect the track measurement, however they may smear or fully

corrupt the time measurement introducing another source of inefficiency.

The gas Cherenkov detector is not affected by this issue, but on the other hand its granularity is only indirect, in the sense that a multi anode Micro Channel Plate photomultiplier (MCP-PMT) could possibly allow to disentangle Cherenkov photons from different protons. Indeed the reconstruction of the time of two or more protons in the detector is affected by the uncertainty in associating MCP-PMT channel information to individual protons. This question is investigated in Section 5.3 with GEANT simulation. The MCP-PMT devices have also a limited life time in terms of integrated charge, which requires using the device at reduced gain, preventing the optimal time resolution.

Solid state timing detectors have the important advantage of being very thin and allowing for fine granularity. Typically solid state detectors are a few hundred microns thick making it possible to stack ten or more detectors, which to a first approximation improves the time resolution by the square root of the number of layers. A resolution of 30 ps per detector, possibly achieved as a result of the current R&D effort, would allow for a timing system with the baseline 10 ps resolution. On the other hand the possibility of defining small size pixels permits reducing the rate per channel, which improves the time measurement and reduces significantly the inefficiency due to double hits. Of course the detectors should be able to sustain the high radiation doses involved in this application, which requires still considerable development.

Taking into account the previous considerations, we have chosen as the baseline timing detector the L-bar Quartic (Quartz Timing Cherenkov) design with 5×4 = twenty 3×3 mm^2 independent channels. The SiPM photodetectors are relatively far from the beam, in a region where the neutron flux is $\sim 10^{12}$ neq/cm^2 per 100 fb^{-1}. SiPM devices that tolerate this radiation level are available, as found in the framework of the HCAL Upgrade project, however a increase of the leakage current is observed [7]. The SiPMs will probably require replacement after 100 fb^{-1}, which is feasible given the small number of devices involved. We will also consider the possibility of using GaInP photosensors, under development for the upgrade of the CMS endcap calorimeter, given its potentially better tolerance to radiation. Two Quartic detectors fit inside a cylindrical Roman Pot, providing a combined resolution of the order of 20 ps. The Quartic baseline is presented in Section 5.2.

The relatively high fraction of nuclear interactions in the quartz bars prevents the use of more than two Quartic detectors per spectrometer arm. In order to reduce the amount of the dense material, we explore the possibility of complementing the Quartic measurement by using a short ($\sim$ 10 cm) Gas Cherenkov Time-of-Flight detector (GasToF) inside a second, upstream, cylindrical RP. The GasToF detector with a multi-anode MCP-PMT may be able to time individual photoelectrons to achieve multi-proton capability. Combined with the Quartic measurements, this additional detector could allow to approach the 10 ps time resolution. While GasToF prototypes have been built and validated, there are not yet test beam results confirming the multi-hit performance predicted from simulation. The possible use of GasToF in the experiment is therefore dependent on successful test beam results with final prototypes. The GasToF option is described in Section 5.3.

Both the Quartic and GasToF detectors have a relatively small number of channels and produce electrical pulses with similar characteristics. Therefore the proposed readout system, based on two well known integrated circuits (the amplifier-discriminator NINO and the High Performance time-to-digital converter HPTDC), can be used by both detectors. This solution offers a potential for possible future upgrades as new improved versions of the HPTDC and of the NINO chips are already in the pipeline. A reference clock system, complementary to the CMS timing system, provides time synchronization with less than 1 ps jitter between the detectors in opposite arms. Sections 5.4 and 5.7 describe the Cherenkov readout system and the reference timing system, respectively.

In parallel we intend to pursue the R&D on solid state options for timing, in particular diamond sensors and silicon sensors with avalanche gain. There are still many challenges to overcome before any of these options become a viable timing detector for CT-PPS. This includes the improvement of the intrinsic detector resolution, the demonstration of resistance to radiation, and the development of suitable low

noise and fast electronics. Prototypes will be built and evaluated in test beams. The small area, and therefore cost, of the timing detectors allows to foresee the replacement of the CT-PPS timing baseline when a better solution is available. The solid state options and respective R&D plans are described in Sections 5.5 and 5.6.

5.2 The baseline Quartic detector

5.2.1 Cherenkov detectors for timing

Cherenkov light is prompt and therefore ideal for fast timing, although the amount of light is small compared to that in scintillator. Radiators need to be transparent, i.e. with a long absorption length $L_{abs}(\lambda)$, where λ is the optical wavelength, preferably into the ultraviolet, $\lambda \approx 200$ nm, where most photons are generated. The number of Cherenkov photons radiated is proportional to $1 - 1/n^2(\lambda)$; more completely (for charge Q = 1, and β = 1):

$$\frac{d^2N}{dxd\lambda} = \frac{2\pi\alpha}{\lambda^2}\left(1 - \frac{1}{n^2(\lambda)}\right),$$

where α is the fine structure constant.

The approximate rule for the number of photoelectrons in a typical detector is:

$$N_{pe} \sim 90\ \mathrm{cm}^{-1} \cdot \mathrm{L(cm)}\ \sin^2\theta_{ch} \sim 50\ \mathrm{cm}^{-1},$$

which gives about 200 photoelectrons for a quartz detector of length 40 mm, to be scaled by a factor for the acceptance of the photons.

The light is emitted along the particle's path in a cone with half angle (Cherenkov radiation angle) θ_{ch} given by $\cos(\theta_{ch}) = 1/n(\lambda)$. We have developed fast detectors with both gas and solid radiators. The gas Cherenkov detector, or GasToF, is described in Section 5.3. The Cherenkov light is much smaller than in a solid radiator but is very collimated. It is detected with a MCP-PMT, and by timing individual photoelectrons one can measure the time of more than one proton from the same bunch crossing.

Among solid radiators, fused silica, SiO_2, or quartz (ultraviolet grade, UVT) is commonly used, and it is chosen as our baseline material. As $n(\lambda) \sim 1.48$, there is much more light per cm than in a gas, but since $\theta_{ch} \sim 48°$, the light does not arrive as promptly, and fine segmentation, in our case with quartz bars, is limited. The refractive index of quartz varies from 1.455 at λ = 700 nm to 1.475 at λ = 350 nm. The corresponding Cherenkov angles are 46.6° and 47.3°. Over this wavelength range the optical absorption length of quartz is $>$ 110 cm. The density of quartz is 2.20 g·cm^{-3}, the radiation length is 12.3 cm and the interaction length λ_I = 44.5 cm.

We have developed detectors [8] with quartz bars of 3 × 3 mm^2 cross section in the form of an "L", called L-bar Quartic (Quartz TIming Cherenkov), the light being detected with SiPMs. This configuration allows segmentation in both x and y. The photodetectors are located at $\sim$ 8 cm from the beam in the horizontal plane and can be partially shielded to reduce their radiation dose.

5.2.2 Quartic design for Roman pots, with L-bar geometry

In the Quartic design there is an array of 3×3 mm^2 "radiator bars", R, parallel to the beam. The Cherenkov angle is the complement of the critical angle for Total Internal Reflection (TIR) on the bar sides, and as the proton paths are almost exactly parallel to the bars all the Cherenkov light is internally reflected to the back end of the radiator, as shown schematically in Figure 70. Most (about 2/3) of the light is transmitted to the SiPM along the light-guide (LG) bar , also with total internal reflection. The

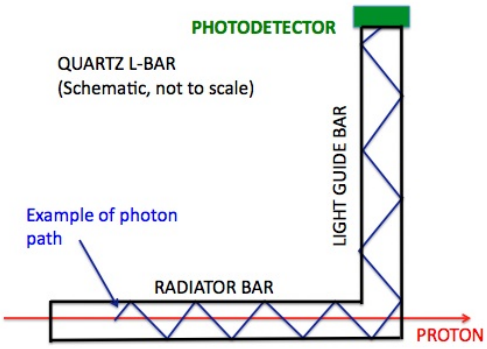

Figure 70: Cherenkov light rays in the radiator and light guide bar, for n = 1.48, in the plane of the "L" ($\phi_{ch} = 90°$).

remaining ∼1/3 is reflected back to the entrance of the radiator bar, where there will be a black absorbing surface. The LG bars end in a (vertical in the horizontal RP) plane, 73 mm from the beam pipe wall. This distance is a compromise between being away from the beam for radiation issues, and keeping the LG bars short to minimise the absorption, number of reflections, and optical dispersion. The spread of the travel time of the photoelectrons is mainly caused by the length of the radiator bar. The component of the speed of the light along the radiator bar is $dz/dt = c/n^2 \sim 0.140$ mm/ps.

Sapphire, Al_2O_3, has a higher refractive index, $n \sim 1.78$ and hence about 27% more light per cm, however it is denser and has a shorter nuclear interaction length (λ_I = 24.8 cm cf 44.5 cm). To minimize interaction issues we choose quartz. Our baseline is to have two Quartic modules per arm, in one RP. The second RP foreseen for timing detectors can be used for housing a GasToF (Section 5.3), or solid-state timing detectors (Section 5.5). In both cases, the alternative timing detectors will be installed upstream of the Quartics, to provide complementary time measurements. Detailed studies of the Quartic and other timing detectors can be found in Refs.[3, 8, 9, 10, 11].

Figure 71 shows the design of a test module, with two 30 mm and two 40 mm bars in line, used in beam tests at Fermilab [8]. The beam comes from the right, and the two SiPM boards, each with two SiPMs, are at the top in the figure. The radiator bars were separated by 100 μm wires and held in place by plates with narrow ridges such that they only minimally touch the bars. The distance between the LG bars was dictated by the borders of the SiPMs. It results in different R-bar and LG-bar lengths. SiPMs with thinner borders ("buttless") are becoming available and could reduce this spread in lengths. A feature of the design is that protons through the shorter R-bars, farther from the beam, also traverse the LG-bar of the longer bars. Half of the Cherenkov light emitted in LG bars is totally internally reflected to the SiPM; In the case of a single particle in the detector from one bunch crossing the extra signal can be used, but in the case of two or more protons it has the undesirable effect of reducing the efficiency. The results of these beam tests are described in Section 5.2.7.

We then made a module with an 4×5 array of quartz bars with an "edgeless design", appropriate for a MBP. This was valuable in enabling us to solve many practical issues arising with a compact, edgeless array. Beam tests (not expected to show different resolution from the earlier two-bar module) showed light leakage between the bars, resulting in reduced efficiency, and leading us to increase the inter-bar spacing from 100 μm to 200 μm for the actual device. Since the first stage of the CT-PPS project is to use horizontal RPs, we modified the Quartic design. The RPs assigned for the timing detectors have longitudinal space 140 mm and the Quartic detector is designed such that two can fit in one RP. It should be noted that while multiple scattering of the protons is not an issue, as the tracking stations are upstream, the effect of inelastic interactions can be important. If an inelastic interaction occurs the signal in that and any following detectors is likely to be large and spread out in time, as well as not being confined to one bar.

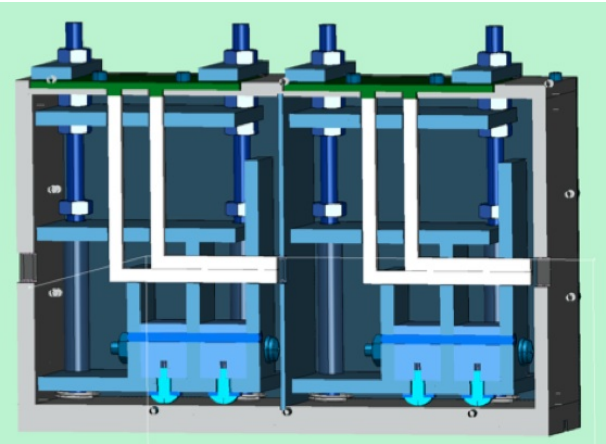

Figure 71: Design of an L-bar box with two modules, each with two L-bars, as used in the tests. The beam comes from the right, and the SiPMs are at the top.

The CT-PPS Quartic "module" is a light tight box with a very thin ($\sim$ 100 μm) side wall on the beam side, and blackened interior. This side wall may be removed on insertion in the pot as the interior will be dark; it is to protect the inside prior to insertion and to optically close the box for beam tests. One module consists of (4$\times$5 = 20) independent 3$\times$3 mm^2 bar elements. This allows a time measurement of two or more protons from the same bunch crossing (which has a time spread $\sigma_t \sim 150$ ps) if they are in different elements. The active area is 12.6 mm (vertically, y) $\times$ 15.8 mm (horizontally, x). This includes 200 μm spacers (a wire grid) to separate the bars, allowing total internal reflection, and avoiding light leakage. The dimensions of the bars are given in Figure 72. The ends of the light guide bars arrive at an array of SiPMs, coupled with a thin silicon "cookie" for good optical coupling. We use SiPMs Hamamatsu MPPC Type S12572-050 mounted in a flat plate holder (3D-printed plastic). The SiPMs fit in rectangular holes in the plate and as they are not fixed to the read-out board they can be very simply replaced. The SiPMs are connected to the read-out board through an anisotropic conducting sheet (embedded very short wires give an electrical connection through the sheet but not in the plane).

Figure 73 shows isometric views of a module. The front view shows the 4 (in y) $\times$ 5 (in x) bar array, and the top view shows the position of the LG bars (in precise round holes in a plate). The side view shows a removeable inspection plate, not needed inside the pot. Figure 74 shows the design of the SiPM read-out board.

Figure 75 shows a 3D view of the module. It is 68 mm long, so that so that two modules can be installed in one RP (140 mm in z). The U-shaped holder near the front of the bar-array, holds them in place with screws applying a little pressure, but only touching along a (3D-printed) "knife edge". The bars are separated from each other (and from the bottom of the pot) by a 200 μm wire grid. A similar frame will position the LG bars, which also pass though a 3D-printed positioning plate. The bottom plate (not shown in this figure) is not structural and can be removed. The complete block of bars is inserted as a unit (with temporary clamps) from that side.

The bars pass through circular holes for locating the bars against the SiPMs, with better than 25 μm accuracy. These holes are countersunk, as the 20 bars all have to be inserted together. The U-clamp is then tightened and the temporary clamp removed. The complete bar assembly is then slid into the box on precision grooves; the front window is placed in position later, after position and optical checks are done. Figures 76 and 77 show the assembly of two modules in one RP. We have the option of displacing one module in x, y with respect to the other by 250 μm (e.g.) to avoid any dead regions between the bars. Alignment of the radiator bars parallel to the protons (at the level of $\lesssim$ 10 mrad) will be needed to maximise light collection and avoid light leakage into neighbouring bars.

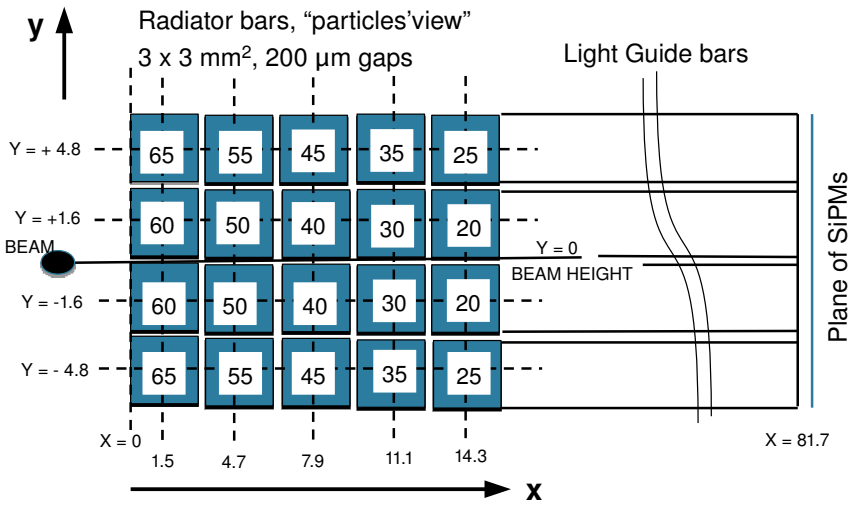

Figure 72: Schematic layout of quartz bars looking in the direction of the protons. Numbers on the 3 x 3 mm^2 radiator bars are their lengths in mm, and coordinates (mm) are the centers of the bars. The light guide bar lengths are chosen to all end in a common plane 81.7 mm from the edge closest to the beam.

5.2.3 Photodetectors: Silicon photomultipliers

Silicon photomultipliers, SiPMs, are solid state photon counters comprised of a large number of avalanche photodiodes (APDs) or "pixels" of order 20 μm dimensions, with a high gain (up to 10^6) in Geiger mode, with an applied voltage just above the breakdown voltage (about 30V to 70V depending on the type). Each discharged pixel has a recovery time of $\sim$50 ns, but with e.g. 100 photoelectrons per event and thousands of pixels per mm^2 this is acceptable with 25 ns bunch-crossing time. For the SiPMs, the single photon detector efficiency is the product of the quantum efficiency and the fractional area coverage of the APDs. SiPMs are rugged, simple to use and relatively cheap per unit, but at present are only available commercially with effective active areas from 1×1 mm^2 to 3.5×3.5 mm^2. Smaller SiPMs have less capacitance and are intrinsically faster.

The SiPMs, Hamamtsu MPPC type S12572-050 (Figure 79), operate at $\sim$72V, just above the breakdown voltage (they operate in Geiger mode, discharging one or two pixels per detected photon). These have 3600 pixels of 50 μm diameter. The single photon detection efficiency and the wavelength-dependence of the response is shown in Figure 80. Improved efficiency in the UV is being investigated. Individual HV values can be applied to each SiPM, and their leakage currents monitored through a high-resistance (6.4 MΩ) bleed resistor to ground. While the gains of SiPMs are very sensitive to temperature, the time resolution is not. Air cooling is expected to be sufficient; an alternative is to use the same cooling system as for the tracking detectors. The temperature of the SiPM boards will be monitored with thermistors. The SiPM board receives an individually controllable bias voltage $\sim$72V from a local programmable supply. The signals are read out with miniature coaxial cable with SMA connectors.

5.2.4 Integration with Roman Pots

The longitudinal space in the RPs is approximately 140 mm. The L-bar geometry allows installation of Quartic two modules in one RP (Figures 76 and 77). The two modules in a pot will be fitted together

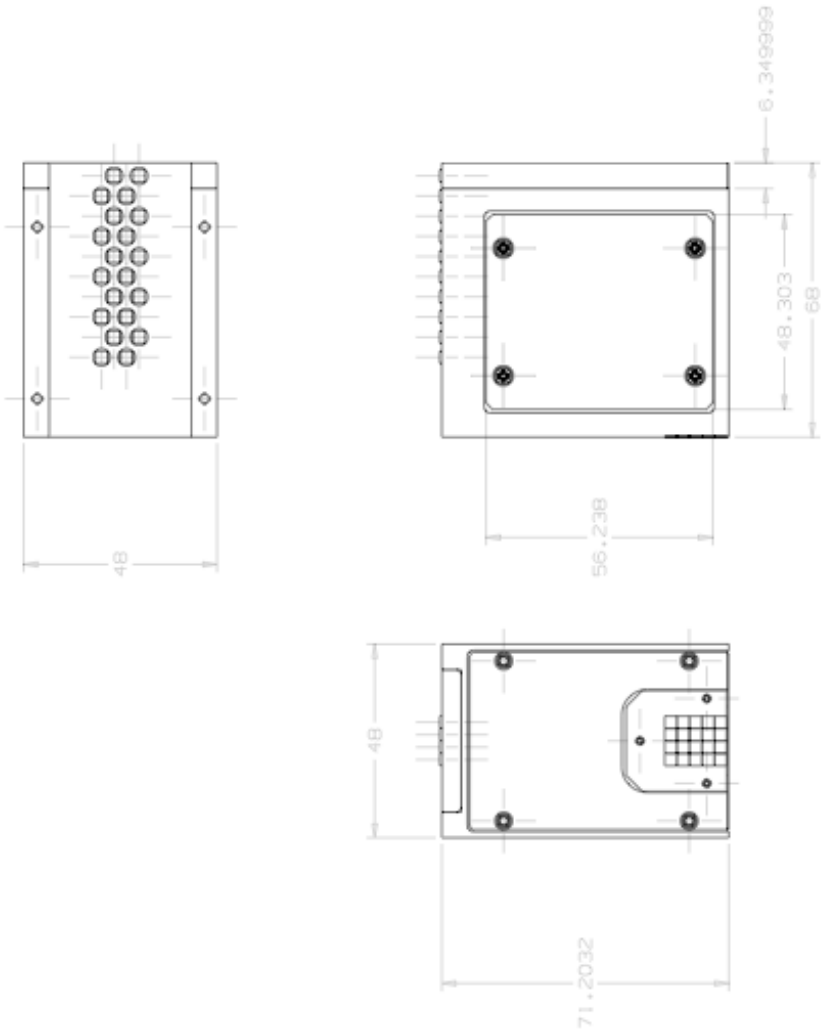

Figure 73: Design of the Quartic module for the Roman pot. The bottom right figure is the front (proton's) view, with the beam to the right. The top left shows the light guide bars at the SiPM plate.

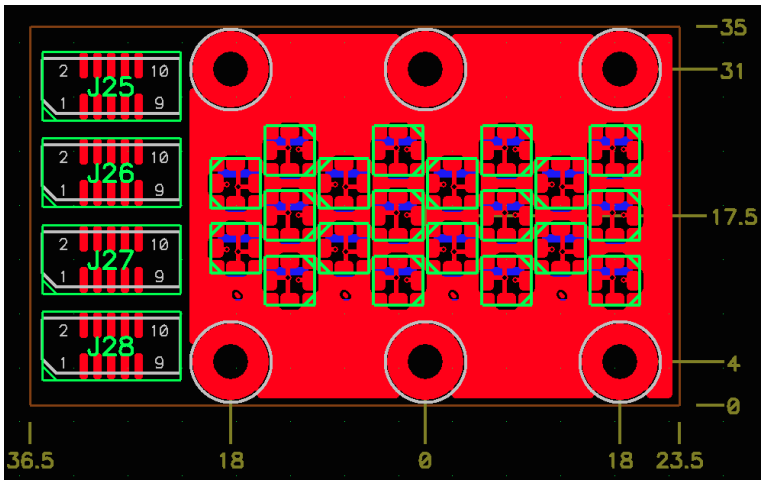

Figure 74: Design of SiPM readout board (s.Los). Three of the multi-way connectors J25 - J28 are for the high voltage and one for monitoring leakage currents and temperature.

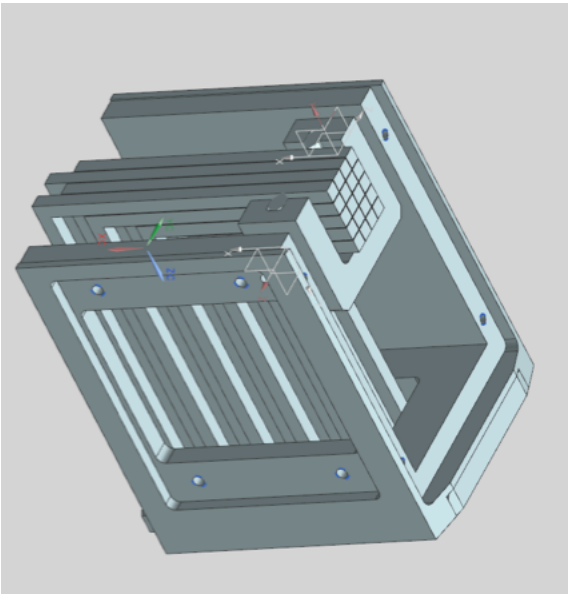

Figure 75: Design (B. Ellison, FNAL) of module for insertion in Roman pot (two in one pot).

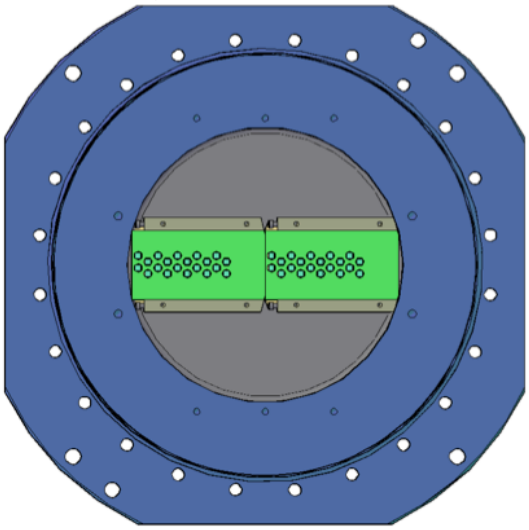

Figure 76: Assembly of two Quartic modules in Roman pot.

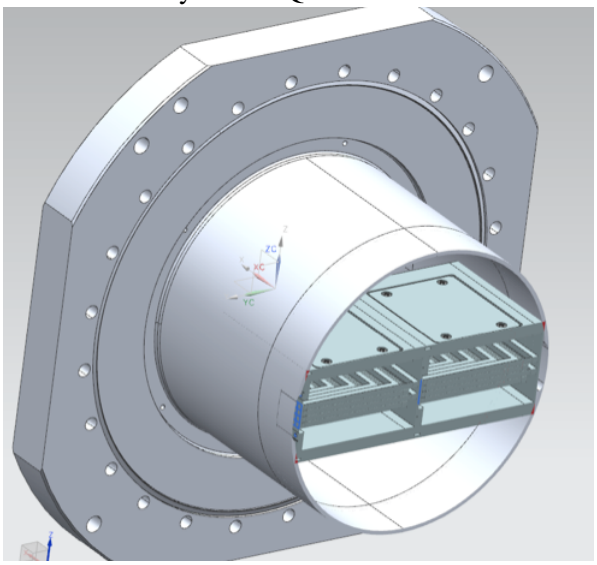

Figure 77: Assembly of two Quartic modules in Roman pot. The beam comes from the left.

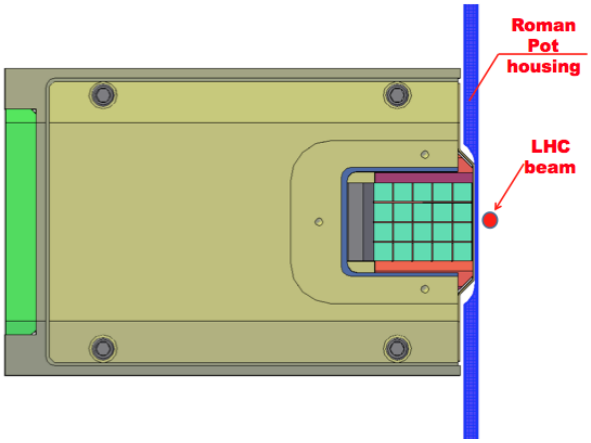

Figure 78: "Particle eye view" of bar array in pot. This is a modified design (D.Druzhkin) reducing the material close to the beam.

precisely using dowel pins.

Figures 73 and 75 show the design of the module for insertion into the horizontal RP. A slightly modified version (Figure 78) reduces the material close to the beam. The protons enter through a thin window (nominally 100 μm aluminium, but it has no mechanical purpose, it is for absorption of reflected light and light exclusion). The array of radiator bars is clamped on the three sides away from the beam with a plastic U-clamp, touching each bar only along a fine line. For assembly of the bar array a 4-sided clamp is placed temporarily around the front of the array. The SiPM plate and read-out board are precisely positioned by dowels with respect to the L-bar positioning plate.

5.2.5 Monitoring, alignment, and *in situ* calibration

The rates in each bar are monitored both online and offline. The rates are expected to be up-down symmetric about the beam height (as can also be determined from the tracker), column-by-column. This gives a measure of the centre of the beam in y, assuming the backgrounds are relatively small. For a given row in y the rates will fall with x with two components: protons from collisions and beam halo background. The former will be compared with predicted t-distributions, and it is valuable to measure the latter. When the RPs are inserted at the beginning of stores the rates will be carefully monitored, e.g. partially withdrawing in the event of an abnormal increase.

Initial relative alignment of the Quartic bars and tracker will be achieved by matching the individual bar edges in x and y with the track distributions.

A pair of light-emitting diodes will be mounted inside the module in such a way that some light is captured in each bar. This will be pulsed when there is no beam as a control of all the SiPMs and their readout.

Occupancy of the bars will be monitored in real time, as functions of the instantaneous luminosity and background conditions. Geometrical matching between the bar array and the trackers will also be measured; the 200 μm gaps between the bars can also provide a check.

A calibration of the absolute time difference between the protons, Δt_{pp}, can be derived by matching $z_{pp} = z_X$ using real events of the type $p + p \to p + X + p$, where X is a set of particles measured in the central detector. After kinematic matching of X to the protons (four-momentum conservation) the 2D plot of z_{pp} vs z_X will show a ridge which calibrates both $z_{pp} = 0$ as well as checking the time scale.

While the time difference between the "left" and "right" protons, $t_L - t_R$, gives z_{pp}, the time sum, or $(t_L + t_R)/2$ (minus a constant), would provide another, orthogonal, variable for pileup rejection if the

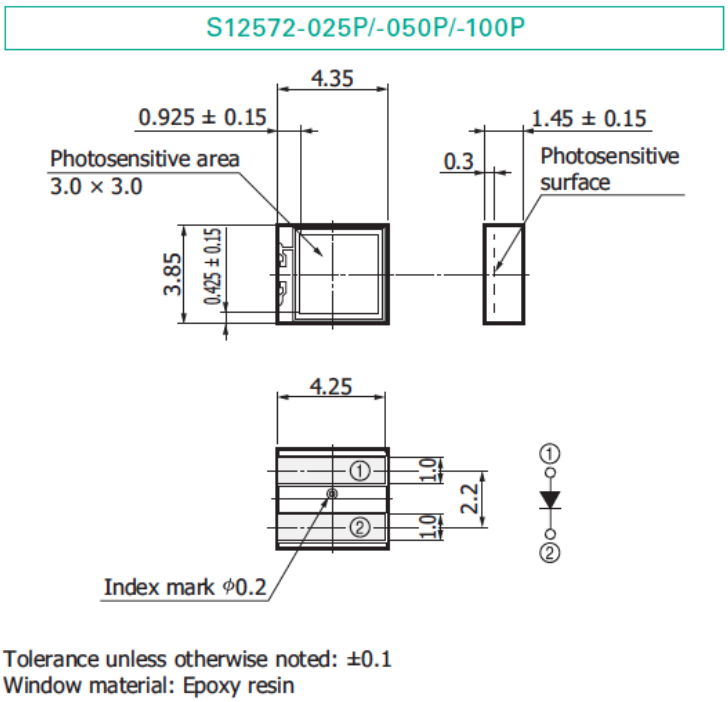

Figure 79: Details of Hamamatsu MPPC (SiPM) S12572-050.

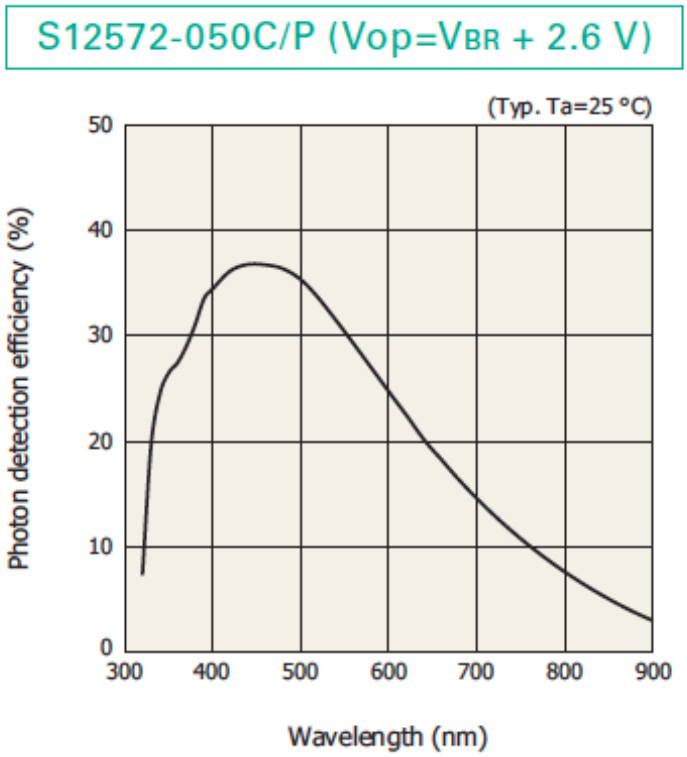

Figure 80: Photon detection efficiency of Hamamatsu S12572 SiPM. This is the product of the quantum efficiency and the fill factor (50 μm pixels).

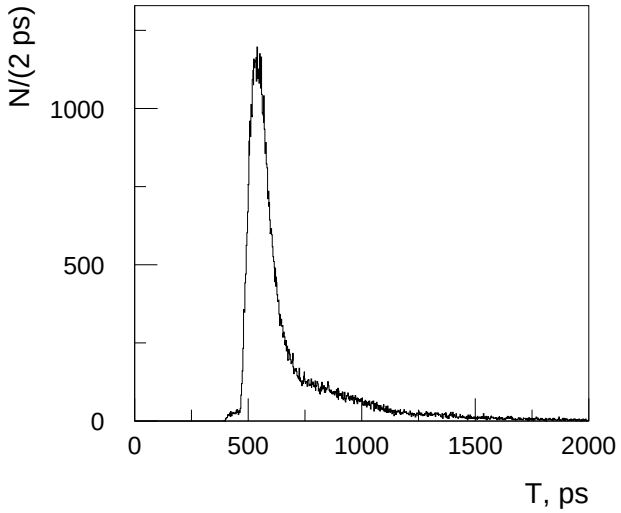

Figure 81: GEANT4 simulatios showing the arrival time distribution (1 bin = 2 ps) of Cherenkov photons at the SiPM for a quartz L-bar with 20 mm radiator length and 40 mm light guide.

actual event time were known much better than the spread in collision times, ∼150 ps.

5.2.6 Monte Carlo (GEANT4) simulations

We use GEANT4 to simulate the behavior of the L-bar configuration. Cherenkov photons are generated along the proton path with wavelength-dependent refractive index $n(\lambda)$ and transmission $T(\lambda)$ of fused silica. The emission polar angle θ_{ch} is determined by the refractive index $n(\lambda)$, with $cos(\theta_{ch}) = 1/n(\lambda)$, and ϕ_{ch} is the azimuthal angle around the proton. The propagation of the optical photons takes into account the surface and bulk properties of the bar (wavelength-dependent photon speed and absorption). In the interval $250 < \lambda < 600$ nm about 450 Cherenkov photons are emitted per cm of radiator. We estimate the distribution of the photons arrival time at the SiPM, as a function of λ. This spectrum is then convoluted with the single photon detection efficiency to simulate the photoelectron time distribution. For each photoelectron, a Gaussian time spread with width given by the single-photoelectron time resolution is generated and summed, to simulate an output signal. We measure the time (from the proton arrival time) when the signal is at least 50% of the initial signal amplitude.

The coupling between the bar and and the photodetector is a potential source of inefficiency. In the test beam studies grease was used, but it is difficult to simulate it correctly. In the simulations we applied an overall efficiency factor to account for both reflectivity and coupling losses to match with test beam data.

The surface reflectivity of the bar is an important factor. In a 60 mm LG bar of 3×3 mm^2 cross section one has typically 35 reflections and, if the average internal reflectivity is 98%, only 50% of the light reaches the photodetector. Furthermore the leaking light can give undesirable cross-talk between the bars. We aim for close to 100% internal reflectivity.

Figure 81 shows the estimated arrival time distribution for photons that produce photoelectrons from a 20 mm radiator bar, with a 40 mm long light guide. The fast leading edge corresponds to photons emitted with azimuth angle $\phi_{ch} \sim 90^\circ$ close to the LG bar direction, and the tail of the pulse corresponds to other ϕ_{ch} angles that have more reflections in the LG. The small delayed pulse is caused by photons that are not immediately trapped by the LG bar, are reflected back to the entrance of R and return.

Figure 82(a) shows the simulated mean pulse height as a function of the radiator bar length, assuming

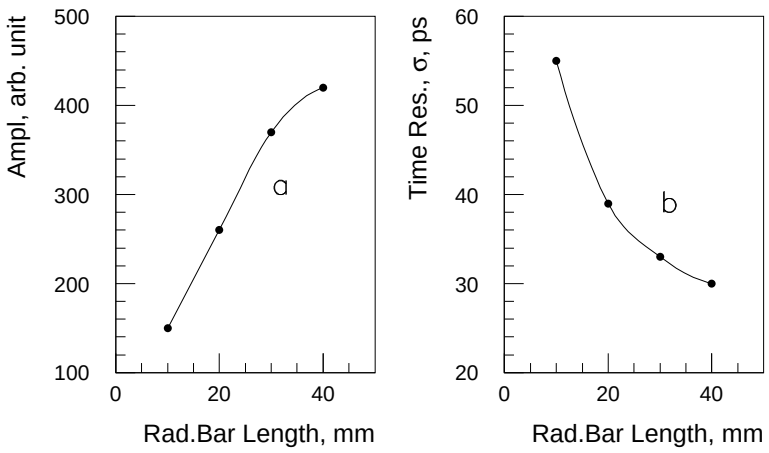

Figure 82: a) GEANT4 simulation of the pulse height (arbitrary units) of the L-bar as a function of the radiator bar length. (b) The simulated time resolution as a function of radiator bar length R. The LG bar is 80 mm and the average reflectivity is 99%.

99% reflectivity at all surfaces, and Figure 82(b) shows the estimated time resolution. The LG bar lengths were 80 mm. While the actual resolution depends on some factors that are not well known (e.g. reflectivity and coupling to the photodetector), the qualitative behaviour of a rapid improvement from R = 10 mm to 25 mm, followed by a slower improvement, is as expected.

The surface reflectivity R_s of the bars is an important factor. A long light guide bar allows the SiPM to be located in a lower radiation field and where it can be better shielded. The simulations showed that with R_s = 0.98 the resolution is σ_t = 39 (30) ps for R = 20 (40) mm. This is very similar to what was found in the beam tests (see below). TIR would be even more critical with smaller cross section bars, as the number of reflections is $\propto 1/w$, with w the width of the bar. As we expected, the detector simulation shows the efficiency to be uniform over the 3 $\times$ 3 mm^2 aperture.

The full transmission of the Cherenkov light along the radiator bar depends on the perfect matching between the Cherenkov angle and the (complement of the) total internal reflection angle. A small angle between the proton direction and the radiator bar axis will allow some light to leak out. We simulated this; e.g. with a radiator bar length of 40 mm and an angle of 1/40 = 25 mrad = 1.4° in the plane containing the LG, 20% of the light is lost. In the CT-PPS the accepted protons have an angular spread of $<$ 0.5 mrad, but precise alignment is clearly very important.

5.2.7 Beam tests

A prototype Quartic with L-bars was tested in the Fermilab test beam, with 120 GeV protons, using a mechanical design that does not include some features needed for the CT-PPS version. See Ref. [8] for more details of the test procedures and results. This test module was not edgeless and had two pairs of bars (separated by only 100 μm) rather than a 4$\times$5 block. Two identical modules (Figure 71) were placed in line, such that a proton traverses four bars, either 30 mm or 40 mm long. The quartz bars were supplied by Specialty Glass [12]. The photons were detected in a 3$\times$3 mm^2 SiPM, the Hamamatsu MPPC S10931-050P with bias 72V. The signals were output on SMA connectors. We used a clipping capacitance (9.1 pF) to shorten the pulse, followed by an ORTEC VT120 $\times$20 preamplifier.

The beam was defined by a 2$\times$2 mm^2 trigger counter, and a Photek PMT240 MCP-PMT at the back provided a reference time signal with $\sigma_t \sim$ 8 ps. Figure 83 shows the signals recorded in a 5 GS/s DRS4 waveform digitiser for a typical event. The top three traces are the SiPM signals of three 30 mm

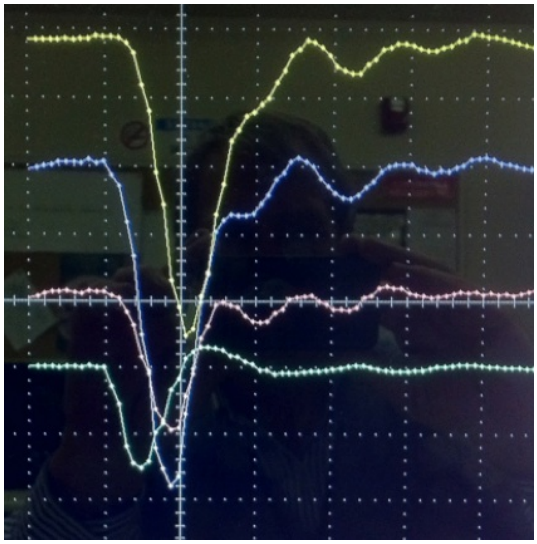

Figure 83: Waveforms in the DRS-4 of one proton through three L-bars and the PMT240 (bottom trace). The time scale is 2 ns/div and the vertical scale 20 mV/div for the top three traces (SiPM's) and 50 mV/div for the bottom trace (reference PMT240).

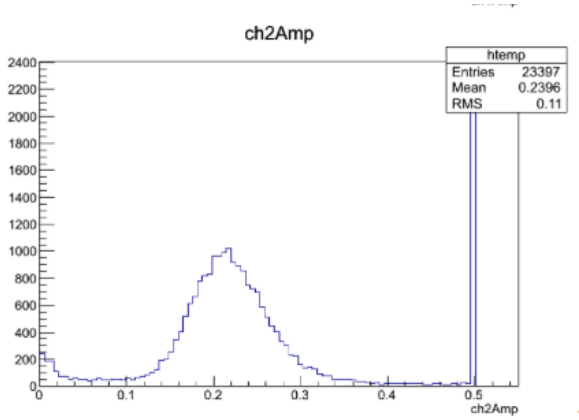

Figure 84: Pulse height distribution in a 40 mm radiator bar. The overflow is due to interactions.

Cherenkov bars, 20 mV/div, 2 ns/div (200 ps per sample), joined by straight-line segments, and the bottom trace (50 mV/div) is the PMT240 reference signal. Typical pulse heights are about 80 mV with an 800 ps risetime. Figure 84 shows the pulse-height distribution for one bar, consistent with $N_{pe} \sim 50$. The entries in the overflow bin are due to interactions, upstream or in the bar. Good timing measurements were obtained by a linear fit to the two points before and after the 50% of pulse maximum amplitude, finding the time at which that line crossed the 50% level, and then applying a time-slewing correction. More complete waveform fits were found to be not significantly better.

From the spread in signal amplitudes we estimated that the number of photoelectrons is $N_{pe} \sim 80 - 100$. Figure 85 shows, after applying pulse height-slewing corrections, the time difference between one bar and the reference time signal, with a time resolution of $\sigma = 35.3$ ps. After unfolding the electronics and reference time resolutions, the time resolution of the 30 mm bars was $\sim$ 33 ps. Alternatively, without using the PMT240 reference time but comparing the different bar times we found σ_t = 31 ps. We plan to have two modules in-line in one pot, which are expected to give a time resolution of 21 ps.

After these corrections, the time differences between the four short bars and the reference PMT240 signal had widths, from Gaussian fits, σ_t = 35 - 40 ps, with $\langle \sigma_t \rangle$ = 37.5 ps. Figure 85 shows one example, with $\sigma(\Delta t)$ = 34.9 ps, showing no background or inefficiency. The single-photon time resolution of the SiPM

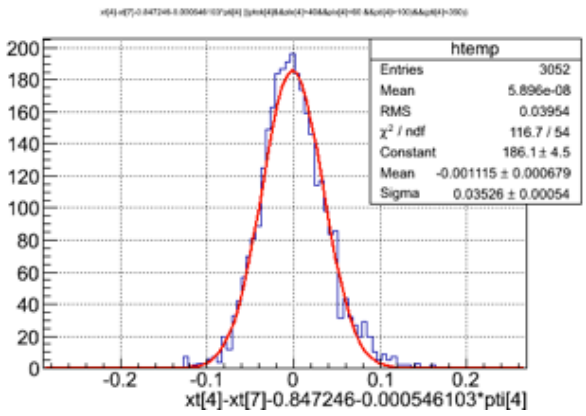

Figure 85: The time difference between one L-bar (30 mm radiator, 40 mm light guide, Hamamatsu MPPC type S10362-330050C) and the reference time signal (PMT240 in beam). It shows σ = 35.3 ps.

we used is quoted by Hamamatsu to be $\sim$ 300 ps; giving an expected time resolution for 100 p.e. of 300 ps/$\sqrt{100}$ = 30 ps, in reasonable agrement with the observations.

5.2.8 Future developments

We have described the baseline Quartic detectors, which could be ready for installation in 2015 when the RPs have been installed and commissioned. Several potential improvements will be investigated. These include finer segmentation, especially near the beam, a more compact SiPM array ("buttless" type), and the use of a multi-anode MCP-PMT in place of SiPMs. The latter have had photocathode lifetime problems limiting their use in such a high-rate environment, but developments to mitigate that are encouraging.

Also, faster SiPMs with higher photon detection efficiency and possibly more sensitivity in the UV may become available, potentially allowing easy replacement.

SiPMs from STMicroelectronics (STM) with new P-on-N structure (rather than N-on-P SiPMs, also from STM) show significantly better timing properties [9] *. Tests with a PiLas (Picosecond Injection Laser) showed the photon detection efficiency at λ = 405 nm, 5 V above breakdown voltage (28 V), to be 43% higher (31.1% cf 21.7%). Also the SPTR, is 174 ps cf 231 ps, i.e. smaller by 25% than for STM N-on-P detectors. Together these improvements lead one to expect that the single bar resolution can be improved from the measured 32 ps to $\sim$20 ps.

Unlike the large central CMS detectors, due to the small number of channels, upgrades to the timing detectors can be considered on a yearly timescale, and we expect to continue the necessary R&D. Also, if timing detectors based on other principles, e.g. solid state detectors, demonstrate good performance and acceptable properties (e.g. radiation hardness) they can supplement, or possibly replace, the Quartic detectors.

5.2.9 Costs and timescale

Table 13 gives a provisonal cost estimate for a set of four Quartic modules, namely two modules in an RP in each arm. The completion of the detailed design of the modules, including the SiPM readout boards, can be completed within two months of funding being made available. The construction and assembly can be done within the following two months, depending on the availability of the workshop personnel.

*We thank STMicroelectronics for providing samples.

Item	unit	Number	Unit price (US$)	Total (US K$)	Comment
Quartz bars	bar	20×4 = 80	350	28	Specialty Glass
MPPC/SiPMs	(20)/module	80	80	6.4	e.g. Hamamatsu
Other components	module	4	250	1.0	
Total modules				35.4	
Low voltage	Station	2	600	1.2	
Current monitor	Central	1	2500	2.5	
Temp. Monitor	station	2	1000	2.0	
Cables					(CERN)
Shipping				<1	
Board design	person-weeks	3	4K	12	Fermi design office
Mechanical design	person-weeks	3	4 K	12	Fermi design office
Assembly	person weeks	4	4 K	16	Fermi workshops

Table 13: Provisional costs for a pair of Quartic modules, each of 20 bars, in each arm, not including DAQ. Design and Assembly costs reduce by $\sim \times 0.5$ if done outside Fermilab.

The timescale for making the quartz bars is about 8 weeks from receipt of order. The bar assembly can be installed last in the module. If funds are provided very soon, it should be possible to deliver the four modules to CERN by the end of 2014.

5.2.10 Summary of Quartic detectors

The L-bar Quartic design satisfies the requirements of edgelessness (within about 100 μm), sufficient radiation hardness, ability to measure several protons within a bunch crossing (time spread σ = 150 ps) if in separate bars, and to be active every 25 ns (the bunch separation). We plan to construct and install a pair of L-bar Quartic modules, with SiPM photodetectors, in a RP on each arm, and use them in 2015 to assess their performance in realistic conditions, as well as for physics in the low pileup runs. The modules will be constructed at Fermilab and the signals from the SiPM board sent to a local DAQ (which will be the responsibity of the Lisbon Group).

Further development will continue to improve their time resolution and possibly the spatial segmentation. Therefore R&D will continue, and improved versions could be ready for installation at the end of 2015.

5.3 Gas Cherenkov detector

GasToF is a gas Cherenkov detector with direct detection of the very forward light cone, without use of internal reflections. It is intrinsically very fast, providing excellent time resolution, even with single photons. Since in its standard configuration the Cherenkov light is simply reflected by a thin, flat 45° mirror onto a photocathode of a Micro Channel Plate photomultiplier (MCP-PMT), its optics is trivial thanks to the small chromatic dispersion and the very small Cherenkov angle in gases. This also makes it

robust, without active elements in the highly-irradiated volume, while introducing a very small amount of material, and hence little multiple scattering and nuclear interactions. The radiator is the relatively dense, inert C_4F_{10} gas with refraction index $n \sim 1.002$, with the Cherenkov light spectrum peaking in the deep UV (~ 200 nm). To provide a uniform performance to its edge the thin side wall is also reflective. All the other inner walls of the GasToF will be blackened to ensure a good directionality (only a few degrees) of the detector. Together with a relatively large particle velocity threshold this makes it immune to stray, soft backgrounds. Finally, by changing the gas pressure one can vary both the light-cone angle and hence the amount of Cherenkov light.

Numerous tests with the fastest single-anode MCP-PMTs confirmed that the GasToF performance is eventually driven by the photodetector transit-time spread, and demonstrated an ultimate time resolution of $\sim$ 15 ps for single-photoelectron signals, using the Hamamatsu R3809 6 μm pore devices [2]. However, such single-channel detectors are not capable of dealing with multiple, simultaneous hits, unless a more expensive multi-anode solution, with appropriate electronics, is used.

For the CT-PPS high luminosity running a new GasToF design is proposed using the Photonis XP85112 8×8 anode 10 μm pore MCP-PMTs with a 35 ps transit-time spread [13]. In Figure 86, a perspective view is given of a baseline GasToF detector with 12 cm "optical" length and this 64-anode tube.

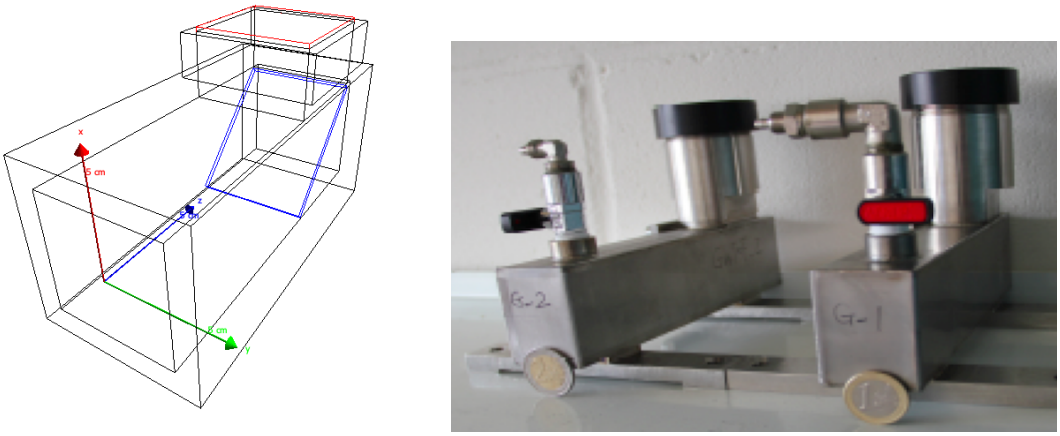

Figure 86: GasToF view (left) generated by its G4 simulation package, assuming 12 cm optical length (= distance between the entrance window and deep UV mirror) and a 53×53 mm^2 photocathode 6 cm above the detection plane. (Right) Photograph of a couple of single anode GasToF detectors used for the beam tests [2].

To ensure high efficiency in the deep UV, beneficial for the photocathode lifetime, a special MgF_2 coated mirror is used, as well as a fused silicon, UV-transparent PMT window (see Figure 87). In addition, a new technology of producing MCP-PMTs based on atomic layer deposition, thanks to very low ion emission in microchannels, ensures high lifetime for this device. Better than 6 C/cm^2 maximal accumulated anode charge per photocathode area has been observed by the PANDA collaboration (Figure 88).

A 12 cm long GasToF detector filled with the C_4F_{10} at 2 atm will typically produce a signal of 7 photoelectrons for one high-energy proton, once the photoelectron collection efficiency (CE) is taken into account. In Figure 89, an averaged distribution of photoelectrons at the photocathode placed 12 cm above the detection plane is shown. One should note that such a detector could be installed both in a MBP pocket, as well as in a RP (after changing its configuration to a side-reflecting one).

On average the signal of 7 (collected) photoelectrons is spread out over about 25 channels (i.e. anodes), resulting in a low ($\sim$ 30%) average channel occupancy. Even two protons which are perfectly colinear can be well measured, almost without affecting each other, if they are separated in time by $\gtrsim$ 50 ps. The single channel occupancy, while running the CT-PPS, will be significantly lower – the design will be

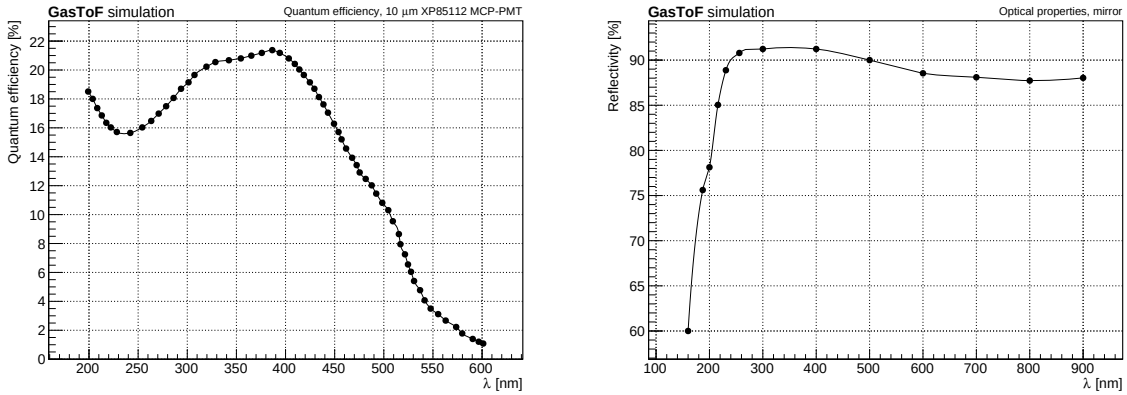

Figure 87: (Left) QE of the XP85112 MCP-PMT with a fused silica window; (Right) reflectivity of the MgF_2 coated mirror.

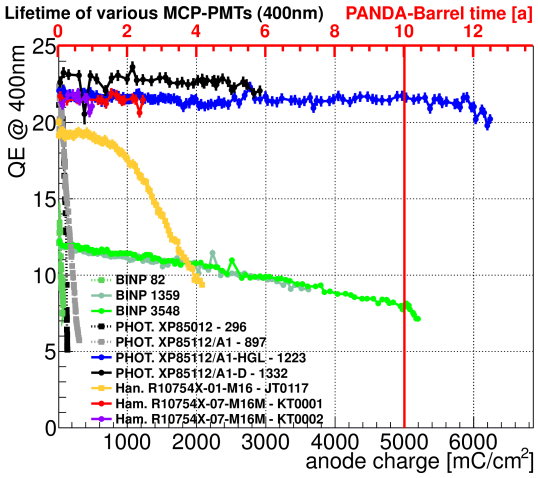

Figure 88: Quantum efficiency of different MCP-PMTs as a function of the integrated anode charge.

such that the highest single channel occupancy is about 10%, making the detector capable of efficiently dealing even with triple hits. This low occupancy will be achieved partly by the spatial distribution of incident protons, as well as by varying the photocathode position and/or by deforming the mirror slightly, in order to distribute the light more widely. This low channel occupancy will also ensure the highest single channel signal rate to be <4 MHz, acceptable for the HPTDC-based readout.

In Figure 89 the GEANT4 (G4) simulated distribution of photoelectrons between 64 anode channels is shown for the protons, as arriving at the CT-PPS. It is calculated assuming a reflective wall on the beam side of the detector.

Finally, if the impact of the electronics can be neglected, the expected time resolution of a single GasToF detector is about 15 ps for a high-energy proton. This could be further improved if MCP-PMTs with a smaller transit-time spread become available.

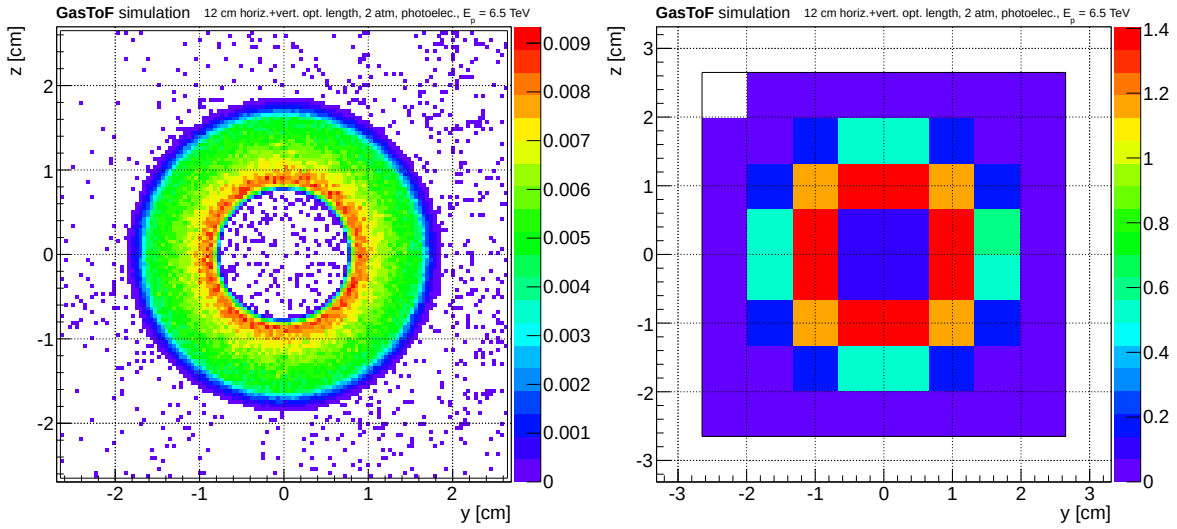

Figure 89: Example of the GasToF performance for a 12 cm detector with the gas at 2 atm, and assuming central, on-axis 6.5 TeV protons.The G4 distributions of photoelectrons (without CE) at a photocathode displaced by 12 cm, where the right plot give the average number photoelectrons 'per anode'.

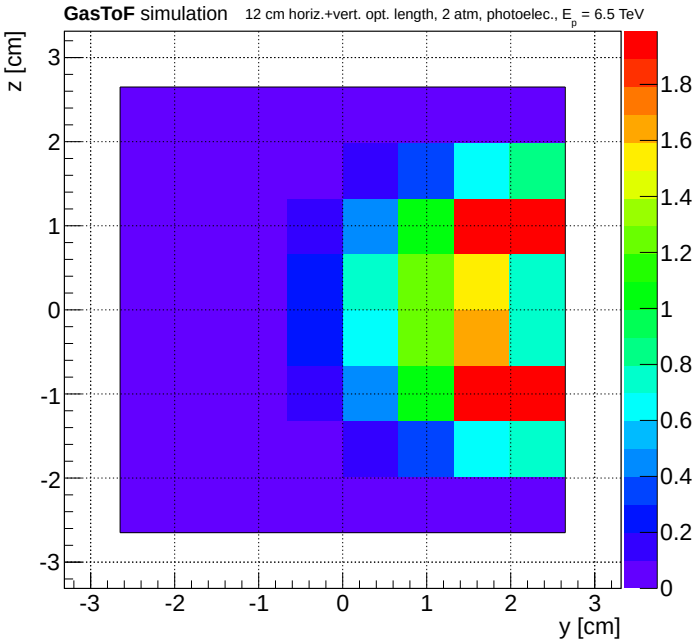

Figure 90: Example of the GasToF performance for a 12+12 cm detector (with the gas at 2 atm) for protons reaching the PPS. The G4 distribution of photoelectrons among the MCP-PMT 64 channels for minimum bias protons tracked trough the LHC beam line, assuming $\mu = 50$ - each bin represents an average number of photoelectrons (without CE) per beam collision.

5.4 Readout System of the Cherenkov Detectors

5.4.1 Requirements

The task of the readout system is to provide time and amplitude measurements of the pulses generated by the photosensors associated to the Cherenkov detectors, and to transmit the digitized data to the data acquisition system. Given the similar characteristics of the Quartic and Gastof detectors, the readout system is expected to be suitable for both detectors.

The Cherenkov timing detectors are composed of a number of modules installed in one or more RP (or MBP). The readout system follows the same modularity, and is composed of independent units (readout module) interfacing to the CT-PPS DAQ/Trigger system. Each readout module has 64 channels suitable for use with the baseline Quartic module (20 channels), but also with possible Quartic modules with finer granularity and with the Gastof 8×8 anode MCP-PMT.

Each electronic channel must be able to handle very fast pulses (rise time $\sim$ 1 ns) from silicon photo-multipliers or micro-channel plates. The photon yield of the Cherenkov signals per channel range from 1 photon in the case of Gastof MCP to about 100 photons in the case of Quartic. The SiPM gain is of the order of 10^6 while the MCP-PMT will be operated at about 10 times lower gain to limit the total charge collected (see Section 5.3). Therefore the dynamic range of the input signals is in the range of 20 fC to 20 pC.

The timing precision of the readout system is required to be 20 ps, which, combined with a similar precision of the Quartic detector, would yield 30 ps precision per module, and global precision (two modules) of about 20 ps. When associated to one Gastof detector, assuming 7 photoelectrons per proton and a precision of 30 ps per MCP-PMT channel, we may estimate that the readout system would provide a measurement with 15 ps precision.

The readout system is also required to provide the measurement of the input pulse amplitude. While this measurement is not directly used in the reconstruction of the collision vertex, the knowledge of the amplitude is mandatory for detector calibration, time corrections (e.g. "time-walk") and pulse pile-up rejection.

The readout system is required to have double hit resolution better than 25 ns, suitable for operation with 25 ns bunch separation without loss of efficiency, and to sustain a maximum rate of 6 MHz per channel, corresponding to a maximum channel occupancy of 20% at 25 ns LHC beam operation, averaged over all channels. While the average occupancy of the Quartic channels (3×3 mm^2 quartz bars) is 20% for average pile-up of 50 events, the highly non-uniform occupancy of the detector (the occupancy of the innermost channels reach 70%) induces a significant readout inefficiency for a number of pile-up events larger than 25. To sustain twice this value, as foreseen in Run2, a fine-granularity Quartic version will be required. In the case of the Gastof detector, a channel occupancy smaller than 20% is expected (see Section 5.3).

The readout system is required to provide on-detector L1 trigger matching, allowing extraction of the detector data in a time window around the L1 time, local event building and data transmission to the DAQ system. The data rate of a readout module, assuming readout of 10 channels after zero suppression, 3 bunch crossings time window, 32 bit event data per channel, and 100 kHz L1 rate, is estimated to be 100 Mb/s.

The timing detector readout system is expected to provide hit information and time measurement at the bunch crossing rate to be used by the trigger system. By combining the information from the two PPS arms, the L1 can estimate the z-vertex coordinate, allowing to select events in the tails of the z-vertex distribution where the pileup density is smaller. This capability would provide a reduction of the L1 rate of high cross-section processes so that it fits within the L1 rate constraints, selecting at the same time the events less affected by pileup. The trigger requirement implies the use of a low latency TDC delivering

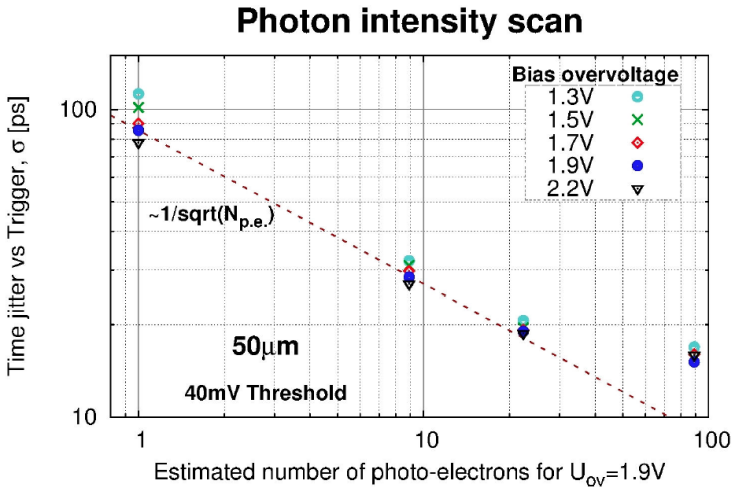

Figure 91: Time resolution of laser pulses as a function of the number of photo-electrons measured with MPPC and the NINO-HPTDC electronics chain.

conversion data at the bunch crossing rate.

In order to achieve the desired time resolution, the front-end timing electronics must be located in the RPs or a nearby region (1-2 m distance). This raises issues of radiation tolerance since the radiation levels in the RPs, in the region 200 m from IP, are expected to be 100 Gray and 10^{12} neq/cm^2 for 100 fb^{-1} of integrated luminosity. Together with machine experts, we have explored the feasibility of digging a hole in the tunnel floor concrete below the timing RPs, which would provide a substantial reduction of the radiation exposure. While this possibility is technically feasible, the proposal could not be accommodated in the present LHC LS1 schedule but would be possible if necessary in the winter technical stop 2015-16.

5.4.2 System design

The main guideline in the design of the timing detector readout system was to reuse well known components with adequate performance, allowing to streamline the design and implementation of the system so that it may be possible to evaluate the timing detectors in the LHC beam in 2015.

We have therefore decided to base our system on the amplifier-discriminator NINO and the time-to-digital converter HPTDC. Both chips have been developed by CERN's microelectronics group for the LHC experiments. The HPTDC chip is used in the CMS muon system, while the NINO and HPTDC chips are associated in the time-of-flight detector of the ALICE experiment. These chips are now widely used in many applications, including PET Time-of-Flight.

The EndoTOFPET-US collaboration [†] has studied the time resolution of the NINO-HPTDC readout chain, using laser pulses detected by 3×3 mm^2 SiPMs (Hamamatsu MPPC) with SPAD size of 50μm [14]. The measured time resolution as a function of the number of photo-electrons is shown in Figure 91. For 100 photoelectrons a resolution better than 20 ps is achieved.

The NINO amplifier-discriminator is implemented in a 8 channel ASIC. A newer version with 32 channels developed by an external group is also suitable. The time binning and number of channels of the HPTDC ASIC is configurable. In our case we use the HPTDC high-resolution mode, which provides 8 channels with 25 ps time binning. The timing readout system is designed to be integrated in the common CT-PPS DAQ and Control system, based on the CMS Pixel FED and FEC boards. The FED board

[†]This project have been funded by the European Union 7th Framework Program (FP7/ 2007-2013) under Grant Agreement No. 256984 (EndoTOFPET-US)

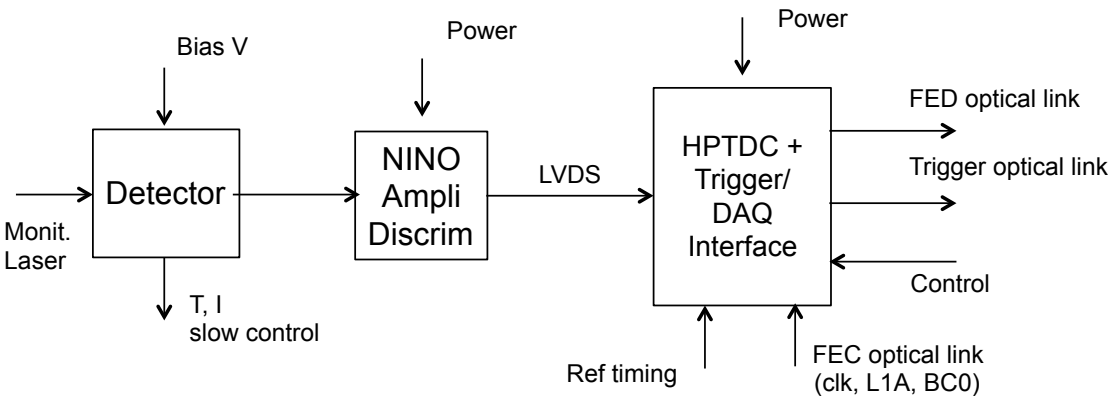

Figure 92: Diagram of the timing readout system.

provides input to 400 Mb/s optical links transmitting detector data, builds event packages and transmits them to the central DAQ. The FEC board transmits fast controls (LHC clock, L1 and fast signals) to the detector, as well as front-end configuration data. We plan to use the same components used in the Pixel detector to implement the on-detector interface to the FED and FEC board, namely the transmission and reception optical hybrids and the CCU control chips.

Physically, the timing readout system is implemented in two electronics boards (see Figure 92): 1) the frontend board, housing 8 NINO chips and installed in the RP, which receives the SiPM signals transmits the LVDS output on the feed-through connector; 2) the digital board, which receives the LVDS output of the discriminators and houses 8 HPTDC chips. The digital board integrates a radiation resistant FPGA to serve as readout controller of the HPTDC chips, and provides on-board connectors to the opto-hybrid mezzanines (PoH and DoH). If required, the digital board could be installed a few meters away of the RPs in a radiation protected place.

5.4.3 Amplifier-discriminator NINO

NINO is an 8-channel amplifier and discriminator implemented in CMOS 250 nm. Each channel is a fully differential ultra fast ($\leq$ 1 ns peaking time) preamplifier-discriminator with a minimum detection threshold that can be adjusted from 10 to 100 fC for input current pulses in the ns range. The architecture is presented into Figure 93. An input stage permits a fast current to voltage conversion and presents low input impedance (which can be adjusted from 30 to 100 Ohm). Voltage gain amplification is then provided with four cascaded identical high bandwidth differential pair amplifiers. Saturation of the signal permits to have voltage pulse information at the output of the circuit (the pulse width thus varies as a function of the total input charge). A further block permits to set a threshold for the differential amplifiers and to perform compensation of eventual offset.

The NINO circuit integrates two additional blocks that can be set active or passive from outside the circuit: a hysteresis circuit and a stretcher. The hysteresis circuit is a feedback loop placed between the outputs of the 4th and 2nd differential stages. It permits to have discrimination levels different for rising and falling edges of the comparator. The stretcher is a circuit placed between the 4th differential stage and the driver. It permits to stretch the output pulse width, so that by default the minimum pulse width is about 13 ns. This permits to use the NINO circuit together with the HPTDC chip, which can perform timing measurements every $\sim$10 ns only. The stretcher permits to measure both the leading and the trailing edges. The power consumption per channel is 32 mW and 36.6 mW for Rin = 50 Ohm and for Rin = 30 Ohm, respectively.

The NINO chip allows the readout of SiPM or MCP-PMT photosensors and therefore is suitable both for the Quartic and Gastof detectors. The double pulse resolution is better than 10 ns, compatible with the

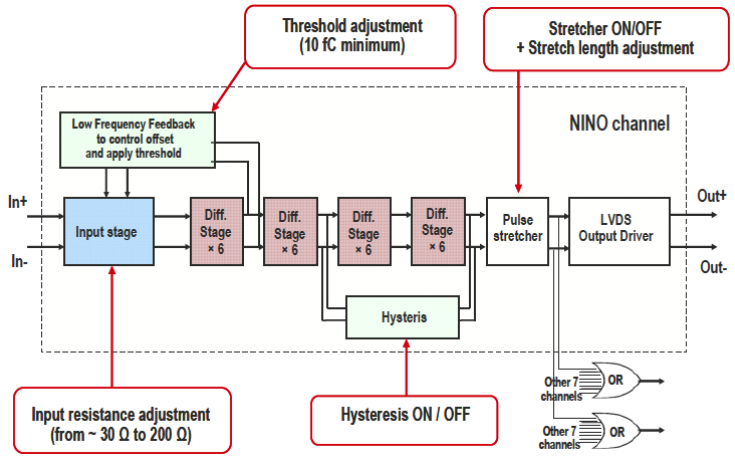

Figure 93: Block diagram of a NINO channel.

Parameter	Value
Peaking time	1ns
Signal range	100fC-2pC
Noise (with detector)	< 5000 e- rms
Front edge time jitter	< 25ps rms
Power consumption	30 mW/ch
Discriminator threshold	10fC to 100fC
Differential Input impedance	40Ω< Zin < 75Ω
Output interface	LVDS

Figure 94: Summary of main parameters of the NINO chip.

LHC bunch separation of 25 ns. The pulse width of the NINO discriminator output is equal to the time-over-threshold, and therefore is a function of the input pulse amplitude. The intrinsic time resolution of the NINO chip was measured to be below 10 ps rms (see Figure 95). Other characteristics of the ASIC are summarized in Figure 94.

The technology used in the NINO chip (IBM CMOS 0.25μm) is radiation-damage tolerant. The chip is expected to sustain up to 10^{14} neq/cm^2 without problems. The total dose may impact the sub-threshold leakage current. Radiation tests are foreseen to quantify this effect. NINO chips are available either packaged or as naked chips.

5.4.4 Time-to-digital converter HPTDC

The HPTDC was developed in the Micro-electronics group at CERN for the LHC experiments. The HPTDC architecture is shown in Figure 96. The time base for the TDC measurements is a Delay Locked Loop (DLL) with 32 delay elements and a clock synchronous counter, both driven by the same clock reference. The clock reference can be taken directly from the clock input of the TDC chip or can come from an on-chip PLL. The Phase Locked Loop (PLL) can perform clock multiplication to increase time resolution or can be used as a filter to remove jitter on the input clock.

A hit measurement is performed by storing the state of the DLL and the coarse counter when a hit (leading and/or trailing edge) is detected. Each channel can buffer 4 measurements until they are written into a 256-word-deep level 1 buffer shared by a group of 8 channels. The individual channel buffers work as small derandomizer buffers before the merging of hit measurements into the L1 buffer. Measurements

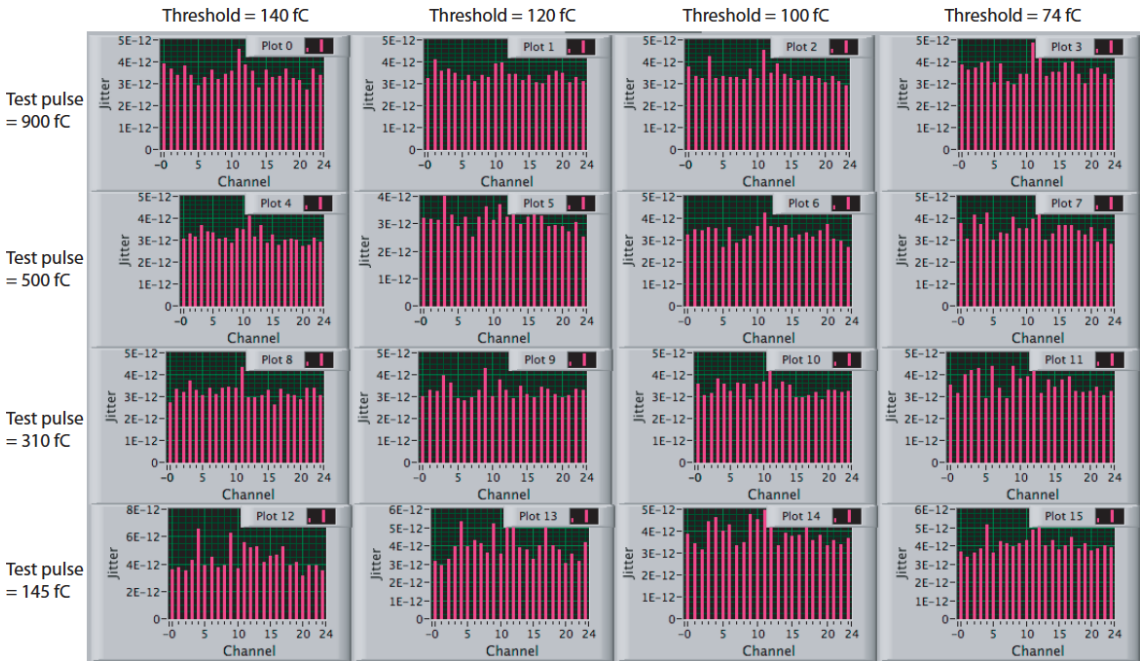

Figure 95: Measurement of the time jitter (in seconds) of the NINO chip for different values of input pulse charge and threshold.

stored in the level 1 buffer can be passed directly to a common 256-word-deep read-out FIFO, or a trigger matching function can select events related to a trigger.

The trigger information, consisting of a trigger time tag and an event id, can be stored temporarily in a 16 word deep trigger FIFO. A time window of programmable size is available for the trigger matching to accommodate the time spread of hits related to the same event. Accepted data can be read out in a direct parallel format or serialized at a programmable frequency. The HPTDC chips can be configured to work with 8 input channels in High Resolution mode. In this mode the time binning is 25 ps. The time resolution after time calibration correction is expected to be $\sim$ 20 ps.

The HPTDC provides the option of dual time measurement, in which the time tags of both the raising and falling edges of the input pulses are determined. As the HPTDC double pulse resolution is 10 ns, this mode can be used with NINO pulses, which have a minimum width of 13 ns. The dual time measurement allows to quantify the time-over-threshold, providing therefore a measurement of the amplitude of the detector pulses. In our timing readout system the HPTDC will be used with a clock of 80 MHz. At 80 MHz, taking into account the need for dual time measurements, the maximum input rate per channel is 5 MHz.

The HPTDC is implemented in standard 250 nm CMOS technology that is not guaranteed to be fully radiation hard. However, given the well understood characteristics of this technology under radiation, the HPTDC chip will most likely work correctly up to total dose levels above 30Krad, with a slight increase in power consumption. The chip is also not guaranteed to be insensitive to Single Event Upsets (SEU) but all internal memories and state machines are self checking, thus enabling the TDC itself to identify a malfunction. In the frame of the CMS DT electronics development, HPTDC chips were tested up to 5×10^{10} 60 MeV protons/cm^2, which is one order of magnitude below the expected radiation level in our application. Radiation tests are foreseen to measure SEU rate as a function of particle fluence.

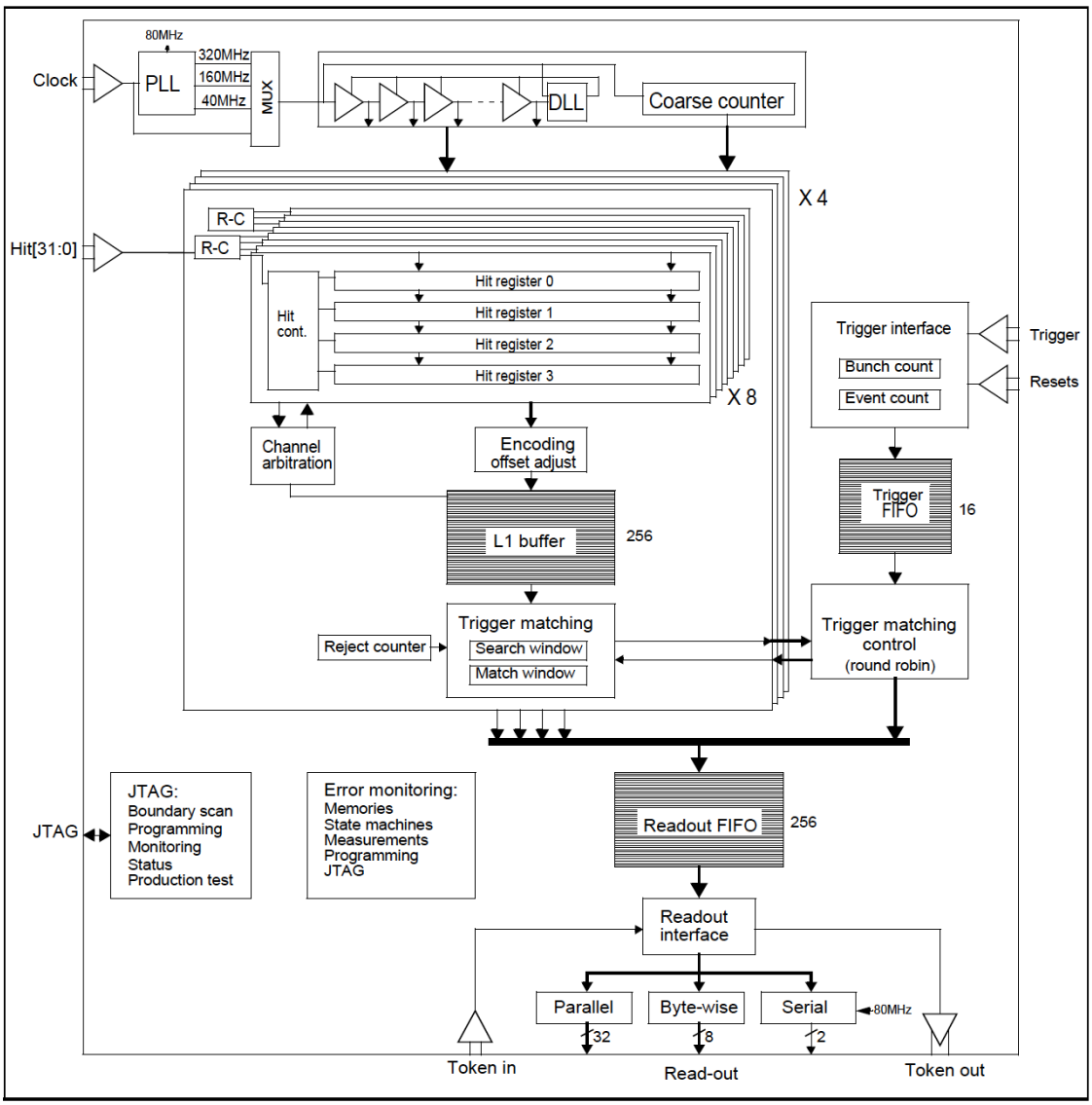

Figure 96: Architecture of HPTDC.

5.5 Diamond detectors

We are investigating solid state detectors with high segmentation to reduce the channel occupancy. The simulations show that the probability to have a double hit in a Quartic channel, especially in the 3×3 mm^2 bars close to the beam, can reach up to $\sim 50\%$. The idea to limit this bias is to use a different technology that can host smaller size pixels. Such detectors can also be thin and light, allowing a large number N in series thus gaining resolution by $1/\sqrt{N}$. A stack can be placed upstream of the QUARTICs or may eventually replace them.

We can reduce the pixel size until the inefficiency reaches a reasonable level, but this brings to a large increase in the channel number, which would require special ASICs not yet available on the market. The necessity to have a better timing detector in a reasonable period requires a different approach. The main idea is that the track density of diffractive protons in the horizontal plane is not uniform, and neither is the main overlapping background.

To reduce the channel number we need a pixel surface that is inversely proportional to the track density. This choice results in pixel surfaces at the edge close to the beam that are of the order of 1.5 mm^2. Silicon detector pixels have a time response that changes enormously from the center to the edge if the pixel surface is large ($\sim$1 mm^2), that brings to search for alternative technologies.

The natural choice is to use diamond detectors for several reasons: the diamond detector pixel size does not affect the signal response dramatically; the pixels pad shape is given by just the metallization pattern; and we can have pixels of different size on the same diamond crystal. On the other hand the charge released from a diamond sensor is small in absolute numbers ($\sim$6000e). A low noise amplifier is needed to keep the S/N ratio large enough. The main noise source is the input impedance of the amplifier, since the diamond resistivity is enormous. The second requirement calls for an R&D phase to optimise the amplifier parameters. Current amplifiers have a low noise suppression, while charge integrating amplifiers with optimum filtering have rise times of the order of 1 ns.

The small mass and thickness ($\sim$500 μm) of a diamond detector allows the construction of a telescope with up to 9 planes to be hosted in the cylindrical pots. The redundancy of planes allows a robust reduction of the overall time resolution. The minimal number of non-uniform pixels needed for a good efficiency at high luminosity is around 16. With such a small number of channels we can think of developing discrete component amplifiers. In our current R&D we are testing various configurations with discrete-component RF amplifiers to find the optimum design. Each plane is a layer with dimensions of 15×20 mm^2 of diamond sensors with increasing pitch from the beam edge to the periphery.

The readout board will host the sensors plus the preamplifier hybrids on the outside. On the same board, single threshold discriminators will detect the edge of the signal for each pixel. The time walk of single threshold discriminators, due to charge fluctuations, can be corrected if we measure the time over threshold for each signal. The NINO [15] chip has this capability and the output signal length is proportional to the time over threshold of the input analog signal. The maximum rate that this device can afford is around 30 MHz. That means that the mean rate for each pixel has to be less than 10 MHz. For a pileup with μ=50 the worst case for one pixel is a rate of approximately 5 MHz. The readout board will send out 16 LVDS signals each one giving the pixel information of time of arrival on the leading edge and the charge released on the signal length. Up to nine readout boards can be packed to form a timing telescope (stack), and inserted into a timing RP. Many measurements of a "time-track" allows continuous monitoring of the efficiency and time resolution of each layer, and in some events one may improve the overall time resolution by rejecting an "outlier" with bad χ^2 to the fitted time-track.

The cooling system of the apparatus will be active on the metallic layers of the board itself without special piping on the sensors side. The TDC board will be placed on a concrete hole in the ground below the RP structure. This location has a reasonable radiation level that allows the use of FPGA. Studies done on ion and neutron beams on Altera Cyclone FPGA show that even in the surrounding area of the

beam pipe we could expect a SEU rate of 1 every 3 hours. In case of SEU we foresee the request of a Resync to be performed on the TDC board only. We are developing TDCs inside an FPGA that can have a time resolution of ≈10 ps. The same technology is used for the Quartic detectors, but the algorithm that will be used this time will perform single threshold and time over threshold measurements plus a correction matrix. The advantage of using on-board FPGAs is that the Trigger and DAQ information can be formatted properly in the same board. The DAQ pattern will be formatted with: a header with start of frame patterns and counters, the list of TOA (Time Of Arrival) and TOT (Time Over Threshold) for each fired pixel, and a footer. This information is transmitted in raw format without online corrections. The trigger will perform an on-line rejection based on track number (see Chapter 6). We will define a trigger row as a majority AND of aligned pixels in subsequent planes. This trigger-row definition rejects noisy channels that can contaminate the time measurement. Track counting will be done on-board locally, and if the event is accepted the time of arrival will be assembled into 4 words and sent to the central trigger unit (based on the TOTEM LONEG board).

5.6 Fast timing silicon detectors

The development of Low-Gain Avalanche Diode (LGAD) [16, 17] has made it possible to manufacture silicon detectors with output signals that are about a factor of 10 larger than those of traditional sensors. This increased signal brings many benefits such as the possibility of developing thin detectors with large enough signals, good performances even for small charge collection efficiency, and it is key for excellent timing capabilities. LGADs have therefore made possible the development of silicon sensors optimized to achieve excellent timing performance, the so called *Ultra-Fast Silicon Detectors* [18, 19, 20] (UFSD).

The possibility to use and control charge multiplication in un-irradiated silicon detectors has been the subject of intense study within the RD50 collaboration [21]. LGADs, as developed by CNM, are $n-on-p$ silicon sensors with a high ohmic p bulk that have a p^+ implant extending over several microns underneath the n-implant. Figure 97 shows the $n^{++}-p^+-p-p^{++}$ structure of an LGAD.

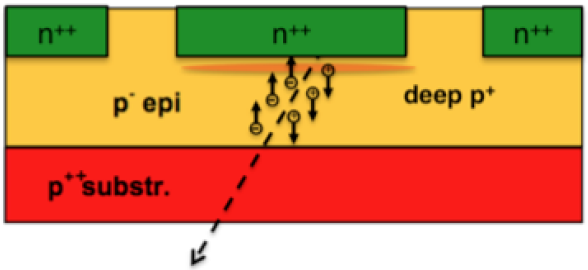

Figure 97: Schematic of a Low-Gain Avalanche Diode. The extra deep p^+ layer creates a strong electric field that generates charge multiplication.

This additional p^+ implant generates a large local field at a depth of about $1-5$ μm whose value is chosen to generate a gain of 10-100. The design of UFSD exploits the effect of charge multiplication in LGADs to obtain a silicon detector that can measure time with high accuracy [22].

UFSD have been manufactured by CNM in several geometries including pixels, strips and large diodes. Figure 98 shows the gain of three 5x5 mm^2 UFSD as a function of the bias voltage. The value of the gain is computed by comparing, at each voltage, the charge collected from a UFSD to that of a standard silicon pad of the same geometry. The spread in gain values shown in the plot is due to different doping concentrations of the p^+ gain layer and is consistent with the specifications from the manufacturer.

The time resolution (σ_t) of a silicon detector can be expressed as the sum of three terms: (i) Time Walk, (ii) Jitter, and (iii) TDC binning (if used):

$$\sigma_t^2 = \sigma_{TW}^2 + \sigma_J^2 + \sigma_{TDC}^2. \tag{5.8}$$

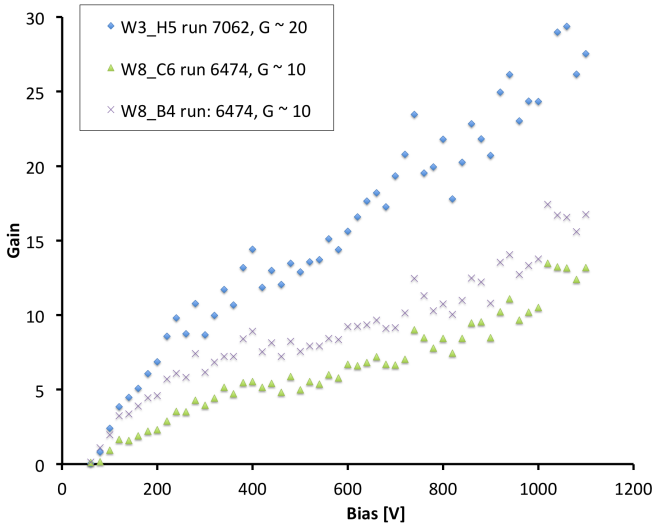

Figure 98: Value of the gain for three 5x5 mm^2 UFSD as a function of the bias voltage. The value of the gain is computed by comparing, at each voltage, the charge collected from a UFSD to that of a standard silicon pad of the same geometry.

The TDC binning introduces a fixed uncertainty equal to $\sigma_{TDC} = TDC_{bin}/\sqrt{12}$. As TDCs become faster and faster [23], we assume $TDC_{bin} = 20$ ps and therefore this effect will not be important.

Using the explicit expressions of σ_{TW}, σ_J and σ_{TDC}, Eq. (5.8) can be rewritten as:

$$\sigma_t^2 = ([\frac{V_{th}}{S/t_r}]_{RMS})^2 + (\frac{N}{S/t_r})^2 + (\frac{TDC_{bin}}{\sqrt{12}})^2, \tag{5.9}$$

where

N: Noise: $N \propto \frac{C_{Det}}{\sqrt{t_r}}$. We assume it to be dominated by the voltage term.

S: Signal amplitude.

t_r: Preamplifier rise time.

V_{th}: Comparator threshold.

TDC_{bin}: TDC bin width. We assume a value of 20 ps.

To evaluate the performance of UFSD we have developed a simulation program called Weightfield2 [24]. With the parametrization described in Eq.(5.9), which is able to correctly reproduce the timing capabilities of state of the art silicon detectors, and the simulation program Weightfield2, which has been validated using laboratory data, the timing capabilities of UFSD can be simulated.

As Eq.(5.9) shows, time resolution is controlled, for constant noise N, by the ratio S/t_r, which is the rate dV/dt of the output signal of the detector: large dV/dt values are key to obtain excellent time resolutions. Figure 99 shows, as a function of the internal gain, the simulated values of dV/dt for UFSD normalized to that of a standard silicon sensor. The values of biasing voltage V shown in the legend are such that the sensors have the same electric fields. The figure shows that gain allows obtaining values of dV/dt that are a factor of 5-10 higher than those of standard sensors.

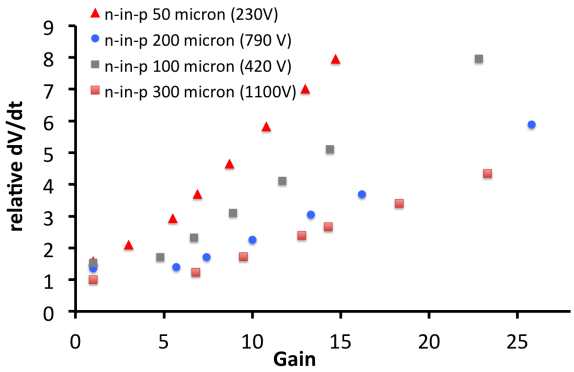

Figure 99: Simulated values of dV/dt for UFSD as a function of the internal gain. The values shown in the legend are such that the sensors have the same electric fields.

5.6.1 Measurements

Using a split 1064 nm laser beam, tuned to reproduce the signal amplitude of a minimum ionizing particle, we simultaneously illuminated pairs of silicon sensors, standard and/or UFSD, and computed, using waveform digitizers, the time difference of the two signals as a function of the bias voltage [25]. The sensors were all manufactured by CNM, 300-micron thick, 5×5 mm^2 pads (see Figure 100).

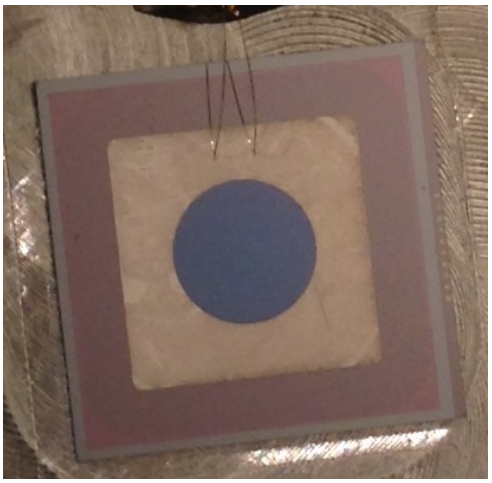

Figure 100: Sensors used for the timing tests: manufactured by CNM, 300-micron thick, 5×5 mm^2 pads.

This measurement allows extracting the time jitter of each detector (Figure 101), where the results have been obtained using a read-out chain composed by the Cividec broadband amplifiers $C2$ [26] followed by either the SAMPIC or Wavecatcher waveform digitizer [27]. For this specific measurement we used the $W8\_C6$ and $W8\_B4$ sensors, which have almost equal gain, as shown in Figure 98.

As the figure shows, the signals from sensors without gain have a time jitter of about 80-100 ps, with a moderate dependence on the bias voltage, while signals from UFSD exhibit a dramatic reduction of the jitter with increasing bias voltage (due to the onset of the gain mechanism), down to values of about 40 ps at $V_{bias} \sim 1000$ V.

Using the simulation program Weightfield2 and the experimental results shown in Figure 101, the time jitter of UFSD at different gain values can be computed. A time jitter of less than 20 ps is achievable for gains of about 15, see Figure 102.

The relative importance of the jitter and time walk components, (see Eq.(5.8)), to the total value of the time resolution depends on the choice of the read-out scheme. In a read-out scheme in which the signal

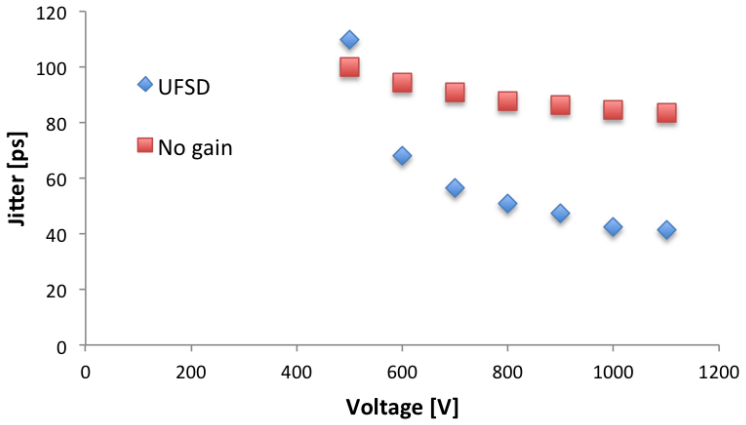

Figure 101: Measured time jitter for UFSD and standard silicon sensors as a function of the bias voltage. The set-up comprised a 1064 nm PILAS laser, a pair of silicon sensors read-out by the Cividec broadband amplifiers $C2$ followed by the SAMPIC or Wavecatcher digitizer.

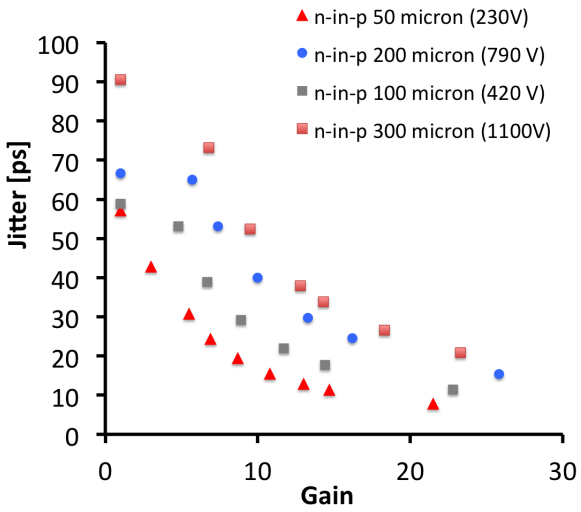

Figure 102: Simulated UFSD time jitter for different sensor thicknesses.

timing is determined by a single threshold, and time walk correction is implemented by either using a Constant Fraction Discriminator or Time-over-Threshold (as it is, for example, in the NINO + HPTDC scheme), jitter tends to be the dominant component. On the other hand, in read-out schemes that use multiple sampling, such as those based on the DRS4 or SAMPIC chip, both components are reduced quite significantly, and each contributes to the time resolution more equally.

A measurement of the time resolution of UFSD at a testbeam is planned for the Fall 2014.

5.6.2 Radiation tolerance of UFSD

The radiation tolerance of UFSD is currently under investigation.

A set of sensors has been irradiated with reactor neutrons with the following fluence steps: 1, 5, 20, 100 10^{14} n/cm^2, with a pause of 80 minutes of annealing at 60^o C between irradiations [28]. The effect of radiation damage on the gain is shown in Figure 103: after a fluence of 10^{14} n/cm^2 the gain has decreased by about 15% , at $5 \cdot 10^{14}$ n/cm^2 by about 60%, and finally at a fluence of $1 \cdot 10^{15}$ n/cm^2 it has become 1/6 of its initial value. The reason of this behavior is currently under study.

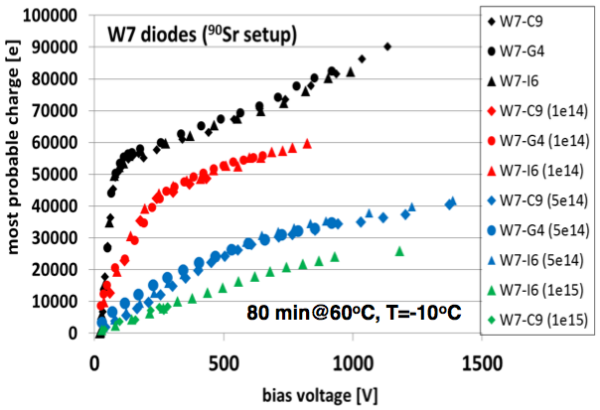

Figure 103: Effect of radiation damage on the gain: after a fluence of 10^{14} n/cm^2 the gain has decreased by about 15%, at $5 \cdot 10^{14}$ n/cm^2 has decreased by about 60%, and finally at a fluence of $1 \cdot 10^{15}$ n/cm^2 has become 1/6 of its initial value.

The total fluence of neutron at the LHC, in the position where the PPS will be placed, is estimated to be $3 \cdot 10^{15}$ neq/cm^2 (this TDR and also [29]) for an integrated luminosity of about 100 fb^{-1}. These values imply that UFSD can be used in data taking operation for integrated luminosity up to several inverse femptobarn without a noticeable degradation of timing performance.

A different set of sensors was been sent to Los Alamos for proton irradiation; they were exposed to fluences ranging from 10^{12} to $3 \cdot 10^{16}$ p/cm^2. The results are not available yet.

5.6.3 Future developments

Given its very good time resolution and low material budget, UFSD is a natural choice for the timing detectors of PPS. With this choice, the PPS timing detector would be built as a sequence of silicon planes, very similar to those of the tracking detector. As UFSD have shown very good time resolution for pad sensors with geometries up to 5x5 mm^2, large pads can be arranged to cover the active area of the PPS. Figure 104 shows a possible layout of such a plane, using several UFSD pads manufactured on the same substrate. While designing the optimal sensor, it is necessary to consider the pad capacitance: time resolution is better in thin detectors, only if the value of the pad capacitance is kept small. The choice of read-out scheme will ultimately determine the allowed range of capacitance values, and therefore determine the maximum pad size for a given sensor thickness. For optimum performance, it's possibile to design each UFSD plane composed by two sensors: a thinner one, for best time resolution with small pads, and a thicker one, with larger pads.

Following the performance of similar devices such as Silicon Photomultipliers and Avalanche Photo Diodes, we expect a lower gain for tracks impinging in between pads. This effect will be studied in upcoming testbeams.

Another important feature is that UFSD can be designed with a rather slim dead area toward the bottom of the RP, near the beam. This advantage is due to the UFSD reduced thickness: in planar pixel silicon detectors, the distance between the last pixel and the detector edge has to be of the order of the detector thickness. As UFSD are rather thin, 50-100 micron, the dead distance can be kept quite small.

As each plane of UFSD is thin, up to 6 planes of UFSD can be housed in a RP, while a cylindrical RP can house several more. Assuming 9 independent time measurements, an overall resolution of less than 10 ps can be achieved.

Such design of the PPS timing detector has the advantage that planes of UFSD are relatively easy to manufacture and the specific geometry of the pads can be adapted to match the occupancy density, with

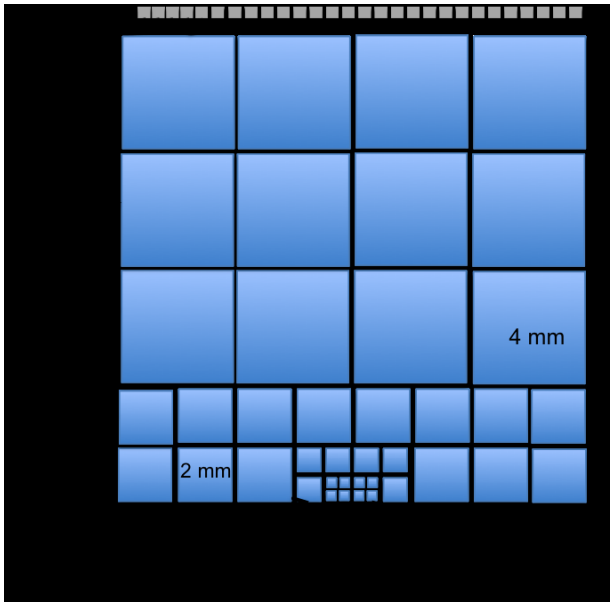

Figure 104: Possible layout of a single plane for the timing detector of the PPS. Each plane is composed of several UFSD pads manufactured on the same substrate. The size of each pad reflects the varying occupancy of the detector.

smaller pads at the center of the detector plane, near the beampipe. They have a very low material budget, and the cost for full set of planes plus spares (24 + 24) is around 40k Euros.

We are currently in the process of manufacture two additional sets of sensors: the first one will be on a 200-micron thick FZ substrate, and will use either boron and indium as dopant for the gain layer. This production, expected in the Fall of 2014, will help us consolidate the design process, compare the performance of 300- and 200-micron thick sensors, and measure the radiation hardness of indium-doped sensors. The second production, aimed for the Spring 2015, will use 50- and 100-micron SOI sensors, and it will have full PPS sensor geometry. As time resolution improves for reduced sensor thickness, we expect the 50- and 100-micron thick detector to achieve a significant break-through in performance, allowing us to manufacture the final UFSD sensor geometry for the PPS for the Fall 2015.

The read-out electronics for such a detector can either be derived from the configuration that was used in the tests presented above (a broadband amplifier followed by a waveform digitizer), or can be adapted from the electronics developed for diamond and silicon multi-layers detectors [30].

The aim of the group developing SAMPIC is to obtain a system able to achieve sub-10 ps timing resolution, 1GHz input bandwidth, no dead time at the LHC, and data taking at 2 Gigasamples per second. The present version does not match these requirements and does not have trigger capability at the cell level. An upgrade of SAMPIC with several of these features will be available by the end of 2014. The cost per channel is estimated to be of the order of 10$.

5.6.4 3D silicon sensors

3D sensors, already considered as baseline for the PPS tracking system, can be considered promising candidates also for timing measurements. Thanks to their unique structure, very short drift times can be achieved by choosing small inter-electrode spacing without reducing the substrate thickness, thus preserving the signal amplitude. TCAD simulations show that a rise time and a collection time of 10 ps and 500 ps respectively can be achieved for inter-electrode distance of 50 micron. First measurements performed with a non optimized readout electronics have shown that resolutions between 30 and 180 ps,

depending on the signal amplitude, have been reached for a 90Sr source [31].

5.7 Timing and Trigger Control

CT-PPS will be integrated in the CMS Trigger Control and Distribution System (TCDS) as an additional partition. The TCDS distributes to the CT-PPS readout systems the CMS master clock, as well as the L1 Accept and other Fast Commands. In particular, CT-PPS plans to make use of the Hard Reset signal to reset the FPGAs in the Tunnel.

In the reverse direction, CT-PPS system sends to TCDS the Trigger Throttling Signals (TTS) indicating the occupancy of the readout buffers. The CT-PPS trigger system provides trigger bits to the Global Trigger which can be combined with any other trigger condition to create CT-PPS specific L1 trigger algorithms.

The CT-PPS timing measurements requires a complementary timing system capable to provide a very low jitter ($\sim$1 ps) replica of the master clock to the front-end TDCs.

R&D on suitable systems have been carried in the past by both the CMS and TOTEM collaborations. The CMS development is based on a electrical option in use at SLAC Linac Coherent Light Source (LCLS) and the TOTEM system is based on an optical option developed for FAIR at GSI.

CT-PPS plans to commission in a test beam the timing detectors in association with the CMS timing system prior to the installation in the experiment in the fall of 2015. Moreover, in the framework of CT-PPS and of the TOTEM Upgrade programme, the TOTEM timing system is foreseen to be installed in LHC during LS1, to be commissioned in situ and used in the runs with $\beta^* = 90$m in 2015 and in CT-PPS test runs.

The two collaboration have concluded that both systems are required. The conflicting schedules and physics goals in 2015 prevent a possible share of an unique system. In general grounds, it is also wise to have two versions of a system that is critical for the operation of both experiments, allowing redundancy and added monitoring. We should point out that for the first time these technologies will be used in the LHC experiments. We expect that the parallel operation of electrical-based and optical-based systems would bring invaluable experience with these technologies in view of a possible extended usage in future HL-LHC experiment's upgrades.

5.7.1 Reference Timing System (CMS)

We have chosen a simple and robust technique for achieving sub-picosecond time synchronization of the detector stations located at approximately $\pm$220 m from the interaction region. A single electronics module is placed in each arm and they are synchronized via an RF feedback system, operating at a frequency of about 480 MHz, over a single coaxial cable. This scheme is based on a system in use at SLAC for synchronization of the Linac Coherent Light Source (LCLS) experiments with the electron accelerator beam [32].

The basic operating principle of the LCLS concept we have adopted is shown in Fig. 105. The slave oscillator in one arm is phase-locked with the master using a feedback loop set up along the coaxial cable. This is accomplished by sending the slave RF oscillator signal back to the master location, comparing the transmitted phase with the master, and returning a DC signal proportional to the difference back to the slave, along the same coaxial cable, which is then used to control the slave oscillator phase offset. One of the explicit benefits of this concept is that it will automatically compensate for the phase drift from any temperature-induced changes in the cable length. Figure 106 shows photographs of the slave and master electronics modules from the LCLS timing system upon which the CT-PPS version is based.

Such a system has proven to be extremely reliable. LCLS typically conducts experiments for ten months

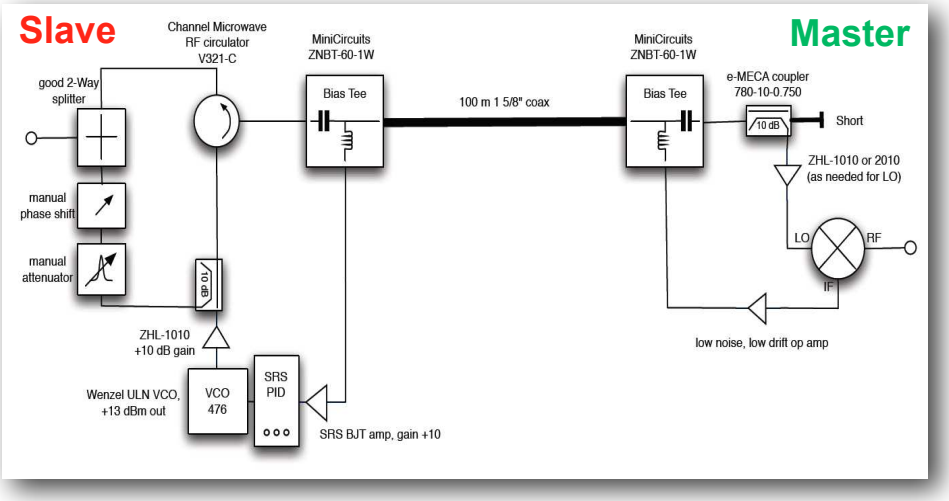

Figure 105: Master/slave clock synchronization concept diagram.

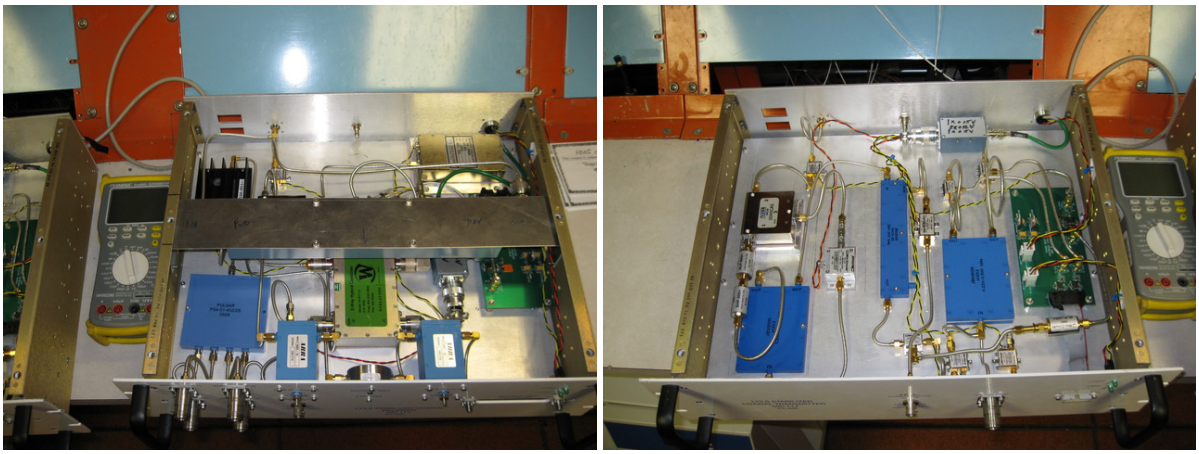

Figure 106: The slave (left) and master (right) timing electronics modules.

out of the year and the timing systems are never shut off. Two timing systems have been deployed at the LCLS and have operated continuously without a single failure, or loss of the phase lock, for a combined time of seven years [33].

In order to measure the actual system performance in the configuration suitable for CT-PPS we procured 500 m of AVA7RK-50 coaxial cable, see Table 14, for testing with an existing spare RF timing system at SLAC. This length is suitable to connect both detector arms at ± 220 m. We selected a lower-loss cable than the one currently used at SLAC so that the total signal attenuation for our longer cable was no more that of the shorter cable used in LCLS experiments.

We tested the high-frequency stability of the timing system output using an Agilent Technologies E5025B 10MHz-7GHz Signal Source Analyzer. To measure the total jitter we integrate the noise contributions from 10 Hz to 100 MHz. Since the intrinsic jitter of the phase-locked RF system is so small, we used a very stable Wenzel 476 MHz oscillator as the input oscillator. The jitter contributed by the RF stabilized system with the 500 m cable between the master and slave units was 30 fs. The Wenzel oscillator by itself had a jitter of 50 fs.

Since we intend to feed the output of the stabilized RF system to a TDC, we have also tested the jitter introduced by the conversion from RF to digital signal. We selected a fast comparator HMC974LC3C from Hittite, which has an analog input bandwidth of 10 GHz and rise/fall time of 25 ps with PECL

Table 14: Properties of AVA7RK-50 low-loss coaxial cable used for reference timing module synchronization.

Property	Value
Attenuation at 400 MHz	1.351 dB/100 m
Velocity	92%
Outer Diameter	51.1 mm (2.01 in)
Insulation	Non-halogenated, fire-retardant polyolefin

output. We measured the jitter contribution from this component to be 220 fs. The effect of the RF stabilizer itself on the jitter is therefore negligible by comparison.

5.7.2 Reference Timing System (TOTEM)

The challenge of combining measurements with picosecond range precision for Timing signals generated in locations separated by large distances (order of 220 m) requires a clock distribution system capable of the highest precision and of the utmost time stability.

The following pages aim at describing the Clock Distribution system for the TOTEM Vertical Pot Timing Upgrade [34]. The choice of the system is based on several requirements:

- it must be operational in the early phase after LS1, already in 2015.
- it has to be based on infrastructures which can be deployed during LS1
- for additional safety and ease of operation, it must allow to monitor continuously the phase and the jitter, and to keep the possibility open in the future, if necessary, to apply a fine tuning in real time.
- this system should be fully scalable in order to accommodate in the following years, without modifications, additional detectors, transmission lines, and clock distribution points.

The system is adapted from the *Universal Picosecond Timing System*[35], developed for FAIR (Facility for Antiproton and Ion Research), the international accelerator facility for research with antiprotons and ions at present under construction at GSI (D), where a Bunch phase Timing System (BuTiS) based on this concept has been implemented [36].

The optical clock distribution network will use a Dense Wavelength Division Multiplex (DWDM) technique that makes it possible to transmit multiple signals of different wavelengths over a common single mode fiber. This will allow to use standard telecommunication modules compliant to ITU (International Telecommunications Union) international standards. Moreover, exploiting the DWDM technique, it will be possible to transmit more than one reference clock signal along a single fiber, guaranteeing the possibility of adding more reference signals in the future, w.r.t. what is used in the present design. The choice of an optical technology will make it possible an efficient reuse of the optical infrastructures already deployed in IP5 and along the tunnel.

The experiment requires two very stable clocks for the precise timing reference and the bunch identification. These reference clock signals are sent from the counting room to a set of receivers positioned near the timing detectors in various location of the LHC tunnel on both sides of IP5. A third signal added on

the same optical fiber will be simply reflected back to be used to continuously measure the time delay of each optical transmission line: these delay measurements are necessary to correct the time information generated at the detector location for fiber delay variations (thermal and mechanical instabilities). In addition, this will allow an event by event monitor of the status of the clock signals, opening the possibility of adding these informations to the data stream as well.

The system can be logically subdivided in four major blocks: the Transmission Unit, the Distribution Unit, the Measurement Unit and the Receiving Unit. One Receiving Unit must be installed very near each RP location, the Transmission, Distribution and Measurement Units will be located in the TOTEM racks in the IP5 counting room. A block diagram of the entire system is reproduced in Figure 107.

Measurements performed with the prototype of the "BuTiS" system show that the influence of the transmission system on the signal jitter, is of the order of 0.4 ps [36], mainly dependent on the quality of the clock source signal, the noise added by the optical components and the bandwidth of the transmission system itself. Using a transmission system based on this concept, the total jitter of the TOTEM clock transmission system will also be due mainly to the inherent jitter of clock sources and the end user electronics.

Transmission Unit

The Transmission Unit optically modulates the two reference clocks in signals with different wavelength λ_1 and λ_2. Via DWDM these optical signal are multiplexed into a single fiber and re-transmitted at a specific wavelength using a 1,550 nm band laser to the Distribution Unit. The signal is amplified with an erbium-doped fiber amplifier (EDFA) to compensate the attenuation due to further splitting and the multiplexers.

A Thorlabs PRO8000[‡] platform has been chosen to generate the two DWDM wavelengths on channels ITU 32 and ITU 34 . This complete platform is designed to operate and control electrical and optical modules for telecommunication testing and application developments from a broad family of interchangeable modular devices and can be controlled by an external computer using industrial control protocols. The modulation of the optical signals is performed by two military grade Mach-Zehnder modulators of 20GHz bandwidth. The EDFA amplifier developed for this platform will be used. This unit can be rack mounted and is suitable for use in the experiment control room harsh environment.

Distribution Unit

The DWDM optical signal, as generated by the Transmission Unit, needs to be split in order to be transmitted to the four Receiving Units. Moreover a third DWDM modulated optical signal of wavelength λ_M is needed to measure the transmission delays over each fiber and is added to the other two clock signals.

The JDSU[§] Multiple Application Platform (MAP-200) has been chosen for the Distribution Unit optical amplification. This platform is a highly configurable, scalable and industrially controlled system that can host several optical modules with a wide range of functions.

[‡]Thorlabs, Inc. : www.thorlabs.com. PRO8000 platform: http://www.thorlabs.com/newgrouppage9.cfm?objectgroup_id=895 .

[§]JDS Uniphase Corporation: www.jdsu.com. Multiple Application Platform (MAP-200): http://www.jdsu.com/en-us/test-and-measurement/products/a-z-product-list/Pages/map.aspx .

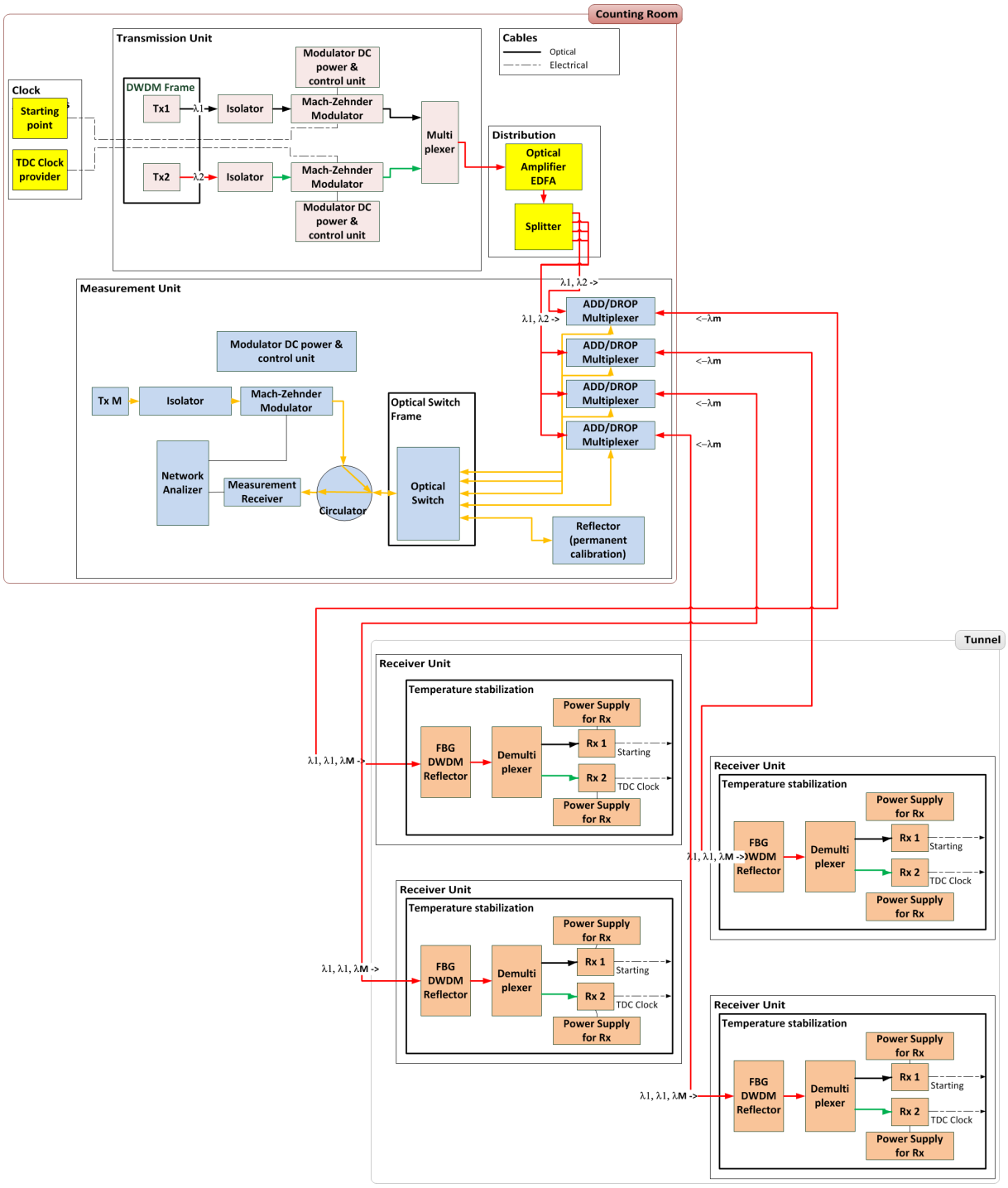

Figure 107: The block scheme of the clock distribution system.

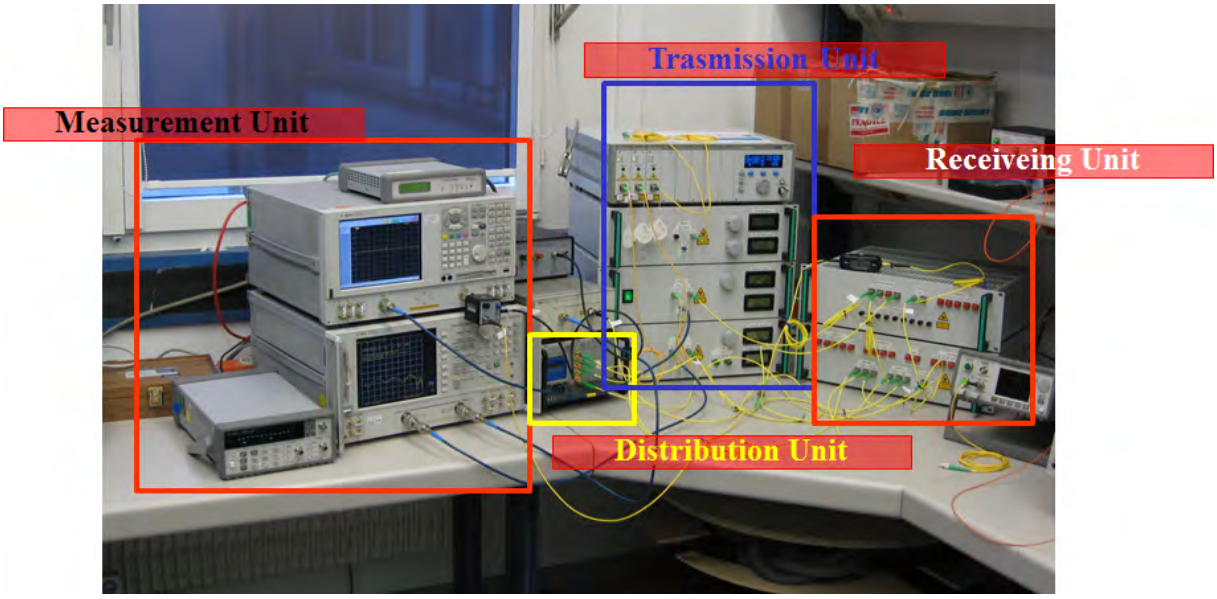

Figure 108: The clock distribution system under test at GSI.

Measurement Unit

In the unit, the signal delays will be determined. A reference signal is generated and optically modulated using the wavelength λ_M and sent with an optical switch to every Receiving Unit and to a reflector, which will be used for calibration. .

Then add/drop multiplexers combine this reference signal to the 4 DWDM optical signals generated in the Transmission Unit and split in the Distribution Unit. Now the multiplexed signal contains three optical wavelengths: λ_1, λ_2 and λ_M, and is transmitted to the Receiving Units located in the tunnel at $\pm$220m and $\pm$210m.

The reference signal once at the Receiving Unit will be reflected back. The optical add/drop multiplexer separates the λ_M optical signal coming back form the RUs and pass it back to the switch. A "circulator", placed between the DWDM generator and the switch, distributes the reflected signals to a measurement instrument without interrupting the transmission from the generation module to the switch. A phase comparison of the reflected signal with the reference one is performed, using a vector network analyzer. The phase differences obtained by this measurement determine the delay of each clock signal distribution channel.

As for the Transmission Unit, a Thorlab PRO8000 module,and the same Mach-Zender modulator, will be used. The DWDM wavelengths proper of channel ITU 36 , will be used to modulate the reference signal.

Receiving Unit

The Receiving Unit separates the multi-wavelength optical signal back into individual signals. The signal from the single mode fiber (SMF) encounters first a Bragg grating (FBG) DWDM reflector and reflects back the signal component of λ_M wavelength. The other components of the signal is routed to a DWDM demultiplexer that separates the two wavelengths, λ_1 and λ_2, and outputs them on separate fibers for conversion to electrical signals and makes them available to the front end electronics and the DAQ card. This unit should be located as close as possible to every RP location. A temperature stabilization of this unit, depending on the temperature characterization of the installation point in the tunnel, may be needed to reduce the long term shift of the measured delay.

5.8 Plans and Schedule

An important objective of the CT-PPS exploratory phase (2015-16) is to demonstrate the timing performance and the pile-up rejection capabilities of the baseline detector. We plan to carry out this activity in the fall of 2015 and beginning of 2016, after the programme of validation of RP operation at high luminosity described in 1.3.

The baseline Quartic detector modules will be evaluated in test beams in the Spring-Summer 2015, when the readout system will become available. GasToF prototype modules will be built and will also be evaluated in the same test beam. In parallel an extensive R&D programme on the timing solid state technologies will be carried including test beam activities.

The integration of the local DAQ hardware and online software in the central CMS Trigger/DAQ system and clock distribution system (TCDS) will be tested in the CMS Electronics Integration Center in the Spring-Summer 2015.

The Quartic detector and the front-end readout system is expected to be ready for installation in the cylindrical RPs in the fall of 2015. One cylindrical RP per arm has already been installed in LS1, allowing the installation Quartic timing detectors during a short technical stop. The installation procedure will be tested beforehand in the lab using a spare cylindrical pot.

References

[1] M.G. Albrow et al., "The FP420 R&D Project: Higgs and New Physics with forward protons at LHC", JINST 4 (2009) T10001.

[2] L. Bonnet, J. Liao and K. Piotrzkowski, "Study on GasToF: A 10 ps resolution timing detector", NIM A762 (2014) 77.

[3] M.G.Albrow, "Fast timing detectors for leading protons at LHC: QUARTIC", Proc. Workshop on Picosecond Photon Sensors for Physics and Medical Applications, Clermont-Ferrand, March 2014 (to be published in Acta Physica Polonica).

[4] G. Chiodini, "Timing Diamond Detector for MIP", Workshop on Picosecond Photon Sensors for Physics and Medical Applications, Clermont-Ferrand, March 2014.

[5] M. Ciobanu et al., "In-beam diamond start detectors", IEEE Trans. Nucl. Sci. 58 (2011) 2073.

[6] N. Cartiglia et al., "Timing capabilities of Ultra-Fast Silicon Detector", Workshop on Picosecond Photon Sensors for Physics and Medical Applications, Clermont-Ferrand, March 2014

[7] CMS Technical Design Report for the Phase 1 Upgrade of the Hadron Calorimeter, Technical Report CERN-LHCC-2012-015. CMS-TDR-010, CERN, Geneva, (Sep, 2012).

[8] M.G. Albrow et al., "Quartz Cherenkov counters for fast timing: QUARTIC", JInst **7** P10027 (2012).

[9] M. Mazzillo et al., IEEE Nucl. Sci. Symposium NI-187 p.391.

[10] A. Ronzhin et al., "Tests of timing properties of silicon photomultipliers", NIM A616 (2010) 38.

[11] J. Va'vra *et al.*, "Beam Test of a Time-of-Flight Detector Prototype", NIM A606 (2009) 404.

[12] Specialty Glass Products, 2885 Terwood Rd., Willow Grove, PA 19090, USA.

[13] http://www.photonis.com/en/ism/63-planacon.html

[14] S. Gundacker et al., "Time of flight positron emission tomography towards 100 ps resolution with L(Y)SO: an experimental and theoretical analysis", JINST 8 (2013) P07014.

[15] F. Anghinolfi et al. "NINO: an ultra-fast and low-power front-end amplifier/discriminator ASIC designed for the multigap resistive plate chamber". NIM A 533 (2004) 183.

[16] P. Fernandez et al, " Simulation of new p-type strip detectors with trench to enhance the charge multiplication effect in the n-type electrodes", NIM A 658 (2011) 98.

[17] G. Pellegrini et al., "Technology developments and first measurements of Low Gain Avalanche Detectors (LGAD) for High Energy Physics applications", Hiroshima Conference, HSTD9, Hiroshima, Japan, NIM A, in print (2014).

[18] H. F. W. Sadrozinski, "Exploring charge multiplication for fast timing with silicon sensors", 20th RD50 Workshop, Bari, Italy, May 30-June 1, 2012, and references therein https://indico.cern.ch/conferenceOtherViews.py?view=standard&confId=175330.

[19] H. F. W. Sadrozinski, S. Ely, V. Fadeyev, Z. Galloway, J. Ngo, C. Parker, B. Petersen and A. Seiden *et al.*, "Ultra-fast silicon detectors," Nucl. Instrum. Meth. A **730** (2013) 226.

[20] H. F. W. Sadrozinski et al., "Sensors for Ultra-Fast Silicon Detectors", HSTD9, Hiroshima, Japan. NIM A, in print.

[21] RD50 collaboration,http://rd50.web.cern.ch/rd50/.

[22] N Cartiglia et al., "Performance of ultra-fast silicon detectors", JINST 9 (2014) C02001.

[23] A. Rivetti, et al.,"Electronics for Fast Tracking Detector", HSTD9, Hiroshima, Japan. NIM A, in print.

[24] F. Cenna et al, "Weightfield2", 9th Trento Workshop on Innovative Silicon Detector, Genova, 2014. available at http://personalpages.to.infn.it/~cartigli/weightfield2

[25] R. Arcidiacono et al, "Timing properties of Ultra-Fast Silicon Detectors", 2nd Workshop on Detectors for Forward Physics at LHC, http://indico.cern.ch/event/295567/other-view?view=standard

[26] http://www.cividec.at/.

[27] E. Delagnes, D. Breton, F. Lugiez, R. Rahmanifard, "A low power multi-channel single ramp ADC with up to 3.2 GHz virtual clock", IEEE Trans. Nucl. Science 54 (2007) 1735.

[28] G. Kramberger et al, " Radiation hardness of Low Gain Amplification Diodes (LGAD)", 9th Trento Workshop on Innovative Silicon Detector, Genova, 2014.

[29] M. Dyndal et al, "The tracking System of APF", 2nd Workshop on Detectors for Forward Physics at LHC, http://indico.cern.ch/event/295567/session/2/contribution/9/material/slides/0.pdf

[30] R. Cardarelli, "Development of Diamond and Silicon Multi-Layer Detector and related front-end electronics, 2nd Workshop on Detectors for Forward Physics at LHC", http://indico.cern.ch/event/295567/other-view?view=standard

[31] S. Parker et al, "Increased speed: 3D silicon sensors; fast current amplifiers", Nucl. Science IEEE Transactions, Volumes 58, Issue 2, April 2011.

[32] J. Frisch *et al.*, "Status of the LCLS Experiment Timing System", Proceedings of IBIC2012, Tsukuba, Japan (2012), SLAC-PUB-15254.

[33] S. Smith SLAC, private communication, July 31, 2014.

[34] TOTEM Collaboration, "TOTEM Upgrade Proposal", CERN-LHCC-2013-009; LHCC-P-007 and "Timing Measurements in the Vertical Roman Pots of the TOTEM Experiment", CERN-LHCC-2014-020 (TOTEM-TDR-002).

[35] Bousonville, M. and Rausch, J., "Universal picosecond timing system for the Facility for Antiproton and Ion Research", Phys. Rev. ST Accel. Beams 12 (2009) 042801. http://link.aps.org/doi/10.1103/PhysRevSTAB.12.042801

[36] P. Moritz and B. Zipfel. "Recent Progress on the Technical Realization of the Bunch Phase 701 Timing System BuTiS", Conf.Proc., C110904 (2011) 418.

6 Trigger Strategy

The triggers used for CT-PPS physics are expected to capture the interesting final states in the kinematical range covered by the PPS acceptance with large efficiency (see Chapters 1 and 2). In the following discussion we distinguish leptonic and hadronic final states, and we consider separately physics processes with small and large cross-section, as the trigger strategy depends strongly on these cases.

In two-photon physics the main exclusive states are $X = e^+e^-, \mu^+\mu^-, \tau^+\tau^-$ and W^+W^- in the high mass region ($\geq$ 300 GeV), which is accessible to CT-PPS with both protons detected. The leptonic final states are captured by the full suite of CMS lepton triggers (single and double). The trigger efficiency in these cases is expected to be very high given that the lepton thresholds are at the level of 30 GeV or below. Final states with hadronic decays of one W or one tau will be accessible using the suite of lepton+jet triggers. Again, the foreseen CMS thresholds are sufficiently low to guarantee high efficiency in the kinematical region covered by PPS. Table 15, taken from the CMS L1 Trigger Upgrade TDR ([1]), shows the menu of main L1 Triggers at the instantaneous luminosity of 2×10^{34} cm^{-2} s^{-1}. In the High Level Trigger (HLT) the thresholds are 20-30% higher.

Trigger Algorithm	Rate [kHz]	95% Threshold [GeV]	Plateau Efficiency
Single e/γ	11	57	1.0
Single iso e/γ	15	31	0.9
Single Mu	14	22	0.9
Single iso Mu	15	19	0.82
Single Tau	12	100	0.95
Single iso Tau	13	83	0.7
iso e/γ + e/γ	12	23 16	0.9
(iso)Mu+Mu	9.4	15 10	0.8
(iso)Tau+Tau	7.2	64 62	0.67
iso e/γ + Mu	11	21 10	0.85
(iso)Mu + e/γ	8.3	18 15	0.83
iso e/γ + Tau	8.3	21 57	0.86
isoMu + Tau	5.8	14 47	0.8
Single Jet	5.9	205	1.0
Double Jet	4.2	130 130	1.0
Quad Jet	5.0	4@55	1.0
Single iso e/γ + Jet	11	27 78	0.9
Single Mu + Jet	9.7	18 52	0.93
Single iso e/γ + H_T^{miss}	12	27 110	0.9
Single Mu + H_T^{miss}	11	18 86	0.93
H_T	3.0	380	1.0
Total Rate	95		

Table 15: L1 trigger menu and estimated rates in Run2 (energy 14 TeV, $L = 2.2 \times 10^{34}$ cm^{-2} s^{-1}, bunch spacing of 25 ns, pile-up of 50).

In case the CT-PPS detectors could be operated at a distance from the beam smaller than the baseline of 15 sigma, increasing the acceptance at low masses ($\geq$ 100-200 GeV), the lepton and lepton+jets central triggers would need to be combined with trigger information provided by the CT-PPS detectors. Below we discuss possible strategies.

The trigger requirements for the CT-PPS jet physics are more complicated because the inclusive QCD jet background is very large, even for the relatively large jet thresholds that match to the CT-PPS mass acceptance. Jet rates above the allowed L1 or HLT bandwidth will require the addition of cuts on the protons kinematics.

At HLT, we may require events with protons detected in both CT-PPS arms. While under large pileup

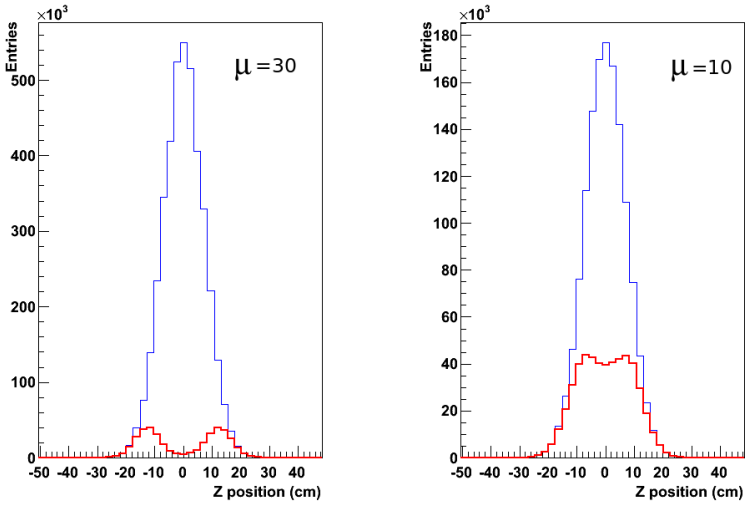

Figure 109: Longitudinal distribution of vertices for μ=30 (left) and μ=10 (right) for 100K zero-bias triggers. Blue and red curves show respectively the cumulative distribution of the vertexes and the distributions of the vertices separated by at least 1 cm from any of the others.

the rejection power of this condition alone is small, we expect a large rate reduction when requiring the kinematics of the jets to match the proton kinematics. Loose cuts on the difference between the primary vertex z-coordinate, invariant mass, longitudinal and transverse momentum of the central system as measured in the central detectors and as estimated from the two proton kinematics, could be applied at HLT. If needed the same criteria could also be applied to leptonic final states, with adaptations for the cases involving missing transverse energy.

At Level 1 (L1) there are several strategies to reduce the trigger rates [2]. The first cut to be applied is on the track multiplicity on the proton telescopes. The selection cut requires no more than two tracks per side to reduce the number of combinations. This means four possible combinations for the protons, eliminating most of the background created by the showers developed in front of the detectors. Since the tracking pixel electronics does not have a fast output for trigger purposes, we foresee to use the timing detectors for this purpose. This cut is highly efficient when the occupancy per timing pixel is small.

Additionally, we plan to implement a trigger condition that allows selecting events in the tails of the distribution of the collision z-vertex (see Figure 109). In high pileup conditions not all events can be disentangled when the primary vertex density is too high. Using the timing information of the two protons, we plan to compute at L1 an estimate of the vertex of the primary collision of interest to select a subset of events with pileup density lower than average. This approach has an increased efficiency for an unambiguous vertex reconstruction, and will allow to select high-cross section processes more effectively than by just pre-scaling the events.

As discussed in Section 5.1, a board with FPGAs is placed in the immediate proximity of the timing detector package containing also the TDCs. The embedded trigger logic can be programmed to compute the time of arrival of each hit. A pattern containing the time of arrival of (a maximum of two) timing pixels on both arms can be sent to the trigger board in the service cavern through optical links. We plan to use an existing trigger board used in TOTEM (LONEG board).

In the Trigger Board, an FPGA is dedicated to the computation of the timing variables from the timing information generated by the front-end electronics. The four time sums (absolute time of arrival) and the four time differences (Z position of the probable primary vertex) can be evaluated and a cut can be applied to remove evens containing combinations outside the region of interest. Late arrival (from the time sums) is an indication of secondary particles hits, while the z-vertex position (from the time difference) is less less likely to be disentangled from other primary vertices.

In a MC study [2], based on inclusive DPE events and with pileup $\mu = 50$, cuts on the sums and differences of the four proton arrival time combinations are applied in order to optimize the isolation of the primary vertex for a given time detector resolution (a resolution of 25 ps was assumed). In this configuration a rate of 47 kHz (RP double arm) is achieved, with a purity of the DPE sample of 0.12 and a trigger efficiency of 9%.

The LONEG board is connected with 8 bits to the L1 trigger. Originated at 210 m from the IP, a trigger signal can be included within the CMS L1 latency. The algorithms foreseen for the multi-jet final states are a combination with different di-jet trigger algorithms with the protons. An optimization of jet thresholds has to be made in function of the machine luminosity.

In a future upgrade of the timing detectors, a L1 CT-PPS trigger based on high granularity and multi-layer detectors capable to compute the two-proton kinematics and compare it with the kinematics of the centrally produced system would be desirable. The proposed R&D program includes the development of suitable integrate circuits building upon the existing TOFPET chip developed by an institute of the collaboration [3].

References

[1] CMS Technical Design Report for the Level-1 Trigger Upgrade, Technical Report CERN-LHCC-2013-011. CMS-TDR-012, CERN, Geneva, (Aug. 2013).

[2] M. Berretti, "Performance studies of the Roman Pot timing detectors in the forward region of the IP5 at LHC", TOTEM-NOTE 2014-001.

[3] M. Rolo et al., "TOFPET ASIC for PET applications", JINST 8, C02050, Feb 2013.

7 Organization, Responsibilities and Cost

7.1 Participating Institutes

The institutes of the CMS and TOTEM Collaborations presently involved in the CT-PPS project are listed below.

CMS Collaboration

1. Université Catholique de Louvain, Louvain-la-Neuve, BELGIUM
2. Universidade do Estado do Rio de Janeiro, BRAZIL
3. Centro Brasileiro de Pesquisas Fisicas, Rio de Janeiro, BRAZIL
4. IPM, Institute for Research in Fundamental Sciences, Tehran, IRAN
5. Università di Genova and INFN Sezione di Genova, ITALY
6. Università di Torino, Università del Piemonte Orientale, Novara, and INFN Sezione di Torino, ITALY
7. LIP, Laboratório de Instrumentação e Física Experimental de Partículas, Lisboa, PORTUGAL
8. Institute for High Energy Physics, Protvino, RUSSIA
9. CERN, European Organization for Nuclear Research, Geneva, SWITZERLAND
10. Fermi National Accelerator Laboratory, Batavia, Illinois, USA
11. Lawrence Livermore National Laboratory, USA
12. The University of Kansas, Kansas Lawrence, USA
13. The University of Iowa, Iowa City, USA
14. The Rockefeller University, New York, USA

TOTEM Collaboration

1. Institute of Physics of the ASCR, Prague, CZECH REPUBLIC
2. University of West Bohemia, Pilsen, CZECH REPUBLIC
3. Helsinki Institute of Physics and Department of Physics, University of Helsinki, FINLAND
4. INFN Sezione di Bari, Università di Bari and Politecnico di Bari, ITALY
5. Università di Siena and INFN Sezione di Pisa, ITALY
6. CERN, European Organization for Nuclear Research, Geneva, SWITZERLAND

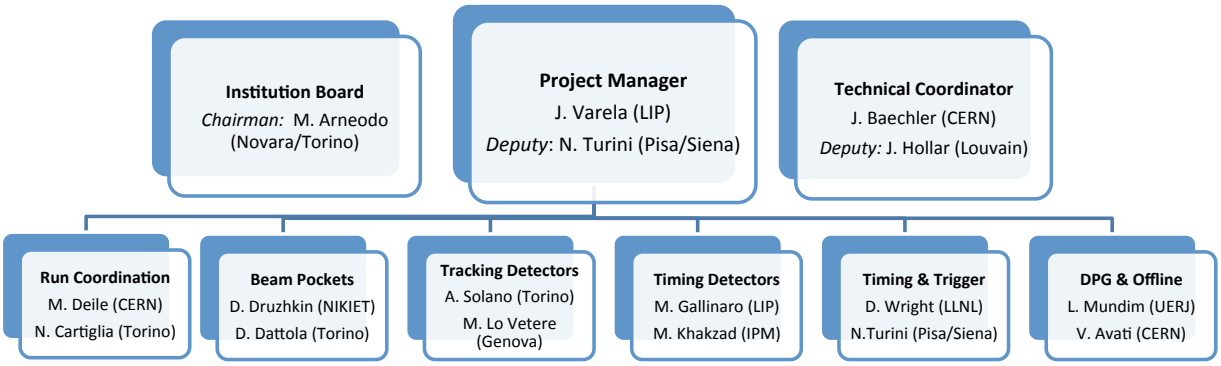

Figure 110: CT-PPS organizational chart.

7.2 Project organization

The framework and organization of the CMS-TOTEM Precision Proton Spectrometer (CT-PPS) joint project is defined in a Memorandum of Understanding (MoU) signed in December 2013 between CERN as the host laboratory and the CMS and TOTEM Collaborations. In this Section we highlight the most important aspects.

The scope of CT-PPS includes detector construction and operation, interface to CMS central DAQ and trigger, detector performance and offline software (Detector Performance Group - DPG). The CMS component of the joint project is viewed by CMS as a Sub-System, it will interface to the CMS coordination areas, and will be represented in the CMS Management and Executive Boards. The TOTEM component of the joint project is viewed by TOTEM as a Project, and as such will have an interface to TOTEM Coordination and will be represented in the TOTEM Management Board.

The CT-PPS project has an Institution Board (IB) with responsibility for the project oversight, including the provision of resources. Institutions in the CMS and TOTEM Collaborations can participate in the IB. The IB Chairperson is elected by the board.

Decisions about the programme, in particular the general planning of data taking, require the consensus of the two Collaborations through the respective managements. The procedures to be followed by Run Coordination in the day-to-day operation of CT-PPS will be defined and agreed upon by the two Collaborations. Other decisions are normally taken by consensus, and should reflect the interests of the two Collaborations. Decision procedures to be applied in the cases where consensus is not possible have been defined.

The project has a Coordination Team which is composed by:

- Project Manager and Deputy Project Manager
- Technical Coordinator and Deputy Technical Coordinator

The members of the Coordination Team are proposed by the CMS and TOTEM managements, and are endorsed by the project IB and by the CBs of the two Collaborations. The Steering Committee (SC) is formed by the Coordination Team, the IB Chairperson and the Sub-project Coordinators. The SC is chaired by the Project Manager (PM). The Sub-project Coordinators are appointed by the PM and endorsed by the IB. The CT-PPS organizational chart is presented in Figure 110. Adequate representation of both collaborations in the coordination positions is guaranteed.

The functions of the Project Manager are the following:

- To lead the CT-PPS project, taking into account the project goals and the available resources.
- To lead the SC to define a set of project milestones and then steer the project to meet them, assuring the necessary flow of resources and information throughout the project.
- To work closely with the Technical Coordinator and the Sub-project Coordinators to review technical progress and to manage the planning.
- To work closely with the IB Chairperson and Institute Representatives to make sure that the needed resources are available and that the interests of the groups are properly taken into account.
- To prepare for reviews of important technical and engineering decisions.

The IB Chairperson has the following functions:

- To prepare and chair the IB meetings.
- To oversee the project resources in coordination with Institute Representatives and PM.
- To maintain and update the project Cost Book and Funding Agencies (FA) contributions.
- To elaborate and update the cost time profile and the cost sharing among FAs.

The Technical Coordinator has the following functions:

- To assure the technical coherence, integration and operating procedures of the subsystems, infrastructure and machine interface needed to operate CT-PPS successfully.
- To oversee the installation, documentation, maintenance and upgrade of the CT-PPS experimental equipment.
- To work with the Project Manager in the preparation of technical reviews.
- To link the CT-PPS project with CMS and TOTEM Technical Coordinators.
- To link the CT-PPS project with the CERN's technical services and with the LHC machine.

The Steering Committee acts as a team to ensure that:

- Realistic and detailed plans are prepared.
- Adequate resources and supervision are committed to the different activity lines.
- The planning is consistent with the project milestones and budget.
- Technical specifications for parts and interfaces between parts of the system are established, well defined, documented and followed.

7.2.1 Physics organization

The physics analysis is organized in a dedicated group open to physicists in the CMS and TOTEM Collaborations. The group has two co-conveners with mandates of two years. The group reports to the CMS and TOTEM Collaborations at the level considered appropriate by the Collaborations. Approval and publication of results follow the rules of the current agreement on joint approvals and publications.

7.3 Responsibilities and resources

The construction responsibilities and interests of the institutes in the CT-PPS project are defined below.

- INFN/ Bari:

  Timing detectors for the vertical pots based on solid-state detectors (Si, diamond) and the corresponding reference timing system; data analysis and specifically search for resonant states.

- CERN/TOTEM

  RP, RP operation, Si strips, offline software, proton reconstruction, R&D for timing detectors. Timing systems.

- INFN/Genova

  Electronics for the tracking system downstream of the PSI46dig chip. The group can count on the support of the INFN electronics workshop in Genoa.

- LLNL

  The group has done R&D on the reference timing system in collaboration with Fermilab and the accelerator division at SLAC. The group intends to work on the reference clock design, construction, and commissioning.

- Fermilab

  Quartic detector including photosensors, mechanics and integration in the RPs.

- Helsinki

  R&D on silicon option for timing detectors (in close collaboration with the Helsinki CMS silicon detector upgrade group). Participation in assembly and testing of solid state timing detector modules.

- IHEP (Protvino)

  Quartic (sapphire and quartz bars), Monte-Carlo simulation for Quartic, difractive processes Monte-Carlo generators, data analysis.

- Iowa

  The group will work closely with Fermilab on the following subjects. Test beam measurement of the Quartic detector. Manufacturing of Quartz bars, mechanics and readout system. SiPM photodetectors. Interested in the engineering of the movable pipe design, on the detector simulation, on the TB data analysis and the TB instrumentation and data taking.

- LIP, Lisbon

  Readout system for the Cherenkov Timing Detectors: the group is working in the design of the timing readout system, will develop the timing readout hardware project, and will contribute to the timing readout firmware/software and commissioning. R&D on integrated circuits for solid state timing detectors. Timing detector simulations.

- Louvain

  Geant4 simulation of GasToF detectors. Contribute (in collaboration with Teheran) to Geant4 simulation of MBP. Design of new GasToF prototype for TB studies. Design of the new GasToF detectors with multi-anode MCP-PMTs: short version for installation in Roman Pots and long one for MBP; test beam data taking and analysis.

- Pilsen

  Timing system reference clock and the development of the corresponding radiation-tolerant electronics.

- Prague

  Cooling for the new RP (the 'vortex' system based on decompression of air, no moving parts).

- Rio/CBPF

  Trigger studies. Offline software. Offline database.

- Rio/UERJ

  The group is interested in various aspects of the project, from timing to tracking and infrastructures. Timing backend system and frontend firmware. The group has strong ties to CBPF and UNICAMP.

- Rockefeller

  The group will work on physics analysis and MC development.

- Siena

  Development of the clock distribution system (together with the Bari group); R&D of solid state timing detectors (diamonds etc). The group is also interested in developing front-end electronics for solid state timing detectors and in the development and integration of proton trigger.

- Tehran/IPM

  The group is interested in the Geant4 simulation of Gastof and the movable beam pipe; it is also willing to participate to test beams, MCP-PMT testing and to contribute to the readout of the timing detectors.

- Torino/Novara

  The fields of interest include: 3D sensors and front-end electronics for the tracking system, development of novel timing detectors and design/prototyping work for the movable beam pipe.

Material and manpower resources for detector development and construction are provided by the institutes in the IB. Resources for infrastructure are provided from the common project and Maintenance and Operation (M& O) budgets of the two Collaborations, administered by the respective Technical Coordinators.

The material resources required during and beyond the exploratory phase are provided by the Collaborations with the following indicative partition:

- CMS: tracking detectors (pixels), timing detectors, clock distribution, trigger/DAQ, Movable Pipes and associated infrastructure.
- TOTEM: tracking detectors (silicon strips), trigger/DAQ, timing R&D, clock distribution, Roman Pots and associated infrastructure

The human resources and contributions provided by the CT-PPS institutes are summarized in the Tables 16 and 17. A summary of the participation of institutes in CT-PPS sub-projects is given in Table 18.

	Core Team	Technical support	Main contributions	Other contributions	IB contacts
CMS					
Belgium					
Louvain	3 physicists 1 student		Offline software Gastof detector Gastof and MBP simulation		krzysztof.piotrzkowski@cern.ch jonathan.jason.hollar@cern.ch
Brazil					
UERJ	6 physicists 3 students 1 engineer		Offline software Timing backend system and frontend firmware	Tracking sensor testing	alberto.santoro@cern.ch luiz.mundim@cern.ch
CBPF	4 physicists		Offline software		gilvan.augusto.alves@cern.ch maria.elena.pol@cern.ch
CERN					
CMS TC group		1 engineer	RP mechanics engineering/craftmanship		
Italy					
Torino	6 physicists 1 student		Tracking pixel sensors MBP design and prototyping	Pixel ROC and assembly	cartiglia@to.infn.it arneodo@to.infn.it
Genova	3 physicists	Electronics technician	Pixel ROC and assembly Pixel readout system	Tracking pixel sensors Pixel backend and DAQ	Fabrizio.Ferro@ge.infn.it maurizio.lo.vetere@cern.ch
Iran					
IPM	4 physicists 2 students		Geant simulations. Readout system of the Cherenkov Timing Detectors		
Portugal					
LIP	3 physicists 3 students	1 engineer	Readout system of the Cherenkov Timing Detectors	Timing backend and DAQ R&D on IC for solid state timing detectors	joao.varela@cern.ch Michele.Gallinaro@cern.ch
Russia					
IHEP Protvino	5 physicists		Generators. Simulation software. Quartic detector.		Vladimir.Petrov@cern.ch Roman.Rioutine@cern.ch
US					
Fermilab	1 physicists, 1 engineer		Quartic timing sensors, including photosensors and mechanics		albrow@fnal.gov butler@fnal.gov
Livermore	2 physicists		Reference clock system		wright@cern.ch
Kansas	1 physicist		Quartic detector		mjmurray@ku.edu
Iowa	2 physicists 2 engineers		Quartic detector		f-ingram@uiowa.edu yasar-onel@uiowa.edu
Rockefeller	2 physicists		Simulation		dino@rockefeller.edu

Table 16: Human resources and contributions provided by the CT-PPS institutes in CMS.

7.4 Planning and cost estimate

The CT-PPS plan includes an exploratory phase in 2015-16 followed by a production phase until LS2. The objectives of these two phases have been presented in Section 1.1.

In 2015 we will use in each arm of the spectrometer two old RPs with new RF shields housing available TOTEM silicon strip detectors, and one new cylindrical RP housing two quartic modules. The Quartic detectors will be installed in the second half of 2015 during a technical stop.

At the year-end technical stop 2015-16 the new pixel detectors would replace the silicon strips. The plans of installation of timing detectors for operation in 2016 will depend on the results of the evaluation in beam of the prototypes (see Sections 5.3, 5.5 and 5.6). Provided that the R&D is successfully concluded, a MBP structure could also be installed for tests in 2016. Detailed plans for this installation have not yet been defined.

7.4.1 Cost estimate of baseline detector

The cost estimates of the CT-PPS detector are summarized in Table 20. It should be noted that these cost estimates are for Materials and Services (M&S) only. In this estimate we have considered the baseline detector, including the following costs:

	Core Team	Technical support	Main contributions	Other contributions
TOTEM				
CERN	6 physicists, 1 engineer, 2 students		RP Design, R&D, Interfaces to LHC, Operation, Edgeless Si Strip Tracking, Offline Software (in particular forward proton reconstruction), Physics Analysis, R&D Timing Detectors	Verification of movable beam pipe components. Timing systems.
Czech Republic Prague	2 physicists		Cooling.	
Pilsen	3 engineers, 2 students		Time reference, trigger and Readout Electronics.	
Finland Helsinki	1 physicist, 2 students		Solid State Timing detectors. Physics Analysis.	
Italy (INFN) Bari	4 physicists, 1 engineer, 2 students		Cabling infrastructure, Time reference (option Optical Fibers), Solid State Timing detectors, Readout and DAQ. Data analysis.	
Pisa/Siena	4 physicists, 2 engineers, 1 student		Cabling infrastructure, Time reference (option Optical Fibers), Solid State Timing detectors, Trigger electronics and firmware.	Offline Software (in particular detector simulation)
Collaboration CommonFund	2 engineers, 1 student		Electronics, Controls.	Firmware

Table 17: Human resources and contributions provided by the CT-PPS institutes in TOTEM.

1. Final prototype or pre-production fabrication required to validate a final design or product quality, prior to production.
2. Engineering costs incurred during production at a vendor or contractor, not at a CMS and TOTEM member Institution.
3. Production fabrication and construction costs, including quality assurance and system testing during the assembly process.
4. Transportation costs, integration and installation.

The TOTEM expenditure executed in 2013-14 on the Roman Pot project is summarized in Table 21. It includes:

1. The cost of the relocation to the 210m region of the 4 (out of 12) RPs used by CT-PPS tracking detectors, as well as the cost of the new RF shielding;
2. The cost of two new cylindrical RPs for the CT-PPS timing detectors, including the movement system (motors and control), RP infrastructure (cables, cooling, vacuum, LV), and ferrites (fabrication, machining, bake out, cleaning).

	Infrastructure	RP	MBP	Tracking sensors	Tracking readout	Timing sensors	Timing readout	Trigger & timing	Offline SW
CMS									
Belgium									
Louvain			x			x			x
Brazil									
UERJ					x		x		x
CBPF									x
CERN									
CMS TC group	x	x	x						
Italy									
Torino			x	x	x	x			
Genova				x	x				x
Iran									
IPM			x				x		x
Portugal									
LIP						x	x	x	x
Russia									
IHEP Protvino						x			x
US									
Fermilab						x			
Livermore								x	
Kansas									
Iowa						x	x		
Rockefeller									x
TOTEM									
CERN	x	x	x			x		x	x
Czech Republic									
Prague	x	x							
Pilsen						x		x	
Finland									
Helsinki						x			x
Italy (INFN)									
Bari	x					x		x	x
Pisa/Siena	x					x		x	x
Collaboration									
CommonFund	x								

Table 18: Summary of the participation of institutes in CT-PPS sub-projects.

These values include the costs of CERN services manpower. The manpower from the TOTEM collaboration having contributed to the project are not accounted for.

The TOTEM contributions to the silicon strip detectors to be used in 2015 and to the reference timing system are not included in the tables, neither the original cost of the four relocated RPs housing the tracking detectors.

In this chapter, all monetary values are expressed in CHF. The following conventional exchange rates have been used to convert EUR and USD to CHF:1 USD = 1.0 CHF; 1 EUR = 1.2 CHF.

7.4.2 Objectives, plans and cost of R&D programme

Besides the construction of the baseline detectors, we propose to carry the R&D programme on Movable Beam Pipes and Timing Detectors described in Sections 3.6, 5.3, 5.5 and 5.6. In Table 19 we summarize the physics motivations, objectives and time scale of the proposed R&D programme.

The results of the R&D programme will be evaluated in reviews to be carried out in the falls of 2015, 16 and 17. These reviews will establish the basis for the decisions on the detector configuration to be used in the following year(s).

We have estimated the cost of the development of prototypes of the new Timing Detectors and of proto-

types of Movable Beam Pipes (Table 22). Cost estimates of the construction of final versions of any of these items will be established after the evaluation of prototypes and the choice on the possible upgrades.

We have included in the Table 22 the cost of two additional cylindrical chambers, RP cylinder and ferrites, integrated in present stations, to accommodate new timing detectors in 2016.

7.4.3 Expected funding and cost sharing

The global cost of the project is expected to be borne by all institutions participating in the project. Discussions with the Funding Agencies are ongoing to define the sharing of the total project cost.

Table 19: Physics motivations, objectives and time scale of the proposed R&D programme.

Area	R&D item	Physics motivation	Objectives	Time scale
Timing detectors	Ultimate rejection of pileup background requires time resolution of 10 ps (factor 2 better than the Quartic baseline), cell size ~1mm^2 close to the beam (factor 10 smaller than Quartic baseline), and electronics with trigger capabilities (overcoming the limitation imposed by the triggerless pixel frontend).		Timing detectors with time resolution of 10 ps, with material less than few % nuclear interaction, and with high granularity. Trigger system based on proton kinematics.	
	High granularity Quartic	Quartic bars w/ 10 times smaller cross section allowing to reduce the double hit induced inefficiency to a negligible level.	Upgrade the central 3x3 mm^2 quartz bars of the baseline detector with bars of ~1mm^2 cross section. Study of optical wrapping and small area SiPM s.	R&D concluded in 2015
	Gastof prototypes	Excellent time resolution and thin material in the protons path. Intended for use in association with high granularity detector capable to add multi-hit discrimination.	Build a prototype detector for evaluation in test beam in 2015. If successful, build a second detector for installation in 2016 in both arms of PPS.	R&D concluded in 2015
	Diamond prototypes	Thin and fast detector technology. High granularity required for multi-hit discrimination. Allows trigger system based on proton kinematics.	Evaluate prototype detectors and fast electronics in test beams. Demonstrate resistance to 100 fb^{-1}. Demonstrate high rate capability.	R&D concluded in 2016/17
	Timing silicon prototypes	Thin and fast detector technology. High granularity required for multi-hit discrimination. Allows trigger system based on proton kinematics.	Evaluate prototype detectors and fast electronics in test beams. Demonstrate resistance to 100 fb^{-1}. Demonstrate high rate capability.	R&D concluded in 2016/17
	Trigger integrated electronics	Trigger system based on proton kinematics matching the central system allowing to reduce the central trigger thresholds.	Integrated electronics allowing trigger based on mm^2 granularity detector.	R&D concluded in 2016/17
Beam pockets	Moving Beam Pipes prototypes	Beam pocket with low RF impedance.	Build a MBP prototype for installation in the beam during the winter break of 2015-16.	R&D concluded in 2016/17

Area	Item	Cost (kCHF)
Tracking detector	Sensors	150
	Front-end electronics	60
	Back-end system	30
	Mechanics	10
	Services	20
	Tracking detector total	***270***
Timing detector	Sensors & mechanics (Quartic)	40
	Front-end electronics	60
	Back-end system	30
	Services	70
	Timing detector total	***200***
Timing & Trigger	Reference timing system	40
	Trigger system	40
	Timing & Trigger total	***80***
	Grand Total	**550**

Table 20: Estimated cost of the baseline CT-PPS project.

Area	Item	Cost (kCHF)
RP Infrastructure *)	Tracking RPs: Relocation of four RP stations. RP Faraday cages.	87
	Timing RPs: Two cylinder RPs stations. Prototypse and final production. Movement system. Infrastructure (cables, cooling, vacuum, LV). Ferrites.	322
	Development	29
	RP Infrastructure total	***438***

*) Cost includes CERN services manpower

Table 21: TOTEM expenditure executed in 2013-14 on the Roman Pot project.

Area	Item	Cost (kCHF)
Timing detectors	High granularity Quartic	30
	Gastof prototypes *)	70
	Diamond prototypes	50
	Timing silicon prototypes	50
	Timing integrated electronics	50
	Timing R&D total	***250***
Beam pockets	Moving Beam Pipe prototype mechanics	30
	MBP motorization (for one prototype)	50
	Two additional cylindrical RPs	70
	Beam pockets R&D total	***150***
	Grand Total	***400***

*) Cost corresponds to two detectors (2x 35 kCHF). The second detector will be built after results of the TB measurements

Table 22: Cost estimates of R&D prototypes.